Molecular Engineering of Polymer Semiconductors for Electronics and Photonics

Ye-Jin Hwang

A dissertation
submitted in partial fulfillment of the
requirements for the degree of

Doctor of Philosophy

University of Washington
2015

Reading Committee:
Samson A. Jenekhe, Chair
Qiuming Yu
Christine K. Luscombe

Program Authorized to Offer Degree:
Department of Chemical Engineering

University of Washington

Abstract

Molecular Engineering of Polymer Semiconductors for Electronics and Photonics

Ye-Jin Hwang

Chair of the Supervisory Committee:
Samson A. Jenekhe
Department of Chemical Engineering

There has been tremendous progress in the development of conjugated polymer semiconductors in the last two decades for diverse applications in organic electronics and photonics. Most notably, advances in *p*-type (*hole-conducting*) polymers have enabled the development of high-performance organic field-effect transistors (OFETs) as well as more efficient fullerene-based organic photovoltaics (OPVs). In contrast, *n*-type (*electron-conducting*) polymer semiconductors remain relatively scarce and consequently the performance of *n*-channel OFETs and all-polymer solar cells has lagged far behind *p*-channel OFETs and fullerene-based OPVs. This dissertation mainly focuses on the design and synthesis of new *n*-type polymer semiconductors for device applications in *n*-channel OFETs and non-fullerene OPVs. It aims to achieve better understanding of the relationships between molecular structure, processing, morphology, and device performance.

New *n*-type polymer semiconductors were developed based on strong electron withdrawing naphthalene diimide (NDI) building block with various selenophene derivatives as co-monomers. The resulting highly crystalline poly(naphthalene diimide)s (PNDIs) gave the electron mobility as high as 0.24 $\mathrm{cm^2/Vs}$ in *n*-channel OFET measurements in air which is comparable or even higher mobility compared to most of the *p*-channel transistors. Using NDI-selenophene copolymer, PNDIS-HD, as acceptor, a photovoltaic performance with a power conversion efficiency (PCE) of 3.3 % (J_{sc} = 7.78 $\mathrm{mA/cm^2}$, V_{oc} = 0.76 V, FF = 0.55) was achieved in all-polymer solar cells, and this work has stimulated a lot of current interest in *fullerene-free* OPVs.

In further studies in all-polymer solar cells, highly enhanced photovoltaic performance was achieved by chemical modifications of acceptor polymers and controlling self-organization kinetics of polymer/polymer blend films. From these studies, a critical role of the bulk crystallinity of acceptor polymer was revealed, and provided an important criterion for the molecular design of high performance polymer acceptors. Furthermore, all-polymer solar cells with more favorable bulk morphology by slow self-organization of polymers facilitated by room temperature film aging resulted in enhanced charge carrier mobility and photocurrent. Resulting all-polymer solar cells with PCE over 7 % showed a great potential of non-fullerene solar cells and demonstrated for the first time a viable alternative pathway to organic photovoltaics.

TABLE OF CONTENTS

LIST OF FIGURES

LIST OF CHARTS

LIST OF SCHEMES

LIST OF TABLES

ACKNOWLEDGEMENTS

I wish to express my sincere gratitude to Professor Samson A. Jenekhe, my PhD dissertation advisor, for his guidance and support. His insightful comments and suggestions have been indispensable to the completion of my research, and his valuable life advices have helped me to grow into a better person. I also appreciate Professors Qiuming Yu, Christine K. Luscombe, Cole DeForest, Lilo D. Pozzo, and Qifeng Zhang for their time serving on my committee and for providing valuable suggestions.

I would like to thank the following past and present members of the Jenekhe research group: Dr. Taeshik Earmme, Dr. Felix Sunjoo Kim, Dr. Pei-Tzu Wu, Dr. Selvam Subramaniyan, Dr. Haiyan Li, Dr. Nishit Murari, Dr. Soon-Ok Jeon, Dr. Eilaf Ahmed, Dr. Guoqiang Ren, Dr. Hao Xin, Dr. Takahiro Kojima, Prof. Taewoo Kwon, Prof. Unyong Jeong, Yujeong Lee, Emily Hollenbeck, Matthew J. Crane, Brett A. E. Courtright, Frank N. Eberle, Xiaomei Ding, Dr. Daiki Kuzuhara, and Thao Nguyen. They have influenced my research and life through insightful discussions, succeessful collaborations, encouraging each other, and sharing happy moments.

I would like to acknowledge the Department of Chemical Engineering at UW, the National Science Foundation, the Office of Naval Research, the U.S. Department of Energy, Basic Energy Sciences, and Solvay S. A. for financial support of different parts of this research.

Finally, I would like to take this opportunity to express my gratitude and love to my parents, my brother, and my entire family and friends in Korea for their unconditional love, support, and encouragement. Without them, this work would not have been possible.

Chapter 1. INTRODUCTION

1.1 BACKGROUND

In 1977, Alan MacDiarmid, Hideki Shirakawa, and Alan J. Heeger discovered conducting polymers, which triggered intensive studies on this new generation of polymers that exhibit semiconducting electrical and optical properties.[1] Applications of the new materials in organic electronics and photonics, including organic light emitting diodes (OLEDs), organic field-effect transistors (OFETs), and organic photovoltaics (OPVs), have gained enormous attention due to their attractive mechanical properties (light weight, flexibility, transparency) and cost effective solution processibility, which are more attractive for future low cost organic electronics and solar energy technologies than conventional metals or inorganic semiconductors.[2]

There has been remarkable progress in the development of polymer semiconductors for organic electronics and photonics in the last two decades. However, there is large disparity between advances in *p*-type (hole-conducting) polymer semiconductors and *n*-type (electron-conducting) polymer semiconductors. *n*-Type polymer semiconductors have been relatively scarce compared to *p*-type polymer semiconductors, and consequently the performance of *n*-channel OFETs has lagged far behind *p*-channel OFETs. Similarly, the performance of all-polymer solar cells, composed of both donor and acceptor polymers, has lagged far behind fullerene-based OPVs. Yet, fullerene-based electron acceptors which are currently widely used in OPVs have significant disadvantages such as limited light absorption in the visible region, poor thermal/photochemical stability, poor morphology control, and high cost.[3] The development of suitable *n*-type semiconducting polymers is thus of great interest in the fields of organic electronics and OPVs.

1.2 Π-CONJUGATED POLYMER SEMICONDUCTORS

π-Conjugated polymer semiconductors have been extensively investigated due to their attractive mechanical, electrochemical, and optoelectronic properties that can be utilized in diverse electronics and photonics, such as organic light emitting diodes (OLEDs), organic field-effect transistors (OFETs) and organic photovoltaics (OPVs).[1]

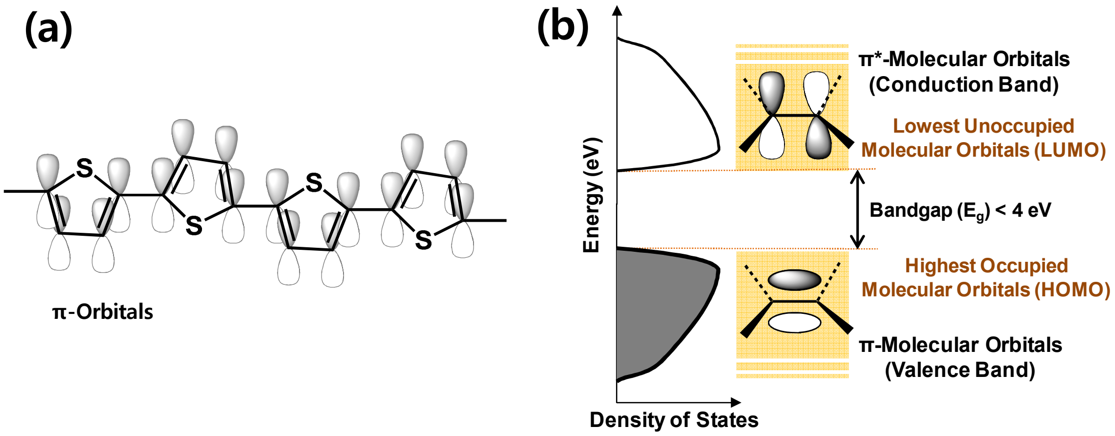

Figure 1. (a) Schematic of π-conjugation in a representative example of polymer Semiconductor, polythiophene. (b) Schematic of electronic energy-density of state diagram of a π-conjugated polymer semiconductors.

π-Conjugated polymers have alternating single and double bonds, and π-orbital overlap leads to electron delocalization along the poymer backbone and provide charge carrier path (**Figure 1**). According to the molecular orbital (MO) theory, two carbon atoms form bonding orbital and antibonding orbital, and thus π-band is divided into π (valence) and π* (conduction) band. Since one band can hold two electrons, π band is completely filled with electrons while π* band is empty. The energy difference between the highest occupied molecular orbital (HOMO) in the π band and the lowest unoccupied molecular orbital (LUMO) in π* band is the energy bandgap (E_g). E_g of conjugated polymers is finite (not zero) due to the bond length alternation (Peierls Instability Theory). Thus, conjugated polymers are intrinsic semiconductors and have unique properties, including conductivity, photoconductivity, luminescence, fluorescence, charge transport, and redox properties.[4]

Using polymer semiconductors in electronics and photonics can offer many advantages over using inorganic semiconductors.[5] Not only the low cost of the materials, but also the solution processibility of polymers enables the low cost and large area roll-to-roll device fabrication processing. Polymer semiconductors are mechanically flexible and have light weight that can be beneficial for the future technology. The most attractive feature of polymer semiconductors is that the E_g is readily tunable by molecular design, and thus their electrochemical and optical properties can be tuned by molecular engineering (molecular design and device engineering). The molecular factors that determine the energy bandgap include conjugation length (π-electronic delocalization length), backbone planarity, intermolecular orbital interections, intramolecular charge transport, resonance energy of aromatic and quinoidal forms, and electron donating/electron withdrawing strength of monomers[6].

Depending on the major charge carrier, conjugated polymer semiconductors can be classified as either *p*-type (*hole-transporting*) or *n*-type (*electron-transporting*). The majority of the polymer semiconductors is *p*-type, and advances in the synthesis of diverse *p*-type polymers have enabled the development of high-performance OFETs[7] with a hole mobility over 10 cm^2/Vs as well as more efficient fullerene-based single junction OPVs[8] with a power conversion efficiency (PCE) over 10 %. In contrast, *n*-type polymer semiconductors remain relatively scarce due to the scarcity of building blocks and synthetic difficulties, and thus the performance of *n*-channel OFETs (< 1 cm^2/Vs) has lagged far behind *p*-channel OFETs. Similarly, the performance of all-polymer solar cells, which utilize *n*-type polymers as acceptors, has lagged far behind fullerene-based OPVs. Therefore, the development of suitable *n*-type polymers is of great interest in contemporary polymer chemistry and the fields of organic electronics and photonics.

1.3 ORGANIC ELECTRONICS AND PHOTONICS

1.3.1 *Organic Field-Effect Transistors*

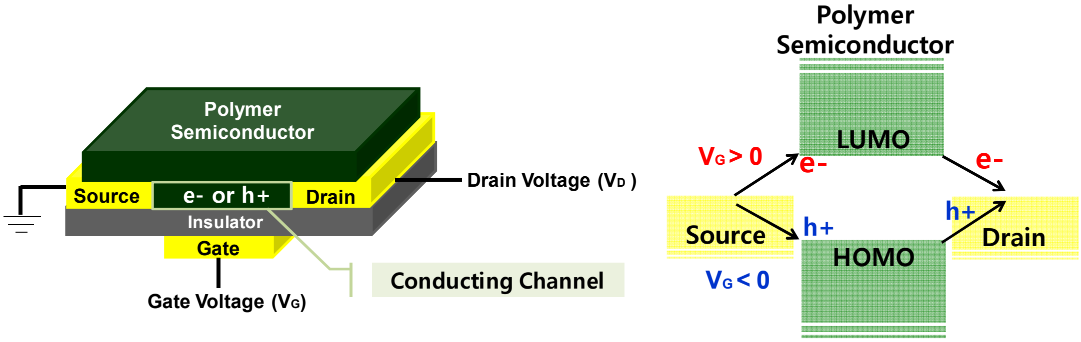

Figure 2. Operation mechanism of organic field-effect transistors.

Organic field-effect transistors (OFETs) represent one of the important building blocks for developing organic electronics due to their switching characteristics with three electrodes, including source, drain, and gate.[9] Organic semiconductors bridge the source and drain, and generate the conducting channel upon applying gate voltage. Once electric-field is formed by applying drain voltage, charge carriers (holes or electrons) are flow from source to drain. In the case of *p*-channel OFETs, gate voltage is negatively charged and holes travel through the HOMO level of the polymer semiconductor as charge carriers while *n*-channel OFETs operates with positive gate voltage and electron charge carriers travel through the LUMO level of the polymer semiconductor (**Figure 2**).

Important parameters of OFETs are charge-carrier mobility (μ), threshold voltage (V_{th}), and current on/off ratio (I_{on}/I_{off}). Charge-carrier mobility means how fast charge carriers can move through the channel, threshold voltage indicating how fast the transistor can be switched on, and current on/off ratio is the difference of source-drain current between on-state and off-state. Thus, high performance OFETs indicates high charge carrier mobility and large current on/off ratio with small threshold voltage. The charge-carrier mobility can be calculated from the slope of the transfer curve ($(I_{ds})^{-0.5}$ versus V_{gs}) in the saturation region using the equation: $I_{ds} = (W/2L)\ \mu\ C_i(V_{gs} - V_t)^2$, where I_{ds} is the drain-source current in the saturated region, W/L is the channel width to length ratio, μ is the field-effect mobility, C_i is the capacitance per unit area of the dielectric layer (17nF/cm^2), whereas V_{gs} and V_t are the gate and threshold voltages, respectively.[10]

To design and synthesize new polymer semiconductors for OFETs, there are several important factors that should be considered. The most important factor is a solid state packing structure and crystallinity of polymers. For better performance in OFETs, high degree of order and short packing distances (π-stacking distance and lamellar packing distance) with high crystallinity of polymers are highly desired, and high conjugation length (high molecular weight of polymers) and backbone planarity can affect those features. To achieve planar polymer backbone, it is important to choose the rigid monomers as well as the side alkyl chains with right length and distribution. For example, long and branched alkyl side chains are generating larger steric hindrances that can decrease the planarity of the polymer backbone compared to the short and linear alkyl side chains. Since solution processibility of the polymer semiconductors is another important factor, it is important to find right size of the side chains that can provide sufficient solubility while keeping the backbone planarity. As an effort to make rigid monomers, covalently bridged monomers or ladder type monomer units have been developed.[11]

In addition to the solid state packing structure of the polymers, electronic structures of polymers are other important factors in the application of OFETs to lower the hole and electron injection barriers. For *p*-channel OFETs, conjugated polymers with sufficiently high lying HOMO energy levels or low ionization potential (IP) (IP ≤ 5.3 eV) can facilitate hole injection from the typical source and drain gold (Φ ≈ 5.2eV) electrodes. In the case of *n*-channel OFETs, conjugated polymers with sufficiently low lying LUMO energy levels or high electron affinity (EA) (EA ≥ 3.8 eV) will allow injection of electrons from gold or aluminum (Φ ≈ 4.3 eV) electrodes. Removing the charge trapping sites in the device is also important to enhance the performance of OFETs. The performance of OFETs can also be limited by the trapping sites from the impurities of materials and end-groups (−Br or –Sn(Me)$_3$) of polymers that comes from the Stille coupling or Suzuki coupling polymerizations.[12] These end-groups can be easily removed by end-capping reactions, and significantly enhanced charge carrier mobilities have been observed as an end-capping effect.[13]

1.3.2 *Organic Photovoltaics*

Among the most important scientific challenges facing society today is finding a way to meet the energy needs of the world's growing population via an environmentally sustainable paradigm.[14] Organic photovoltiac (or solar cell) is of great interest due to potential to provide a low-cost, light-weight, and flexible source of renewable energy as a semiconductor device that converts absorbed sunlight (photons) into electricity.[15] Considerable research effort on photovoltaic materials and devices has led to much progress in the last two decades. However, energy from current photovoltaic technologies is too expensive compared with that from fossil fuels. Novel materials and devices that could potentially revolutionize solar energy conversion technologies, making them cost-competitive with fossil fuels, are needed.

Typical bulk heterojunction (BHJ) OPVs consist of two electrodes (anode and cathode) and an active layer, which is a binary blend of donor (*p*-type) and acceptor (*n*-type) organic semiconductors, in between them as shown in **Figure 3**, and additional hole and electron transporting layers of conductive polymers or metal oxides. OPVs operate in following four key steps: (i) absorption of photons and exciton generation, (ii) charge separation, (iii) charge transport, (iv) charge collection (**Figure 3**). In active layer (organic semiconductors), absorbed photon with a larger energy than the E_g of organic semiconductors, excite electron from the valence band to the conduction band and generate exciton which is a bound electron-hole pair. This exciton diffuses to the donor/acceptor interfaces in the active layer and dissociated to charges (hole and electron) by either electron or hole transfer using the HOMO/LUMO energy level offsets between donor and acceptor as a driving force. Separated charges are now transported through donor and acceptor phases, respectively, and hole is collected at the anode and electron is collected at the cathode.

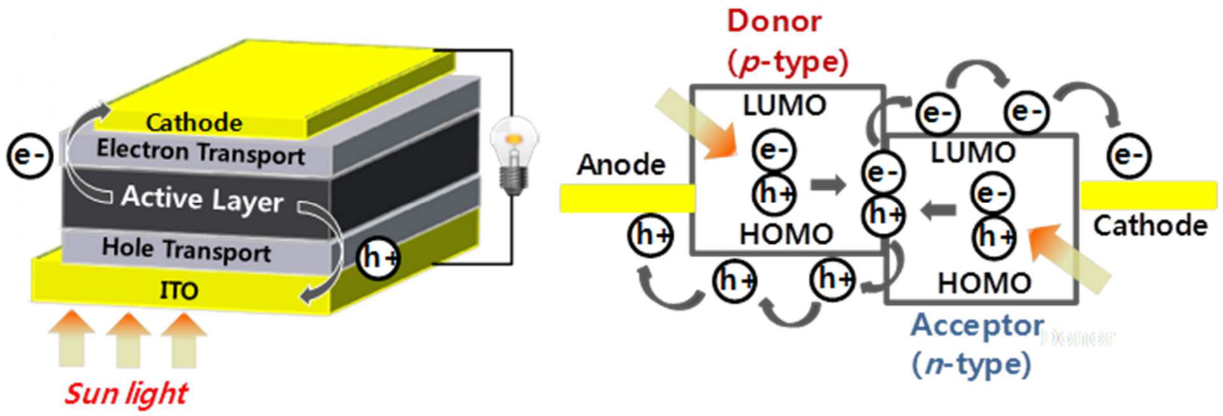

Figure 3. Simplified conventional OPV device structure and operation mechanism of OPVs.

Important parameters of organic photovoltaics are short circuit current (J_{sc}), open circuit voltage (V_{oc}), and fill factor (FF), which determine the overall power conversion efficiency (PCE): PCE $= \frac{J_{sc} \times V_{oc} \times FF}{P_{in}}$. J_{sc} is the current that flows through the solar cells when the voltage across the device is zero (no external bias applied), due to the light generated current. V_{oc} is the maximum voltage available in solar cells, and closely related to the energy difference between the HOMO energy level of donor and the LUMO energy level of acceptor. FF is defined as the ratio of the maximum power from the solar cell to the product of V_{oc} and J_{sc}. FF is determined from the competitive process between sweep-out and charge carrier recombination.

Each photoconversion process of OPV devices has to be optimized to achieve high photovoltaic parameters and thus high PCE. First, the light harvesting can be maximized by using active layer which has a broad light aborption in the visible and near infrared region with small energy bandgap and high absorption coefficient. There has been a tremendous effort to reduce energy bandgaps of donor polymer semiconductors, and has been successful by manipulating D-A approaches[16], which contains electron donating and electron withdrawing moieties in on polymer backbone. Second, the thin film morphology of the active layer should be controlled to prevent geminate (exciton) and bimolecular (charge) recombination. The excitons generated in current organic/polymer semiconductors are Frenkel excitons which have large binding energies (~1.0 eV) and a short diffusion lengths (10 – 20 nm).[17] Thus, small phase separated domains of donor and acceptor within exciton diffusion length is crucial to prevent the geminate recombination, and domains should be well interconnected for efficient charge transport by preventing bimolecular recombination and enhancing the charge carrier mobility. Third, the HOMO/LUMO energy level offsets of donor and acceptor should be large enough (≥ 0.3 eV) for efficient charge separations. Finally, ohmic contact should be provided to minimize the contact resistance and enhance charge collection efficiency.

1.4 MOLECULAR ENGINEERING: MOLECULAR DESIGN & DEVICE ENGINEERING

The performance of OFETs and OPVs depends largely on the molecular structure and material properties of conjugated polymer semiconductors as well as device processing conditions. The MSE (Materials Science and Engineering) tetrahedron applied to conjugated polymer semiconductors for OFETs and OPVs (**Scheme 1**) shows intimate relationships between the four fundamental aspects, including performance, molecular structure, material properties, and device processing. Understanding the correlations between those four aspects by molecular engineering is thus crucial to overcome the challenges and achieve high performance in conjugated polymer devices. Material properties are readily tunable by molecular design and synthesis, and device processing conditions should be optimized based on the material properties to maximize the performance.

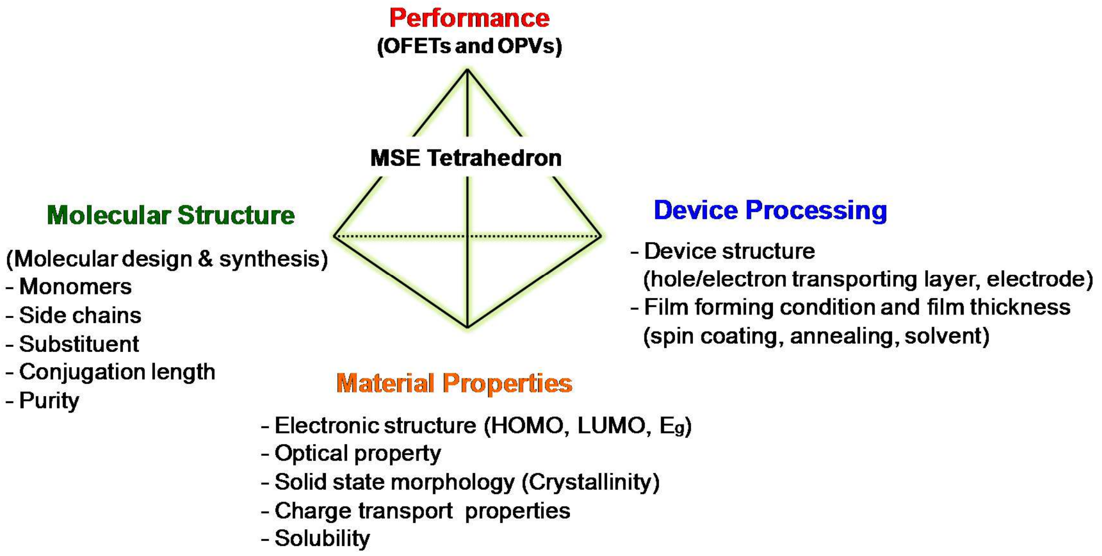

Scheme 1. MSE tetrahedron as applied to conjugated polymer semiconductors for OFETs and OPVs.

There are many molecular design factors that are known to affect largely on the material properties, including electronic structure, optical properties, solid state morphology, crystallinity, charge transport properties, and solubility. The most important factor is the choice of the monomer since the monomer governs the properties of resulting polymer. Depending on the electron donating or electron withdrawing strength of monomer, electronic structures can be tuned, and thus energy bandgap and optical properties can be controlled. Various substituents can be attached to the monomer at the post polymerization step, and give a large impact on the monomer properties as well. In addition, resulting HOMO/LUMO energy levels decide charge transport properties (electron transporting (*p*-type), hole transrporting (*n*-type), or ambipolar charge transport) of polymers. The size and distribution of the alkyl side chains should be carefully considered to control the backbone planarity and crystallinity of polymers while maintaining a sufficient solubility on common organic solvents for solution processibility. A long and bulky alkyl side chains provide a good solubility, but bulky side chains close to each other tend to cause large steric hindrance and thus disturb the backbone planarity leading to the highly disordered solid state morphology and low crystallinity.

In addition, a significant effect of the molecular weight dependence of performance in OFETs and OPVs that is originated from the extended conjugation length and increased crystallinity with increased molecular weight, has been studied.[18] Finally, the performance in both OPVs and OFETs is extremely sensitive to the material purity unless polymers have unavoidable molecular weight distribution due to the nature of step growth polymerization that has been widely used for conjugated polymer synthesis. Possible impurities in conjugated polymers are the remaining palladium catalysts, end groups (bromide, boronic ester, or trimethyl tin complexes), and unreacted monomers. Experimental studies have reported that more than a factor of two decrement in power conversion efficiency was observed with 0.2 % of impurity in the system,[19] and a large (3.4 fold) enhancement in the field-effect mobility was observed with end-capped conjugated polymer by minimization of the possible charge trapping sites with reduced end-groups.[20]

For further enhancement of the performance in OFETs and OPVs, device engineering is an essential step to optimize the thin film morphology and reduce the charge collecting barriers.

Diverse device processing conditions have been successfully applied for controlling the morphology of the OFET and OPV devices. One of the critical factors that affects on the film morphology is processing solvent. The morphology of the active layer can be significantly modified by spin-coating of films from different solvents or co-solvent system due to the different solvent evaporation rate as well as the different solubility between donor and acceptor components. The self-organization and phase separation kinetics of polymer blend films can also be controlled by using various annealing conditions, including thermal annealing, solvent vapor annealing, self-assembly of polymer nanowires, and use of processing additives. The charge collecting barriers can be reduced by using metal electrodes with different work functions and additional hole or electron transporting organic (PEDOT:PSS) or metaloxides (ZnO, TiO_2) layers to reduce the electrode/active layer energy gap and to improve the surface morphology for better contact. In addition, surface modifiers, such as ethanolamine and polyethylenimine, that modify the work function of metals or metal oxides by forming strong interface molecular dipoles have been frequently used.

1.5 MAJOR CHALLENGES AND RESEARCH OBJECTIVES

1.5.1 *Major Challenges*

There has been tremendous progress in the synthesis and development of π-conjugated polymer semiconductors for diverse applications in OFETs and OPVs in the last two decades. Charge carrier mobility of OFETs is reached up to 10 cm^2/Vs [7] and BHJ-OPV cells based on fullerene ($PC_{71}BM$) acceptors and donor polymers currently have the highest power conversion efficiencies (5-10% PCEs)[8] achieved by optimization of factors such as molecular engineering of polymers, processing conditions, various annealing protocols, and use of processing additives or different dielectrics. Most notable, advances in the synthesis of diverse *p*-type polymers have enabled the development of high-performance organic field-effect transistors (OFETs) as well as more efficient fullerene-based organic photovoltaics (OPVs). In contrast, *n*-type polymer semiconductors remain relatively scarce due to the lack of available building blocks and synthetic difficulties. The performance of *n*-channel OFETs (< 1 cm^2/Vs) and all-polymer solar cells (PCE < 5 %) is also inferior compared to the *p*-channel OFETs (< 10 cm^2/Vs) and fullerene-based OPVs (5-10% PCEs).

Both *p*-channel OFETs and *n*-channel OFETs are needed for developing low power complimentary electronic circuits. In OPVs, new *n*-type polymers that can replace fullerenes are desired as well. Although fullerene molecules have proven to be excellent acceptor materials in bulk heterojunction (BHJ) polymer/fullerene solar cells, they are inherently chemically, thermally, and photochemically unstable in ambient air, which limits their potential in practical OPVs. Compared to fullerene based acceptors, *n*-type polymers as an acceptor can offer many potential advantages over fullerene acceptors. The facile tunability of various properties of such *n*-type conjugated polymers, including optical absorption, electronic structure, crystallinity, solubility, and charge transport, exemplifies their attractive features. The greater thermal stability and mechanical strength of *n*-type conjugated polymers can ensure more morphologically and environmentally rugged all-polymer solar cells. Compared to the negligible visible and near infrared light harvesting by fullerene acceptors, *n*-type conjugated polymers can contribute to light harvesting in the solar cells as much as the donor polymer and photoinduced hole transfer becomes an important pathway for charge photogeneration as is photoinduced electron transfer.[21]

In addition to the scarcity of the *n*-type polymer semiconductors, lack of knowledge on the critical factors that govern the compatibility and polymer blend film morphology limits the performance of all-polymer soalr cells. The inferior performance of all-polymer solar cells compared to fullerene/polymer devices is mainly due to the low photocurrent (J_{sc}) and fill factor (*FF*), which are the morphology dominated photovoltaic parameters.[22] However, the material factors that can be used for the choice of donor and acceptor polymer pair are currently limited to the electronic structure and optical properties of polymers, and there is no criteria available to predict the morphological compatibility of polymers in all-polymer solar cells.

1.5.2 *Research Objectives*

The primary objective of this thesis research is to design and synthesize new polymer semiconductors and study their structure-property-performance relationships in OFETs and OPVs. The main focus is to address current scientific and technical challenges in the field. The specific scope of the research include:

(i) Design and synthesis of new polymer semiconductors for OFETs and OPVs. Progress in organic electronics and photonics has been mainly driven by advances in new polymer semiconductors, and thus exploring a new class of building blocks and development of new classes of polymer semiconductors are crucial for further progress of the field. In Chapter 2, new classes of polymer semiconductors based on thienothiadiazole (TTD) or naphthalene diimide (NDI) building blocks and their electronic structures, optical properties, and solid state morphology are discussed. TTD based copolymers where found to have narrow optical band gap (~ 1 eV) with broad optical absorption band that extends to 1400 nm; their *p*-channel field-effect mobility and photovoltaic properties as a donor polymer were also investigated. In contrast, polymer semiconductors incorporating NDI and selenophene derivative showed a great potential as an electron-transporting materials in *n*-channel OFETs because of their low lying LUMO energy levels and highly ordered lamellar crystalline structure. The photovoltaic properties of all-polymer solar cells using NDI copolymers as an acceptor are also discussed in Chapter 3.

(ii) Determine the key factors that govern compatibility and blend morphology of polymer/polymer blends toward highly efficient all-polymer solar cells. Lack of knowledge of the critical factors that govern the compatibility and blend morphology of polymer blends limits the performance of all-polymer soalr cells. In particular, the morphology dominated photovoltaic parameters such as photocurrent and fill factor are inferior compared to the corresponding fullerene-based OPVs. Thus, it is vital to understand material properties that govern the polymer/polymer blend morphology and improve photocurrent and fill factor. In Chapter 4, miscibility, phase separation behavior of polymers, and surface and bulk blend film morphology are explored based on the different molecular structure of acceptor polymers that modified by using different comonomers, side chain engineering, and random copolymerization. From these studies, side chain engineering strategy is found to be effective as a means of improving the photocurrent, optimizing polymer/polymer blend morphology, and thus enhancing the performance. Moreover, the bulk crystallinity is found to be a material property that can be used as an important criterion for selecting donor/acceptor pairs in polymer/polymer blend solar cells. Information obtained from these studies can provide potential design strategy to develop new polymers that meet the requirements and considerations as suitable *n*-type polymer semiconductors.

(iii) Optimization of device engineering of all-polymer solar cells. Due to the differences in molecular geometry of the acceptor polymers (linear semi-flexible/semi-rigid chains) than the fullerene acceptors (spherical nanoparticle) and consequently differences in polymer/polymer blend morphology, understanding the unique film formaning conditions of polymer/polymer blend are essential for further progress in all-polymer solar cells by achieving the ideal blend morphology. In Chapter 5, two different film forming conditions (thermal (175 ˚C) annealing and room temperature film aging) are tested in all-polymer solar cells composed of NDI-selenophene copolymer as an acceptor and small bandgap benzodithiophene (BDT)-thieno[3,4-b]thiophene (TT) copolymer as a donor. Slow solvent evaporation rate in the room temperature film-aged polymer/polymer blend solar cells enabled improvement in electron mobility and the favorable bulk morphology resulted in about two-fold enhanced photovoltaic performance compared with the related thermally annealed devices. In addition to engineering the film forming condition, the effect of several surface modifiers, including ethanolamine and polyethylenimine that can modify the work function of metals or metal oxides by forming strong interface molecular dipoles are discussed.

(iv) Effects of 3D molecular conformation of acceptors in non-fullerene OPVs. The 3D molecular conformation can affect many molecular and bulk properties of nonfullerene acceptors, including electronic structures, intermolecular interactions, solid state packing motif, and anisotropic/isotropic charge transport properties. Therefore, optimizing the 3D molecular structure can potentially improve the photovoltaic properties of nonfullerene electron acceptors in organic solar cells. In Chapter 6, systematical studies of the effects of the 3D molecular structure on the photovoltaic properties are presented based on tetraazabenzodifluoranthene diimide (BFI) based dimeric small molecule acceptor as a model compound. For the first time, a superior photovoltaic performance was observed in nonfullerene OPVs compared with corresponding $PC_{71}BM$ based devices with the acceptor having highly twisted angle between building blocks, and demonstrated that optimizing 3D conformation of acceptors is a promising rational design strategy towards more efficient small molecule and polymer acceptors in non-fullerene OPVs.

1.6 REFERENCES

1. (a) Shirakawa, H.; Louis, E. J.; MacDiarmid, A. G.; Chiang, C. K.; Heeger, A. J. *Chem. Commun.* **1977**, 587. (b) Chiang, C. K.; Fincher, Jr. C. R.; Park, Y. W.; Heeger, A. J.; Shirakawa, H.; Louis, E. *J. Phys. Rev. Lett.* **1977**, *39*, 1098.

2. (a) Jenekhe, S. A. The Special Issue on Organi Electronics. In *Chem. Mater.* **2004**, *16*, 4381. (b) Forrest, S. R.; Thompson, M. E., Organic Electronics and Optoelectronics. In *Chem. Rev.* **2007**, *107*, 923. (c) Bredas, J. -L.; Marder, S. R.; Reichmanis, E. The Special Issure on π-Functional Materials. In *Chem. Mater.* **2011**, *23*, 309.

3. (a) Halls, J. J. M.; Walsh, C. A.; Greenham, N. C.; Marseglia, E. A.; Friend, R. H.; Moratti, S. C.; Holmes, A. B. *Nature* **1995**, *376*, 498. (b) Jenekhe, S. A.; Yi, S. *Appl. Phys. Lett.* **2000**, *77*, 2635. (c) Alam, M. M.; Jenekhe, S. A. *Chem. Mater.* **2004**, *16*, 4647. (d) McNeill, C. R. *Energy Environ. Sci.* **2012**, *5*, 5653. (e) Ahmed, E.; Ren, G.; Kim, F. S.; Hollenbeck, E. C.; Jenekhe, S. A. *Chem. Mater.* **2011**, *23*, 4563. (f) Li, H.; Earmme, T.; Ren, G.; Saeki, A.; Yoshikawa, S.; Murari, N. M.; Subramaniyan, S.; Crane, M. J.; Seki, S.; Jenekhe, S. A. *J. Am. Chem. Soc.* **2014**, *136*, 14589.

4. (a) Kittel, C. *Introduction to Solid State Physics*. 7th ed.; John Wiley &Sons: New York, **1996**. (b) Sze, S. M.; Ng, K. K., *Physics of Semiconductor Devices*. 3rd ed.; John Wiley &Sons: New York, **2007**.

5. (a) Bredasm J. -L. *J. Chem. Phys.* **1985**, *82*, 3808. (b) Jenekhe, S. A. *Nature* **1986**, *322*, 345. (c) Agrawal, A. K.; Jenekhe, S. A. *Macromolecules* **1991**, *24*, 6806. (d) Forrest, S. R. *Nature* **2004**, *428*, 911. (e) Klauk, H.; Halik, M.; Zschieschang, U.; Eder, F.; Rohde, D.; Schimid, G.; Dehm, C. *IEEE Trans. Electron. Dev.* **2005**, *52*, 618. (f) Bao, Z. *Adv. Mater.* **2000**, *12*, 227. (g) Sirringhaus, H.; Kawase, T.; Friend, R. H.; Shimoda, T.; Inbasekaran, M.; Wu, W.; Woo, E. P. *Science* **2000**,

290, 2123. (h) Yan, H.; Chen, Z.; Zheng Y.; Newman, C.; Quinn, J. R.; Dotz, F.; Kastler, M.; Facchetti, A. *Nature* **2009**, *457*, 679. (i) Guo, X.; Kim. F. S.; Jenekhe, S. A.; Watson, M. D. J. Am. Chem. Soc. 2009, 131, 7206. (j) Earmme, T.; Hwang, Y. -J.; Murari, N. M.; Subramaniyan, S.; Jenekhe, S. A. *J. Am. Chem. Soc.* **2013**,*135*, 14960.

6. (a) Yu, G.; Gao, J.; Hummelen, J. C.; Wudl, F.; Heeger, A. J. *Science* **1995**, *270*, 1789. (b) Jenekhe, S. A.; Yi, S. *Appl. Phys. Lett.* **2000**, *77*, 2635. (c) Alam, M. M.; Jenekhe, S. A. *J. Phys. Chem. B* **2001**, *105*, 2479. (d) Alam, M. M.; Jenekhe, S. A. *Chem. Mater.* **2004**, *16*, 4647. (e) Thompson, B. C.; Frechet, J. M. J. *Angew. Chem., Int. Ed.* **2008**, *47*, 58. (f) Gunes, S.; Neugebauer, H.; Sariciftci, N. S. *Chem. Re*v. **2007**, *107*, 1324. (g) Zhang, X.; Jenekhe, S. A. *Macromolecules* **2000**, *33*, 2069. (h) Kulkarni, A. P.; Zhu, Y.; Jenekhe, S. A. *Macromolecules* **2005**, *38*, 1553. (i) Babel, A.; Wind, J. D.; Jenekhe, S. A. *Adv. Funct. Mater.* **2004**, *14*, 891. (j) Yamamoto, T.; Yasuda, T.; Sakai, Y.; Aramaki, S. *Macromol. Rapid Commun.* **2005**, *26*, 1214. (k) Yamamoto, T.; Kokubo, H.; Kobashi, M.; Sakai, Y. *Chem. Mater.* **2004**, *16*, 4616. (l) Pang, H.; Skabara,P.; Crouch, D. J.; Duffy, W.; Heeney, M.; McCulloch, I.; Coles, S. J.; Horton, P. N.; Hursthouse M. B. *Macromolecules* **2007,** *40,* 6585.

7. (a) Kang, I.; Yun, H. -J.; Chung, D. S.; Kwon, S. K.; Kim, Y. -H. *J. Am. Chem. Soc*. **2013**, *135*, 14896. (b) Sun, B.; Hong, W.; Yan, Z.; Aziz, H.; Li, Y. *Adv. Mater*. **2014**, *26*, 2636.

8. (a) Dou, L.; You, J.; Yang, J.; Chen, C.-C.; He, Y.; Murase, S.; Moriarty, T.; Emery, K.; Li, G.; Yang, Y. *Nature Photon*. **2012**, *6*, 180. (b) Zhang, M.; Guo, X.; Zhang, S.; Hou, J. *Adv. Mater*. **2014**, *26*, 1118.

9. Kang, S. -M.; Leblebici, Y. *CMOS Digital Integrated Circuits: Analysis and Design.* McGraw-Hill: New York, 1996.

10. (a) Horowitz, G. *Adv. Mater*. **1998**, *10*, 365. (b) Dimitrakopoulos, C. D.; Malenfant, P. R. L. *Adv. Mater.* **2012**, *14*, 99.

11. (a) Babel, A.; Jenekhe, S. A. *J. Am. Chem. Soc.* **2003**, *125*, 13656. (b) Wong, K.-T.; Chao, T.-C.; Chi, L.-C.; Chu, Y.-Y.; Balaiah, A.; Chiu, S.-F.; Liu, Y.-H.; Wang, Y. *Org. Lett.* **2006**, *8*, 5033.

12. Park, J. K.; Jo, J.; Seo, J. H.; Moon, J. S.; Park, Y. D.; Lee, K.; Heeger A. J.; Bazan, G. C. *Adv. Mater*. **2011**, *23*, 2430.

13. (a) Wu, P. T.; Xin, H.; Kim, F. S.; Ren, G.; Jenekhe, S. A. *Macromolecules*, **2009**, *42*, 8817. (b) Hwang, Y. -J.; Murari, N. M.; Jenekhe, S. A. *Polym. Chem*. **2013**, *4*, 3187.

14. See the Special Issue: Harnessing Materials for Energy. MRS Bulletin **2008**, 33, 261.

15. Green, M. A., *Silicon Solar Cells: Advanced Principles and Practice*. Bridge Printery: Sidney, 1995.

16. (a) Agrawal, A. K.; Jenekhe, S. A. *Macromolecules* **1991**, *24*, 6806. (b) Agrawal, A. K.; Jenekhe, S. A. *Macromolecules* **1993**, *26*, 895.

17. (a) Spanggaard, H.; Krebs, F. C., *Sol. Energ. Mat. Sol*. **2004**, *83*, 125. (b) Pope, M.; Swenberg, C. E., *Electronic Processes in Organic Crystals and Polymers.* Oxford: New York, 1999.

18. (a) Goh, C. et al. *Appl. Phys. Lett.* **2005**, *86*, 122110. (b) Kang, H. et al. *J. Am. Chem. Soc.* **2015**, *137*, 2359.

19. (a) Sun, Y. M.; Welch, G. C.; Leong, W. L.; Takacs, C. J.; Bazan, G. C.; Heeger, A. J. *Nat. Mater.* **2012**, *11*, 44. (b) Kyaw, A. K. K.; Wang, D. H.; Wynands, D.; Zhang, J.; Nguyen, T.-Q.; Bazan, G. C.; Heeger, A. J. *Nano Lett.* **2013**, *13*, 3796.

20. Hwang, Y. –J.; Murari, N. M.; Jenekhe, S. A. *Polym. Chem*. **2013**, *4*, 3187.

21. (a) Wienk, M. M.; Kroon, J. M.; Verhees, W. J. H.; Knol, J.; Hummelen, J. C.; Hal, P. A. V.; Janssen, R. A. J. *Angew. Chem., Int. Ed.* **2003**, *42*, 3371. (b) Reese, M. O.; Nardes, A. M.; Rupert, B. L.; Larsen, R. E.; Olson, D. C.; Lloyd, M. T.; Shaheen, S. E.; Ginley, D. S.; Rumbles, G.; Kopidakis, N. *Adv. Funct. Mater*. **2010**, *20*, 3476. (c) Creegan, K. M.; Robbins, J. L.; Robbins, J. L.; Millar, J. M.; Sherwood, R. D.; Tindall, P. J.; Cox, D. M.; Smith, A. B.; McCauley, J. P.; Jones, D. R.; Gallagher, R. T. *J. Am. Chem. Soc.* **1992**, *114*, 1103. (d) Wudl, F. *Acc. Chem. Res.* **1992**, *25*, 157. (e) Hummelen, J. C.; Knight, B. W.; LePeq, F.; Wudl, F.; Yao, J.; Wilkins, C. L. *J. Org. Chem*. **1995**, *60*, 532. (f) Ahmed, E.; Ren, G.; Kim, F. S.; Hollenbeck, E. C.; Jenekhe, S. A. *Chem. Mater.* **2011**, *23*, 4563. (g) E. Zhou, J. Cong, K. Hashimoto, K. Tajima, *Adv. Mater*. **2013**, *25*, 6991. h) D. Mori, H. Benten, I. Okada, H. Ohkita, S. Ito, *Adv. Energy Mater*. **2014**, *4*, 1301006. i) P. Cheng, Y. Long, X. Zhao, J. Hou, Y. Li, X, Zhan, *Energy Environ. Sci.* **2014**, *7*, 1351. j) Y. Zhou, et at. *Adv. Mater*. **2014,** *26*, 3767.

22. Jackson, N. E.; Savoie, B. M.; Marks, T. J.; Chen, L. X.; Ratner, M. A. *J. Phys. Chem. Lett.* **2015**, *6*, 77.

Chapter 2. POLYMER SEMICONDUCTORS FOR ORGANIC FIELD-EFFECT TRANSISTORS.

The results in this chapter are reprinted with permission from Hwang, et al. *Macromolecules* **2012**, *45*, 3732 (Copyright 2012 American Chemical Society) and Hwang, et al. *Polym. Chem.* **2013**, *4*, 3187 (The Royal Society of Chemistry).

2.1 THIENOTHIADIAZOLE-BASED CONJUGATED COPOLYMERS FOR ELECTRONICS AND OPTOELECTRONICS

2.1.1 *Introduction*

Solution processable conjugated polymer semiconductors are of growing interest for diverse applications in electronics and optoelectronics.[1-6] The fine-tuning of the electronic structure, charge transport, and optoelectronic properties of π-conjugated polymers is greatly facilitated by the donor-acceptor (D-A) approach, whereby electron-donating (D) and electron-accepting (A) units are incorporated into the conjugated polymer chain in a modular fashion.[7-11] The resulting intramolecular charge transfer (ICT) in such a D-A copolymer can be a powerful means of tailoring the electronic structure and properties of this class of organic semiconductors, depending on the electron-releasing and electron-withdrawing strengths of the D and A building blocks. A large number of D-A conjugated polymer semiconductors based on benzodiazole acceptors such as benzo[c][1,2,5]thiadiazole (BTD),[12-15] benzoselenadiazole (BSe),[16] and benzoxadiazole (BX)[17] have been extensively studied. D-A copolymers containing these benzodiazole acceptor units are known to exhibit absorption maximum (λ_{max}) in the range of 535-689 nm with optical band gaps of 1.5-2.3 eV.[12-17]

Compared to the related electron-poor rings such as benzothiadiazole, benzoselenadiazole and benzoxadiazole, which have been extensively investigated in the construction of D-A conjugated copolymers, thienothiadiazole (TTD) has not been fully explored as a building block. This is surprising considering that it is a much stronger electron acceptor than benzothiadiazole (BTD) and the others in the homologous series and that the first example of a TTD-containing conjugated polymer, poly(4,6-di(2-thienyl)thieno[3,4-c][1,2,5]thiadiazole),[18-20] was introduced almost 2 decades ago.[18] Recently, a TTD-containing copolymer, poly(5,7-bis(4-decanyl-2-thienyl)-thieno(3,4-b)diathiazole-thiophene-2,5) (PDDTT), was used to fabricate ultrasensitive polymer photodetectors exhibiting performance that was comparable to high performance inorganic photodetectors in the 400-1450 nm spectral range.[22] In contrast, bulk heterojunction solar cells made form PDDTT/fullerene blends had a poor performance with the highest efficiency of only 0.11 %.[22] The high lying HOMO energy level of - 4.71 eV and low molecular

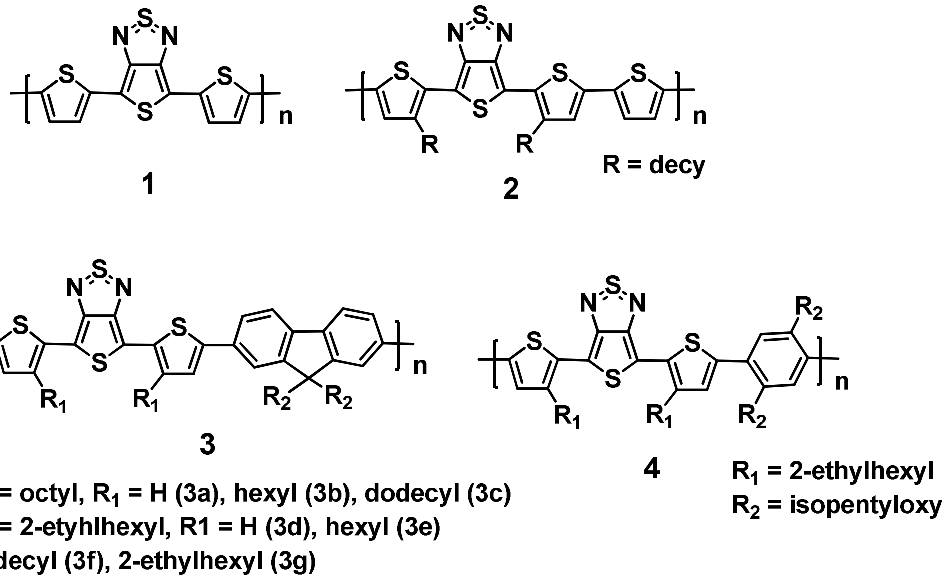

R_2 = octyl, R_1 = H (3a), hexyl (3b), dodecyl (3c)
R_2 = 2-etyhlhexyl, R1 = H (3d), hexyl (3e)
dodecyl (3f), 2-ethylhexyl (3g)

R_1 = 2-ethylhexyl
R_2 = isopentyloxy

Chart 1. Molecular structures of known thieno[3,4-c][1,2,5]thiadiazole-based conjugated copolymers.

weight of PDDTT appear to be a reason for the poor photovoltaic properties.[21, 22] More recently, another TTD-based copolymer with fluorene as a donor moiety was reported by Kminek et al.[23-26] Unfortunately, the observed photovoltaic response was also poor under non-standard and not meaningful illumination (Xe lamp with UV filter WG35 for 45 mW/cm^2). These previous limited studies of TTD-containing polymers (**Chart 1**) suggest that the potential of this strong acceptor building block remains to be realized in the development of new conjugated copolymers for electronics and optoelectronics. The molecular weight of known TTD-containing polymers synthesized by Stille or Suzuki coupling polymerization is generally low to moderate (M_n = 3.1-31.7 kDa).[21-26] Most notably, the charge transport properties, including the field-effect charge carrier mobility, of TTD-containing polymer semiconductors and thus their applications in field-effect transistors have yet to be reported.

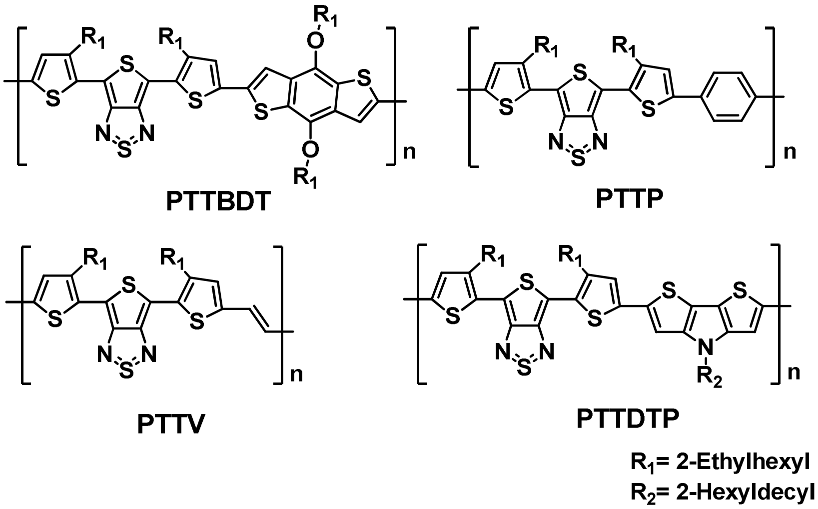

Chart 2. Molecular structures of new thieno[3,4-c][1,2,5]thiadiazole-based conjugated copolymers.

In this chapter, I will discuss the synthesis and properties of four new D-A conjugated copolymers based on thieno[3,4-c][1,2,5]thiadiazole acceptor and various donor moieties. The new poly(thienothiadiazole)s (PTTDs), including poly(4,6-bis(3-ethylhexyl-2-thienyl)thieno[3,4-c][1,2,5]thiadiazole-alt-phenylene) (PTTP), poly(4,6-bis(3-ethylhexyl-2-thienyl)thieno[3,4-c][1,2,5]thiadiazole-alt-4,8-bis(2-ethylhexyloxy)benzo[1,2-b:4,5-b']dithiophene) (PTTBDT), poly(4,6-bis(3-ethylhexyl-2-thienyl)thieno[3,4-c][1,2,5]thiadiazole-alt-vinylene) (PTTV) and poly(4,6-bis(3-ethylhexyl-2-thienyl)thieno[3,4-c][1,2,5]thiadiazole-alt-N-(1-hexyldecyl)dithieno[3,2-b:2',3'-d]pyrrole) (PTTDTP), were synthesized by Stille coupling polymerization. The molecular structures of the new PTTDs are given in **Chart 2**. Optical absorption spectroscopy shows that the PTTDs have very narrow band gaps of 0.9-1.2 eV. Electrochemically derived electronic structures show that the new polymers have a LUMO energy level of -3.4 to -3.6 eV and a HOMO energy level of -4.9 to -5.1 eV. The charge transport and photovoltaic properties of the PTTDs were investigated by organic field-effect transistor (OFETs) and bulk heterojunction (BHJ) solar cells, respectively. The thienothiadiazole-based copolymers had a moderate field-effect mobility of holes as high as 4.6×10^{-3} cm^2/Vs while the maximum photovoltaic efficiency was 0.38 %.

2.1.2 *Experimental Section*

Materials. 2,5-Bromo-3,4-dinitrothiophene and *trans*-1,2-bis(tri-n-butyl-stannyl)ethylene were purchased from Fisher Scientific Inc. 2,6-Dibromo-4,8-bis(2-ethylhexyloxy)benzo[1,2-b:4,5-b']dithiophene was purchased from Luminescence Technology Corp (Taiwan). All other chemicals were purchased from Sigma-Aldrich. 4,6-Bis(5-bromo-3-ethylhexyl-2-thienyl)thieno[3,4-c][1.2.5]thiadiazole (**5**)[24] and 2,6-di(trimethyltin)-N-(1-hexyldecyl)dithieno[3,2-b:2',3'-d]pyrrole[27] were synthesized according to known procedures.

Poly(4,6-bis(3-ethylhexyl-2-thienyl)thieno[3,4-c][1,2,5]thiadiazole-alt-phenylene) (PTTP). 4,6-Bis(5-bromo-3-ethylhexyl-2-thienyl)thieno[3,4-c][1.2.5]thiadiazole (**5**) (269.5 mg, 0.39 mmol), 1,4-bis(tributylstannyl)benzene (256.8 mg, 0.39 mmol), $Pd_2(dba)_3$ (7.16 mg, 0.0078 mmol) and $P(o\text{-tolyl})_3$ (9.53 mg, 0.0313 mmol) were added into a 100 mL three-neck round-bottom flask. The flask equipped with a condenser was then degassed and filled with argon three times. Afterwards, 15 mL of chlorobenzene was added and degassed and filled with argon three times. The reaction mixture was refluxed for 24 h under argon. After cooling down to room temperature, the polymerization mixture was poured and stirred into 200 mL methanol and 5 mL hydrochloric acid solution for 5 h. The polymer precipitated out as a dark green solid and was filtered using a filter paper. The polymer was purified by Soxhlet extraction with methanol and acetone (183 mg; yield = 73.6 %). ^{1}H NMR ($CDCl_3$, 300 MHz): δ (ppm) 7.7 (6H), 3.0 (4H), 1.83 (2H), 1.3-0.8 (28H).

Poly(4,6-bis(3-ethylhexyl-2-thienyl)thieno[3,4-c][1,2,5]thiadiazole-alt-4,8-bis(2-ethylhexyloxy)benzo[1,2-b:4,5-b']dithiophene) (PTTBDT). 4,6-Bis(5-bromo-3-ethylhexyl-2-thienyl)thieno[3,4-c][1.2.5]thiadiazole (**5**) (385.42 mg, 0.562 mmol), 2,6-di(tributylstannyl)-4,8-bis(2-ethylhexyloxy) benzo[1,2-b:4,5-b']dithiophene (432.7 mg, 0.562 mmol), $Pd_2(dba)_3$ (10.29 mg, 0.011 mmol) and $P(o\text{-tolyl})_3$ (13.7 mg, 0.045 mmol) were added into a 100 mL three-neck round-bottom flask. The flask equipped with a condenser was then degassed and filled with argon three times. Afterwards, 35 mL of chlorobenzene was added and degassed and filled with argon three times. The reaction mixture was refluxed for 72 h under argon. After cooling down to room temperature, the polymerization mixture was poured and stirred into 200 mL methanol and 5 mL hydrochloric acid solution for 5 h. The polymer precipitated out as a dark green solid and was filtered using a filter paper. The polymer was purified by Soxhlet extraction with methanol and hexane (320 mg; yield = 60 %). ^{1}H NMR ($CDCl_3$, 300 MHz): δ (ppm) 7.16 (2H), 7.0 (2H), 3.99 (4H), 2.9 (4H), 1.9-0.9 (60 H).

Poly(4,6-bis(3-ethylhexyl-2-thienyl)thieno[3,4-c][1,2,5]thiadiazole-alt-vinylene) (PTTV). 4,6-Bis(5-bromo-3-ethylhexyl-2-thienyl)thieno[3,4-c][1.2.5]thiadiazole (**5**) (612.6 mg, 0.89 mmol), *trans*-1,2-bis(tri-n-butyl-stannyl)ethylene (539.2 mg, 0.89 mmol), $Pd_2(dba)_3$ (16.3 mg, 0.018 mmol) and $P(o\text{-}tolyl)_3$ (21.66 mg, 0.071 mmol) were added into a 100 mL three-neck round-bottom flask. The flask equipped with a condenser was then degassed and filled with argon three times. Afterwards, 30 mL of chlorobenzene was added and degassed and filled with argon three times. The reaction mixture was refluxed for 16 h under argon. After cooling down to room temperature, the polymerization mixture was poured and stirred into 200 mL methanol and 5 mL hydrochloric acid solution for 5 h. The polymer precipitated out as a dark solid and was filtered using a filter paper. The polymer was purified by Soxhlet extraction with methanol, hexane and chloroform (450 mg; yield = 86.5 %). ^{1}H NMR ($CDCl_3$, 300 MHz): δ (ppm) 7.14 (2H), 7.0 (2H), 4.08 (4H), 2.03 (2H), 1.35-0.8 (28H).

Poly(4,6-bis(3-ethylhexyl-2-thienyl)thieno[3,4-c][1,2,5]thiadiazole-alt-N-(1-hexyldecyl)dithieno[3,2-b:2',3'-d]pyrrole) (PTTDTP). 4,6-Bis(5-bromo-3-ethylhexyl-2-thienyl)thieno[3,4-c][1.2.5]thiadiazole (**5**) (221.8 mg, 0.323 mmol), 2,6-di(trimethyltin)-N-(1-hexyldecyl)dithieno[3,2-b:2',3'-d]pyrrole (235.8 mg, 0.323 mmol), $Pd_2(dba)_3$ (5.92 mg, 0.00646 mmol) and $P(o\text{-}tolyl)_3$ (7.87 mg, 0.0258 mmol) were added into a 100 mL three-neck round-bottom flask. The flask equipped with a condenser was then degassed and filled with argon three times. Afterwards, 13 mL of chlorobenzene was added and degassed and filled with argon three times. The reaction mixture was refluxed for 48 h under argon. After cooling down to room temperature, the polymerization mixture was poured and stirred into 200 mL methanol and 5 mL hydrochloride solution for 5 h. The polymer precipitated out as a dark solid and was filtered by a filter paper. The polymer was purified by Soxhlet extraction with methanol and hexane (220 mg;

yield = 70.8 %). ^{1}H NMR (CDCl$_3$, 300 MHz): δ (ppm) 7.14 (2H), 6.99 (2H), 4.07 (4H), 2.03 (2H), 1.3-0.7 (61H).

2,6-Di(trimethyltylstannyl)-4,8-bis(2-ethylhexyloxy)benzo[1,2-b:4,5-b']dithiophene. 2,6-Dibromo-4,8-bis(2-ethylhexyloxy)benzo[1,2-b:4,5-b']dithiophene (330 mg, 0.546 mmol) was added into a 100 mL three-neck round-bottom flask. Afterwards, 14 mL THF was added under argon. The mixture was cooled to -78 °C in a dry ice bath and n-BuLi (0.75 mL, 1.19 mmol) was added dropwise. After stirring the mixture for 45 min at -78 °C, trimethyltinchloride (1.27 mL, 1.27 mmol) was added in one portion. Dry ice bath was removed after 5 min and the mixture was warmed up to room temperature. After stirring 2 h at room temperature, the reaction mixture was poured into water and extracted with diethyl ether 3 times. The organic phase was dried with sodium sulfate anhydrous and the solvent was evaporated by vacuum rotary evaporator. Yellow crystals were obtained and subsequently used in polymerization without further purification (553 mg; yield = 92 %). ^{1}H NMR (CDCl$_3$, 300 MHz): δ (ppm) 6.99 (2H), 4.08 (2H), 2.05 (1H), 1.33-0.63 (30 H), 0.33 (18H).

Characterization. To analyze the molecular and physical properties of the four copolymers, ^{1}H NMR, thermogravimetric analysis (TGA), X-ray diffraction (XRD) and gel permeation chromatography (GPC) analysis were performed. ^{1}H NMR spectra at 300 MHz were recorded on a Bruker-AF300 spectrometer. TGA thermograms were obtained on a TA Instruments Q50 TGA at a heating rate of 20 °C/min under nitrogen gas flow. XRD data were obtained from Bruker AXS D8 Focus diffractometer with a Cu Kα beam, and the samples were prepared by drop-casting of polymer solutions with chlorobenzene onto glass substrates and annealed at 200 ˚C for 10 mintures. GPC analysis of the copolymers was performed on GPC Model 120 (DRI, PLBV400HTViscometer) against polystyrene standards in chlorobenzene at 60˚C. Absorption spectra of the copolymers were measured on a Perkin-Elmer model Lambda 900 UV/vis/near-IR spectrophotometer. Solution and solid state absorption spectra were obtained from polymer solutions in chloroform and as thin films on glass substrates, respectively.

Cyclic voltammetry (CV) experiments were done on an EG&G Princeton Applied Research potentiostat/galvanostat (model 273A) in an electrolyte solution of 0.1 M tetrabutylammonium hexafluorophosphate (Bu_4NPF_6) in acetonitrile. A three-electrode cell was used in this analysis. Platinum wires were used as counter and working electrodes, and Ag/Ag^+ (Ag in 0.1 M $AgNO_3$ solution, Bioanalytical System, Inc.) was used as a reference electrode. Ferrocene/ferrocenium was used as an internal standard by running CV at the end, and this data was used to convert the potential to saturated calomel electrode (SCE) scale. The films of the copolymers were coated onto the Pt wires by dipping the wires into 1 wt% polymer solutions in chloroform or chlorobenzene.

Fabrication and characterization of field-effect transistors. Organic field-effect transistors (OFETs) were made on top of heavily *n*-doped silicon with thermally grown oxide (200 nm) substrates. Gold source-drain electrodes (W=800 μm and L=40 μm) with a thin chromium adhesive layer were photographically patterned to form bottom-contact transistor devices. The surface of the oxide was treated with octyltrichlorosilane (OTS8) by spin-coating a chloroform solution of OTS8 (4 mM) onto a cleaned substrate, followed by rinsing with toluene and annealing at 100 °C for 10 min in a fume hood. Polymer thin films spun from a solution in 1,2-dichlorobenzene (4–8 mg/mL) were annealed at 200 °C for 10 min under argon environment. Devices were tested by using an HP4145B semiconductor parameter analyzer in nitrogen-filled dry box. Electrical parameters were calculated by using the standard equation for metal-oxide-semiconductor field-effect transistors in the saturation region similar to our previous reports.[28, 5(b)]

Fabrication and characterization of photovoltaic cells. Solar cells were fabricated by first spin-coating a PEDOT buffer layer on top of ITO-coated glass substrates (10 Ω/□) at 3500 rpm for 40 s and annealing at 150 °C for 10 min under vacuum. The thickness of PEDOT was around 30 nm. The active layer was spin-coated on top of the PEDOT in a glove box at a speed of 620 rpm for 20 s and annealed at 180 °C for 10 min. The device substrates were then loaded into a thermal evaporator for cathode deposition. The cathode, consisting of 1.0 nm LiF and 100 nm Al layers, was sequentially deposited through a shadow mask on top of the active layers after the chamber vacuum reached 8×10^{-7} torr. The solar cells have an active area of 9.0 mm^2. The active layer had thickness of 60-80 nm. Film thickness was measured on an Alpha-Step 500 profilometer. Current-voltage characteristics were measured by using an HP4155A semiconductor parameter analyzer. The light intensity of AM 1.5 sunlight from a filtered Xe lamp was calibrated by a Si photodiode calibrated at the National Renewable Energy Laboratory (NREL). All the characterization steps were carried out under ambient laboratory air and further details can be found in our previous report.[29]

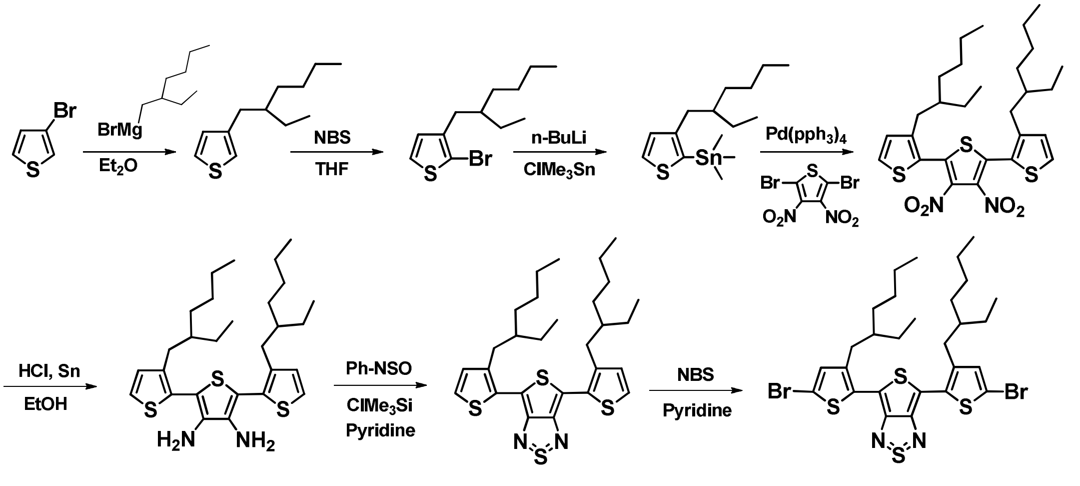

Scheme 2. Synthetic route to 4,6-bis(5-bromo-3-ethylhexyl-2-thienyl)thieno[3,4-c][1,2,5]thiadiazole (**5**).

2.1.3 *Results and Discussion*

Synthesis and Characterization. The synthetic route to the dibromide monomer **5** is presented in **Scheme 2**. The final monomer **5** was obtained in three steps from dinitroterthiophene **8**. Reduction of compound **8** with hydrochloric acid and tin powder gave the compound **7**, and following ring closing reactions of compound **7** with N-thionylaniline and chlorotrimethylsilane in pyridine the thienothiadiazole compound **6** was obtained. Finally, boromination of compound **6** with N-bromosuccinimide (NBS) gave the monomer **5**. Monomer **5** was obtained as a blue solid and its molecular structure was verified by ^{1}H NMR and LC mass spectrometry. The new polythienothiadiazoles (PTTDs) were synthesized by Stille coupling polymerization in the presence of $Pd_2(dba)_3$ and $P(o\text{-tolyl})_3$ using chlorobenzene as the solvent (**Scheme 3**). Color changes from blue to green were observed during the polymerization reaction, and as a result, PTTP and PTTBDT were collected as dark green solids. In the case of PTTV and PTTDTP, the color of the polymerization solutions changed from blue to reddish purple, and dark solids were obtained. PTTP, PTTBDT and PTTDTP are readily soluble in common organic solvents (e.g. chloroform, chlorobenzene) at room temperature. In the case of PTTV, the polymer precipitated after only 5 h Stille coupling polymerization; consequently, the final dark solid was only partially soluble in chlorobenzene even at 120 °C. The low solubility of the vinylene-linked PTTV comes from its highly coplanar and rigid backbone.

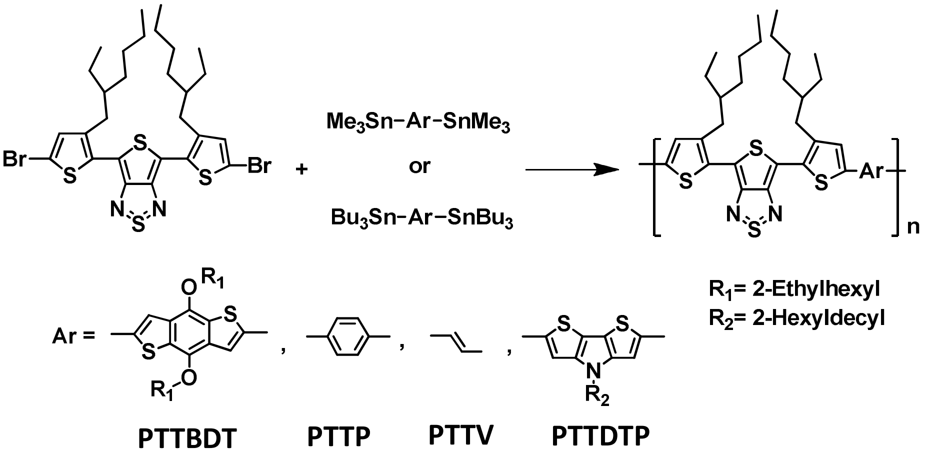

Scheme 3. Synthesis of polythienothiadiazoles (PTTDs).

The molecular structures of the new PTTDs were verified primarily by ^{1}H NMR spectra, which were in good agreement with the proposed structures of the copolymers. The molecular weight and polydispersity of the copolymers were measured by gel permeation chromatography (GPC) against polystyrene standards in chlorobenzene at 60 °C. The number-average molecular weight (M_n) varied from 6.4 kDa in PTTBDT to 24.0 kDa in PTTDTP. In the case of PTTV, ^{1}H NMR and GPC measurement could not be done because of the low solubility in organic solvents. The molecular weight of the PTTDs is thus moderate and can probably be increased further by optimizations of the polymerization conditions, including the monomer concentration of solution, catalyst, and temperature. The thermal stability and thermal transition properties of the PTTDs were evaluated by thermogravimetric analysis (TGA) and differential scanning calorimetry (DSC), respectively. The onset decomposition temperature (T_d) of all four polymers under nitrogen flow was in the range of 320–380 °C, indicating good thermal stability of the copolymers. The DSC scans of the PTTDs did not show any distinct transitions up to 350 °C (**Table 1**).

Table 1. Molecular Weight and Thermal Stability of PTTDs.

copolymer	M_w[a] (kDa)	M_n[a] (kDa)	M_w / M_n[a]	T_d[b] (°C)
PTTBDT	13.0	6.4	2.1	320
PTTP	10.0	8.3	1.2	360
PTTV	-	-	-	380
PTTDTP	46.0	24.0	1.9	350

[a] Molecular weights were determined by GPC using polystyrene standards. [b] Onset decomposition temperature measured from TGA under nitrogen.

Electrochemical Properties. The redox properties and electronic structures of the new D-A conjugated copolymers were investigated by cyclic voltammetry (CV) of thin films on platinum (Pt) electrodes. The oxidation and reduction cyclic voltammograms of PTTDs are shown in **Figure 4**. The cyclic voltammograms of all four copolymers (PTTP, PTTBDT, PTTV, PTTDTP) showed a much larger oxidation current than reduction current. The oxidation waves were all irreversible whereas the reduction waves were quasi-reversible.

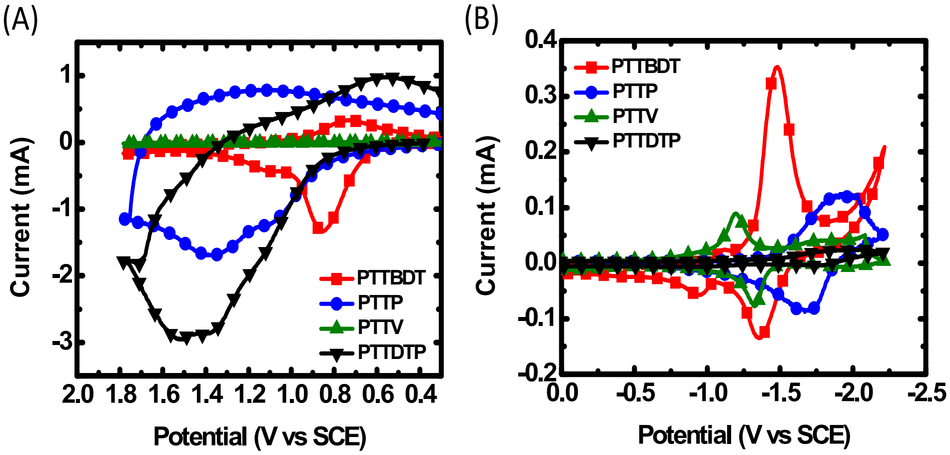

Figure 4. Cyclic voltammograms of PTTDs thin films in 0.1 M Bu_4NPF_6 solution in acetonitrile at a scan rate of 40 mV/s: oxidation scans (A) and reduction scans (B).

The ionization potential (IP)/electron affinity (EA) and their associated HOMO/LUMO energy levels were estimated from the onset redox potentials (vs SCE) extracted from the cyclic voltammograms (IP = eE_{ox}^{onset} + 4.4 eV, EA = eE_{red}^{onset} + 4.4 eV).[30] The IP and EA values are summarized in **Table 2**. The IP value or HOMO level of the copolymers at 4.9–5.1 eV varied only slightly with donor moiety. The EA value or LUMO level of the PTTD copolymers also varied in a very narrow range from 3.4 eV for PTTP to 3.6 eV for PTTV and PTTDTP. Compared to the known TTD-containing copolymer, poly(5,7-bis(4-decanyl-2-thienyl)-thieno(3,4-b)diathiazole-thiophene-2,5), which has HOMO/LUMO energy levels of 4.71 eV/3.59 eV,[21] the present PTTDs have HOMO/LUMO energy levels that vary slightly with the donor moieties. The electrochemical band gap (E_g^{el} = IP – EA) of the PTTDs varied from 1.3 eV in PTTDTP to 1.6 eV in PTTP and PTTBDT; the electrochemical band gap is 0.40-0.60 eV larger than the optical band gap E_g^{opt} (**Table 2**) and this can in part be explained by the strongly bound excitons in the materials.[1(c), 31] We note that the N-(1-hexyldecyl)dithieno[3,2-b:2',3'-d]pyrrole (DTP)-linked copolymer, PTTDTP, had the smallest band gap among the four new PTTDs as a result of increased HOMO level and decreased LUMO level. In contrast, the weak donor moieties of PTTBDT and PTTP brought decreased HOMO level and increased LUMO level and thus a larger band gap energy.

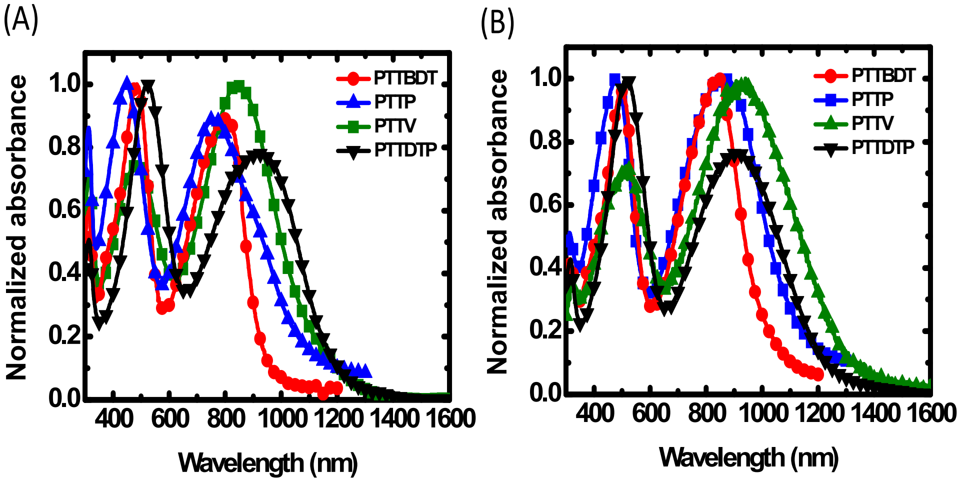

Figure 5. Optical absorption spectra of PTTDs in dilute chloroform solution (A) and as thin films on glass substrates (B).

Optical properties. The normalized optical absorption spectra of the PTTDs in dilute (10^{-6} M) chloroform solutions and as spin-coated thin films on glass substrates are shown in **Figure 5**. All four copolymers are characterized by two absorption bands in both dilute solutions and as thin films. The higher energy absorption band can be assigned to a π-π* transition whereas the lower energy absorption band can be assigned to an intramolecular charge transfer (ICT) interaction between the TTD acceptor and the various donor moieties.[4] In dilute solution, the absorption maximum (λ_{max}) of the higher energy band varied from 445 nm in PTTP to 521 nm in PTTDTP. The λ_{max} of the ICT absorption band varied from 760 nm in PTTP to 909 nm in PTTDTP.

The ICT band of the thin film absorption spectra of the PTTDs is significantly red-shifted compared to the solution spectra. Although the higher energy band centered at 481-515 nm shifted very little from the solution spectra, the ICT absorption maximum varied from 843 nm in PTTBDT to 941 nm in PTTV. Compared to the solution spectra, PTTP and PTTV showed a large redshift of 104 nm and 106 nm, respectively, in the ICT absorption band, whereas PTTBDT had a little redshift of 37 nm and PTTDTP was unchanged. The large redshift in the thin film absorption spectra compared to the solution spectra, can be explained by the increased planarization and strong intermolecular interactions of the copolymer chains in the solid state.

Table 2. Optical and Electrochemical Properties of PTTDs.

copolymer	EA[a] (eV)	IP[b] (eV)	E_g^{el} (eV)	λ_{max}[c] (nm)	λ_{max}[d] (nm)	E_g^{opt} (eV)
PTTBDT	3.5	5.1	1.6	485, 806	499, 843	1.2
PTTP	3.4	5.0	1.6	445, 760	481, 864	1.1
PTTV	3.6	5.1	1.5	484, 835	514, 941	0.9
PTTDTP	3.6	4.9	1.3	521, 909	515, 911	0.9

[a] Electron affinity was obtained based on EA = eE_{redox}^{onset} + 4.4 eV. [b] Ionization potential was obtained based on IP = eE_{ox}^{onset} + 4.4 eV. [c] The absorption maximum in dilute solution. [d] The thin film absorption maximum.

The optical band gap of the PTTDs varied from 1.2 eV in PTTBDT to 0.9 eV in PTTV and PTTDTP (**Table 2**). The relatively weak donor moieties of PTTP and PTTBDT and thus smaller ICT interactions can explain their larger optical band gaps compared to PTTV and PTTDTP. The relatively narrow band gap of PTTV can be explained by the increased coplanarity enabled by the rigid vinylene group in its backbone. The rather small optical band gap of PTTDTP is derived from the strong electron-donating N-(1-hexyldecyl)dithieno[3,2-b:2',3'-d]pyrrole (DTP) donor moiety, which facilitates the strongest ICT interaction among the four polymers. Compared to other organic semiconductors already reported based on different acceptor moieties, such as BTD or the others in the homologous series including BSe and BX,[12-17] the new thienothiadiazole-based PTTDs have a broad absorption that extends to near infrared region. The four new copolymers are thus good candidates for applications in photodetectors and photovoltaics.

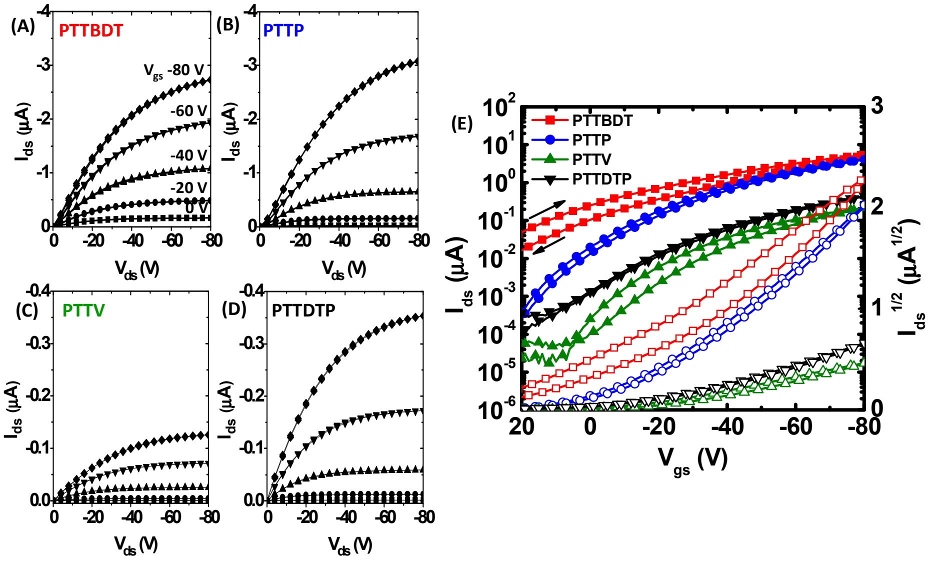

Figure 6. Output (A-D) and transfer (E) characteristics of the OFETs based on the polythienothiadiazoles (PTTDs). Forward and backward scans are overlaid in both output and transfer curves. Solid symbols represent I_{ds} and open symbols represent $I_{ds}^{1/2}$. V_{ds} = -80 V in panel (E).

Field-Effect Transistors. The charge transport properties of the new copolymer semiconductors were investigated by fabricating and testing organic field-effect transistors (OFETs) with bottom-contact and bottom-gate geometry on hydrophobically modified gate dielectric layer. All of the PTTD transistors exhibited p-channel characteristics with good current modulation and saturation, as shown in **Figure 6.** Output (A-D) and transfer (E) characteristics of the OFETs based on the polythienothiadiazoles (PTTDs). Forward and backward scans are overlaid in both output and transfer curves. Solid symbols represent I_{ds} and open symbols represent $I_{ds}^{1/2}$. V_{ds} = -80 V in panel (E).. The electrical parameters of the PTTD OFETs are collected in **Table 3**. PTTDs showed comparable charge carrier mobility compared to other small band gap polymer semiconductor that has been reported.[32] PTTP and PTTBDT showed saturation hole mobilities of 4.6×10^{-3} cm^2/Vs and 3.2×10^{-3} cm^2/Vs, respectively. On the other hand, PTTV and PTTDTP had lower carrier mobilities of 2.5×10^{-4} cm^2/Vs and 6.1×10^{-4} cm^2/Vs, respectively. The one order of magnitude lower carrier mobility of PTTDTP compared to the other PTTDs can be explained by the difference in crystallinity as revealed by XRD. PTTBDT films showed a diffraction peak at $2\theta = 5.54°$ with the corresponding d-spacing of 15.9 Å, and PTTP showed a diffraction peak at $2\theta = 6.06°$ with the d-spacing of 14.6 Å. These peaks are considered to be from (100) diffraction of lamellar planes of edge-on oriented polymers. We were not able to resolve any peaks from other diffractions. In contrast, PTTDTP film showed very weak X-ray diffraction peaks with intensity of 200 or less, indicating largely amorphous morphology. Lower carrier mobility of PTTV film can be explained by the poor film quality caused by less solubility of PTTV in common organic solvents. No sign of significant contact resistance was observed in the output curves of the PTTD transistors. The HOMO energy levels of the copolymers (4.9–5.1 eV) are well-matched with the work function of the gold source/drain electrodes (5.1 eV), suggesting that the hole transport is not limited by charge injection barrier in the series of PTTDs. Electron-transport was not observed despite the relatively low-lying LUMO energy levels (3.4–3.6 eV) of PTTDs.

The on/off current ratios of PTTP and PTTV OFETs were 10^4 and those of PTTBDT and PTTDTP devices were 10^3. Overall, small hysteresis between forward and backward scans was observed except for the transfer curves of PTTBDT and PTTV. The PTTBDT transistor also exhibited a large positive threshold voltage of 18.3 V on average and a relatively large off-current of 0.01–0.1 μA. The OFETs based on the other copolymers had negative threshold voltages (-8.1 V for PTTV, -12.5 V for PTTP, and -16.2 V for PTTDTP) and lower off-current of less than 1 nA. The origin of the large hysteresis, the large off-current, and a positive threshold voltage in PTTBDT transistors are not clear at present. Extrinsic molecules and/or impurities might have caused unintentional doping, resulting in the large hysteresis and off-current as well as the positive threshold voltage.

Table 3. Field-effect Charge Transport and Photovoltaic Properties of PTTDs.

Copolymer	**μ_h (cm²/Vs)**	**I_{on}/I_{off}**	**V_t (V)**	**J_{sc}[a] (mA/cm²)**	**V_{oc}[a] (V)**	**FF[a]**	**η_{avg} (η_{max})[a] (%)**
PTTBDT	3.2×10^{-3}	10^3	18.3	2.33	0.41	0.36	0.35 (0.38)
PTTP	4.6×10^{-3}	10^4	-12.5	1.04	0.19	0.28	0.05 (0.06)
PTTV	2.5×10^{-4}	10^4	-8.1	-	-	-	-
PTTDTP	6.1×10^{-4}	10^3	-16.2	1.45	0.22	0.31	0.09 (0.1)

[a] Photovoltaic properties of PTTDs:$PC_{71}BM$ (1:2 wt/wt) solar cells.

Photovoltaic Properties. Bulk heterojunction (BHJ) polymer solar cells using a PTTD as donor and the fullerene derivative [6,6]-phenyl-C71-butyric acid methyl ester ($PC_{71}BM$), as acceptor were fabricated and characterized. The ratio of PTTD:$PC_{71}BM$ was fixed at 1:2 (wt:wt) in all the

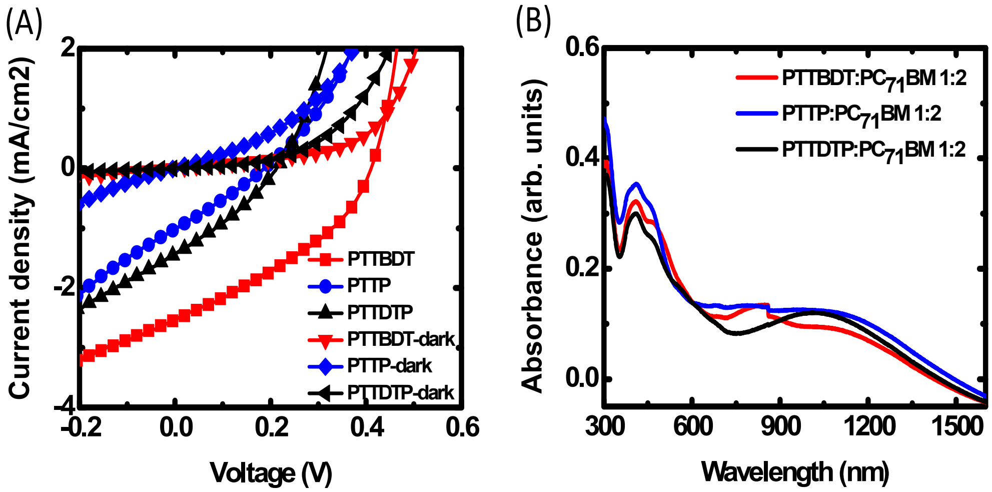

Figure 7. J-V curves (A) and absorption spectra (B) of PTTD:PC$_{71}$BM (1:2 wt/wt) solar cells devices.

Representative current density—voltage (*J*—*V*) curves of the PTTD:PC$_{71}$BM solar cells are shown in **Figure 7(A)** and the solar cell parameters are summarized in **Table 3**. The low solubility of PTTV in dichlorobenzene precluded fabrication of PTTV solar cells. The average power conversion efficiency (PCE) of PTTP, PTTBDT, and PTTDTP solar cells was rather low at 0.05%, 0.35%, and 0.09%, respectively. The corresponding short-circuit current density (J_{sc}), open circuit voltage (V_{oc}), and fill factor (*FF*) of these solar cells are 1.04-2.33 mA/cm^2, 190-410 mV and 0.28-0.36, respectively. The peak efficiency obtained in the best solar cell of PTTBDT:PC$_{71}$BM was 0.38% with a J_{sc} of 2.55 mA/cm^2, a V_{oc} of 0.42 V, and a *FF* of 0.36. Although the absorption of the PTTDs and thus light harvesting in BHJ devices extends to the near infrared (**Figure 7B**), all the photovoltaic parameters (J_{sc}, V_{oc}, FF) are rather low. The low power conversion efficiency of BHJ solar cells based on the PTTDs and fullerenes may be because of the following reasons. The high-lying HOMO energy levels (-4.9 to -5.1 eV) of the PTTDs relative to the LUMO energy level of the PCBM (-4.0 eV) resulted in small V_{oc} of 0.19-

0.36 V. The poor quality of the spin coated polymer/fullerene blend films and the low to moderate mobility of holes in the polymers could explain the low fill factor of the solar cells.

2.1.4 *Conclusions*

I have synthesized and investigated the electronic structure and properties of a series of four new thieno[3,4-c][1,2,5]thiadiazole (TTD)-based donor-acceptor conjugated copolymers. The new polythienothiadiazoles were obtained with low to moderate molecular weights (M_n = 6.4-24.0 kDa) by Stille coupling polymerization. X-ray diffraction of the PTTD films showed that only two (PTTBDT and PTTP) were sufficiently crystalline. The electrochemically-derived HOMO/LUMO energy levels of the copolymers were 4.9-5.1 eV/3.4-3.6 eV below vacuum. The new thienothiadiazoles have narrow optical band gap (~1 eV) with broad absorption, which extends to 1400 nm in the case of PTTV and PTTDTP.

The field-effect mobility of holes in the PTTDs varied from 4.6×10^{-3} cm^2/Vs in PTTP to 2.5×10^{-4} cm^2/Vs in PTTV. BHJ solar cells fabricated from the three soluble PTTDs had a maximum power conversion efficiency of 0.38 %. These results suggest that the new PTTDs have potential applications in electronic and optoelectronic devices. Moreover, the TTD moiety is found to be a strong electron-acceptor building block for the development of D-A copolymers semiconductors.

2.1.5 *References*

1. Recent reviews: (a) Facchetti, A. *Chem. Mater.* **2011**, *23*, 733-758. (b) Boudreault, P. T.; Najari, A.; Leclerc, M. *Chem. Mater.* **2011**, *23*, 456-469. (c) Kim, F. S.; Ren, G.; Jenekhe, S. A. *Chem. Mater.* **2011**, *23*, 682-732. (d) Cheng, Y. J.; Yang, S. H.; Hsu, C. S. *Chem. Rev.* **2009**, *109*, 5868–5923.

2. (a) Gelinck, G.; Heremans, P.; Nomoto, K.; Anthopoulos, T. D. *Adv. Mater.* **2010**, *22*, 3778-3798. (b) Zaumseil, J.; Sirringhaus, H. *Chem. Rev.* **2007**, *107*, 1296-1323.

3. (a) Babel, A.; Jenekhe, S. A. *J. Am. Chem. Soc.* **2003**, *125*, 13656-13657. (b) Osaka, I.; Sauve, G.; Zhang, R.; Kowalewski, T.; McCullough, R. D. *Adv. Mater.*, 2007, **19**, 4160-4165.

4. Jenekhe, S. A.; Lu, L.; Alam, M. M. *Macromolecules* **2001**, *34*, 7315-7324.

5. (a) Yan, H.; Chen, Z.; Zheng, Y.; Newman, C.; Quinn, J. R.; Dotz, F.; Kastler, M.; Facchetti, A. *Nature*, 2009, **457**, 679-686; (b) Kim, F. S.; Guo, X.; Watson, M. D.; Jenekhe, S. A. *Adv. Mater*. **2010**, *22*, 478-482.

6. Zhan, X.; Tan, Z.; Domercq, B.; An, Z.; Zhang, X.; Barlow, S.; Li, Y.; Zhu, D.; Kippelen, B.; Marder, S. R. *J. Am. Chem. Soc.* **2007**, *129*, 7246-7247.

7. Guo, X.; Kim, F. S.; Jenekhe, S. A.; Watson, M. D. *J. Am. Chem. Soc.* **2009**, *131*, 7206-7207.

8. Tsao, H. N.; Cho, D. M.; Park, I.; Hansen, M. R.; Mavrinskiy, A.; Yoon, D. Y.; Graf, R.; Pisula, W.; Spiess, H. W.; Mϋllen, K. *J. Am. Chem. Soc.* **2011**, *133*, 2605-2612.

9. Beaujuge, P. M.; Pisula, W.; Tsao, H. N.; Ellinger, S.; Mullen, K.; Reynolds, J. R. *J. Am. Chem. Soc*. **2009**, *131*, 7514-7515.

10. (a) Wu, P.-T.; Bull, T.; Kim, F. S.; Luscombe, C. K.; Jenekhe, S. A. *Macromolecules* **2009**, *42*, 671-681. (b) Ahmed, E.; Kim, F. S.; Xin, H.; Jenekhe, S. A. *Macromolecules* **2009**, *42*, 8615-8618.

11. (a) Subramaniyan, S.; Xin, H.; Kim, F. S.; Shoaee, S.; Durrant, J. R.; Jenekhe, S. A. *Adv. Energy Mater.* **2011**, 1, 854-860.(b) Subramaniyan, S.; Xin, H.; Kim, F. S.; Jenekhe, S. A. *Macromolecules* **2011**, 44, 6245-6248. (c) Ahmed, E.; Subramaniyan, S.; Kim, F. S.; Xin, H.; Jenekhe, S. A. *Macromolecules* **2011**, 44, 7207-7219.

12. Blouin, N.; Michaud, A.; Leclerc, M. *Adv. Mater*. **2007,** *19*, 2295-2300.

13. Svensson, M.; Zhang, F. L.; Veenstra, S. C.; Verhees, W. J. H.; Hummelen, J. C.; Kroon, J. M.; Inganas, O.; Andersson, M. R. *Adv. Mater.* **2003,** *15*, 988-991.

14. Zhou, Q. M.; Hou, Q.; Zheng, L. P.; Deng, X. Y.; Yu, G.; Cao, Y. *Appl. Phys. Lett*. **2004,** *84*, 1653-1655.

15. Padhy, H.; Huang, J. H.; Sahu, D.; Patra, D.; Kekuda, D.; Chu, C. W.; Lin, H. C. *J. Poly. Sci.: Part A: Polym. Chem*. **2010,** *48*, 4823-4834.

16. Zhao, W.; Cai, W.; Xu, R.; Yang, W.; Gong, X.; Wu, H.; Cao, Y. *Polymers* **2010,** *51*, 3196-3202.

17. Sonar, P.; Singh, S. P.; Soh, M. S.; Li, Y. International Patent Application No. PCT/SG2010/000174, March 3, **2011.**

18. Tanaka, S.; Yamashita, Y. *Synth. Met*. **1993,** *55-57*, 1251-1254.

19. Delgado, M. C. R.; Hernandez, V.; Navarrete, J. T. L.; Tanaka, S.; Yamashita, Y. *J. Phys. Chem. B* **2004,** *108*, 2516-2526.

20. Bakhshi, A. K.; Ago, H.; Yoshizawa, K.; Tanaka, K.; Yamabe, T. *J. Chem. Phys*. **1996,** *104*, 5528-5538.

21. Xia, Y.; Wang, L.; Deng, X.; Li, D.; Zhu, X.; Cao, Y. *Appl. Phys. Lett.* **2006,** *89*, 081106/1-081106/3.

22. Gong, X.; Tong, M.; Xia, Y.; Cai, W.; Moon, J. S.; Cao, Y.; Yu, G.; Shieh, C. L.; Nilsson, B.; Heeger, A. J. *Science* **2009,** *325*, 1665-1667.

23. Kminek, I.; Cimrova, V.; Vyprachticky, D.; Pavlackova, P. *Macromol. Symp*. **2008,** *268*, 100-104.

24. Kminek, I.; Vyprachticky, D.; Kriz, J.; Dybal, J.; Cimrova, V. *J. Polym. Sci: Part A: Polym. Chem.* **2010,** *48*, 2743-2756.

25. Cimrova, V.; Kminek, I.; Vyprachticky, D. *Macromol. Symp*. **2010,** *295*, 65-70.

26. Cimrova, V.; Kminek, I.; Pavlackova, P.; Vyprachticky, D. *J. Polym. Sci: Part A: Polym. Chem.***2011,** DOI 10.1002/POLA.

27. Zhang, X.; Steckler, T. T.; Dasari, R. R.; Ohira, S.; Potscavage, W. J. Jr; Tiwari, S. P.; Coppee, S.; Ellinger, S.; Barlow, S.; Bredas, J. L.; Kippelen, B.; Reynolds, J. R.; Marder, S. R. *J. Mater. Chem*. **2010,** *20*, 123-134.

28. Babel, A.; Wind, J. D.; Jenekhe, S. A. *Adv. Funct. Mater*. **2004,** *14*, 891-898.

29. Xin, H.; Guo, X.; Kim, F. S.; Ren, G.; Watson, M. D.; Jenekhe, S. A. *J. Mater. Chem*. **2009,** *19*, 5303-5310.

30. Agrawal, A. K.; Jenekhe, S. A. *Chem. Mater*. **1996,** *8*, 579-589.

31. Sariciftci, N. S. Primary Photoexcitations in Conjugated Polymers: Molecular Excitons vs Semiconductor Band Model; World Scientific: Singapore, 1997.

32. Yang, C.; Cho, S.; Chiechi,R. C.; Walker, W.; Coates N. E.; Moses, D.; Heeger, A. J.; Wudl, F. *J. Am. Chem. Soc.* **2008**, 130, 16524-16526.

2.2 NAPHTHALENE DIIMIDE BASED ORGANIC SEMICONDUCTORS FOR ORGANIC FIELD-EFFECT TRANSISTORS

2.2.1 *Introduction*

Organic field-effect transistors (OFETs) represent one of the important building blocks for developing organic and printed electronics for a variety of applications.[1-3] Both *p*-channel OFETs and *n*-channel OFETs are needed for developing low power complimentary electronic circuits.[1,3,4] The availability of many diverse *p*-type conjugated polymers has enabled the development of *p*-channel polymer OFETs with high performance (> 1 cm^2 V^{-1} s^{-1}).[5-8] n-Type polymer semiconductors remain relatively scarce and the performance of *n*-channel polymer OFETs[9-17] has consequently lagged significantly behind those of *p*-channel OFETs. Although there are many known electron-deficient building blocks for the synthesis of n-type organic semiconductors,[9, 18-20] perylenediimide (PDI)[21-24] and naphthalene diimide (NDI)[13,24-28] have been more extensively investigated for the synthesis of solution processable n-type polymer semiconductors.

We herein focus on NDI-based conjugated polymer semiconductors because of their attractive features, including easier synthesis, better solubility, and increased crystallinity compared to PDI-based conjugated polymers.[9,25] The highest field-effect electron mobility in an *n*-type polymer semiconductor has indeed been observed in an NDI-bithiophene copolymer, P(NDIOD-T2), with mobilities that vary from 0.06 cm^2 V^{-1} s^{-1} in bottom gate/top contact OFETs to as high as 0.85 cm^2 V^{-1} s^{-1} in top gate/bottom contact OFETs based on polymer dielectrics.[13] However, similar NDI-bithiophene copolymers are known to exhibit ambipolar charge transport depending on the OFET device architecture.[25,27] We have previously reported a detailed study of a series of alternating NDI-arylene copolymer semiconductors where the arylene was varied among thiophene derivatives.[25] We showed that when the arylene moiety in the copolymer was a strong electron-donating thiophene derivative such as bithiophene, dithienothiophene, and dialkoxybithiophene, almost symmetric ambipolar charge transport was obtained.[25]

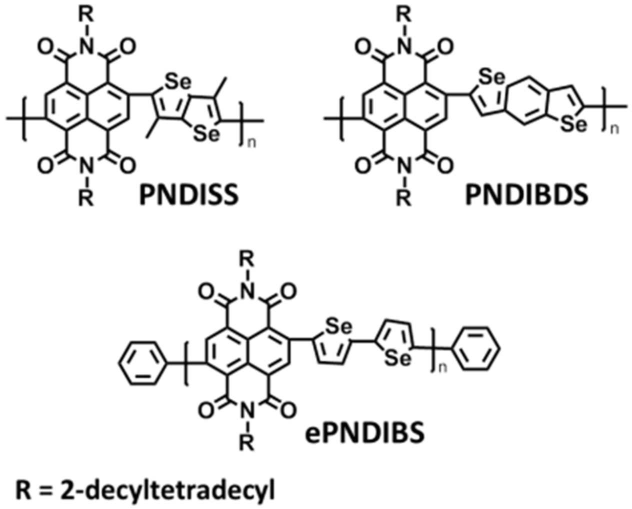

Chart 3. Molecular structures of poly(naphthalene diimides).

In this chapter, the synthesis, properties, and n-channel OFET device performance of n-type polymer semiconductors based on NDI and selenophene derivatives are discussed. The conjugated polymers, whose molecular structures are shown in **Chart 3**, include the new copolymers: poly{[N,N'-bis(2-ecyltetradecyl)-naphthalene-1,4,5,8-bis(dicarboximide)-2,6-diyl]-*alt*-2,5-(3,6-dimethyl-selenolo[3,2-b]selenophene)} (PNDISS) and poly{[N,N'-bis(2-ecyltetradecyl)-naphthalene-1,4,5,8-bis(dicarboximide)-2,6-diyl]-*alt*-2,6-(benzo[1,2-b:4,5-b′]diselenophene)} (PNDIBDS). In addition, we synthesized and investigated the phenyl end-capped derivative of poly{[N,N'-bis(2-decyltetradecyl)-naphthalene-1,4,5,8-bis(dicarboximide)-2,6-diyl]-*alt*-5,5'-(2,2'-biselenophene)} (ePNDIBS). Our present studies were motivated by interest in exploring the effects of the incorporation of selenophene derivatives on the structural and charge transport properties of poly(naphthalene diimides)(PNDIs) relative to the well studied thiophene derivatives. We also examined the effects of end-capping on the charge transport properties of the present n-type polymer semiconductors in the light of prior reports of end-capping effects in p-type conjugated polymers.[29] Our previous study of the NDI-biselenophene copolymer (PNDIBS) without end-capping showed that its electron mobility (0.07 cm^2 V^{-1} s^{-1}) was comparable to that of the corresponding NDI-bithiophene derivative (PNDIBT)[30] even though the biselenophene polymer had enhanced crystallinity due to Se-Se interactions.[30-35] Herein we show that end-capping leads to a large enhancement of the field-effect electron mobility of high molecular weight ePNDIBS but not in lower molecular weight ePNDISS or ePNDIBDS. Average electron mobility as high as 0.24 cm^2 V^{-1} s^{-1} was observed in ePNDIBS compared to 0.07 cm^2 V^{-1} s^{-1} seen in the non-end-capped PNDIBS. X-ray diffraction analysis of the NDI-selenophene derivative copolymers showed that their films had a lamellar crystalline structure in which the interchain d_{100} and π-stacking d_{010} distances varied significantly with the molecular structure of the selenophene derivative.

2.2.2 *Experimental Section*

Materials. 4,9-Dibromo-2,7-bis(2-decyltetradecyl)benzo[lmn][3,8]phenanthroline-1,3,6,8-tetraone was purchased from Sunatech. All other chemicals were purchased from Sigma-Aldrich. 3,6-Dimethyl-selenolo[3,2-b]selenophene,[36] 2,2'-biselenophene,[30,37] and benzo[1,2-b:4,5-b']diselenophene[35] were synthesized according to the known literature procedures.

2,2-Biselenophene. A solution of selenophene (5 g, 38.16 mmol) in anhydrous diethylether was added into a 250 mL round-bottom flask. The flask was degassed and filled with argon gas before bring it to 0 ℃ in an ice bath. Then, 2.5 M butyllithium solution in hexane (15.264 mL, 38.16 mmol) was added dropwise, and the solution was stirred for an hour at room temperature. After copper (II) chloride (6.81 g, 50.18 mmol) was added portionwise at -78 ℃, the reaction mixture was stirred overnight at room temperature. The mixture was quenched with ether and filtered. The solid was washed with water, 1 N HCl aqueous solution, and 5 % sodium hydrogen carbonate aqueous solution. The solid was purified by column chromatography with hexane and chloroform. Recrystallization in MeOH provide final product as a yellow solid. 2,2-Biselenophene (2 g, 21 %), ^{1}H NMR ($CDCl_3$, 300 MHz): δ (ppm) 7.9 (1H), 7.23 – 7.29 (2H).

5,5'-Bis(trimethylstannyl)-2,2'-biselenophene. 2,2-Biselenophene (2 g, 7.69 mmol) was added into a 250 mL round-bottom flask. Under argon atmosphere, 60 mL THF was then added. The mixture was cooled to -78 °C in a dry ice bath and 2.5 M butyllithium solution in hexane (7.69 mL, 19.23 mmol) was added dropwise. After stirring the mixture for an hour at room temperature, 1 M trimethyltinchloride solution in THF (16.2 mL, 16.2 mmol) was added in one portion at -78 °C. Dry ice bath was removed after an hour and the mixture was warmed up to room temperature. After stirring overnight at room temperature, the reaction mixture was poured into water and extracted with diethyl ether 2 times. The organic phase was dried with sodium sulfate anhydrous and the solvent was evaporated by vacuum rotary evaporator. After recrystallization in MeOH, yellowish white solids were obtained and subsequently used in polymerization. 5,5'-Bis(trimethylstannyl)-2,2'-biselenophene (286.3 mg, 6.5 %), ^{1}H NMR ($CDCl_3$, 300 MHz): δ (ppm) 7.36 – 7.39 (4H), 0.3 - 0.48 (18H). Melting temperature (T_m) : 110 °C.

3,6-Dimethyl-selenolo[3,2-b]selenophene. 3,6-Dimethyl-4-octyne-3,6-diol (4 g, 28.0 mmol) and selenium (7.9 g) were added into a 100 ml round-bottom flask. The flask equipped with a condenser was purged with argon. Then, the mixture was stirred at 220 °C for a day. The crude product was purified by column chromatography with hexane. The yellowish white powder was obtained and used in next step reaction without further purification. 3,6-Dimethyl-selenolo[3,2-

b]selenophene (500 mg, 6.8 %), ^{1}H NMR ($CDCl_3$, 300 MHz): δ (ppm) 7.49 (2H), 2.38 (6H). Melting temperature (T_m) : 102 °C.

2,5-Dibromo-3,6-dimethyl-selenolo[3,2-b]selenophene. 3,6-Dimethyl-selenolo[3,2-b]selenophene (500 mg, 1.9 mmol) was added into a 250 ml round-bottom flask. The flask was purged with argon before add 14 ml of CH_2Cl_2 and 6 ml of AcOH as a mixed solvent. Afterward, NBS (680 mg, 3.8 mmol) in 15 ml of CH_2Cl_2 was added dropwise. After stirring the mixture for 2 hours at 0 °C, the reaction was quenched by adding water. The crude product was extracted with $CHCl_3$, and purified by column chromatography with hexane. The yellowish white powder was obtained and used in next step without further purification. 2,5-Dibromo-3,6-dimethyl-selenolo[3,2-b]selenophene (306.8 mg, 43 %), ^{1}H NMR ($CDCl_3$, 300 MHz): δ (ppm) 2.26 (6H). Melting temperature (T_m) : 126 °C.

2,5-Bis(trimethylstannyl)3,6-dimethyl-selenolo[3,2-b]selenophene. 2,5-Dibromo3,6-dimethyl-selenolo[3,2-b]selenophene (306.8 mg, 0.73 mmol) was added into a 100 mL round-bottom flask. Under argon atmosphere, 15 mL THF was then added. The mixture was cooled to -78 °C in a dry ice bath and 2.5 M butyllithium solution in hexane (0.7 mL, 1.75 mmol) was added dropwise. After stirring the mixture for an hour at -78 °C, 1 M trimethyltinchloride solution in THF (1.83 mL, 1.83 mmol) was added in one portion at -78 °C. Dry ice bath was removed after 5 min and the mixture was warmed up to room temperature. After stirring overnight at room temperature, the reaction mixture was poured into water and extracted with diethyl ether. The organic phase was dried with anhydrous magnesium sulfate and the solvent was evaporated by vacuum rotary evaporator. After recrystallization with EtOH, yellow crystals were obtained and subsequently used in polymerization. 2,5-Bis(trimethylstannly)3,6-dimethyl-selenolo[3,2-

b]selenophene (134.8 mg, 31.4 %), ^{1}H NMR ($CDCl_3$, 300 MHz): δ (ppm) 2.38 (6H), 0.32 - 0.21 (18H).

2,6-Bis(trimethylsilyl)benzo[1,2-b:4,5-b']diselenophene. 1,4-Dibromo-2,5-bis(2-trimetylsilylethynyl)benzene (2 g, 4.67 mmol) was added into a 500 mL round-bottom flask. Afterwards, 75 mL of ether was added under argon. The mixture was cooled to -78 °C in a dry ice bath and 1.7 M *t*-butyllithium solution in hexane (11 mL, 0.0187 mol) was added dropwise. After stirring the mixture for 15 min at -78 °C, the solution was warmed up to room temperature, and selenium powder (800 mg, 0.01 mol) was added in one portion. After 15 min of stirring, 150 mL of ethanol was added, and the solution was stirred for an hour. The mixture was extracted with chloroform and washed with water two times. The crude product was purified by column chromatography with hexane. The yellowish white powder was obtained and used in next step without further purification. 2,6-Bis(trimethylsilyl)benzo[1,2-*b*:4,5-*b'*]diselenophene (800 mg, 40.1 %), ^{1}H NMR ($CDCl_3$, 300 MHz): δ (ppm) 8.33 (2H), 7.69 (2H), 0.38 (18H). Melting temperature (T_m) : 117 °C.

Benzo[1,2-b:4,5-b']diselenophene. 2,6-Bis(trimethylsilyl)benzo[1,2-*b*:4,5-*b'*]diselenophene (800 mg, 1.87 mmol) was added into a 250mL round-bottom flask. Under argon atmosphere, 34 mL THF was then added. Teterabutylammonium fluoride solution (1M) (3.73 mL, 3.73 mmol) was added at room temperature, and stirred for 3 hours. The reaction mixture was poured into water, and precipitation was filtered using filter paper. The residue was washed with water and ethanol thoroughly, and dried in the vacuum oven overnight. The yellowish white solid was obtained and used in next step without further purification. Benzo[1,2-*b*:4,5-*b'*]diselenophene (250 mg, 47.1 %). ^{1}H NMR ($CDCl_3$, 300 MHz): δ (ppm) 8.36 (2H), 7.98 (2H), 7.60 (2H). Melting temperature (T_m) : 220 °C.

2,6-Bis(trimetylstannyl)benzo[1,2-b:4,5-b']diselenophene. Benzo[1,2-*b*:4,5-*b'*]diselenophene (250 mg, 0.88 mmol) was added into a 100 mL round-bottom flask. Afterwards, 15 mL THF was added under argon. The mixture was cooled to -78 °C in a dry ice bath and 2.5 M butyllithium solution in hexane (0.81 mL, 2.024 mmol) was added dropwise. After stirring the mixture for an hour at room temperature, 1 M trimethyltinchloride solution in THF (2.11 mL, 2.11 mmol) was added in one portion at -78 °C. Dry ice bath was removed after 15 min and the mixture was warmed up to room temperature. After stirring overnight at room temperature, the reaction mixture was poured into water and extracted with diethyl ether. The organic phase was dried with anhydrous magnesium sulfate and the solvent was evaporated by vacuum rotary evaporator. After recrystallization with EtOH, white solid was obtained and subsequently used in polymerization without further purification. 2,6-Bis(trimetylstannyl)benzo[1,2-*b*:4,5-*b'*]diselenophene (194.45 mg, 36.2 %), ^{1}H NMR ($CDCl_3$, 300 MHz): δ (ppm) 8.33 (2H), 7.69 (2H), 0.32-0.51 (18H). Melting temperature (T_m) : 153 °C.

Poly{[N,N'-bis(2-ecyltetradecyl)-naphthalene-1,4,5,8-bis(dicarboximide)-2,6-diyl]-alt-2,5-(3,6-dimethyl-selenolo[3,2-b]selenophene)} (PNDISS). 4,9-Dibromo-2,7-bis(2-decyltetradecyl)benzo[lmn][3,8]phenanthroline-1,3,6,8-tetraone (252 mg, 0.23 mmol), 2,5-bis(trimethylstannyl)-3,6-dimethyl-selenolo[3,2-b]selenophene (134.8 mg, 0.23 mmol), $Pd_2(dba)_3$ (4.2 mg, 0.0046 mmol) and $P(o\text{-tolyl})_3$ (5.58 mg, 0.0184 mmol) were added into a 100 mL three-neck round-bottom flask. The flask equipped with a condenser was then degassed and filled with argon three times. Afterwards, 13 mL of chlorobenzene was added and degassed and filled with argon three times. The reaction mixture was refluxed for 72 h under argon. After cooling down to room temperature, the polymerization mixture was poured and stirred into 200 mL methanol and 5 mL hydrochloric acid solution for 3 h. The polymer precipitated out as a bluish purple solid and was filtered using a filter paper. The polymer was purified by Soxhlet extraction with methanol, hexane, and acetone. PNDISS (170 mg, 66.3 %). ^{1}H NMR ($CDCl_3$, 300 MHz): δ (ppm) 8.89 (2H), 4.19 (4H), 2.25 (6H), 2.10 (2H), 0.88-1.49 (46H). GPC : M_w = 12.3 kDa, M_n = 10.7 kDa, PDI = 1.1. TGA : T_d = 400 °C.

Poly{[N,N'-bis(2-ecyltetradecyl)-naphthalene-1,4,5,8-bis(dicarboximide)-2,6-diyl]-alt-2,6-(benzo[1,2-b:4,5-b']diselenophene)} (PNDIBDS). 4,9-Dibromo-2,7-bis(2-decyltetradecyl)benzo[lmn][3,8]phenanthroline-1,3,6,8-tetraone (350 mg, 0.32 mmol), 2,6-bis(trimetylsilyl)benzo[1,2-*b*:4,5-*b'*]diselenophene (194.45 mg, 0.32 mmol), $Pd_2(dba)_3$ (5.84 mg, 0.0064 mmol) and P(o-tolyl)$_3$ (7.77 mg, 0.0256 mmol) were added into a 100 mL three-neck round-bottom flask. The flask equipped with a condenser was then degassed and filled with argon three times. Afterwards, 18 mL of chlorobenzene was added and degassed and filled with argon three times. The reaction mixture was refluxed for 72 h under argon. After cooling down to room temperature, the polymerization mixture was poured and stirred into 200 mL methanol and 5 mL hydrochloric acid solution for 3 h. The polymer precipitated out as a bluish purple solid and was filtered using a filter paper. The polymer was purified by Soxhlet extraction with methanol, hexane, and acetone. PNDIBDS (280mg, 68.4%). ^{1}H NMR ($CDCl_3$, 300 MHz): δ (ppm) 8.88 (2H), 8.47 (2H), 7.68 (2H), 4.13 (4H), 1.98 (2H), 0.89-1.48 (46H). GPC : M_w = 27.0 kDa, M_n = 13.5 kDa, PDI = 2.0. TGA : T_d = 430 °C.

Poly{[N,N'-bis(2-decyltetradecyl)-naphthalene-1,4,5,8-bis(dicarboximide)-2,6-diyl]-alt-5,5'-(2,2'-biselenophene)} (ePNDIBS). 4,9-Dibromo-2,7-bis(2-decyltetradecyl)benzo[lmn][3,8]phenanthroline-1,3,6,8-tetraone (250 mg, 0.23 mmol), 5,5'-bis(trimethylstannyl)-2,2'-biselenophene (133.4 mg, 0.23 mmol), $Pd_2(dba)_3$ (4.2 mg, 0.0046 mmol) and P(o-tolyl)$_3$ (5.6 mg, 0.0184 mmol) were added into a 100 mL three-neck round-bottom flask. The flask equipped with a condenser was then degassed and filled with argon three times. Afterwards, 13 mL of chlorobenzene was added and degassed and filled with argon three times. The reaction mixture was refluxed for 72 h under argon. End-capping reaction was started by adding tributyltinbenzene. Bromobenzene was added after 12 hours and the reaction mixture was kept at 120 °C overnight. After cooling down to room temperature, the polymerization mixture was poured and stirred into 200 mL methanol and 5 mL hydrochloric acid solution for 3 h. The polymer precipitated out as a bluish green solid and was filtered using a filter paper. The polymer was purified by Soxhlet extraction with methanol, hexane, and acetone. ePNDIBS (263 mg, 95.5 %). ^{1}H NMR ($CDCl_3$, 300 MHz): δ (ppm) 8.73 (2H), 7.27-7.46 (4H), 4.23 (4H), 2.00 (2H), 0.76-1.46 (46H). GPC : $M_w = 106.5$ kDa, $M_n = 40.1$ kDa, PDI = 2.6. TGA : $T_d = 420$ °C.

Charateriztion. The molecular and physical properties of PNDIs were investigated by ^{1}H NMR, gel permeation chromatography (GPC) analysis, thermogravimetric analysis (TGA) and X-ray diffraction (XRD). ^{1}H NMR spectra at 300 MHz were recorded on a Bruker-AF300 spectrometer, and GPC analysis of the copolymers was performed on GPC Model 120 (DRI, PLBV400HTViscometer) against polystyrene standards in chlorobenzene at 60℃. Thermal stability of PNDIs was tested on a TA Instruments Q50 TGA at a heating rate of 20 °C/min under nitrogen gas flow. X-ray diffraction patterns were obtained from Bruker D8 Discover with a Cu Kα beam using GADD XRD system, and the solid samples were prepared by drop-casting of highly concentrated polymer solutions (20 mg/mL) in chloroform onto glass substrates with annealing at 200 ℃ for 10 minutes.

Electrochemical properties of PNDIs were investigated by cyclic voltammetry (CV). CV experiments were done on an EG&G Princeton Applied Research potentiostat/galvanostat (model 273A) in an electrolyte solution of 0.1 M tetrabutylammonium hexafluorophosphate

(Bu_4NPF_6) in acetonitrile at a scan rate of 100 mV/s. Platinum wires were used as counter and working electrodes, and Ag/Ag^+ (Ag in 0.1 M $AgNO_3$ solution, Bioanalytical System, Inc.) was used as a reference electrode. Ferrocene/ferrocenium was used as an internal standard, and the reference potential was converted to the saturated calomel electrode (SCE) scale. The samples for CV were prepared by dip-coating the copolymer solutions in chloroform onto Pt wires. Optical properties of PNDIs were measured on a Perkin-Elmer model Lambda 900 UV/vis/near-IR spectrophotometer. Solution and solid state absorption spectra were obtained from dilute (10^{-6} M) polymer solutions in chloroform and as thin films on glass substrates, respectively.

Fabrication and Characterization of Field-Effect Transistors. OFETs with bottom gate/top contact (BGTC) geometry were fabricated on heavily n doped <100> silicon wafer (0.002-0.004 Ω/cm) which served as gate electrode while its 200 nm of thermally grown SiO_2 served as the gate dielectric ($C \approx 17 nF\ cm^{-2}$). The wafer surface was cleaned and modified by sequential ultra-sonication in acetone and isopropanol followed by plasma treatment and surface modification by octyltrichlorosilane (OTS 8) self-assembled monomer (SAM). For silane modification, the wafer was spin coated in air with 0.1M solution of OTS 8 in chloroform at 3000 rpm for 10 seconds, rinsed with toluene and dried at 100 ° C for 10 minutes. The polymer thin films were fabricated on the modified substrate by spin coating 8 mg/mL of polymer solutions in chlroform at 2000 rpm for 60 seconds inside the glove box followed by annealing at 200℃ for 10 minutes on the hot plate. The gold source/drain electrodes with channel length (L) of 1000 μm and width (W) of 100 μm were deposited by vacuum evaporation through a shadow mask. All the electrical characteristics of the OFET devices were measured using HP 4145B semiconductor parameter analyzer in the nitrogen atmosphere.

2.2.3 *Results and Discussion*

Synthesis and Characterization. The comonomers 2,2'-biselenophene[30,36], 3,6-dimethyl-selenolo[3,2-b]selenophene[37] and benzo[1,2-*b*:4,5-*b'*]diselenophene[38] were synthesized by following the known literature procedures. 2,2'-Biselenophene was synthesized from the lithiated selenophene by copper ($CuCl_2$) mediated coupling reaction, and used in stannylation to get 5,5'-bis(trimethylstannyl)-2,2'-biselenophene. 3,6-Dimethyl-selenolo[3,2-b]selenophene was synthesized by the known one-pot synthesis procedure of 2,5-dimethyl-3-hexyne-2,5-diol with selenium.[37] The reaction was done under dried conditions without any solvent to maximize the temperature and pressure without using an autoclave reactor which may explain the lower yield (6.8 %) compared to the 16 % yield obtained in a reaction carried in an autoclave reactor.[37] Since 3,6-dimethyl-selenolo[3,2-b]selenophene was known to be easily over brominated on the methyl position with the reported procedure, which run the reaction at room temperature for 3 hours,[39] ran the reaction at 0 ℃ for 2 hours to avoid undesired over brominated by-products. In the case of benzo[1,2-*b*:4,5-*b'*]diselenophene monomer synthesis, which includes ring-closing reaction with selenium of lithiated 1,4-dibromo-2,5-bis(2-trimetylsilylethynyl)benzene and desilylation, all reactions were straight forward with moderate yield of 40 %. After stannylation, all of the

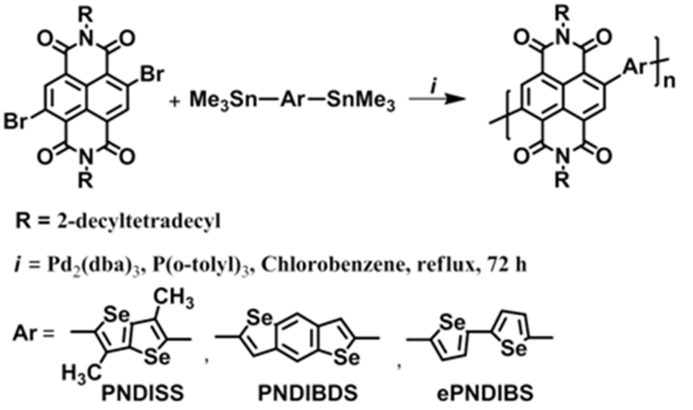

Scheme 4. Synthesis of poly(naphthalene diimides) (PNDIs).

final monomers, 5,5’-bis(trimethylstannyl)-2,2’-biselenophene, 2,5-bis(trimethylstannyl)-3,6-dimethyl-selenolo[3,2-b]selenophene and 2,6-bis(trimetylstannyl)benzo[1,2-*b*:4,5-*b'*]diselenophene were recrystallized in methanol or ethanol, and used in polymerization.

The new PNDIs were synthesized by Stille coupling copolymerization of 4,9-dibromo-2,7-bis(2-decyltetradecyl)benzo[lmn][3,8]phenanthroline-1,3,6,8-tetraone with various selenophene derivatives in the presence of $Pd_2(dba)_3$ and $P(o\text{-tolyl})_3$ in chlorobenzene solvent (**Scheme 4**). At the end of the Stille coupling synthesis of PNDIBS, the end-capping reaction to obtain ePNDIBS was carried by adding bromobenzene and tributyltinbenzene sequentially. All the PNDIs were readily soluble (> 30 mg/mL) in common organic solvents, including chloroform, toluene and chlorobenzene at room temperature, and their molecular structures were verified by ^{1}H NMR. Gel permeation chromatography (GPC) against polystyrene standard in chlorobenzene at 60 °C was performed to investigate molecular weight and polydispersity index (PDI) of the PNDIs. The weight-averaged molecular weight (M_w) varied from 12.3 kDa in PNDISS to 106.5 kDa in ePNDIBS, and PDI was 1.1-2.6 (**Table 4**). Thermogravimetric analysis (TGA) gave the decomposition temperature (T_d) in the range of 400-430 °C (**Table 4**), which indicates good thermal stability of the PNDIs. The differential scanning calorimetry (DSC) scan of PNDIs did not show any distinct transition up to 350 °C.

Table 4. Molecular Weight and Thermal Stability of PNDIs.

copolymer	M_w^a (kDa)	M_n^a (kDa)	M_w / M_n^a	T_d^b (°C)
PNDISS	12.3	10.7	1.1	400
PNDIBDS	27.0	13.5	2.0	430
ePNDIBS	106.5	40.1	2.6	420

[a] Molecular weights were determined by GPC using polystyrene standards. [b] Onset decomposition temperature measured from TGA under nitrogen.

Electronic Structure and Optical Properties. The electronic structure of the PNDIs containing selenophene derivatives (PNDISS, PNDIBDS, ePNDIBS), as characterized by the electron affinity (EA), ionization potential (IP) and optical band gap were investigated by cyclic voltammetry (CV) and optical absorption spectroscopy of thin films. The EA and IP and related LUMO/HOMO evergy levels were estimated from the onset reduction potential (EA = eE_{red}^{onset} (vs SCE) + 4.64 eV) and onset oxidation potential (IP = eE_{ox}^{onset} (vs SCE) + 4.64 eV); where the reference electrode (vs Fc/Fc^+) relative to vacuum is taken to be 4.8 eV.[40] The CV reduction waves of thin films on platinum electrodes (**Figure 8**) were characterizaed by two quasi-reversible peaks, which correspond to the sequential formation of the negative polarons and negative bipolarons of the PNDI semiconducting polymer. The observed EA values for the 3 polymers (**Table 5**) were identical at 3.9 eV, in accord with the central role of the common NDI moiety in the copolymer repeating unit. It is noteworthy that the electron affinity of the present PNDIs containing selenophene derivatives is 0.1-0.2 eV larger compared to thiophene derivative- based PNDIs.[25]

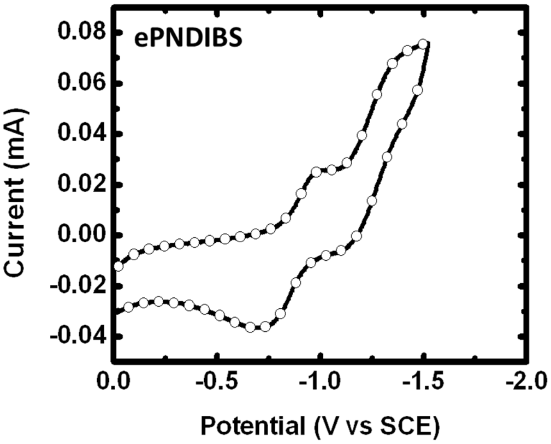

Figure 8. Cyclic voltammogram of ePNDIBS thin film on a Pt electrode in 0.1 M Bu_4NPF_6 solution in acetonitrile at a scan rate of 50 mV s^{-1}.

Cyclic voltammetry scans of the tree PNDIs up to 2.5 V (vs SCE) did not show oxidation wave except ePNDIBS. The IP value obtained from the onset oxidation potential of ePNDIBS was 5.90 eV. This value is larger compared to bithiophene-NDI copolymer which has an IP of 5.77 eV.[25] The larger IP of ePNDIBS compared to the corresponding bithiophene-containing PNDI implies that biselenophene is a weaker electron donating moiety than bithiophene. Given that biselenophene is a stronger electron donating moiety than selenoloselenophene and benzodiselenophene, we expect the IP values of PNDISS and PNDIBDS to be larger than that of ePNDIBS.

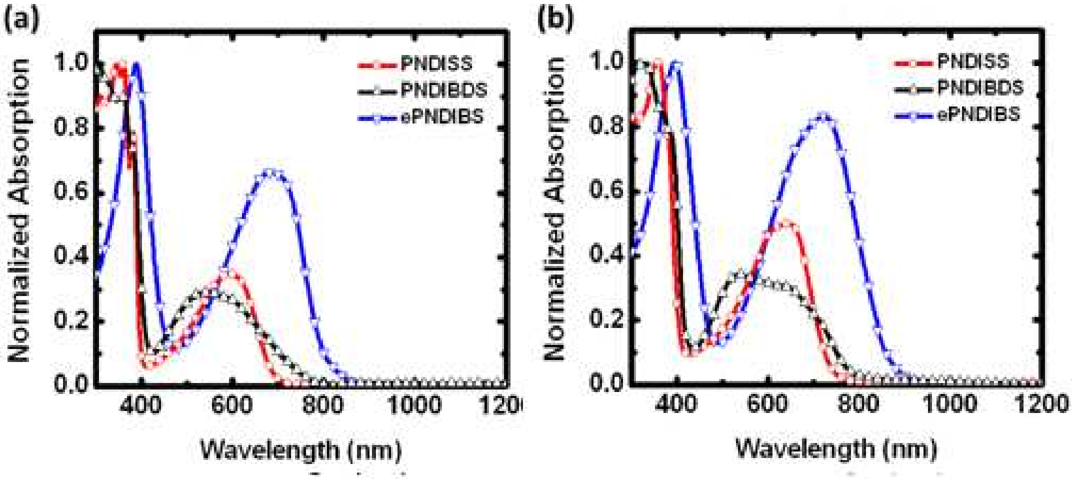

Figure 9. Optical absorption spectra of PNDIs in dilute chloroform solution (a) and as thin films on glass substrates (b).

The optical absorption spectra of the PNDIs in dilute (10^{-6} M) chloroform solution and as thin films on glass substrates are shown in **Figure 9**. Two distinctive absorption bands, a higher energy band which can be assigned as a π–π* transition band and an intramolecular charge transfer (ICT) band in lower energy range, are observed in each polymer.[41] In dilute solution, the absorption maximum (λ_{max}) of the π–π* transition band varied from 309 nm in PNDIBDS to 388 nm in ePNDIBS while the ICT band peak varied from 560 nm in PNDIBDS to 675 nm in ePNDIBS. The absorption bands of ePNDIBS are red-shifted compared to those of PNDISS and PNDIBDS due to the stronger electron donating nature of biselenophene moiety compared to the other two. The thin film absorption spectra are very similar to the solution spectra in that they are characterized by the two bands. However, the thin film absorption bands are red-shifted and the intensity of ICT bands is enhanced compared to the corresponding absorption bands in dilute solution. This can be explained by the increased conjugation length and intermolecular interaction between polymer chains in the solid state. The λ_{max} of the π–π^* transition band and ICT band in thin films are in the range of 333-399 nm and 537-725 nm, respectively. In the case of PNDIBDS, its ICT bands in solution and solid state are relatively weak due to the relatively weak electron donating nature of benzodiselenophene. The absorption edge energy band gap (E_g^{opt}) varied from 1.4 eV in ePNDIBS to 1.72 eV in PNDISS (**Table 5**).

Table 5. Electrochemical and Optical Properties of PNDIs.

copolymer	EA[a] (eV)	IP[b] (eV)	E_g^{el} (eV)	λ_{max}[c] (nm)	λ_{max}[d] (nm)	α_{max}[e] (10^4 cm^{-1})	E_g^{opt} (eV)
PNDISS	3.89	-	-	361, 594	359, 644	2.70	1.72
PNDIBDS	3.90	-	-	309, 560	333, 537	2.56	1.55
ePNDIBS	3.90	5.90	2.00	388, 675	399, 725	3.42	1.40

[a] Electron affinity was obtained based on EA = eE_{red}^{onset} (vs SCE) + 4.64 eV. [b] Ionization potential was obtained based on IP = eE_{ox}^{onset} (vs SCE) + 4.64 eV. [c] The absorption maximum in dilute solution. [d] The thin film absorption maximum. [e] Absorption coefficient at the absorption maximum.

The observed thin film absorption spectrum of ePNDIBS is both red-shifted (~20 nm) and broadened compared to the corresponding NDI-bithiophene copolymers.[24,25] This is likely a result of both the stronger ICT and stronger intermolecular interactions of selenophene derivative compared to the thiophene derivative.[30-35] Although there are no exact corresponding thiophene-based copolymers as PNDISS and PNDIBDS, it can be expected that PNDISS and PNDIBDS have similarly red-shifted and broader optical absorption bands. These features can be a great advantage in optoelectronic applications of the materials. Absorption coefficient of the PNDIs was also measured and it is shown in **Table 5**. The absorption coefficient (α) was in the range of $2.6\times10^4 - 3.4\times10^4$ cm^{-1} which is lower than the p-type polymer poly(3-hexylthiophene) (P3HT) (>10^5 cm^{-1}). The low α value is a result of the large alkyl side chains of the PNDIs and thus could be increased by shortening the side chains.

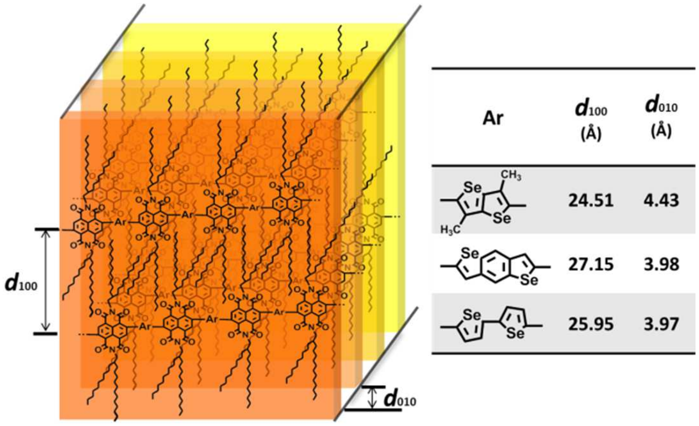

Scheme 5. Lamellar crystalline packing structure of PNDIs.

X-ray Diffraction (XRD) Analysis. The solid state morphology and particularly the lamellar crystalline structure of the series of PNDIs were investigated by X-ray diffraction (XRD) analysis. The XRD patterns of solution cast films of the polymers are shown in **Figure 10**. Observation of a sharp and intense characteristic (100) reflection in the XRD pattern of each polymer means that all the PNDIs self-organize into a lamellar crystalline structure illustrated in **Scheme 5**. The (100) lamellar diffraction peak of the PNDIs was observed at $2\theta = 3.40^\circ$ in ePNDIBS, at $2\theta = 3.60^\circ$ in PNDISS, and at $2\theta = 3.25^\circ$ in PNDIBDS with a corresponding d_{100} spacing that varies from 24.51 Å in PNDISS to 27.15 Å in PNDIBDS. The lamellar packing distance d_{100} is significantly shorter than expected from the alkyl chain length of 43.12 Å ($2\times C_{14}$), and thus we conclude that there is interdigitation of the alkyl side chains between the polymer backbone (**Scheme 5**). A shorter interchain distance (d_{100}) is in PNDISS compared to ePNDIBS, which can be explained by the larger torsion angle of polymer backbone due to strong steric hindrance between the large NDI core and the much smaller selenoloselenophene ring. Similarly, the d_{100} spacings in ePNDIBS and PNDISS are much smaller than in PNDIBDS for the same reasons. Similar trends have been found in thiophene derivative-linked PNDIs as well.[25] The (200) diffraction peaks at 2θ = 6.65°, 7.10° and 6.60° in ePNDIBS, PNDISS and PNDIBDS, respectively, were also observed, in the XRD patterns (**Figure 10**), indicating that these polymers are highly crystalline.

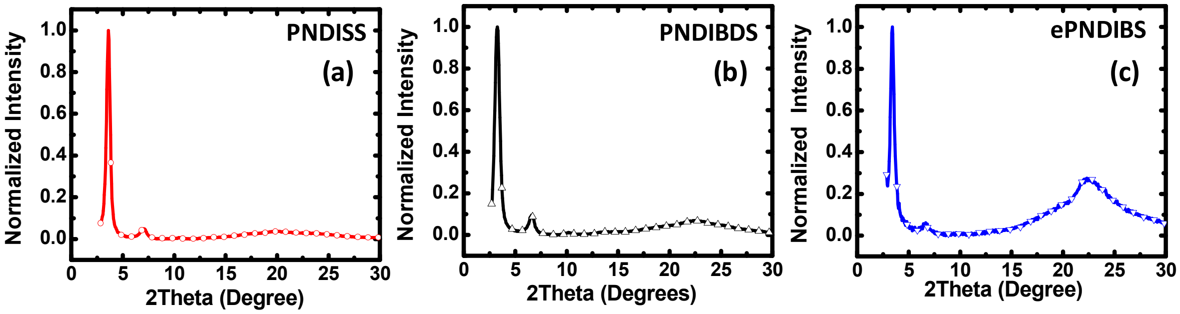

Figure 10. XRD patterns of thin films of PNDIs on glass substrates.

The π−π stacking (010) diffraction was observed as a broad peak at 2θ = 22.35°, 20.0° and 22.3° in ePNDIBS, PNDISS and PNDIBDS, corresponding to d_{010} spacing to 3.97 Å, 4.43 Å and 3.98 Å, respectively. These π-stacking distances are comparable with those reported for other PNDIs (~ 4.0 Å).[25] It is interesting that there is a large dependence of the π−π stacking distance on the comonomer selenophene derivative. Both ePNDIBS and PNDIBDS have a 0.45-0.46 Å shorter π−π stacking distance compared to PNDISS (**Scheme 5**). The much larger π−π stacking distance of PNDISS is a consequence of both the methyl side chains on the comonomer selenoloselenophene (SS) and its overall small size compared to NDI which induce a larger tortion angle between NDI rings in the polymer backbone. In the case of ePNDIBS, the π−π stacking peak is sharper and more intense compared to PNDIBDS, and this indicates higher crystallinity of ePNDIBS. The higher molecular weight of ePNDIBS is likely the reason for its higher crystalline order among the three polymers.

These features of the lamellar crystalline structure of copolymers of NDI and selenophene derivatives, especially the observed large dependence of the lamellar interchain distance d_{100} and π-stacking distance d_{010} on the structure of the selenophene derivatives, have no precedence in the related thiophene analogues. For example, NDI-thienothiophene and NDI-bithiophene copolymers were found to have a similar π-stacking distance of 3.9-4.0 Å in a previous study.[25] The difference in interchain packing distance d_{100} in PNDISS and ePNDIBS found here to be 1.44 Å is much shorter in the corresponding NDI-thienothiophene/bithiophene copolymer pair (1.1 Å). We propose that this differrence in molecular packing trends of the NDI-selenophene derivatives relative to the NDI-thiophene derivatives can be accounted for by the much larger orbitals of selenium compared to those of sulfur.[30-35] Furthermore, we note that the enhanced intermolecular interactions and higher crystalline order in PNDIs containing selenophene derivatives could be beneficial to charge transport and optoelectronic properties of the materials.

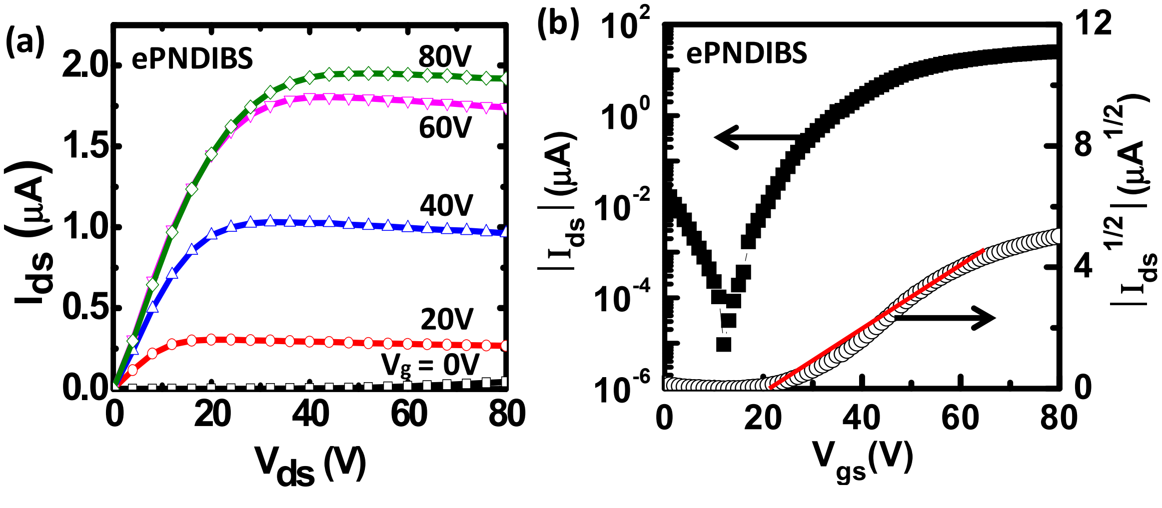

Figure 11. Output (a) and transfer (b) characteristics of ePNDIBS OFETs.

Organic Field-Effect Transistors. The field-effect charge transport properties of the PNDIs containing selenophene derivatives were investigated by fabricating and testing OFETs with bottom gate/top contact (BGTC) architecture. The field effect mobility in the saturation region was calculated from the slope of $(I_{ds})^{-0.5}$ versus V_{gs} using the equation: $I_{ds} = (W/2L)\mu C_i(V_{gs} - V_t)^2$, where I_{ds} is the drain-source current in the saturated region, W/L is the channel width to length ratio, μ is the field-effect mobility, C_i is the capacitance per unit area of the dielectric layer (17nF cm^{-2}), whereas V_{gs} and V_t are the gate and threshold voltages, respectively. The field effect mobilities of at least 5 OFET devices were measured and averaged for each polymer. Representative output and transfer curves are exemplified in **Figure 11** for ePNDIBS OFETs. The average electron mobility, threshold voltage, and on/off current ratio are summarized in **Table 6**. The threshold voltage of the n-channel OFETs from ePNDIBS, PNDISS and PNDIBDS were found to be in the range of 12-15 V, which is close to ideal for the operation and low power consumption of circuits built from these transistors. The n-channel OFETs generally had high I_{on}/I_{off} ratio in the range of 10^4 to 10^6.

All the OFETs showed typical n-type behavior with well-defined linear and saturation regions with excellent current modulation in the output and transfer characteristics. OFETs based on PNDISS showed unipolar n-channel transport characreristics and the average saturation region electron mobility was 0.008 cm^2 V^{-1} s^{-1}. In contrast, ePNDIBS and PNDIBDS devices showed ambipolar characteristics although the p-channel currents were more than four orders of magnitude lower than the n-channel currents. A much higher average electron mobility of 0.24 and 0.01 cm^2 V^{-1} s^{-1} for ePNDIBS and PNDIBDS, respectively, was obtained. Among the factors that could explain the observed trends in the field-effect electron mobility of the series of new PNDIs (**Table 6**) are the lamellar crystalline packing, molecular weight, and end capping. The similarity of the molecular weights of PNDISS and PNDIBDS (**Table 4**) suggests that the smaller π-stacking distance in PNDIBDS likely accounts for its higher carrier mobility in this group. On the other hand, PNDIBDS (0.398 nm) has a very similar π-stacking distance as in ePNDIBS (0.397 nm) and yet the latter has a factor of 24 higher electron mobility. In this case, the higher molecular weight of ePNDIBS and possibly end capping could explain its much higher electron mobility.

Table 6. Field-effect Charge Transport Properties of PNDIs in n-Channel OFETs.

Copolymer	μ_e ($cm^2\,V^{-1}\,s^{-1}$)	I_{on}/I_{off}	V_t (V)
PNDISS	0.008	10^5	15
PNDIBDS	0.01	10^4	15
ePNDIBS	0.24	10^6	12

End capping of conjugated polymers is known to dramatically influence their charge transport and optoelectronic properties.[29] The observed enhancement of the carrier mobilities in end-capped polymer semiconductors relative to their non-end-capped versions has been explained in terms of minimization of charge trapping sites.[29] It is thought that end groups remaining from un-reacted functional groups of the monomers (e.g. Br, $Sn(Me_3)$) or ill-defined ones after quenching of the polymerization reaction can act as charge trapping sites.[29] End-capping with well-defined groups such as phenyl could thus minimize or eliminate charge trapping sites at chain ends. In this context, the presently observed field-effect electron mobility of 0.24 $cm^2\,V^{-1}\,s^{-1}$ for end-capped ePNDIBS is to the compared to previously reported, similarly measured, electron mobility of 0.07 $cm^2\,V^{-1}\,s^{-1}$ for the PNDIBS sample without phenyl end-capping and very similar molecular weight (M_w = 110.0 kDa, M_n = 42.4 kDa, PDI = 2.6).[26] End-capping rather than molecular weight thus appears to account for the observed high mobility of ePNDIBS.

The large (3.4-fold) enhancement of electron mobility in ePNDIBS encouraged us to also synthesize end-capped versions of PNDISS and PNDIBDS (ePNDISS, ePNDIBDS) for comparison. However, the field-effect carrier mobilities of ePNDISS and ePNDIBDS were essentially unchanged from those of PNDISS and PNDIBDS in **Table 6** even though the molecular weight and other properties were very similar. This result is surprising given our current understanding of end-capping effects on the charge transport properties of π-conjugated polymers.[29] In fact, given that the concentration of end-groups is higher the lower the molecular weight of the polymer, a greater enhancement in charge transport was expected for ePNDISS and ePNDIBDS than observed in the high molecular weight ePNDIBS. It is not yet clear whether we can conclude that end-capping effects are limited to only high molecular weight polymer semiconductors.

2.2.4 *Conclusions*

New *n*-type polymer semiconductors incorporating naphthalene diimide (NDI) and selenophene derivative in a donor-acceptor structure were synthesized by Stille coupling polymerization. The new poly(naphthalene diimide)s (PNDIs) were obtained with moderate to high molecular weights (M_w = 12 - 107 kDa) and good solution processability. The optical properties of the PNDIs are characterized by narrow band gaps (1.4-1.7 eV) and high absorption coefficients of $(2.6\text{-}5.5) \times 10^4$ cm^{-1} at the absorption maxima. The visible-near IR optical absorption band of the biselenophene-linked PNDI was significantly broadened and red shifted compared to that of the corresponding bithiophene-linked PNDI. X-ray diffraction analysis of films of the PNDIs showed that they were highly crystalline, revealing a lamellar interchain packing distance of 2.45-2.75 nm and a π-stacking distance of 0.397-0.443 nm depending on the selenophene derivative in the backbone. Bottom gate and top contact *n*-channel OFETs incorporating the new polymers gave field-effect electron mobilities of 0.008 to 0.24 cm^2 V^{-1} s^{-1}. We observed a large (3.4-fold) enhancement in the field-effect electron mobility in the phenyl end-capped high molecular weight NDI-biselenophene copolymer whereas no change was seen in the carrier mobility of similarly end-capped PNDISS and PNDIBDS materials.

2.2.5 *References*

1. *Organic Field-Effect Transistors*, ed. Z. Bao and J. Lacklin, CRC Press, Boca Raton, Florida, 2007.
2. C. Wang, H. Dong, W. Hu, Y. Liu and D. Zhu, *Chem. Rev.*, 2012, **112**, 2208.
3. J. Zaumseil and H. Sirringhaus, *Chem. Rev.*, 2007, **107**, 1296.
4. H. Klauk, U. Zschieschang, J. Pflaum and M. Halik, *Nature*, 2007, **445**, 745; F. S. Kim, E. Ahmed, S. Subramaniyan and S. A. Jenekhe, *Appl. Mater. Interfaces*, 2010, **2**, 2974.
5. H. Bronstein, Z. Chen, R. S. Ashraf, W. Zhang, J. Du, J. R. Durrant, P. S. Tuladhar, K. Song, S. E. Watkins, Y. Geerts, M. M. Wienk, R. A. J. Janssen, T. Anthopoulos, H. Siringhaus, M. Heeney and I. McCulloch, *J. Am. Chem. Soc.*, 2011, **133**, 3272.
6. J. Fan, J. D. Yuen, W.Cui, J. Seifter, A. R. Mohebbi, M. Wasng, H. Zhou, A. Heeger and F. Wudl, *Adv. Mater.*, 2012, **24**, 6164.
7. J. Mei, D. H. Kim, A. L. Ayzner, M. F. Toney and Z. Bao, *J. Am. Chem. Soc.*, 2011, **133**, 20130.
8. S. Subramaniyan, F. S. Kim, G. Ren, H. Li and S. A. Jenekhe, *Macromolecules*, 2012, **45**, 9029.
9. J. E. Anthony, A. Facchetti, M. Heeney, S. R. Marder and X. Zhan, *Adv. Mater.*, 2010, **22**,

3876.

10. A. Babel and S. A. Jenekhe, *Adv. Mater.*, 2002, **14**, 371.
11. A. Babel and S. A. Jenekhe, *J. Am. Chem. Soc.*, 2003, **125**, 13656.
12. L. L. Chua, J. Zaumseil, J. F. Chang, E. C. W. Ou, P. K. H. Ho, H. Sirringhaus and R. H. Friend, *Nature,* 2005, **434**, 194.
13. H. Yan, Z. Chen, Y. Zheng, C. Newman, J. R. Quinn, F. Dötz, M. Kastler and A. Facchetti, *Nature*, 2009, **457**, 679.
14. Z. Chen, M. J. Lee, R. S. Ashraf, Y. Gun, S. A. Seifried, M. M. Nielsen, B. Schroeder, T. D. Anthpoulos, M. Heeney, I. McCulloch and H. Sirringhaus, *Adv. Mater.*, 2012, **24**, 647.
15. Y. Takeda, T. L. Andrew, J. M. Lobez, A. J. Mork and T. M. Swager, *Angew. Chem. Int. Ed.*, 2012, **51**, 9042.
16. B. A. Jones, A. Facchetti, M. R. Wasielewski and T. J. Marks, *J. Am. Chem. Soc.,* 2007, **129**, 15259.
17. C. R. Newman, C. D. Frisbie, D. A. da Silva, J. A. Bredas, P. C. Ewbank and K. R. Mann, *Chem. Mater*. 2004, **16**, 4436.
18. A. P. Kulkarni. C. J. Tonjola, A. Babel and S. A. Jenekhe, *Chem. Mater*., 2004, **16**, 4556.
19. C. J. Tonzola, M. M. Alam, W. Kaminsky and S. A. Jenekhe, *J. Am. Chem. Soc*., 2003, **125**, 13548.
20. T. Yamamoto, *Macromol. Rapid Commun*., 2002, **23**, 583.
21. X. Zhan, Z. A. Tan, B. Domercq, Z. An, X. Zhang, S. Barlow, Y. F. Li, D. Zhu, B. Kippelen and S. R. Marder, *J. Am. Chem. Soc*., 2007, **129**, 7246.
22. E. J. Zhou, K. Tajima, C. H. Yang and K. Hashimoto, *J. Mater. Chem*., 2010, **20**, 2362.
23. L. J. Huo, Y. Zhou and Y. F. Li*, Macromol. Rapid Commun*., 2008, **29**, 1444.

24. Z. Chen, Y. Zheng, H. Yan and A. Facchetti, *J. Am. Chem. Soc.*, 2009, **131**, 8.

25. X. Guo, F. S. Kim, M. J. Seger, S. A. Jenekhe and M. D. Watson, *Chem. Mater.*, 2012, **24**, 1434.

26. M. M. Durban, P. D. Kazarinoff and C. K. Luscombe, *Macromolecules*, 2010, **43**, 6348.

27. F. S. Kim, X. Guo, M. D. Watson and S. A. Jenekhe, *Adv. Mater.*, 2010, **22**, 478.

28. S. G. Hahm, Y. Rho, J. Jung, S. H. Kim, S. Sajoto, F. S. Kim, S. Barlow, C. E. Park, S. A. Jenekhe, S. R. Marder and M. Ree, *Adv. Funct. Mater.*, 2013, DOI: 10.1002/adfm.201202065.

29. P. T. Wu, H. Xin, F. S. Kim, G. Ren and S. A. Jenekhe, *Macromolecules,* 2009, **42**, 8817; J. K. Park, J. Jo, J. H. Seo, J. S. Moon, Y. D. Park, K. Lee, A. J. Heeger and G. C. Bazan, *Adv. Mater*. 2011, **23**, 2430.

30. Y. J. Hwang, G. Ren, N. M. Murari, S. A. Jenekhe, *Macromolecules*, 2012, **45**, 9056.

31. T. Yammamoto, Z. H. Zhou, T. Kanbara, M. Shimura, K. Kizu, T. Maruyama, Y. Nakamura, T. Fukuda, B. L. Lee, N. Ooba, S. Tomuru, T. Kurihara, T. Kaino, K. Kubota and S. Sasaki, *J. Am. Chem. Soc.*, 1996, **118**, 10389.

32. Z. Chen, H. Lemke, S. A. Seifried, M. Caironi, M. M. Nielsen, M. Heeney, W. Zhang, I. McCulloch and H. Sirringhaus, *Adv. Mater.*, 2010, **22**, 2371.

33. J. Hollinger, A. A. Jahnke, N. Coombs and D. S. Seferos, *J. Am. Chem. Soc.*, 2010, **132**, 8546.

34. H. W. Lin, W. Y. Lee, C. Lu, C. J. Lin, H. C. Wu, Y. W. Lin, B. Ahn, Y. Rho, M. Ree and W. C. Chen, *Polym. Chem.*, 2012, **3**, 767.

35. W. H. Lee, S. K. Son, K. Kim, S. K. Lee, W. S. Shin, S. J. Moon and I. N. Kang, *Macromolecules*, 2012, **45**, 1303.

36. K. S. Choi, K. Sawada, H. Dong, M. Hoshino and J. Nakayama, *Heterocycles*, 1994, **38**,

143.

37. Y. M. Kim, E. Lim, I. N. Kang, B. J. Jung, J. Lee, B. W. Koo, L. M. Do and H. K. Shim, *Macromolecules*, 2006, **39**, 4081.

38. K. Takimiya, Y. Konda, H. Ebata, N. Niihara, T. Otsubo, *J. Org. Chem*., 2005, **70**, 10569.

39. J. Nakayama, H. Dong, K. Sawada, A. Ishii and S. Kumakura, *Tetrahedron*, 1996, **52**, 471.

40. A. J. Bard and J. L. R. Faulkner, *Electrochemical Methods: Fundamentals and Applications*, John Wiley & Sons, New York, 2nd edn., 2001; S. Trassatti, *Pure Appl. Chem*., 1986, **58**, 955.

41. S. A. Jenekhe, L. Lu and M. M. Alam, *Macromolecules*, 2001, **34**, 7315.

Chapter 3. N-TYPE POLYMER SEMICONDUCTORS FOR ALL-POLYMER SOLAR CELLS.

The results in this chapter are reprinted with permission from Hwang, et al. *Macromolecules* **2012**, *45*, 9056 (Copyright 2012 American Chemical Society) and Earmme and Hwang, et al. *J. Am. Chem. Soc*. **2013**,*135*, 14960 (Copyright 2013 American Chemical Society).

3.1 N-TYPE NAPHTHALENE DIIMIDE-BISELENOPHENE COPOLYMER FOR ALL-POLYMER SOLAR CELLS

3.1.1 *Introduction*

Much progress has been made in the development of polymer/fullerene solar cells[1-7] with power conversion efficiency now near 10 %.[8-10] Nevertheless, polymer/polymer bulk heterojunction (BHJ) solar cells[11-23] are of increasing interest largely because of the many disadvantages of fullerenes[24] on the one hand and potential beneficial advantages of n-type polymer semiconductors as acceptor materials on the other hand. Although currently less developed and less efficient, the all-polymer BHJ solar cell composed of a binary blend of a p-type (donor) polymer and an n-type (acceptor) polymer[11] was introduced simultaneously with the polymer/fullerene BHJ solar cell[5] in 1995. Areas of potential advantages of polymer/polymer BHJ solar cells compared to polymer/small molecule systems include: (1) ready tunability of the electronic structure, charge transport, and optical properties of polymers; (2) easy formulation of the coating solution and control of its rheological properties and thus ready achievement of film thinkness in the 150-250 nm range; (3) more predictable and stable phase-separated morphology arising from the thermodynamics and kinetics of phase separation of polymer/polymer blends; and (4) enhanced thermo/mechanical properties and durability of devices. However, a major challenge in developing all-polymer BHJ solar cells has been the scarcity of solution processable n-type polymer semiconductors that combine high carrier mobility with high electron affinity and suitable optical absorption spectra.[11-23, 25-29]

Early observation of high field-effect electron mobility ($\mu_e = 0.1$ cm^2/Vs) transport in the n-type polymer, poly(benzimidazobenzophenanthroline) (BBL), was exploited in all-polymer solar cells with a bilayer architecture exhibiting a power conversion efficiency (PCE) of 1.5 % under AM1.5 1 sun illumination.[13, 14] Perylene diimide (PDI)-based copolymers of various backbone compositions have been found to exhibit moderate field-effect electron mobilities (0.01-0.05 cm^2/Vs), leading to all-polymer BHJ solar cells with power conversion efficiency of about 0.29 % to as high as 2.23 %.[16-18] More recently, the naphthalene diimide-bithiophene copolymer, (P(NDIOD-T_2)), was shown to exhibit very high electron mobility (> 0.1 cm^2/Vs) in top gate/bottom contact field-effect transistors using various polymeric dielectrics.[26] Initial use of P(NDIOD-T_2) as the acceptor with P3HT as the donor in BHJ devices gave a low PCE of 0.2 %.[21, 23] However, the efficeincy of P(NDIOD-T_2)/poly(3-hexylthiophene) BHJ solar cells was improved to 1.4 % with optimized morphology by using a mixed solvent of p-xylene and chloronaphthalene.[20]

In this chapter, I report the synthesis, properties and application in all-polymer bulk heterojunction solar cells of a new solution processable n-type copolymer semiconductor based on alternating naphthalene diimide (NDI) and biselenophene units, poly{[N,N'-bis(2-decyltetradecyl)-naphthalene-1,4,5,8-bis(dicarboximide)-2,6-diyl]-*alt*-5,5'-(2,2'-biselenophene)} (PNDIBS), whose molecular structure is shown in Figure 1. The new copolymer has a donor-acceptor (D-A) structure incorporating NDI as the electron acceptor moiety, which is known to lead to highly regioregular lamellar crystalline morphology and high carrier mobility.[26-29] We

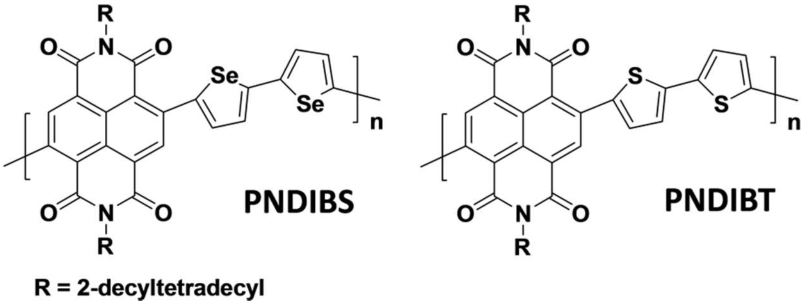

Figure 12. Molecular structures of naphthalene diimide-biselenophene copolymer (PNDIBS) and its bithiophene derivative PNDIBT.

selected biselenophene as the electron donor moiety in the D-A copolymer PNDIBS in view of the larger p-orbitals of selenium, compared to thiophene, and this can inprove orbital overlap and increase the charge carrier mobility. The empty orbitals on selenium can also enhance the electron accepting ability of oligoselenophene and lower the aromaticity of selenophene, which could facilitate the fine tuning of the electronic structure and optical band gap of the copolymer.[30-43] In addition, Se-Se intermolecular interactions could enhance crystallization and inter-chain charge transport.[30-43] X-ray diffraction of PNDIBS thin films revealed a highly crystalline structure, resulting in a high electron mobility of 0.07 cm^2/Vs as determined by bottom gate thin film transistors. All-polymer BHJ solar cells comprising PNDIBS as the acceptor and poly(3-hexylthiophene) (P3HT) as the donor were fabricated and characterized, showing a power conversion efficiency of 0.9 %. We also synthesized and investigated the well-known bithiophene-linked polymer, poly{[N,N'-bis(2-decyltetradecyl)-naphthalene-1,4,5,8-is(dicarboximide)-2,6-diyl]-*alt*-5,5'-(2,2'-bithiophene)} (PNDIBT),[26-28] also shown in **Figure 12**for comparison purposes.

3.1.2 *Experimental Section*

Materials. 4,9-Dibromo-2,7-bis(2-decyltetradecyl)benzo[lmn][3,8]phenanthroline-1,3,6,8-tetraone was purchased from Solarmer. All other chemicals were purchased from Sigma-Aldrich.

2,2-Biselenophene. A solution of selenophene (5 g, 38.16 mmol) in anhydrous diethylether was added into 250 mL round-bottom flask. The flask degassed filled with argon gas before bring it to 0 ˚C in a ice bath. Then, 2.5 M butyllithium solution in hexane (15.264 ml, 38.16 mmol) was added dropwise, and the solution was stirred for an hour at room temperature. After copper (II) chloride (6.81 g, 50.18 mmol) was added portionwise at -78 ˚C, the reaction mixture was stirred overnight at room temperature. The mixture was quenched with ether and filtered. The solid was washed with water, 1 N HCl aqueous solution, and 5 % sodium hydrogen carbonate aqueous solution. The solid was purified by column chromatography with hexane and chloroform. Recrystallization in MeOH provide final product as a yellow solid (2 g; yield = 21 %). ^{1}H NMR (CDCl3, 300 MHz, δ): 7.9 (1H), 7.23 – 7.29 (2H).

5,5’-Bis(trimethylstannyl)-2,2’-biselenophene. 2,2-Biselenophene (2 g, 7.69 mmol) was added into a 250 mL round-bottom flask. Afterwards, 60 mL THF was added under argon. The mixture was cooled to -78 °C in a dry ice bath and 2.5 M butyllithium solution in hexane (7.69 mL, 19.23 mmol) was added dropwise. After stirring the mixture for an hour at room temperature, 1 M trimethyltinchloride solution in THF (16.2 mL, 16.2 mmol) was added in one portion at -78 °C. Dry ice bath was removed after an hour and the mixture was warmed up to room temperature. After stirring overnight at room temperature, the reaction mixture was poured into water and extracted with diethyl ether 2 times. The organic phase was dried with sodium sulfate anhydrous and the solvent was evaporated by vacuum rotary evaporator. After reprecipitation in MeOH, yellowish white solids were obtained and subsequently used in polymerization without further purification (286.3 mg; yield = 6.5 %). ^{1}H NMR (CDCl3, 300 MHz δ): 7.36 – 7.39 (4H), 0.3 - 0.48 (18H).

Poly{[N,N'-bis(2-decyltetradecyl)-naphthalene-1,4,5,8-bis(dicarboximide)-2,6-diyl]-*alt*-5,5'-(2,2'-biselenophene)} (PNDIBS). 4,9-Dibromo-2,7-bis(2-decyltetradecyl)benzo[lmn][3,8]phenanthroline-1,3,6,8-tetraone (536.4 mg, 0.49 mmol), 5,5'-bis(trimethylstannyl)-2,2'-biselenophene (286.3 mg, 0.49 mmol), $Pd_2(dba)_3$ (9 mg, 0.01 mmol) and $P(o\text{-}tolyl)_3$ (12 mg, 0.039 mmol) were added into a 100 mL three-neck round-bottom flask. The flask equipped with a condenser was then degassed and filled with argon three times. Afterwards, 27 mL of chlorobenzene was added and degassed and filled with argon three times. The reaction mixture was refluxed for 72 h under argon. After cooling down to room temperature, the polymerization mixture was poured and stirred into 200 mL methanol and 5 mL hydrochloric acid solution for 3 h. The polymer precipitated out as a bluish green solid and was filtered using a filter paper. The polymer was purified by Soxhlet extraction with methanol, hexane, and acetone (550 mg; yield = 98.3 %).

Poly{[N,N'-bis(2-decyltetradecyl)-naphthalene-1,4,5,8-is(dicarboximide)-2,6-diyl]-*alt*-5,5'-(2,2'-bithiophene)} (PNDIBT). 4,9-Dibromo-2,7-bis(2-decyltetradecyl)benzo[lmn][3,8]phenanthroline-1,3,6,8-tetraone (400 mg, 0.36 mmol), 5,5'-bis(tributylstannyl)-2,2'-bithiophene (271.3 mg, 0.36 mmol), $Pd_2(dba)_3$ (7 mg, 0.007 mmol) and $P(o\text{-}tolyl)_3$ (9 mg, 0.029 mmol) were added into a 100 mL three-neck round-bottom flask. The flask equipped with a condenser was then degassed and filled with argon three times. Afterwards, 22 mL of chlorobenzene was added and degassed and filled with argon three times. The reaction mixture was refluxed for 72 h under argon. After cooling down to room temperature, the polymerization mixture was poured and stirred into 200 mL methanol and 5 mL hydrochloric acid solution for 3 h. The polymer precipitated out as a greenish blue solid and was filtered using a filter paper. The polymer was purified by Soxhlet extraction with methanol, hexane, and acetone (96.2 mg; yield = 87.3 %).

Characterization. The molecular structuer and physical properties of PNDIBS and PNDIBT were investigated by ^{1}H NMR, gel permeation chromatography (GPC) analysis, thermogravimetric analysis (TGA) and X-ray diffraction (XRD). ^{1}H NMR spectra at 300 MHz were recorded on a Bruker-AF300 spectrometer. GPC analysis of the copolymers was performed on GPC Model 120 (DRI, PLBV400HTViscometer) against polystyrene standards in chlorobenzene at 60˚C. TGA thermograms were obtained on a TA Instruments Q50 TGA at a heating rate of 20 °C/min under nitrogen gas flow. XRD data were obtained from Bruker D8 Discover with a Cu Kα beam using GADD XRD system, and the samples were prepared by drop-casting of polymer solutions in chloroform onto glass substrates follwed by annealing at 200 ˚C for 10 minutes.

Optical and electrochemical properties were investigated by UV-Vis absorption spectroscopy and cyclic voltammetry. Absorption spectra were measured on a Perkin-Elmer model Lambda 900 UV/vis/near-IR spectrophotometer. Solution and solid state absorption spectra were obtained from polymer solutions in chloroform and as thin films on glass substrates, respectively. Cyclic voltammetry (CV) experiments were done on an EG&G Princeton Applied Research potentiostat/galvanostat (model 273A) in an electrolyte solution of 0.1 M tetrabutylammonium hexafluorophosphate (Bu_4NPF_6) in acetonitrile at a scan rate of 100 mV/s. A three-electrode cell was used in this analysis. Platinum wires were used as counter and working electrodes, and Ag/Ag^+ (Ag in 0.1 M $AgNO_3$ solution, Bioanalytical System, Inc.) was used as a reference electrode. Ferrocene/ferrocenium was used as an internal standard by running CV at the end, and this data was used to convert the potential to saturated calomel electrode

(SCE) scale. The films of the copolymer were coated onto the Pt wires by dipping the wires into 1 wt% polymer solutions in chloroform. Atomic force microscopy (AFM) imaging (5 × 5 μm area) was done using a Dimension 3100 SPM (Veeco) instrument operating in tapping mode.

Fabrication and Characterization of OFETs. Organic field-effect transistor with top-contact, bottom-gate (TCBG) geometry were fabricated on heavily n doped <100> silicon wafer (0.002-0.004 Ω/cm) which served as gate electrode while a 200 nm thermally grown SiO_2 served as the gate dielectric ($C \approx 17 nF/cm^2$). The wafer surface was cleaned by sequential ultrasonication in acetone and isopropanol followed by plasma treatment and surface modification by octyltrichlorosilane (OTS 8). For silane modification, the wafer was spin coated in air with 0.1M solution of OTS 8 in chloroform at 3000 rpm for 10 seconds, rinsed with toluene and dried at 110˚C for 10 minutes. Each polymer OFET was fabricated on the modified substrate by spin coating 8 $mgml^{-1}$ of polymer solution at 2000 rpm for 60 seconds inside of the glove box followed by annealing at 200 ˚C for 10 minutes on the hot plate. The gold source/drain electrodes with channel length (L) of 1000 μm and width (W) of 100 μm were deposited by vacuum evaporation through a shadow mask. All the electrical characteristics of the devices were measured using HP 4145B semiconductor parameter analyzer in nitrogen atmosphere similar to our previous reports.[53, 54]

Fabrication and Characterization of Solar Cells. A 10 mg/ml PNDIBS solution and 20 mg/ml P3HT (Rieke Metals, Inc.) solution were prepared in chloroform, respectively. Blends of P3HT:PNDIBS were prepared by mixing respective solutions at certain weight ratio (1:3 wt:wt). Solar cells used for photovoltaic and external quantum efficiency (EQE) measurements have a basic device structure of ITO/PEDOT:PSS/active layer/LiF/Al, where the active layer is a blend film spin coated from P3HT:PNDIBS blend solution. The ITO-coated glass (10 Ω/□, Shanghai

B. Tree Tech, China) substrates were cleaned sequentially with acetone, deionized water and isopropyl alcohol in an ultrasonic bath. The 40 nm PEDOT:PSS (Clevios P VP AI 4083) layer was spin-coated on top of ITO and dried at 150 °C for 10 min under vacuum. Each blend was spin-coated on top of the PEDOT:PSS layer for 18 s in a glovebox to make the active polymer blend layer of ~90 nm. The devices were then annealed at 150 °C for 10 min. The devices were loaded in a thermal evaporator (BOC Edwards, 306), where a cathode consisting of 1.0 nm LiF and 80 nm Al was deposited through a shadow mask under high vacuum (8×10^{-7} Torr) to produce 4 solar cells per substarte, each with an active area of 9 mm^2. The current density−voltage (*J*−*V*) curves of solar cells were measured using a HP4155A semiconductor parameter analyzer under laboratory ambient air conditions. An AM1.5 illumination at 100 mW/cm^2 was provided by a filtered Xe lamp and calibrated by using an NREL-calibrated Si diode. External quantum efficiency (EQE) was measured using a QEX10 solar cell quantum efficiency measurement system (PV Measurements, Inc.), and was calibrated with a NREL-certified Si diode before measurement. Further details are given in our previous reports.[6, 49, 55]

3.1.3 *Results and Discussions*

2,2'-Biselenophene was synthesized by copper ($CuCl_2$) mediated coupling of lithiated selenophene by following a literature method for the corresponding 2,2'-bithiophene.[44] The yield (21 %) of the unoptimized reaction was lower than the 54 % reported for the synthesis of 2,2'-bithiophene. 5,5'-Bis(trimethylstannyl)-2,2'-biselenophene was synthesized from 2,2'-biselenophene by stannylation with n-butyllithium and trimethyltin chloride in THF solvent. The new copolymer, PNDIBS, was synthesized by Stille coupling polymerization of 4,9-dibromo-2,7-bis(2-decyltetradecyl)benzo[lmn][3,8]phenanthroline-1,3,6,8-tetraone (4,9-dibromo NDI) and 5,5'-bis(trimethylstannyl)-2,2'-biselenophene in the presence of $Pd_2(dba)_3$ and $P(o\text{-tolyl})_3$ in chlorobenzene solvent. The copolymer was readily soluble in common organic solvents, including chloroform, toluene, and chlorobenzene at room temperature. The molecular structure was verified by ^{1}H NMR. Gel permeation chromatography (GPC) analysis in chlorobenzene at 60 °C relative to polystyrene standard gave number-averaged molecular weight (M_n) of 42.4 kDa, weight-averaged molecular weight (M_w) of 110.1 kDa and thus a polydispersity index (PDI) of 2.6. Thermogravimetric analysis (TGA) showed that PNDIBS has good thermal stability with a decomposition temperature (T_d) of 430 °C under nitrogen flow. The differential scanning calorimetry (DSC) scan of PNDIBS did not show any distinc transition up to 350 °C.

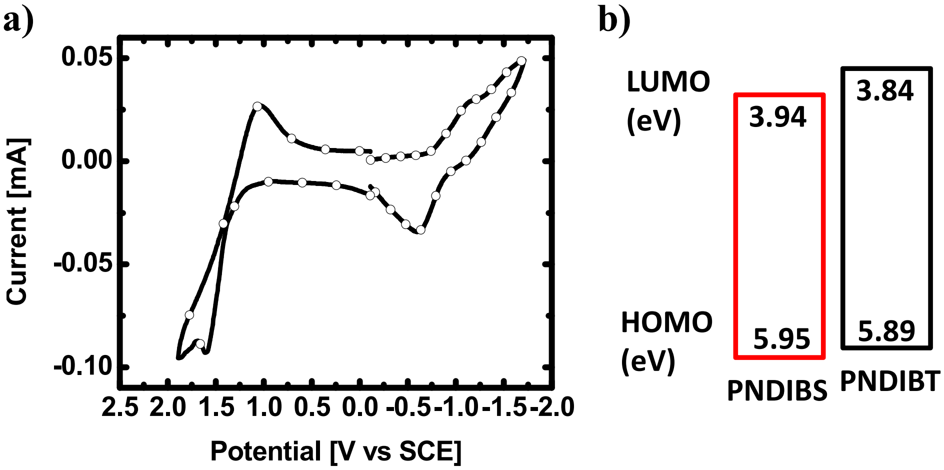

Figure 13. (a) Cyclic voltammogram of PNDIBS thin film in 0.1 M Bu_4NPF_6 solution in acetonitrile at a scan rate of 100 mV/s. (b) Schematic illustration of the HOMO/LUMO energy levels of PNDIBS and PNDIBT.

We estimated the electron affinity (EA) and ionization potential (IP), and thus the HOMO/LUMO energy levels, of PNDIBS by cyclic voltammetry (CV) of thin films on platinum (Pt) electrodes. **Figure 13a** shows the cyclic voltammogram of PNDIBS, revealing quasi-reversible reduction and oxidation waves. The EA and IP values extracted from the onset redox potentials were 3.94 and 5.95 eV, respectively. Comparison of the electronic energy levels of

PNDIBS with those of similarly measured bithiophene-linked copolymer, PNDIBT, is shown in **Figure 13b**. The LUMO level of PNDIBS is 0.1 eV lower lying than that of PNDIBT whereas the HOMO energy level of PNDIBS is 0.05 eV lower.

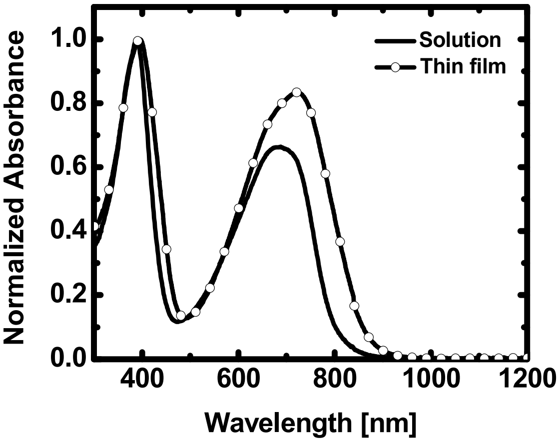

Figure 14. Optical absorption spectra of PNDIBS in dilute chloroform solution and as a thin film on glass substrate.

Optical absorption spectra of PNDIBS in dilute (10^{-6} M) chloroform solution and as a thin film on glass substrate are shown in **Figure 14**. The copolymer shows two distinctive absorption bands, which can be assigned as due to a π–π* transition in the case of the higher energy band (~400 nm) and intramolecular charge transfer (ICT) band (~700 nm).[45] In dilute solution, the absorption maximum (λ_{max}) of the π–π* transition band was 388 nm whereas the ICT band is centered at 688 nm. The corresponding absorption peaks in thin film were 395 nm and 722 nm, showing a significant red shift in the ICT band. The absorption edge optical band gap of PNDIBS is 1.4 eV. Compared to the known bithiophene-linked copolymer PNDIBT, which has an optical band gap of 1.5 eV, the ICT band of the new biselenophene-linked copolymer has a full width at half maximum (FWHM) of 250 nm which is much broader by 50 nm and potentially better in harvesting more of the NIR light.

Electron transport properties of PNDIBS thin films was investigated by using bottom gate/top contact organic field-effect transistors. The devices showed typical n-channel transistor behavior with well-defined linear and saturation regions with excellent current modulation in the output and transfer characteristics (**Figure 15**). The average saturation region field effect mobility of electrons was calculated to be 0.07 cm^2/Vs with on/off current ratio of 10^5 and a threshold voltage of 15 V. This electron mobility is comparable to values reported for other NDI-based n-type polymers under similar botton gate/top contact transistor architectures.[26, 27] A similar measurement on our PNDIBT sample under identical conditions gave an electron mobility of 0.04 cm^2/Vs with on/off current ratio of 10^5. The excellent charge carrier mobility of the new n-type copolymer PNDIBS makes it a promising material for developing all-polymer bulk heterojunction organic photovoltaics.

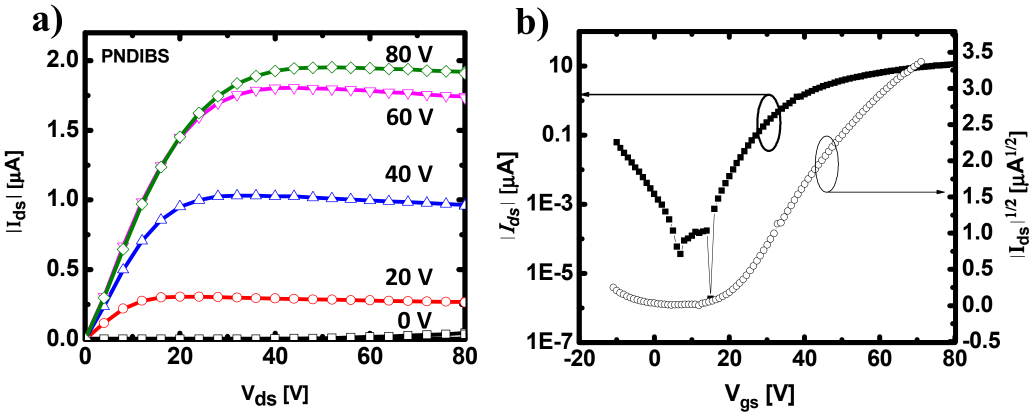

Figure 15. Output (a) and transfer (b) characteristics of PNDIBS OFETs.

The high electron mobility of PNDIBS can be understood by its favorable solid state morphology, molecular packing, and crystallinity, which were investigated by X-ray diffraction (XRD) analysis. As shown in **Figure 16**, the X-ray diffraction pattern of PNDIBS thin film has a strong and sharp (100) diffraction peak at 2θ = 3.4° with a corresponding *d* spacing of 25.95 Å, which originates from lamellar planes consisting of edge-on molecular backbones. The (200) diffraction peak is seen at 2θ = 6.65° and corresponds to *d* spacing of 13.28 Å. The π−π stacking (010) diffraction is observed as a broad peak at 2θ = 22.35° with *d* spacing of 3.97 Å. These characteristics of the thin film morphology of PNDIBS are very similar to observations for other NDI copolymers.[26, 27]

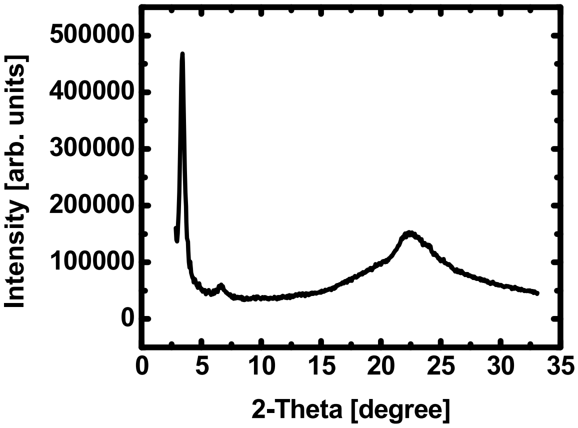

Figure 16. XRD pattern of PNDIBS film on glass substrate.

We investigated the photovoltaic properties of all-polymer BHJ solar cells made from P3HT:PNDIBS blends. The solar cells have the basic device structure of ITO/PEDOT:PSS/active layer/LiF/Al, where the active layer is a spin-coated film composed of P3HT:PNDIBS blends with optimal weight ratio of 1:3 wt:wt. The solar cells with an area of 9 mm^2 were fabricated in a glovebox and tested under AM1.5 solar illumination at 1 sun (100 mW/cm^2) in ambient air. The typical photovoltaic parameters, including the open circuit voltage (V_{oc}), the short-circuit current density (J_{sc}), and fill factors (FF) are collected in **Table 7**.

Only a moderate V_{oc} of 0.47 V was observed in the P3HT:PNDIBS blend solar cells. The observed short circuit current density of 2.39 mA/cm^2 was also modest, although it is comparable to the J_{sc} seen in other non-fullerene polymer solar cells.[11-23] The fill factor of these P3HT:PNDIBS solar cells (0.46) is significantly lower compared with both P3HT:PCBM devices (FF ~ 0.60) and other non-fullerene solar cells. The reasons for the low fill factor are not yet clear but may be related to traps or defects which increase the geminate recombination and thus reduce the FF value. Further photophysical studies are necessary to clarify the reasons for the low FF in these PNDIBS-based solar cells. The overall power conversion efficiency (PCE) achieved in the P3HT:PNDIBS BHJ devices was 0.52%, which is relatively low but comparable to the efficiency of BHJ solar cells based on P3HT and naphthalene diimide-bithiophene copolymer (P(NDIOD-T_2)) acceptor.[20,21,23] P3HT:PNDIBT solar cells, fabricated for comparison purposes, had a V_{oc} of 0.56 V but had a lower J_{sc} and FF of 2.10 mAcm^{-2} and 0.33, respectively, giving a maximum PCE of 0.39 %. We note that because of the large difference in molecular weight between PNDIBS and PNDIBT, a rigorous comparison of the observed photovoltaic properties cannot be made. Nevertheless, the observed electron mobility and photovoltaic properties of our PNDIBT sample are comparable to prior reports and thus provide a useful reference for understanding our related copolymer semiconductor, PNDIBS.

Table 7. Field-effect charge transport and photovoltaic properties of PNDIBS and PNDIBT.

Polymer	μ_e [cm/Vs]	I_{on}/I_{off}	V_t [V]	J_{sc} [mA/cm^2]	V_{oc} [V]	FF	PCE$_{avg}$ (PCE$_{max}$) [%]
PNDIBS^a	0.07	10^5	15	2.39	0.47	0.46	0.49 (0.52)
PNDIBS^b	0.07	10^5	15	3.79	0.53	0.44	0.84 (0.88)
PNDIBT	0.04	10^5	11	2.10	0.56	0.33	0.38 (0.39)

^{a} Processed from chloroform. ^{b} Processed from chloroform:DIO mixture (99:1 vol:vol).

We tried to optimize the performance of the present PNDIBS-based all-polymer BHJ solar cells by exploring the use of a processing additive, which has proved to be effective in optimizing both polymer/fullerene and polymer/non-fullerene acceptor solar cells.[46-50] We fabricated P3HT:PNDIBS (1:3 wt:wt) devices by using chloroform:1,8-diiodooctane (DIO) mixture (99:1 vol:vol) as the solvent. The current density (J)–voltage (V) curves and the external quantum efficiency (EQE) spectrum of the resulting P3HT:PNDIBS BHJ devices are shown in **Figure 17**. A slightly improved V_{oc} of 0.53 V, fill factor of 0.44, and enhanced J_{sc} of 3.79 mA/cm^2 combined to give a PCE of 0.88 % (**Table 7**). This represents a 69 % enhancement in the photovoltaic conversion efficiency by using DIO as a processing additive. We note that a very recent paper,[51] which appeared while this report was in preparation, has similarly found that a processing additive can be effective in enhancing the performance of all-polymer BHJ solar cells. The EQE spectrum of the P3HT:PNDIBS device (**Figure 17b**) shows that the photoresponse begins at ~900 nm, capturing 19% photons in the wavelength range of 700 – 900 nm that contribute to photocurrent, an important demonstration that the new polymer acceptor can harvest photons from the near-IR region of the solar spectrum.

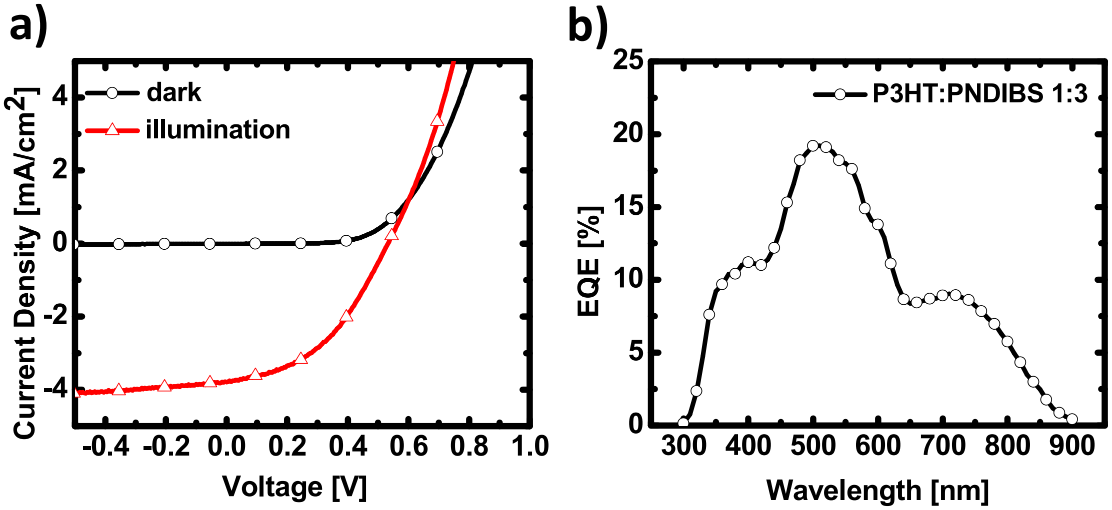

Figure 17. The current density — voltage characteristics (a) under 100 mW/cm^2 1.5AM illumination in air and EQE spectrum (b) of P3HT:PNDIBS (1:3 wt:wt) blend solar cells.

The surface morphology of the P3HT:PNDIBS blend films was investigated by atomic force microscopy (AFM) imaging. Images with an area of 5 μm by 5 μm were acquired from the

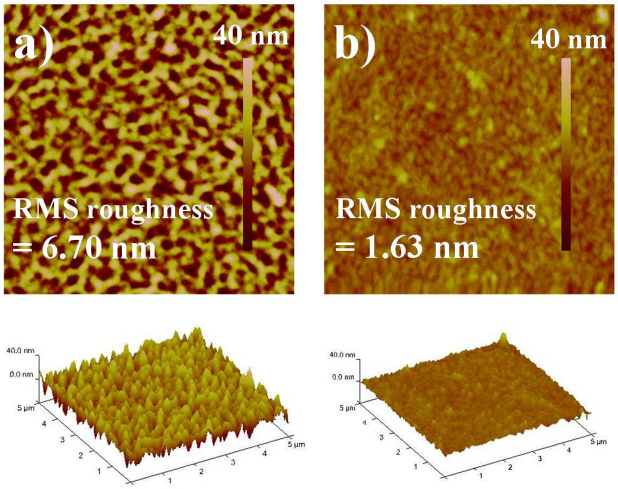

Figure 18. AFM topographical height images (5 × 5 µm) and the corresponding 3D height images of P3HT:PNDIBS (1:3) (a) and P3HT:PNDIBT (1:2) (b) blend films.

actual BHJ solar cells in regions where the cathode material was not deposited. The topographical and phase images are shown in Figure 7 and Figure S9, respectively. AFM height image of P3HT:PNDIBS (1:3) blend film clearly shows a two-phase, co-continuous, morphology reminescent of one obtained by a spinodal decomposition.[52] The bright domains, which also constitute the elevated phase, have width of 50-150 nm and can be assigned to the PNDIBS-rich phase while the dark domains or valleys are thus assigned to the P3HT-rich phase, as suggested by a previous study of blends of the bithiophene-linked copolymer and P3HT using scanning near-field optical microscopy (SNOM).[20] A high surface roughness of R_a = 6.70 nm is measured (**Figure 18**). In the phase image of the blend films, a clear microscale phase separation film is observed on the same scale as that in height image (50 – 150 nm). Comparing the phase and height images of P3HT:PNDIBS blend film, we conclude that the bright domains in the phase image are PNDIBS-rich domains and the darker domains are P3HT-rich domains. In contrast, the AFM height image of P3HT:PNDIBT (1:2) blend film shows a much more homogeneous morphology, with large aggregates of PNDIBT-rich domains on top and fiber-like P3HT-rich domains underneath. The corresponding surface roughness R_a is reduced significantly to 1.63 nm, indicating a much smoother surface. We note that the observed significant difference in the surface morphology of PNDIBS and PNDIBT blend films may be due to the different polymer:polymer blend ratios.

3.1.4 *Conclusions*

I have synthesized a new solution-processable, high molecular weight, naphthalene diimide-biselenophene (PNDIBS) copolymer for use as an electron acceptor (n-type) in all-polymer BHJ solar cells. The new n-type copolymer semiconductor PNDIBS combined a highly ordered lamellar crystalline morphology with a high field-effect electron mobility of 0.07 cm^2/Vs in thin films. Compared to the known naphthalene diimide-bithiophene copolymer, PNDIBS has a smaller optical band gap (1.4 eV) and a visible-near IR absorption band whose full width at half maximum is 50 nm broader. All-polymer BHJ solar cells incorporating the new copolymer PNDIBS as the acceptor and P3HT as the donor were fabricated and shown to have a power conversion efficiency of 0.9 % with a moderate open circuit voltage (0.53 V) and photocurrent (3.79 mA/cm^2).

3.1.5 *References*

(1) Günes, S.; Neugebauer, H.; Sariciftci, N. S. *Chem. Rev.* **2007**, *107*. 1324-1338.

(2) Helgesen, M.; Søndergaard, R.; Krebs, F. C. *J. Mater. Chem.* **2010**, *20*, 36-60.

(3) Brabec, C. J.; Gowrisanker, S.; Halls, J. J. M.; Laird, D.; Jia, S.; Williams, S. P. *Adv. Mater*. **2010**, *22*, 3839-3856.

(4) Boudreault, P. T.; Najari, A.; Leclerc, M. *Chem. Mater*. **2011,** *23*, 456-469.

(5) Yu, G.; Gao, J.; Heummelen, J. C.; Wudl, F.; Heeger, A. J. *Science* **1995**, *270*, 1789-1791.

(6) Subramaniyan, S.; Xin, H.; Kim, F. S.; Shoaee, S.; Durrant, J. R.; Jenekhe, S. A. *Adv. Energy Mater.* **2011**,*1*, 854-860.

(7) (a) Xin, H.; Subramaniyan, S.; Kwon, T. W.; Shoaee, S.; Durrant, J. R.; Jenekhe, S. A. *Chem. Mater*. **2012**, *24*, 1995-2001. (b) Sista, P.; Xue, B.; Holmes, N.; Kularatne, R. S.; Nguyen, H.; Dastoor, P. C.; Belcher, W.; Poole, K.; Janesko, B. G.; Biewer, M. C.; Stefan, M. C. *Macromolecules* **2012**, *45*, 772-780.

(8) Small, C. E.; Chen, S.; Subbiah, J.; Amb, C. M.; Tsang, S. W.; Lai, T. H.; Reynolds, J. R.; So, F. *Nat. Photon*. **2012**, *2*, 115-120.

(9) Dou, L.; You, J.; Chen, C. C.; He, Y.; Murase, S.; Moriarty, T.; Emery, K.; Li, G.; Yang, Y. *Nat. Photon*. **2012**, *3*, 180-185.

(10) He, Z.; Zhong, C.; Su, S.; Xu, M.; Wu, H.; Cao, Y. *Nat. Photon*. **2012**, DOI: 10.1038/NPHOTON.2012.190.

(11) Halls, J. J. M.; Walsh, C. A.; Greenham, N. C.; Marseglia, E. A.; Friend, R. H.; Moratti, S. C.; Holmes, A. B. *Nature* **1995**, *376*, 498-500.

(12) (a) Granström, M.; Petritsch, K.; Arias, A. C.; Lux, A.; Andersson, M. R.; Friend, R. H. *Nature* **1998**, *395*, 257-260. (b) Mori, D.; Benten, H.; Ohkita, H.; Ito, S.;Miyake, K. *Appl. Mater. Interfaces* **2012**, *4*, 3325-3329.

(13) Jenekhe, S. A.; Yi, S. *Appl. Phys. Lett.* **2000**, *77*, 2635-2637.

(14) Alam, M. M.; Jenekhe, S. A. *Chem. Mater.* **2004**, *16*, 4647-4656.

(15) Kietzke, T.; Hörhold, H.-H.; Neher, D. *Chem. Mater*. **2005**, *17*, 6532-6537.

(16) Zhan, X. W.; Tan, Z. A.; Domercq, B.; An, Z. S.; Zhang, X.; Barlow, S.; Li, Y. F.; Zhu, D. B.; Kippelen, B.; Marder, S. R. *J. Am. Chem. Soc*. **2007**, *129*, 7246-7247.

(17) Tan, Z. A.; Zhou, E. J.; Zhan, X. W.; Wang, X.; Li, Y. F.; Barlow, S.; Marder, S. R. *Appl. Phys. Lett.* **2008**, *93*, 073309.

(18) Zhou, E.; Cong, J.; Wei, Q.; Tajima, K.; Yang, C.; Hashimoto, K. *Angew. Chem., Int. Ed.* **2011**, *50*, 2799-2803.

(19) Falzon, M. F.; Wienk, M. M.; Janssen, R. A. J. *J. Phys. Chem. C* **2011**, *115*, 3178-3187.

(20) Schubert, M.; Dolfen, D.; Frisch, J.; Roland, S.; Steyrleuthner, R.; Stiller, B.; Chen, Z.; Scherf, U.; Koch, N.; Facchetti, A.; Neher, D. *Adv. Energy Mater*. **2012**, *2*, 369-380.

(21) Fabiano, S.; Chen, Z.; Vahedi, S.; Facchetti, A.; Pignataro, B.; Loi, M. A. *J. Mater. Chem*. **2011,** *21*, 5891-5896.

(22) Holcombe, T. W.; Woo, C. H.; Kavulak, D. F. J.; Thompson, B. C.; Fréchet, J. M. J. *J. Am. Chem. Soc.* **2009**, *131*, 14160-14161.

(23) Moor, J. R. ; Seifried, A. S.; Rao, A.; Massip, S.; Watts, B.; Morgan, D. J.; Friend, R. H.; Mcneill, C. R.; Sirringhaus, H. *Adv. Energy Mater*. **2011**, *1*, 230-240.

(24) Ahmed, E.; Ren, G.; Kim, F. S.; Hollenbeck, E. C.; Jenekhe, S. A. *Chem. Mater*. **2011**, *23*, 4563-4577.

(25) Babel, A.; Jenekhe, S. A. *J. Am. Chem. Soc*. **2003**, *125*, 13656-13657.

(26) Yan, H.; Chen, Z.; Zheng, Y.; Newman, C.; Quinn, J. R.; Dötz, F.; Kastler, M.; Facchetti, A. *Nature*, **2009**, *457*, 679-686.

(27) Guo, X.; Kim, F. S.; Seger, M. J.; Jenekhe, S. A.*Chem. Mater*. **2012**, *24*, 1434-1442.

(28) Kim, F. S.; Guo, X.; Watson, M. D.; Jenekhe, S. A. *Adv. Mater*. **2010**, *22*, 478-482.

(29) Anthony, J. E.; Facchetti, A.; Heeney, M.; Marder, S. R.; Zhan, X. *Adv. Mater*. **2010**, *22*, 3876-3892.

(30) Yamamoto, T.; Zhou, Z. H.; Kanbara, T.; Shimura, M.; Kizu, K.; Maruyama, T.; Nakamura, Y.; Fukuda, T.; Lee, B. L.; Ooba, N.; Tomaru, S.; Kurihara, T.; Kaino, T.; Kubota, K.; Sasaki, S. *J. Am. Chem. Soc.* **1996**, *118*, 10389-10399.

(31) Hollinger, J.; DiCarmine, P. M.; Karl, D.; Seferos, D. S. *Macromolecules* **2012**, *45*, 3772-3778.

(32) Chen, Z.; Lemke, H.; Seifried, S. A.; Caironi, M.; Nielsen, M. M.; Heeney, M.; Zhang, W.; McCulloch, I.; Sirringhaus, H. *Adv. Mater*. **2010**, *22*, 2371-2375.

(33) Ballantyne, A. M.; Chen, L.; Nelson, J.; Bradley, D. D. C.; Astuti, Y.; Maurano, A.; Chuttle, C. G.; Durrant, J. R.; Heeney, M.; Duffy, W.; McCulloch, I. *Adv. Mater*. **2007**, *19*, 4544-4547.

(34) Li, L.; Hollinger, J.; Jahnke, A. A.; Petrow, S.; Seferos, D. S. *Chem. Sci*. **2011**, *2*, 2306-2310.

(35) Patra, A.; Wijsboom, Y. H.; Leitus, G.; Bendikov, M. *Chem. Mater*. **2011**, *23*, 896-906.

(36) Hollinger, J.; Jahnke, A. A.; Coombs, N.; Seferos, D. S. *J. Am. Chem. Soc*. **2010**, *132*, 8546-8547.

(37) Jo, Y. R.; Lee, S. H.; Lee, Y. S.; Hwang, Y. H.; Pyo, M.; Zong, K. *Synthetic Metals* **2011**, *161*, 1444-1447.

(38) Shahid, M.; Ward, T. M.; Labram, J.; Rossbauer, S.; Domingo, E. B.; Watkins, S. E.; Stingelin, N.; Anthophoulos, T. D.; Heeney, M. *Chem. Sci*. **2012**, *3*, 181-185.

(39) Lin, H. W.; Lee, W. Y.; Lu, C.; Lin, C. J.; Wu, H. C.; Lin, Y. W.; Ahn, B.; Rho, Y.; Ree, M.; Chen, W. C. *Polym. Chem.* **2012**, *3*, 767-777.

(40) Kronemeijer, A. J.; Gili, E.; Shahid, M.; Rivnay, J.; Salleo, A.; Heeney, M.; Sirringhaus, H. *Adv. Mater*. **2012**, *24*, 1558-1565.

(41) Lee, W. H.; Son, S. K.; Kim, K.; Lee, S. K.; Shin, W. S.; Moon, S. J.; Kang, I. N. *Macromolecules* **2012**, *45*, 1303-1312.

(42) Ha, J. S.; Kim, K. H.; Choi, D. H. *J. Am. Chem. Soc*. **2011**, *133*, 10364-10367.

(43) Mishra, S. P.; Javier, A. E.; Zhang, R.; Liu, J.; Belot, J. A.; Osaka, I.; McCullough, R. D. *J. Mater. Chem*. **2011**, *21*, 1551-1561.

(44) Shetti, V. S.; Ravikanth, M. *Inorg. Chem*. **2011**, *50*, 1713-1727.

(45) Jenekhe, S. A.; Lu, L.; Alam, M. M. *Macromolecules* **2001**, *34*, 7315-7324.

(46) Peet, J; Kim, J. Y.; Coates, N. E.; Ma, W. L.; Moses, D.; Heeger, A. J.; Bazan, G. C. *Nat. Mater.* **2007**, *6*, 497-500.

(47) Lee, J. K.; Ma, W. L.; Brabec, C. J.; Yuen, J.; Moon, J. S.; Kim, J. Y.; Lee, K.; Bazan, G. C.; Heeger, A. J. *J. Am. Chem. Soc.* **2008**, *130*, 3619-3623.

(48) Pivrikas, A.; Neugebauer, H.; Sariciftci, N. S. *Sol. Energy* **2011** , *85*, 1226-1237.

(49) Xin, H.; Guo, X.; Ren, G.; Watson, M. D.; Jenekhe, S. A. *Adv. Energy Mater*. **2012**, *2*, 575-582.

(50) Ren, G.; Ahmed, E.; Jenekhe, S. A. *Adv. Energy Mater*. **2011**, *1*, 946-953.

(51) Zhou, E.; Cong, J.; Zhao, M.; Zhang, L.; Hashimoto, K.; Tajima, K. *Chem. Comm*. **2012**, *48*, 5283-5285.

(52) Alam, M. M.; Tonzola, C. J.; Jenekhe, S. A. *Macromolecules* **2003**, *36*, 6577-6587.

(53) Ahmed, E.; Kim, F. S.; Xin, H.; Jenekhe, S. A. *Macromolecules* **2009**, *22*, 8615-8618.

(54) Hwang, Y. J.; Kim, F. S.; Xin, H.; Jenekhe, S. A. *Macromolecules*, **2012**, *9*, 3732-3739.

(55) Wu, P. T.; Bull, T.; Kim, F. S.; Luscombe, C. K.; Jenekhe, S. A. *Macromolecules* **2009**, *42*, 671-676.

3.2 ALL-POLYMER SOLAR CELLS BASED ON NAPHTHALENE DIIMIDE-SELENOPHENE COPOLYMER ACCEPTOR

3.2.1 *Introduction*

Solution-processed organic photovoltaic devices are promising low cost solar energy technologies.[1] Much progress has been made in developing polymer/fullerene solar cells in the last decade, with efficiencies now approaching 10 %.[2] In contrast, the performance of all-polymer solar cells, composed of both *donor* and *acceptor* polymers and free of fullerenes, has remained relatively low with no significant advance in the same period.[3] All-polymer active layers of solar cells have potential advantages over polymer/fullerene systems, including enhanced absorption coefficients, increased photovoltage, superior photochemical, thermal, and mechanical robustness, and facile control of solution viscosity and industrial coating process. Perylene diimide (PDI) and naphthalene diimide (NDI) have been the most widely explored building blocks[3,4] in the design and investigation of acceptor (n-type) polymers for all-polymer solar cells.[3,4] A PDI-based acceptor polymer in combination with polythiophene derivatives has produced bulk heterojunction (BHJ) solar cells with a power conversion efficiency (PCE) of 2.23 %.[3h] An NDI-bithiophene copolymer (PNDI2OD-T2) with very high field-effect electron mobilities (0.1 - 0.85 cm^2/Vs) and moderate bulk electron mobility (~ 10^{-3} cm^2/Vs) has so far shown only low efficiencies of 0.2 - 1.4 % PCE in BHJ solar cells using P3HT donor polymer.[3e,31] Among acceptor polymers in BHJ solar cells, a benzothiadiazole-fluorene copolymer has the highest PCE (2.7 %) reported to date.[3k] The short circuit current density ($J_{sc} <$ 6.3 mA/cm^2) and external quantum efficiency (EQE < 43 %) obtained to date in all-polymer solar cells[3] have also been far lower than in polymer/fullerene devices.[1,2]

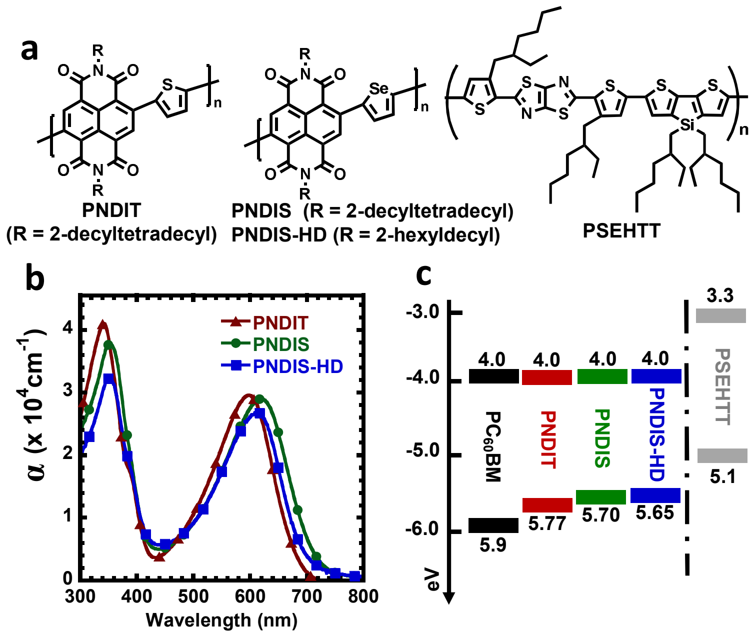

Figure 19. (a) Molecular structures of acceptor (PNDIT, PNDIS, and PNDIS-HD) and donor (PSEHTT) polymers. (b) UV-vis absorption spectra of PNDIT, PNDIS, and PNDIS-HD. (c) LUMO/HOMO energy levels of PNDIT, PNDIS, PNDIS-HD, $PC_{60}BM$, and PSEHTT.

In this chapter, I report all-polymer solar cells with 3.3% PCE enabled by a novel polymer/polymer blend system composed of a new NDI-selenophene copolymer acceptor and a thiazolothiazole-dithienylsilole copolymer donor. Three n-type polymer semiconductors, including an NDI-thiophene copolymer (PNDIT) and two new NDI-selenophene copolymers (PNDIS, PNDIS-HD) whose molecular structures are shown in Figure 1a, are investigated as electron acceptors in BHJ solar cells for the first time. We show that these NDI-based copolymers exhibit *unipolar* electron transport with high field-effect and bulk mobilities. The donor polymer, poly[(4,4′-bis(3-(2-ethyl-hexyl)dithieno[3,2-*b*:″,3′-*d*]silole)-2,6-diyl-*alt*-(2,5-bis-(3-(2-ethylhexyl)thiophen-2- yl)thiazolo[5,4-*d*]thiazole)] (PSEHTT, **Figure 19a**) has been previously shown to be a promising electron donor and hole-conducting material in polymer/fullerene BHJ solar cells.[5] The morphology of the polymer/polymer blends was imaged by atomic force microscopy (AFM). Charge transport in the active layer blends was investigated by organic field-effect transistors (OFETs) and space-charge-limited current (SCLC) measurements. Finally, we show that the all-polymer solar cells can be as efficient as the similarly evaluated $PC_{60}BM$/PSEHTT BHJ devices.

3.2.2 *Experimental Section*

Synthesis.

2,5-Dibromoselenophene. Selenophene (5 g, 0.038 mol) was added into a 250 mL round-bottom flask. The flask was purged with argon before adding 100 mL of chloroform as a solvent. Afterward, NDS (13.575 g, 0.076 mol) was added in three portions. After stirring the mixture overnight at room temperature in the dark, the reaction was quenched by adding water. The crude product was extracted with chloroform, and purified by column chromatography with hexane. Slightly yellow oil was obtained and used in next step without further purification. 2,5-Dibromoselenophene (7.5 g, 68.3 %), ^{1}H NMR ($CDCl_3$, 300 MHz): δ (ppm) 7.02 (2H).

2,5-Bis(trimethylstannyl)selenophene. 2,5-Dibromoselenophene (2 g, 6.92 mmol) was added into a 250 mL round-bottom flask. Afterwards, 50 mL of THF was added under argon atmosphere. The mixture was cooled to -78 °C in a dry ice bath and 2.5 M butyllithium solution in hexane (6.1 mL, 15.23 mmol) was added dropwise. After stirring the mixture for an hour at -78 °C, 1 M trimethyltinchloride solution in THF (15.9 mL, 15.9 mmol) was added in one portion at -78 °C. Dry ice bath was removed after 5 min and the mixture was warmed up to room temperature. After stirring overnight at room temperature, the reaction mixture was poured into water and extracted with diethyl ether two times. The organic phase was dried with sodium sulfate anhydrous and the solvent was evaporated by using a vacuum rotary evaporator. After reprecipitation in MeOH, a white solid was obtained and subsequently used in polymerization without further purification (500 mg; yield = 15.8 %). ^{1}H NMR ($CDCl_3$, 300 MHz): δ (ppm) 7.72 (2H), 0.3 - 0.48 (18H). Melting point (T_m): 122 °C.

2,5-Bis(trimethylstannyl)thiophene. 2,5-Dibromothiophene (1.5 g, 6.2 mmol) was added into a 250 mL round-bottom flask. Afterwards, 40 mL of THF was added under argon atmosphere. The mixture was cooled to -78 °C in a dry ice bath and 2.5 M butyllithium solution in hexane (5.95 mL, 14.88 mmol) was added dropwise. After stirring the mixture for an hour at -78 °C, 1 M trimethyltinchloride solution in THF (15.5 mL, 15.5 mmol) was added in one portion at -78 °C. Dry ice bath was removed after 5 min and the mixture was warmed up to room temperature. After stirring overnight at room temperature, the reaction mixture was poured into water and extracted with diethyl ether two times. The organic phase was dried with sodium sulfate anhydrous and the solvent was evaporated by using a vacuum rotary evaporator. After reprecipitation in MeOH, a white solid was obtained and subsequently used in polymerization without further purification (1 g; yield = 39.2 %). ^{1}H NMR ($CDCl_3$, 300 MHz): δ (ppm) 7.46 (2H), 0.34 - 0.52 (18H). Melting point (T_m): 95 °C

Poly{[N,N'-bis(2-decyltetradecyl)-naphthalene-1,4,5,8-bis(dicarboximide)-2,6-diyl]-alt-5,5'-selenophene)} (PNDIS). 4,9-Dibromo-2,7-bis(2-decyltetradecyl)benzo[lmn][3,8]phenanthroline-1,3,6,8-tetraone (480.6 mg, 0.44 mmol), 2,5-bis(trimethylstannyl)selenophene (200 mg, 0.44 mmol), $Pd_2(dba)_3$ (8 mg, 0.0088 mmol) and $P(o\text{-tolyl})_3$ (10.7 mg, 0.035 mmol) were added into a 100 mL three-neck round-bottom flask. The flask equipped with a condenser was then degassed and filled with argon three times. Afterwards, 22 mL of chlorobenzene was added and degassed and filled with argon three times. The reaction mixture was refluxed for 72 h under argon. After cooling down to room temperature, the polymerization mixture was poured and stirred into 200 mL methanol and 5 mL hydrochloric acid solution for 3 h. The polymer precipitated out as a dark reddish purple solid and was filtered using a filter paper. The polymer was purified by Soxhlet extraction with methanol, hexane, and acetone. **PNDIS** (365 mg; yield = 81.9 %), ^{1}H NMR ($CDCl_3$, 300 MHz): d (ppm) 9.1 (2H), 7.7 (2H), 4.2 (4H), 2.1 (2H), 0.9–1.5 (92H). GPC: Mw = 31.5 kDa, Mn = 26.1 kDa, PDI = 1.2. TGA: T_d = 415 °C.

Poly{[N,N'-bis(2-hexyldexyl)-naphthalene-1,4,5,8-bis(dicarboximide)-2,6-diyl]-alt-5,5'-selenophene)} (PNDIS-HD). 4,9-Dibromo-2,7-bis(2-hexyldecyl)benzo[lmn][3,8]phenanthroline-1,3,6,8-tetraone (200 mg, 0.23 mmol), 2,5-bis(trimethylstannyl)selenophene (104.6 mg, 0.23 mmol), $Pd_2(dba)_3$ (4.2 mg, 0.0046 mmol) and $P(o\text{-tolyl})_3$ (5.6 mg, 0.0184 mmol) were added into a 100 mL three-neck round-bottom flask. The flask equipped with a condenser was then degassed and filled with argon three times. Afterwards, 10 mL of chlorobenzene was added and degassed and filled with argon three times. The reaction mixture was refluxed for 72 h under argon. After cooling down to room temperature, the polymerization mixture was poured and stirred into 200 mL methanol and 5 mL hydrochloric acid solution for 3 h. The polymer precipitated out as a dark reddish purple solid and was filtered using a filter paper. The polymer was purified by Soxhlet extraction with methanol, hexane, and acetone. **PNDIS-HD** (165 mg; yield = 82.3 %), ^{1}H NMR ($CDCl_3$, 300 MHz): d (ppm) 9.15 (2H), 7.8 (2H), 4.2 (4H), 2.05 (2H), 0.8-1.5 (60H). GPC: Mw = 177.9 kDa, Mn = 79 kDa, PDI = 2.3. TGA: T_d = 400 °C.

***Poly{[N,N'-bis(2-decyltetradecyl)-naphthalene-1,4,5,8-bis(dicarboximide)-2,6-diyl]-alt-5,5'-thiophene)} (PNDIT)**.* 4,9-Dibromo-2,7-bis(2-decyltetradecyl)benzo[lmn][3,8]phenanthroline-1,3,6,8-tetraone (350 mg, 0.32 mmol), 2,5-bis(trimethylstannyl)thiophene (130.7 mg, 0.32 mmol), $Pd_2(dba)_3$ (5.84 mg, 0.0064 mmol) and $P(o\text{-tolyl})_3$ (7.77 mg, 0.026 mmol) were added into a 100 mL three-neck round-bottom flask. The flask equipped with a condenser was then degassed and filled with argon three times. Afterwards, 15 mL of chlorobenzene was added and degassed and filled with argon three times. The reaction mixture was refluxed for 72 h under argon. After cooling down to room temperature, the polymerization mixture was poured and stirred into 200 mL methanol and 5 mL hydrochloric acid solution for 3 h. The polymer precipitated out as a dark reddish purple solid and was filtered using a filter paper. The polymer was purified by Soxhlet extraction with methanol, hexane, and acetone. **PNDIT** (310 mg; yield = 92.3 %), ^{1}H NMR ($CDCl_3$, 300 MHz): d (ppm) 9.0 (2H), 7.5 (2H), 4.2 (4H), 2.1 (2H), 0.8-1.45 (92H). GPC: Mw = 31.6 kDa, Mn = 23.9 kDa, PDI = 1.3. TGA: T_d = 430 °C.

Characterization. The molecular structure and physical properties of PNDIBS and PNDIBT were investigated by ^{1}H NMR, gel permeation chromatography (GPC) analysis, thermogravimetric analysis (TGA), and X-ray diffraction (XRD). ^{1}H NMR spectra at 300 MHz were recorded on a Bruker-AF300 spectrometer. GPC analysis of the copolymers was performed on GPC Model 120 (DRI, PLBV400HT viscometer) against polystyrene standards in chlorobenzene at 60 °C. TGA thermograms were obtained on a TA Instruments Q50 TGA at a heating rate of 20 °C/min under nitrogen gas flow. XRD data were obtained from Bruker D8 Discover with a Cu Kα beam using GADD XRD system, and the samples were prepared by drop-casting of polymer solutions in chloroform onto glass substrates followed by annealing at 200 °C for 10 min. Optical and electrochemical properties were investigated by UV-vis absorption spectroscopy and cyclic voltammetry. Absorption spectra were measured on a PerkinElmer model Lambda 900 UV/vis/near-IR spectrophotometer. Solution and solid state absorption spectra were obtained from polymer solutions in chloroform and as thin films on glass substrates, respectively. Cyclic voltammetry (CV) experiments were done on an EG&G Princeton Applied Research potentiostat/galvanostat (model 273A) in an electrolyte solution of

0.1 M tetrabutylammonium hexafluorophosphate (Bu_4NPF_6) in acetonitrile at a scan rate of 100 mV/s. A three-electrode cell was used in this analysis. Platinum wires were used as counter and working electrodes, and Ag/Ag^+ (Ag in 0.1 M $AgNO_3$ solution, Bioanalytical System, Inc.) was used as a reference electrode. Ferrocene/ferrocenium was used as an internal standard by running CV at the end, and this data was used to convert the potential to saturated calomel electrode (SCE) scale. The films of the copolymer were coated onto the Pt wires by dipping the wires into 1 wt % polymer solutions in chloroform.

***Fabrication and Characterization of Inverted Solar Cells*.** Solar cells with the inverted device structure of ITO/ZnO/active layer/MoO_3/Ag were fabricated. ITO/glass substrates were cleaned sequentially in ultrasonic baths of acetone, deionized water, and 2-propanol, and then dried at 60 °C in a vacuum overnight. ITO/glass substrates were treated with oxygen plasma before use. Zinc oxide (ZnO) precursor was prepared as reported in the literature, spin-coated on top of the ITO and annealed at 250 °C for 1 hr in air. The ZnO film thickness was approximately 30 nm which is confirmed by using a profilometer. The active layer was then spin-coated from the polymer mixture solution to make a thin film of 60 nm thickness and thermally annealed at 150 °C for 10 min in a glovebox. The substrates were then loaded in a thermal evaporator (BOC Edwards, 306) to deposit an anode composed of thin layer of 7.5 nm MoO_3 and 100 nm Ag under high vacuum (8×10^{-7} Torr). Five solar cells, each with an active area of 4 mm^2, were fabricated per ITO substrate. The current density–voltage (*J–V*) curves of solar cells were measured using a HP4155A semiconductor parameter analyzer under laboratory ambient air conditions. An AM1.5 illumination at 100 mW/cm^2 was provided by a filtered Xe lamp and calibrated by using an NREL-calibrated Si diode. The external quantum efficiency (EQE) was measured using a QEX10 solar cell quantum efficiency measurement system (PV Measurements, Inc.) and was calibrated with a NREL-certified Si diode before measurement. Film thickness was measured by an Alpha-Step 500 profilometer (KLA-Tencor, San Jose, CA). AFM characterization of surface morphology was done on a Veeco Dimension 3100 Scanning Probe Microscope (SPM) system. The AFM images were directly measured on the same devices used for *J-V* characterization.

Fabrication and Characterization of Field-Effect Transistors. Organic field effect transistors (OFETs) with top-contact, bottom-gate geometry were fabricated on heavily n doped <100> silicon wafer (0.002-0.004 Ω/cm) which served as gate electrode while its 200 nm of thermally grown SiO_2 served as gate dielectric ($C \approx 17nF/cm^2$). The wafer surface was cleaned and modified with sequential ultrasonication in acetone and isopropanol followed by plasma treatment and surface modification by octyltrichlorosilne (OTS-8). For silane modification, the wafer was spin coated in air with 0.1 M solution of OTS-8 in chloroform at 3000 rpm for 10 seconds, rinsed with toluene and dried at 110 °C for 10 minutes. The PNDIs based semiconductor polymers were fabricated on the modified substrate by spin coating 8 mg/mL of polymer solution at 2000 rpm for 60 seconds inside of the glove box followed by annealing at 2000 ℃ for 10 minutes on the hot plate. The gold source/drain electrodes with channel length (*L*) of 1000 µm and width (*W*) of 100 *µm* were deposited by vacuum evaporation through a shadow mask. All the electrical characteristics of the OFET devices were measured using HP 4145B semiconductor parameter analyzer in nitrogen atmosphere.

Space-Charge-Limited Current (SCLC) Measurement. Current-voltage (*J-V*) characteristics of the SCLC devices were measured by using a HP4155A semiconductor parameter analyzer (Yokogawa Hewlett-Packard, Tokyo). The electron mobility was extracted by fitting the *J-V* curves in the near quadratic region according to the modified Mott-Gurney equation.

3.2.3 *Results and Discussion*

PNDIT and PNDIS were synthesized by Stille coupling copolymerization of 4,9-dibromo-2,7-bis(2-decyltetradecyl)benzo[lmn][3,8]-phenanthroline-1,3,6,8-tetraone with 2,5-bis(trimethylstannyl)thiophene and 2,5-bis(trimethylstannyl)selenophene, respectively, in the presence of $Pd_2(dba)_3$ and P(*o*-tolyl)$_3$ in chlorobenzene solvent. PNDIS-HD was similarly synthesized as PNDIS using 4,9-dibromo-2,7-bis(2-hexyldecyl)benzo[lmn][3,8]-phenanthroline-1,3,6,8-tetraone with shorter 2-hexyldecyl (HD) side chain. The monomer and copolymer molecular structures were confirmed by ^{1}H NMR. The number average molecular weight (M_n) of PNDIT and PNDIS was 23.9 and 26.1 kDa with polydispersity index (PDI) of 1.3 and 1.2, respectively. PNDIS-HD had a much higher M_n of 79.0 kDa with a PDI of 2.3. These polymers had onset decomposition temperature (T_d) of 400 - 430 ˚C.

Table 8. Molecular Weight, Thermal Stability, Photophysical, and XRD Properties of NDI-copolymers.

Polymer	M_w (kDa)	M_n (kDa)	PDI	T_d (˚C)	λ_{max}^{sol}	λ_{max}^{film}	E_g (eV)	d_{100} (Å)	d_{010} (Å)
PNDIT	31.5	23.9	1.3	430	326, 542	341, 598	1.77	24.86	4.20
PNDIS	31.6	26.1	1.2	415	341, 556	353, 621	1.70	22.92	4.16
PNDIS-HD	177.9	79.0	2.3	400	341, 556	351, 614	1.65	21.53	4.16

X-ray diffraction (XRD) analysis of solution-cast films of PNDIT, PNDIS, and PNDIS-HD revealed lamellar crystallinity with intense (100) peak. A lamellar d-spacing (d_{100}) of 24.86 Å, 22.92 Å and 21.53 Å, respectively, was observed for PNDIT, PNDIS, and PNDIS-HD. The shorter d_{100} spacing compared to the alkyl chain length (2 × 14 C) of 43.12 Å indicates interdigitation of the alkyl chains. As expected, PNDIS-HD has a smaller d_{100} value compared to the other two polymers with 2-decyltetradecyl side chains. The shorter d_{100} spacing of PNDIS compared to PNDIT is due to a larger torsion angle between NDI and selenophene moieties, which is a consequence of the larger Se orbitals compared to S. The observed π- π stacking distance (d_{010}) of 4.16 Å in PNDIS and PNDIS-HD and 4.2 Å in PNDIT are comparable with values seen in other NDI-based copolymers (~ 4.0 Å).[6]

Optical absorption spectra of PNDIT, PNDIS, and PNDIS-HD thin films (**Figure 19b**) and dilute (~ 10^{-6} M) $CHCl_3$ solutions show two distinctive absorption peaks, one due to π- π* transition at 340 - 360 nm and the other centered at 598 - 621 nm, which is a result of intramolecular charge transfer (ICT) (**Table 8**). It is interesting that the selenophene-linked polymers, PNDIS and PNDIS-HD, have slightly smaller band gaps and broader full-width-at-half-maximum (fwhm) in the ICT bands, which imply potentially better near-infrared light harvesting compared to the thiophene-linked PNDIT. At their visible absorption maxima of 598 - 621 nm, all three NDI copolymers have an absorption coefficient (α) of (2.7 - 2.9) × 10^4 cm^{-1}. In contrast, an absorption coefficient of 1.1 × 10^5 cm^{-1} is observed at the absorption maximum (584 nm) of the donor polymer (PSEHTT). The lowest unoccupied and highest occupied molecular orbitals (LUMO/HOMO) energy levels of the NDI copolymers along with those of $PC_{60}BM$[7] and PSEHTT[5] are shown in Figure 1c. The LUMO energy levels of the NDI copolymers were estimated from cyclic voltammetry while the corresponding HOMO energy levels were obtained from the LUMO levels and the optical band gaps.

Electron transport properties of PNDIT, PNDIS, and PNDIS-HD thin films were characterized by using organic field-effect transistors (OFETs) with bottom gate / top contact geometry. The OFETs showed only n-channel transistor behavior with unipolar electron transport. The average saturated region field-effect electron mobilities of PNDIT, PNDIS, and PNDIS-HD were 2 × 10^{-4}, 2 × 10^{-3}, and 7 × 10^{-3} cm^2/Vs, respectively. The order of magnitude higher electron mobility of PNDIS and PNDIS-HD compared to PNDIT can be understood from the larger π-orbitals of selenium compared to sulfur, which improves overlap of the orbitals. In addition, interaction between Se-Se atoms could enhance the crystallinity of the copolymers and interchain charge transport.[8] The higher electron mobility of PNDIS and PNDIS-HD can also be explained by their favorable solid state morphology and molecular packing with shorter d_{100} and d_{010} spacings compared to PNDIT (**Table 8**). The higher electron mobility of PNDIS-HD with shorter hexyldecyl side chains compared to PNDIS with decyltetradecyl side chains can be largely understood in terms of the higher molecular weight of PNDIS-HD.

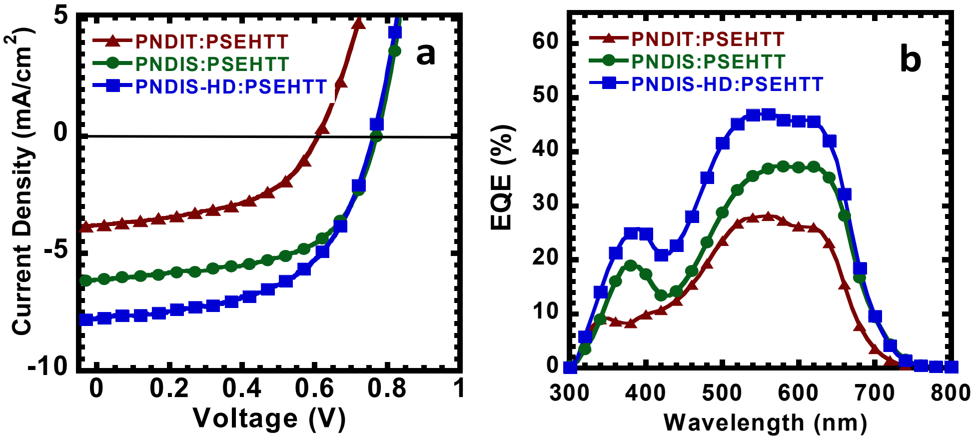

Figure 20. (a) Current density (*J*) – voltage (*V*) characteristics and (b) external quantum efficiency (EQE) spectra of all-polymer BHJ solar cells from 1:1 *wt/wt* blend each of PSEHTT:PNDIT, PSEHTT:PNDIS, and PSEHTT:PNDIS-HD.

We fabricated and evaluated polymer/polymer blend solar cells with inverted device structure of ITO/ZnO/blend/MoO_3/Ag. The active layer blend was PNDIT:PSEHTT, PNDIS:PSEHTT, or PNDIS-HD:PSEHTT, each spin-coated from chlorobenzene with an optimum composition of 1:1 *wt/wt*. The optimal composition (1:1 *wt/wt*) to focus our detailed investigation was determined by the initial performance of solar cells fabricated from different blend compositions (1:0.75, 1:1, and 1:2 *wt/wt*). The photodiodes were fabricated in a glove box and tested under AM 1.5 solar illumination at 100 mW/cm^2 in ambient conditions. Representative current density-voltage (*J-V*) curves of PNDIT:PSEHTT, PNDIS:PSEHTT, and PNDIS-HD:PSEHTT solar cells are shown in **Figure 20a**. The photovoltaic parameters including the short-circuit current density (J_{sc}), the open-circuit voltage (V_{oc}), and fill factor (FF) are summarized in **Table 9**.

Table 9. Photovoltaic Properties of All-polymer Solar Cells.

Active layer (1:1 *wt/wt*)	**J_{sc} (mA/cm^2)**	**V_{oc} (V)**	**FF**	**PCE$_{avg}$ (%)**	**PCE$_{max}$ (%)**
PNDIT:PSEHTT	3.80	0.61	0.56	1.20 ± 0.09	1.30
PNDIS:PSEHTT	6.53	0.75	0.60	2.84 ± 0.15	2.96
PNDIS-HD:PSEHTT	7.78	0.76	0.55	3.16 ± 0.10	3.26

BHJ devices based on the thiophene-linked PNDIT acceptor showed the lowest performance among the three NDI copolymer acceptors, including a maximum 1.30 % PCE and a rather low photocurrent (). The performance of the BHJ solar cells increased significantly by using the selenophene-linked PNDIS acceptor; the observed maximum PCE of 2.96 % means a 2.4-fold increase compared with the PNDIT devices. This improvement arises from the higher J_{sc} of 6.53 mA/cm^2 as well as the increased V_{oc} of 0.75 V. The best performance, with a maximum PCE of 3.26 %, J_{sc} = 7.78 mA/cm^2, and V_{oc} = 0.76 V, was observed in PNDIS-HD:PSEHTT blend solar cells, where the acceptor polymer has smaller hexyldecyl (HD) side chains. We note that both the PCE and photocurrent observed in PNDIS-HD devices are the highest for all-polymer solar cells reported to date.

The EQE spectra of the photovoltaic devices showed that the photocurrent generation starts at 720 nm (**Figure 20b**) and are consistent with the absorption spectra of the blends. The PNDIS-HD:PSEHTT device shows the highest photoconversion efficiency with a maximum EQE of 47% with more than 45% over the 500 - 650 nm wavelength range. The J_{sc} calculated by integrating the EQE spectrum of the PNDIS-HD:PSEHTT solar cell with an AM 1.5 reference spectrum is 7.76 mA/cm^2, which is in excellent agreement with the 7.78 mA/cm^2 measured directly from the *J-V* curve. We note that J_{sc} values calculated from the EQE spectra for the PNDIS and PNDIT devices were also within 3 % of the J_{sc} values from *J-V* measurements. The maximum EQE seen in PNDIS-HD devices is the highest so far in all-polymer solar cells.

We also fabricated polymer/fullerene solar cells with PSEHTT:PC$_{60}$BM (1:2 *wt/wt*) active layer and the same inverted device structure as a reference for comparison with the polymer/polymer blend solar cells. In this case, we used the previously reported optimized composition and processing conditions to deposit the PSEHTT:PC$_{60}$BM active layer, including 3.0 vol% 1,8-diiodooctane (DIO) additive in *o*-dichlorobenzene.[5b] From the *J-V* characteristics (SI, Figure S11a) we obtained J_{sc} = 8.46 mA/cm^2, V_{oc} = 0.64 V, FF = 0.62, and a maximum PCE of 3.3% (average PCE 3.23 ± 0.11). This performance is in good agreement with the previous report.[5b] The EQE spectrum of the optimum PSEHTT:PC$_{60}$BM cell shows the same onset of photocurrent as the above all-polymer devices; however, the 54% maximum EQE is higher than the 47% observed for the all-polymer BHJ solar cells. Although the EQE and the photocurrent of PC$_{60}$BM devices are higher than those of the polymer acceptor, PNDIS-HD, the power conversion efficiencies of BHJ solar cells using the two types of acceptors are identical largely because of the superior photovoltage of the all-polymer devices.

The charge transport properties of the polymer/polymer blends (PSEHTT:PNDIT, PSEHTT:PNDIS, and PSEHTT:PNDIS-HD) in the all-polymer solar cells were investigated by both OFET devices and space-charge-limited current (SCLC) measurements are summarized in **Table 10**. Field-effect electron mobility in PNDIS-HD blends (1.3 × 10^{-4} cm^2/Vs) was slightly better than in PNDIS blends but an order of magnitude higher than in PNDIT blends. In contrast, the field-effect hole mobility was about the same in all three series of blends (3.5 - 6.4) × 10^{-4}

cm^2/Vs. Hole-only devices, composed of ITO/PEDOT:PSS/blend/Au, and electron-only devices, consisting of ITO/ZnO/blend/LiF/Al, enabled estimate of the bulk charge transport properties of the BHJ blend films. Electron mobility in the bulk blend film is also highest in the PNDIS-HD blends (1.0×10^{-4} cm^2/Vs), slightly lower in PNDIS blends (5.8×10^{-5} cm^2/Vs) and a factor of 6 lower in the PNDIT blends (1.8×10^{-5} cm^2/Vs). Balanced and high hole and electron mobilities are thus observed in the PNDIS-HD blends (Table S3), which can largely explain the highest performance in terms of J_{sc}, EQE, and PCE values for the BHJ solar cells using this polymer acceptor.

Table 10. Charge Transport Properties of Polymer/Polymer Blends used in All-polymer Solar Cells.

Blend (1:1 *wt/wt*)	μ_h[a] **(cm^2/Vs) (OFET)**	μ_e[b] **(cm^2/Vs) (OFET)**	μ_h[c] **(cm^2/Vs) (SCLC)**	μ_e[d] **(cm^2/Vs) (SCLC)**
PNDIT:PSEHTT	4.0×10^{-4}	1.0×10^{-5}	4.5×10^{-5}	1.8×10^{-5}
PNDIS:PSEHTT	3.5×10^{-4}	7.5×10^{-5}	9.6×10^{-5}	5.8×10^{-5}
PNDIS-HD:PSEHTT	6.4×10^{-4}	1.3×10^{-4}	2.0×10^{-4}	1.0×10^{-4}

Average charge carrier mobility of blend from p-channel[a] and n-channel[b] organic field-effect transistors (OFETs). [c]Hole and [d]electron mobility of blend extracted from space-charge-limited current (SCLC) measurement using single charge carrier devices.

AFM imaging was used to investigate the surface morphology of the all-polymer solar cells. AFM topographic and the corresponding phase images taken directly from the surfaces of devices are shown in **Figure 21**. The observed phase separated morphology with domain sizes of 200 - 500 nm is identical in all three blend systems (PNDIT, PNDIS, and PNDIS-HD). The similarity of the morphology of all the three different polymer/polymer BHJ devices implies that the observed large variation in the photocurrent and PCE does not originate in the blend morphologies. On the other hand, the large scale of the observed phase separation in the blends suggests that there is still room for further improvement of the photovoltaic properties of

PNDIS:PSEHTT and PNDIS-HD:PSEHTT blends by reducing the domain sizes of the phase separated blend morphology through strategies such as co-solvents[3e,3h] and processing additives.[9]

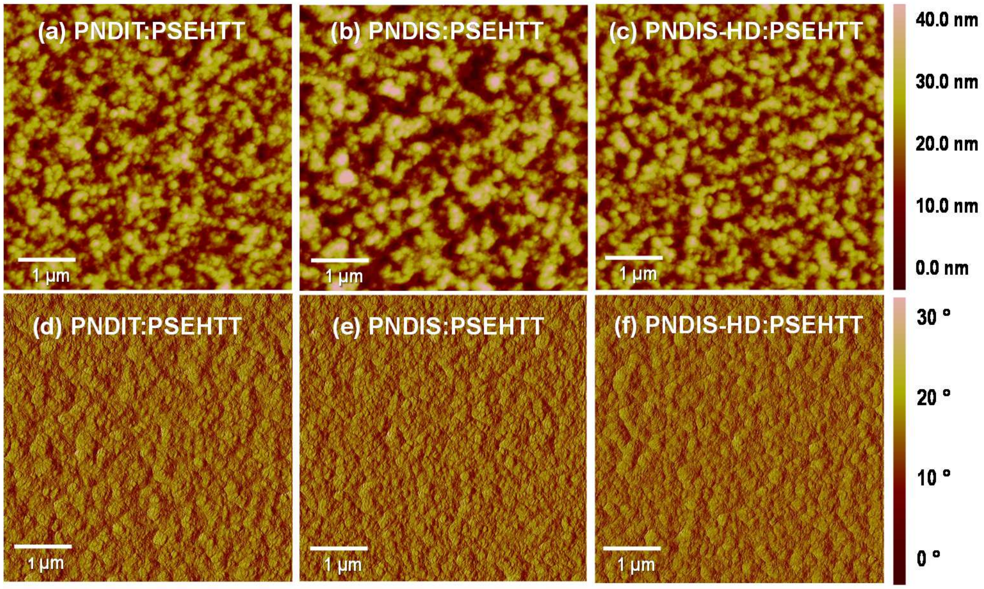

Figure 21. AFM topographical images (5 × 5 µm) of the surfaces of all-polymer solar cells: (a) PNDIT:PSEHTT, (b) PNDIS:PSEHTT, and (c) PNDIS-HD:PSEHTT; and the corresponding phase images of (d) PNDIT:PSEHTT, (e) PNDIS:PSEHTT, and (f) PNDIS-HD:PSEHTT.

3.2.4 *Conclusions*

In conclusion, two new semicrystalline NDI copolymers (PNDIS, PNDIS-HD) and a known one (PNDIT) have been synthesized, characterized and, for the first time, evaluated as acceptors in BHJ organic solar cells. We found that all-polymer solar cells composed of PNDIS-HD acceptor and PSEHTT donor have a record performance (PCE = 3.3 %, J_{sc} = 7.78 mA/cm^2, and EQE = 47 %), which is comparable to similarly evaluated PC$_{60}$BM:PSEHTT BHJ solar cells. Balanced electron and hole transport was observed in the PNDIS-HD:PSEHTT blend active layers. The superior photovoltaic properties of PNDIS-HD compared to PNDIS and prior NDI copolymers[3e,3n] suggest that unipolar electron transport with high bulk mobility, good crystallinity, size of alkyl side chains, and molecular weight are all important factors in the design of suitable acceptor polymers for BHJ solar cells.

3.2.5 *References*

(1) (a) Günes, S.; Neugebauer, H.; Sariciftci, N. S. *Chem. Rev.* **2007**, *107*, 1324. (b) Thompson, B. C.; Fréchet, J. M. J. *Angew. Chem. Int. Ed.* **2008**, *47*, 58. (c) Li, G.; Zhu, R.; Yang, Y. *Nat. Photon.* **2012**, *6*, 153.

(2) (a) You, J.; Dou, L.; Yoshimura, K.; Kato, T.; Ohya, K.; Moriarty, T.; Emery, K.; Chen, C.-C.; Gao, J.; Li, G.; Yang, Y. *Nat. Commun.* **2013**, *4*, 1446. (b) He, Z.; Zhong, C.; Su, S.; Xu, M.; Wu, H.; Cao, Y. *Nat. Photon.* **2012**, *6*, 591. (c) Small, C. E.; Chen, S.; Subbiah, J.; Amb, C. M.; Tsang, S.-W.; Lai, T.-H.; Reynolds, J. R.; So, F. *Nat. Photon.* **2012**, *6*, 115.

(3) (a) McNeill, C. R. *Energy Environ. Sci.* **2012**, *5*, 5653. (b) Facchetti, A. *Mater. Today* **2013**, *16*, 123. (c) Halls, J. J. M.; Walsh, C. A.; Greenham, N. C.; Marseglia, E. A.; Friend, R. H.; Moratti, S. C.; Holmes, A. B. *Nature* **1995**, *376*, 498. (d) Alam, M. M.; Jenekhe, S. A. *Chem. Mater.* **2004**, *16*, 4647. (e) Schubert, M.; Dolfen, D.; Frisch, J.; Roland, S.; Steyrleuthner, R.; Stiller, B.; Chen, Z.; Scherf, U.; Koch, N.; Facchetti, A.; Neher, D. *Adv. Energy Mater.* **2012**, *2*, 369. (f) Jenekhe, S. A.; Yi, S. *Appl. Phys. Lett.* **2000**, *77*, 2635. (g) Zhou, E.; Tajima, K.; Yang, C.; Hashimoto, K. *J. Mater. Chem.* **2010**, *20*, 2362. (h) Zhou, E.; Cong, J.; Wei, Q.; Tajima, K.; Yang, C.; Hashimoto, K. *Angew. Chem. Int. Ed.* **2011**, *50*, 2799. (i) Kietzke, T.; Hörhold, H.-H.; Neher, D. *Chem. Mater.* **2005**, *17*, 6532. (j) Holcombe, T. W.; Woo, C. H.; Kavulak, D. F. J.; Thompson, B. C.; Fréchet, J. M. J. *J. Am. Chem. Soc.* **2009**, *131*, 14160. (k) Mori, D.; Benten, H.; Ohkita, H.; Ito, S.; Miyake, K. *ACS Appl. Mater. Interfaces* **2012**, *4*, 3325. (l) Zhan, X.; Tan, Z. a.; Domercq, B.; An, Z.; Zhang, X.; Barlow, S.; Li, Y.; Zhu, D.; Kippelen, B.; Marder, S. R. *J. Am. Chem. Soc.* **2007**, *129*, 7246. (m) Zhou, E.; Cong, J.; Zhao, M.; Zhang, L.; Hashimoto, K.;

Tajima, K. *Chem. Comm.* **2012**, *48*, 5283. (n) Hwang, Y.-J.; Ren, G.; Murari, N. M.; Jenekhe, S. A. *Macromolecules* **2012**, *45*, 9056. (o) Cao, Y.; Lei, T.; Yuan, J.; Wang, J.-Y.; Pei, J. *Polym. Chem.* **2013**. (p) Moore, J. R.; Albert-Seifried, S.; Rao, A.; Massip, S.; Watts, B.; Morgan, D. J.; Friend, R. H.; McNeill, C. R.; Sirringhaus, H. *Adv. Energy Mater.* **2011**, *1*, 230. (q) Brenner, T. J. K.; Hwang, I.; Greenham, N. C.; McNeill, C. R. *J. Appl. Phys.* **2010**, *107*, 114501.

(4) (a) Anthony, J. E.; Facchetti, A.; Heeney, M.; Marder, S. R.; Zhan, X. *Adv. Mater.* **2010**, *22*, 3876. (b) Mishra, A.; Bäuerle, P. *Angew. Chem. Int. Ed.* **2012**, *51*, 2020.

(5) (a) Subramaniyan, S.; Xin, H.; Kim, F. S.; Shoaee, S.; Durrant, J. R.; Jenekhe, S. A. *Adv. Energy Mater.* **2011**, *1*, 854. (b) Xin, H.; Subramaniyan, S.; Kwon, T.-W.; Shoaee, S.; Durrant, J. R.; Jenekhe, S. A. *Chem. Mater.* **2012**, *24*, 1995.

(6) (a) Hwang, Y.-J.; Murari, N. M.; Jenekhe, S. A. *Polym. Chem.* **2013**, *4*, 3187. (b) Guo, X.; Kim, F. S.; Seger, M. J.; Jenekhe, S. A.; Watson, M. D. *Chem. Mater.* **2012**, *24*, 1434.

(7) Scharber, M. C.; Mühlbacher, D.; Koppe, M.; Denk, P.; Waldauf, C.; Heeger, A. J.; Brabec, C. J. *Adv. Mater.* **2006**, *18*, 789.

(8) (a) Chen, Z.; Lemke, H.; Albert-Seifried, S.; Caironi, M.; Nielsen, M. M.; Heeney, M.; Zhang, W.; McCulloch, I.; Sirringhaus, H. *Adv. Mater.* **2010**, *22*, 2371. (b) Hollinger, J.; Jahnke, A. A.; Coombs, N.; Seferos, D. S. *J. Am. Chem. Soc.* **2010**, *132*, 8546.

(9) Ren, G.; Ahmed, E.; Jenekhe, S. A. *Adv. Energy Mater.* **2011**, *1*, 946.

Chapter 4. MOLECULAR ENGINEERING TOWARD HIGH PERFORMANCE ALL-POLYMER SOLAR CELLS.

The results in this chapter are reprinted with permission from Hwang, et al. *Chem. Commun.* **2014**, *50*, 10801 (The Royal Society of Chmistry) and Hwang, et al. *J. Am. Chem. Soc.* **2015**, *137*, 4424 (Copyright 2015 American Chemical Society).

4.1 MISCIBILITY AND PHASE SEPARATION BEHAVIOR OF POLYMER/POLYMER BLEND IN ALL-POLYMER SOLAR CELLS

4.1.1 *Introduction*

In last few years, there has been remarkable growth in interest of all-polymer bulk heterojunction (BHJ) solar cells. This is due to attractive advantages that *n*-type polymers have as an acceptor instead of fullerene acceptor in conventional polymer/fullerene systems. Compared to fullerenes, *n*-type polymers have better flexibility of tuning the optical and electrochemical properties with various available chemistries, environmental stability, and durability of the device.[1] Recently, all-polymer solar cells showed large progress which now reached power conversion efficiency over 4 %,[2] although the performance of all-polymer solar cells is still far behind that of polymer/fullerene systems (>10%) .[3] One of the challenges in all-polymer solar cells for further progress is to find morphologically well matching donor and acceptor polymers which can form the large donor/acceptor interfacial area for efficient charge dissociation and well connected pathways for transport of separated charges. [4]

Poly(3-hexylthiophene) (P3HT) has been widely used as an efficient donor in organic photovoltaics. However, all-polymer solar cells with P3HT as a donor has shown low performance mainly due to the highly phase separated donor/acceptor morphology in large domain sizes. The performances reported mostly have power conversion efficiency (PCE) lower than 1 %,[5] and there are few reports with over 1 %.[6] In contrast, P3HT/fullerene systems have been successful by understanding the behavior of fullerenes in P3HT, including diffusivity and crystallization which found to be a key factor.[7] In all-polymer solar cell systems, miscibility and phase separation behavior of polymers can be a key to find well matching acceptor polymer for P3HT and further improvement in performance. However, intrinsic studies of P3HT/acceptor polymer system to understand the miscibility and phase separation behavior of polymer/polymer blends are absence.

Herein, I focused on polymer/polymer blends composed of P3HT as a donor and poly(naphthalene diimide) (PNDI) as an acceptor. As an acceptor, two PNDIs, poly{[*N,N'*-bis(2-decyltetradecyl)-naphthalene-1,4,5,8-bis(dicarboximide)-2,6-diyl]-*alt*-2,5-(3,6-dimethyl-selenolo[3,2-b]selenophene)} (PNDISS)[8] and corresponding thienothiophene linked poly{[*N,N'*-bis(2-decyltetradecyl)-naphthalene-1,4,5,8-bis(dicarboximide)-2,6-diyl]-*alt*-2,5-(3,6-dimethyl-thieno[3,2-b]thiophene)} (PNDITT), were chosen since PNDISS and PNDITT were expected to have different morphological properties even with similar molecular structure. Physical properties of PNDISS and PNDITT were firstly investigated, and photovoltaic properties of PNDISS/P3HT and PNDITT/P3HT blends in different compositions (67, 50 and 33 *wt* % P3HT) were examined. The device of P3HT/PNDISS blend with the optimum composition of 33 *wt* % P3HT gave the best PCE of 3.19 % among all the blends with J_{sc} of 7.46 mA/cm^2, V_{oc} of 0.68 V, and *FF* of 0.63. The miscibility and phase separation behavior of P3HT/PNDISS and P3HT/PNDITT blends in different blend compositions were studied based on solid state packing structure, photoluminescence (PL) quenching, and thermal transition of polymers in the blend to understand structure-property-performance relationships. PNDISS is found to be less crystalline than PNDITT and showed better miscibility with P3HT. The composition dependence was also found, and the P3HT/PNDISS blend with the composition of 33 *wt* % P3HT was expected to have the highest miscibility and the lowest tendency of phase separation. From this result, clear dependence of performance on the miscibility and phase separation of donor/acceptor polymer blends was revealed.

4.1.2 *Experimental Section*

Materials: 4,9-Dibromo-2,7-bis(2-decyltetradecyl)benzo[lmn]-[3,8]phenanthroline-1,3,6,8-tetraone was purchased from Suna Tech Inc. All other chemicals were purchased from Sigma-Aldrich or Fisher Scientific Inc. 3,6-Dimethylselenolo[3,2-b]selenophene and 3,6-dimethylthieno[3,2-b]thiophene were synthesized according to the known procedures.[8] Poly(3-hexylthiophene) (P3HT) was purchased from Rieke Metals, Inc. with a weight averaged molecular weight (M_w) of 20-30 kDa with average PDI of 2 and average regioregularity of 95 % or greater.

General synthesis procedure for 3,6-dimethylselenolo[3,2-b]selenophene and 3,6-dimethylthieno[3,2-b]thiophene. 3,6-Dimethyl-4-octyne-3,6-diol and selenium or sulfur powder were added into a 100 mL round-bottom flask. The flask equipped with a condenser was purged with argon. Then, the mixture was stirred at 220 ˚C for a day. The crude product was purified by column chromatography with hexane and used in next step reaction without further purification. 3,6-Dimethylselenolo[3,2-b]selenophene, yield = 6.8%, ^{1}H NMR (300 MHz, $CDCl_3$, δ): 7.49 (2H), 2.38 (6H); mp 102 ˚C. 3,6-Dimethylthieno[3,2-b]thiophene, yield = 33.8 %, ^{1}H NMR (300 MHz, $CDCl_3$, δ): 6.99 (2H), 2.38 (6H); mp 90 ˚C.

General synthesis procedure for 2,5-dibromo-3,6-dimethylselenolo[3,2-b]selenophene and 2,5-dibromo-3,6-dimethylthieno[3,2-b]thiophene. 3,6-Dimethyl-selenolo[3,2-b]selenophene or 3,6-dimethylthieno[3,2-b]thiophene were added into a 250 mL round-bottom flask. The flask was purged with argon before add CH_2Cl_2 and AcOH (2:1 ratio) as a mixed solvent. Aftererward, n-bromosuccineimide in CH_2Cl_2 was added dropwise. After stirring the mixture for 2 hours at 0 ˚C, the reaction was quenched by adding water. The crude product was extracted with $CHCl_3$, and purified bycolumn chromatography with hexane. 2,5-Dibromo-3,6-dimethylselenolo[3,2-b]selenophene , yield = 43%, ^{1}H NMR (300 MHz, $CDCl_3$, δ): 2.26 (6H); mp 126 ˚C. 2,5-Dibromo-3,6-dimethylthieno[3,2-b]thiophene, yield = 77.4 %, ^{1}H NMR (300 MHz, $CDCl_3$, δ): 2.27 (6H); mp 134 ˚C.

General synthesis procedure for 2,5-bis(trimethylstannyl)-3,6-dimethylselenolo[3,2-b]selenophene and 2,5-bis(trimethylstannyl)-3,6-dimethylthieno[3,2-b]thiophene. 2,5-Dibromo-3,6-dimethyl-selenolo[3,2-b]selenophene or 2,5-dibromo-3,6-dimethylthieno[3,2-b]thiophene was added into a 100 mL round-bottom flask. Under argon atmosphere, THF was then added. The mixture was cooled to -78 ˚C in a dry ice bath and 2.5 M n-butyllithium solution in hexane was added dropwise. After stirring the mixture for an hour at -78 ˚C, 1 M trimethyltinchloride solution in THF was added in one portion at -78 ℃. Dry ice bath was removed after 5 min and the mixture was warmed up to room temperature. After stirring overnight at room temperature, the reaction mixture was poured into water and extracted with diethyl ether three times. The organic phase was dried with anhydrous magnesium sulfate and the solvent was evaporated by vacuum rotary evaporator. The product was purified by recrystallization in EtOH. 2,5-Bis(trimethylstannly)-3,6-dimethyl-selenolo[3,2-b]selenophene, yield = 31.4 %, ^{1}H NMR (300 MHz, $CDCl_3$, δ): 2.38 (6H), 0.32–0.21 (18H); mp 143 ˚C. 2,5-

Bis(trimethylstannyl)-3,6-dimethylthieno[3,2-b]thiophene, yield = 46.2 %, ^{1}H NMR (300 MHz, $CDCl_3$, δ): 2.39 (6H), 0.52–0.33 (18H); mp 147 °C.

Poly{[N,N'-bis(2-decyltetradecyl)-naphthalene-1,4,5,8-bis(dicarboximide)-2,6-diyl]-alt-2,5-(3,6-dimethyl-selenolo[3,2-b]selenophene)} (PNDISS). 4,9-Dibromo-2,7-bis(2-decyltetradecyl)benzo[lmn][3,8]phenanthroline-1,3,6,8-tetraone (373.9 mg, 0.34 mmol), 2,5-bis(trimethylstannyl)-3,6-dimethyl-selenolo[3,2-b]selenophene (200 mg, 0.34 mmol), $Pd_2(dba)_3$ (6.2 mg, 0.0068 mmol) and $P(o\text{-tolyl})_3$ (8.3 mg, 0.0272 mmol) were added into a 100 mL three-neck round-bottom flask. The flask equipped with a condenser was then degassed and filled with argon three times. Afterwards, 18 mL of chlorobenzene was added and degassed and filled with argon three times. The reaction mixture was refluxed for 72 h under argon. After cooling down to room temperature, the polymerization mixture was poured and stirred into 200 mL methanol and 5 mL hydrochloric acid solution for 5 h. The polymer precipitated out as a bluish purple solid and was filtered using a filter paper. The polymer was purified by Soxhlet extraction with methanol, hexane, and acetone. PNDISS (405 mg, 97 %), ^{1}H NMR (500 MHz, $CDCl_3$, δ): 8.90 (2H), 4.20 (4H), 2.27 (6H), 2.08 (2H), 0.88–1.49 (46H); GPC: M_w = 18.4 kDa M_n = 17.3 kDa, PDI = 1.1; TGA: T_d = 410 °C.

Poly{[N,N'-bis(2-decyltetradecyl)-naphthalene-1,4,5,8-bis(dicarboximide)-2,6-diyl]-alt-2,5-(3,6-dimethyl-thieno[3,2-b]thiophene)} (PNDITT). 4,9-Dibromo-2,7-bis(2-decyltetradecyl)benzo[lmn][3,8]phenanthroline-1,3,6,8-tetraone (350 mg, 0.32 mmol), 2,5-bis(trimethylstannyl)-3,6-dimethyl-thieno[3,2-b]thiophene (157.5 mg, 0.32 mmol), $Pd_2(dba)_3$ (5.8 mg, 0.0064 mmol) and $P(o\text{-tolyl})_3$ (7.8 mg, 0.0256 mmol) were added into a 100 mL three-neck round-bottom flask. The flask equipped with a condenser was then degassed and filled with argon three times. Afterwards, 15 mL of chlorobenzene was added and degassed and filled with argon three times. The reaction mixture was refluxed for 72 h under argon. After cooling down to room temperature, the polymerization mixture was poured and stirred into 200 mL methanol and 5 mL hydrochloric acid solution for 5 h. The polymer precipitated out as a bluish purple solid and was filtered using a filter paper. The polymer was purified by Soxhlet extraction with methanol, hexane, and acetone. PNDITT (344 mg, 95 %), ^{1}H NMR (500 MHz, $CDCl_3$, δ): 8.89 (2H), 4.19 (4H), 2.25 (6H), 2.10 (2H), 0.85–1.47 (46H); GPC: M_w = 13.3 kDa, M_n = 11.1 kDa, PDI = 1.2; TGA: T_d = 425 ˚C.

Characterization of Polymers**:** The structure and physical properties of polymers were investigated by ^{1}H NMR, gel permeation chromatography (GPC) analysis, thermogravimetric analysis (TGA). ^{1}H NMR spectra at 300 MHz were recorded on a Bruker-AF300 spectrometer for monomers and 500 MHz were recorded on a Bruker-AF500 spectrometer for polymers to verify the molecular structure, and the molecular weight was measured using GPC Model 120 (DRI, PLBV400HTViscometer) against polystyrene standards in chlorobenzene at 60 ˚C. Thermal stability of the polymers was tested on a TA Instruments Q50 TGA at a heating rate of 20 °C/min under nitrogen gas flow.

Electrochemical properties of the polymers were investigated by cyclic voltammetry (CV). CV experiments were performed on an EG&G Princeton Applied Research potentiostat/galvanostat (model 273A) in an electrolyte solution of 0.1 M tetrabutylammonium hexafluorophosphate (Bu_4NPF_6) in acetonitrile at a scan rate of 40 mV/s. Platinum wires were used as counter and working electrodes, and Ag/Ag$^+$ (Ag in 0.1 M $AgNO_3$ solution, Bioanalytical System, Inc.) was used as a reference electrode. As an internal standard, ferrocene/ferrocenium was used, and the reference potential was converted to the saturated calomel electrode [2] scale. The samples for CV were prepared by dip-coating the copolymer solutions in chloroform onto Pt wires.

The optical properties of the polymers were measured using Perkin-Elmer model Lambda 900 UV/vis/near-IR spectrophotometer, and photoluminescence spectra was recorded using excitation wavelength of 550 nm. X-ray diffraction (XRD) was performed in Bruker D8 Discover with a Cu Kα beam using GADD XRD system for drop-casted film of concentrated (15 mg/mL) polymer solutions with annealing at 200 ˚C for 30 minutes. The photoluminescence (PL) emission spectra were obtained with a Photon Technology International (PTI) Inc. model QM2001-4 spectrofluorimeter. Differential scanning calorimetry (DSC) was tested on a TA Instruments Q50 DSC at a heating rate of 20 ˚C/min under nitrogen gas flow.

Fabrication and Characterization of Inverted Solar Cells: The solar cells were fabricated with the inverted device structure of ITO/ZnO/active layer/MoO_3/Ag. ITO substrates were sequentially cleaned with acetone and isopropylalchol in ultrasonic bath, and then dried in a vacuum oven overnight. ITO substrates were treated with oxygen plasma before spin coating the solution of zinc acetate (1 g) in 2-methoxyethanol (10 mL) with ethanolamine (0.28 g) at 5000 rpm for 40 sec. After annealed the film for gelation at 250 °C for an hour in air, ZnO layer was treated with 1 vol % of ethanolamine in 2-methoxyethanol solution and dried at 110 °C for 10 minutes in air. The active layer was then spin-coated from the polymer solution (15 mg/mL, 100 % chloroform) to make a thin film of 80 - 100 nm thickness and thermally annealed at 175 °C for 10 min in a glovebox. The substrates were then loaded in a thermal evaporator (BOC Edwards, 306) to deposit thin layer of 7.5 nm MoO_3 and 100 nm Ag under high vacuum (2×10^{-6} Torr). The current density–voltage ($J - V$) curves of solar cells were measured using a HP4155A semiconductor parameter analyzer in air. An AM1.5 illumination at 100 $mWcm^{-2}$ was provided by a filtered Xe lamp and calibrated by using an NREL-calibrated Si diode. The external quantum efficiency (EQE) was measured using a QEX10 solar cell quantum efficiency measurement system (PV Measurements, Inc.).

4.1.3 *Results and Discussion*

PNDISS and PNDITT were synthesized by Stille coupling polymerization of 4,9-dibromo-2,7-bis(2-decyltetradecyl)benzo[*lmn*][3,8]-phenanthroline-1,3,6,8-tetraone (dibromo NDI) and 2,5-bis(trimethylstannly)-3,6-dimethyl-selenolo[3,2-b]selenophene or 2,5-bis(trimethylstannyl)-3,6-dimethylthieno[3,2-b]thiophene in the presence of $Pd_2(dba)_3$ and $P(o\text{-}tolyl)_3$ with

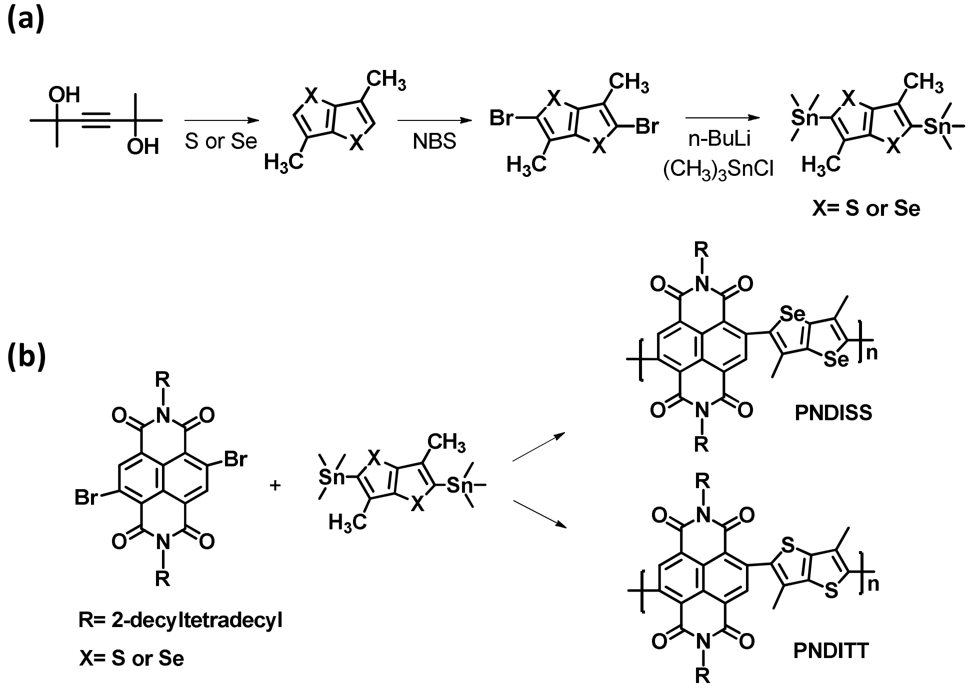

Scheme 6. (a) Synthetic route to 2,5-bis(trimethylstannly)-3,6-dimethyl-selenolo[3,2-b]selenophene and 2,5-bis(trimethylstannyl)-3,6-dimethylthieno[3,2-b]thiophene. (b) Synthesis of poly(naphthalene diimide)s (PNDIs).

chlorobenzene as a solvent for three days. Both comonomers, selenoloselenophene and thienothiophene, were synthesized according to reported dry one-pot reaction without any solvent involved.[8] Bromination with *n*-bromosucciimide (NBS) and stannylation with *n*-butyllithium (*n*-BuLi) and trimethyltin chloride ($(CH_3)_3SnCl$) were followed to get final monomers. Synthetic route of selenoloselenophene, thienothiophene and copolymers are illustrated in **Scheme 6**. Molecular structures of monomers and polymers were confirmed using ^{1}H NMR. PNDISS and PNDITT were highly soluble (>40 mg/mL) in common organic solvent, including chloroform, toluene, and chlorobenzene due to long 2-decyltetradecyl alkyl side chains on NDI core. The weight averaged molecular weight (M_w) of PNDISS and PNDITT were 18.4 kDa and 13.3 kDa with polydispersity index (PDI=M_w/M_n) of 1.1 and 1.2, respectively. Thermogravimetric analysis (TGA) was performed to measure decomposition temperature (T_d) of PNDISS and PNDITT which were 410 ˚C and 425 ˚C, respectively, indicating good thermal stability of polymers.

Table 11. Molecular Weight, Thermal Stability, Optical and Electronic Properties of PNDIs.

Polymer	M_w (kDa)	PDI	T_d (℃)	$\lambda_{max}$$^{a)}$ (nm)	$\lambda_{max}$$^{b)}$ (nm)	E_g^{opt} (eV)	$\alpha_{max}$$^{c)}$ (10^4 cm^{-1})	LUMO$^{d)}$ (eV)	HOMO$^{e)}$ (eV)
PNDISS	18.4	1.1	410	361, 601	361, 654	1.65	3.31	-3.84	-5.49
PNDITT	13.3	1.2	425	342, 588	347, 622	1.72	3.61	-3.84	-5.56

$^{a)}$The absorption maximum in dilute solution. $^{b)}$The thin film absorption maximum. $^{c)}$ Absorption coefficient at the absorption maximum. $^{d)}$Electron affinity was obtained based on $\mathrm{LUMO} = -(\,\mathrm{e}E_{\mathrm{red}}^{\mathrm{onset}}(\mathrm{vs\ SCE}) + 4.64\ \mathrm{eV})$. $^{e)}$Ionization potential was obtained based on $\mathrm{HOMO} = \mathrm{LUMO} - \mathrm{E_g^{opt}}$.

Electronic structures of polymers were investigated by cyclic voltammetry (CV). The lowest unoccupied molecular orbital (LUMO) energy levels that calculated from the onset reduction potential ($\mathrm{LUMO} = -(\mathrm{e}E_{\mathrm{red}}^{\mathrm{onset}}(\mathrm{vs\ SCE}) + 4.64\ \mathrm{eV})$[9] were -3.84 eV for both PNDISS and PNDITT which caused by strong electron withdrawing NDI core that play important role to determine LUMO energy level. The oxidation peaks were not observed, and the highest occupied molecular orbital (HOMO) energy levels were estimated from optical energy band gap ($\mathrm{HOMO} = \mathrm{LUMO} - E_g^{opt}$). Calculated and estimated energy levels of polymers are summarized in **Table 11**.

Optical energy band gaps and absorption spectra of PNDIs as well as the blends of P3HT/PNDI were investigated. The normalized optical absorption spectra of PNDISS and PNDITT in dilute (10^{-6} M) chloroform solution and as thin films on glass substrates are shown in **Figure 22(a)**. Both polymers showed two major absorption bands which can assigned as $\pi-\pi^*$ or $n-\pi^*$ transition band in higher energy range (300-400 nm) and intramolecular charge transfer band in lower energy range (500-700 nm). [10] Compared to PNDITT, PNDISS showed red-shifted λ_{max} (32 nm) and broader full width at half maximum (FWHM) ICT band (~25 nm) in thin film while the absorption in solution were identical. As a result, the optical energy band gap (E_g) of PNDISS which calculated from onset of the absorption band was 1.65 eV, and PNDITT gave slightly larger E_g of 1.72 eV. Absorption coefficient (α) of P3HT, PNDIs, and P3HT/PNDIs polymer blends were calculated (**Figure 22** Error! Reference source not found.**(b, c)**). PNDISS showed slightly higher α_{max} in higher energy band (3.61×10^4 cm^{-1}) compared to those of

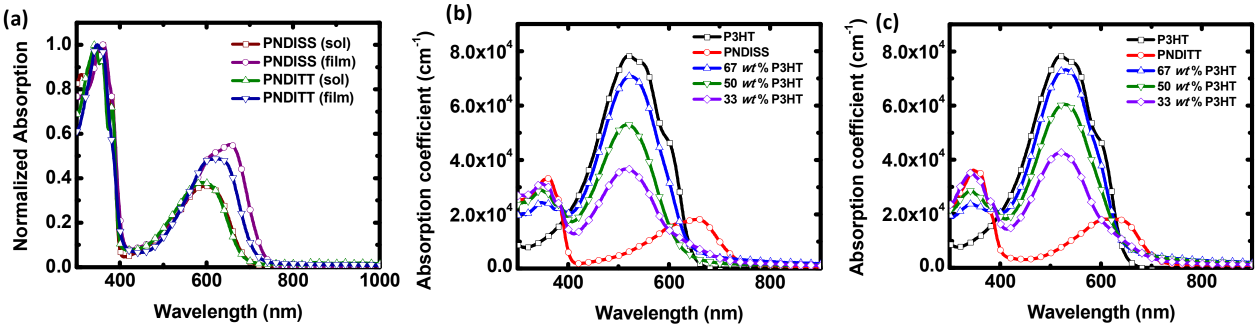

Figure 22. Optical absorption spectra of PNDIs in solution and as thin films (a), absorption coefficient of P3HT:PNDISS blends (b) and P3HT:PNDITT blends (c) as thin films on glass substrates.

PNDITT (3.31×10^4 cm^{-1}) while both polymers showed identical α_{max} of 1.80×10^4 cm^{-1} in ICT bands. P3HT showed more than 2-fold higher α_{max} of 7.83×10^4 cm^{-1} at λ_{max} of 520 nm, and thus unbalanced absorption bands at the blend with composition of 50 *wt* % P3HT was observed. In both P3HT/PNDITT and P3HT/PNDISS blends, gradual decrease of α_{max} of P3HT and increase of α_{max} of PNDIs was observed with decreasing composition of P3HT from 67 *wt* % to 33 *wt* %, and the film with the composition of 33 *wt* % P3HT showed the most balanced absorption bands between PNDIs and P3HT.

Photovoltaic Properties of P3HT/PNDI blends. Photovoltaic properties of P3HT:PNDI blends were investigated to understand the property-performance relationships. All-polymer bulk heterojunction (BHJ) solar cells comprising P3HT as a donor and PNDIs as an acceptor in different D/A blend ratios of 2:1, 1:1, and 1:2, which are correspond to the compostions of 67, 50, and 33 *wt* % of P3HT, were fabricated with device structure of ITO/ZnO/active layer/MoO_3/Ag. The devices were tested under AM 1.5 solar illumination at 100 mW/cm^2 in ambient conditions. Representative current density-voltage (*J-V*) curves and corresponding external quantum efficiency (EQE) of P3HT/PNDIs solar cells are shown in **Figure 23**. The photovoltaic properties including the short-circuit current density, open-circuit voltage (V_{oc}), and fill factor (*FF*) are summarized in **Table 12**.

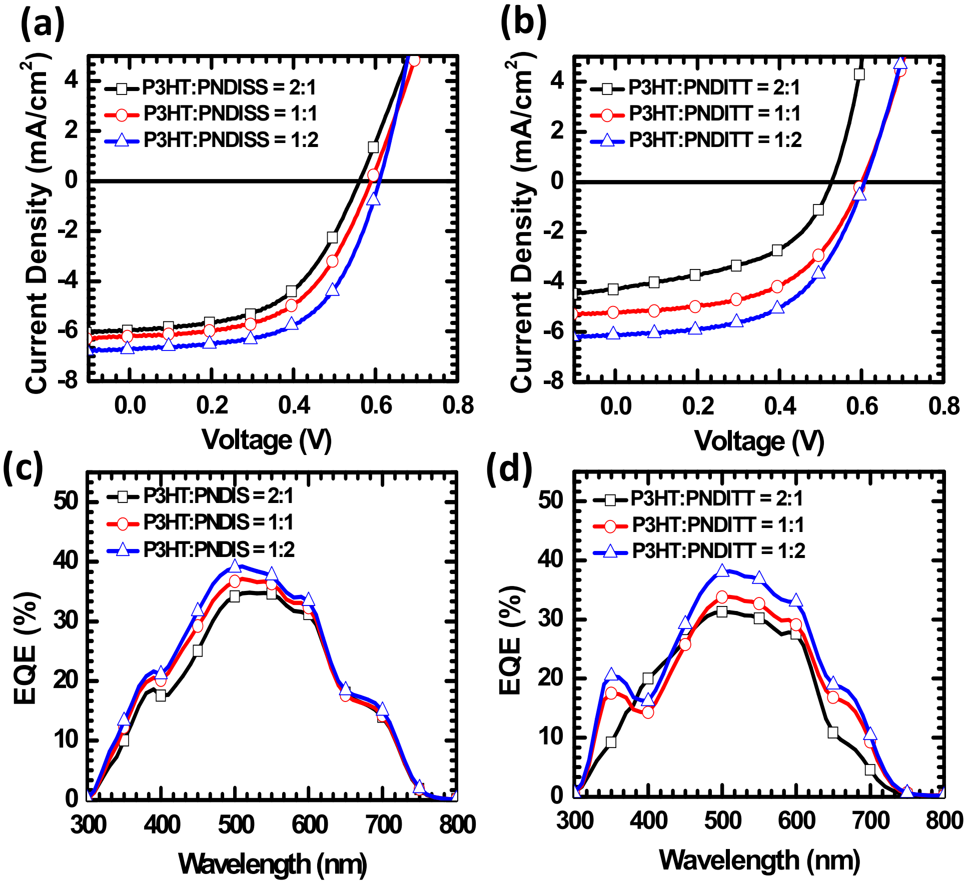

Figure 23. Current density-voltage characteristics (a, b) under 100 mW/cm^2 1.5 AM illumination in air and EQE spectra (c, d) of P3HT:PNDISS and P3HT:PNDITT blend all-polymer solar cells in different compositions (67, 50, and 33 % P3HT).

Higher photovoltaic properties were achieved from P3HT/PNDISS solar cells compared to P3HT/PNDITT solar cells, and a significant composition dependence of photovoltaic parameters for both solar cells was observed. With decreasing composition of P3HT, photovoltaic parameters including J_{sc}, V_{oc}, and *FF* were increased, and thus power conversion efficiency (PCE). In P3HT/PNDITT solar cells, PCE showed more than 85 % of increment from 1.09 % to 2.03 % by changing the D/A blend ratio from 1:2 to 2:1 *wt:wt*, and corresponding J_{sc}, V_{oc}, and *FF* were also increased from 4.24 mA/cm^2 to 6.13 mA/cm^2, from 0.53 V to 0.61 V, and from

0.49 to 0.54, respectively. With PNDISS as an acceptor, same trend of the composition dependence was observed, and the best device with optimum D/A ratio of 2:1 *wt:wt* gave the PCE as high as 2.36 % with J_{sc} of 6.69 mA/cm^2, V_{oc} of 0.61 V, and *FF* of 0.58. From the surface morphology analysis using atomic force microscope (AFM) image, no clear difference was observed between P3HT/PNDITT and P3HT/PNDISS blends. Although, the smallest roughness value of 0.9 nm was obtained from the blend of P3HT/PNDISS in the ratio of 2:1 *wt:wt*.

Table 12. Photovoltaic Properties of All-Polymer Solar Cells.

active layer	J_{sc} (mA/cm^2)	V_{oc} (V)	FF	PCE (%)	EQE_{max} (%)
P3HT:PNDISS (2:1)	5.93 (5.71±0.22)	0.56 (0.557±0.003)	0.53	1.76 (1.68 ± 0.08)	34.80
P3HT:PNDISS (1:1)	6.21 (5.97±0.24)	0.59 (0.587±0.003)	0.53	1.93 (1.83 ± 0.10)	38.31
P3HT:PNDISS (1:2)	6.69 (6.31±0.38)	0.61 (0.608±0.002)	0.58	2.36 (2.21 ± 0.15)	39.20
P3HT:PNDISS (1:2)[a)]	7.46 (7.13 ± 0.22)	0.68 (0.667 ± 0.007)	0.63	3.19 (3.07 ± 0.12)	41.70
P3HT:PNDITT (2:1)	4.24 (4.01±0.23)	0.53 (0.528±0.002)	0.49	1.09 (1.01 ± 0.08)	31.28
P3HT:PNDITT (1:1)	5.21 (5.04±0.17)	0.60 (0.597±0.003)	0.53	1.67 (1.60 ± 0.07)	33.83
P3HT:PNDITT (1:2)	6.13 (5.98±0.15)	0.61 (0.607±0.003)	0.54	2.03 (1.95 ± 0.08)	38.14

[a)] ZnO surface modified by spin coating of 1 vol % ethanolamine in 2-methoxyethanol. The photovoltaic properties were averaged over 5 devices.

Corresponding external quantum efficiency (EQE) spectra of the P3HT/PNDIs based solar cells were shown in **Figure 23 (c, d)**. The EQE spectra of these devices show that the photoresponse begins at ~750 nm and covers the entire visible region which indicates PNDIs contribute to the light harvesting and photocurrent generation since P3HT does not absorb in the range of 300-400 nm and 600-750 nm. Although, the maximum EQE were obtained in the range of 400 to 600 nm which match with the light absorption range of P3HT and the values were varied from 31.28 % in the P3HT/PNDITT 1:2 *wt:wt* device to 39.20 % in the P3HT/PNDISS 2:1 *wt:wt* device. Compared to P3HT/PNDITT devices, slightly broader EQE spectra with higher EQE maximum values were also observed in P3HT/PNDISS devices, and this can be understood by red-shifted absorption band of PNDISS and higher current density of the devices from the *J*-*V* measurement. The photocurrent values calculated from EQE spectra were found to be consistent with the J_{sc} values from $J - V$ curves for all the devices, showing a mismatch between the two values of within 10 %.

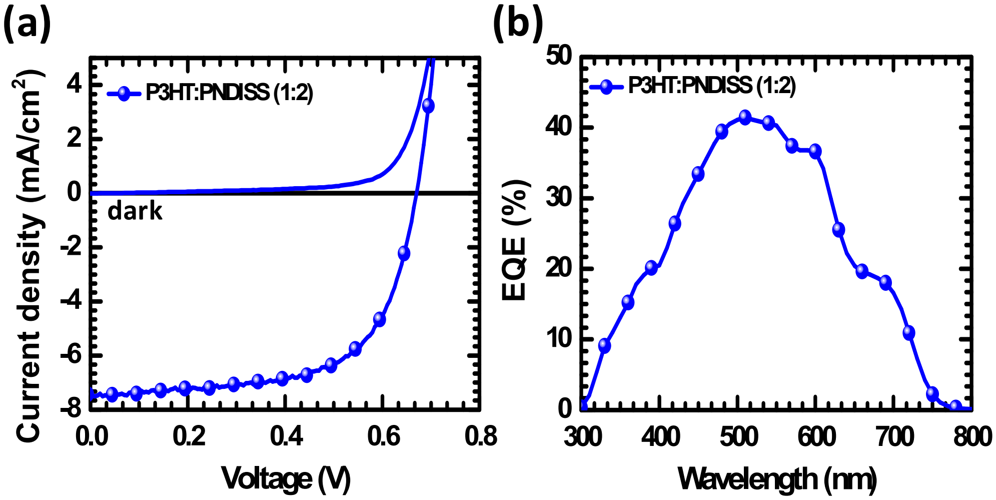

Figure 24. Current density-voltage characteristics (a) and EQE spectra (b) of P3HT:PNDISS all-polymer solar cells in composition of 33 % P3HT with surface treated ZnO layer.

P3HT/PNDISS solar cells with optimum blend ratio of 2:1 *wt:wt* were further optimized by surface modification of ZnO layer with 1 *vol* % of ethanolamine in 2-methoxyethanol which can decrease the work function of ZnO and increase the current density.[11] As a result, significantly improved performance with J_{sc} of 7.46 mA/cm^2, V_{oc} of 0.68 V, and *FF* of 0.63 were obtained, and thus PCE as high as 3.19 % was achieved. Interestingly, not only the current density, but V_{oc} and *FF* were also highly improved with surface modification. It is notable that the fill factor over 0.6 is comparable or even higher than polymer/fullerene systems and it is the first time reporting PCE over 3 % in all-polymer solar cells with P3HT as a donor. Corresponding *J*-*V* curve and EQE spectrum are illustrated in **Figure 24**.

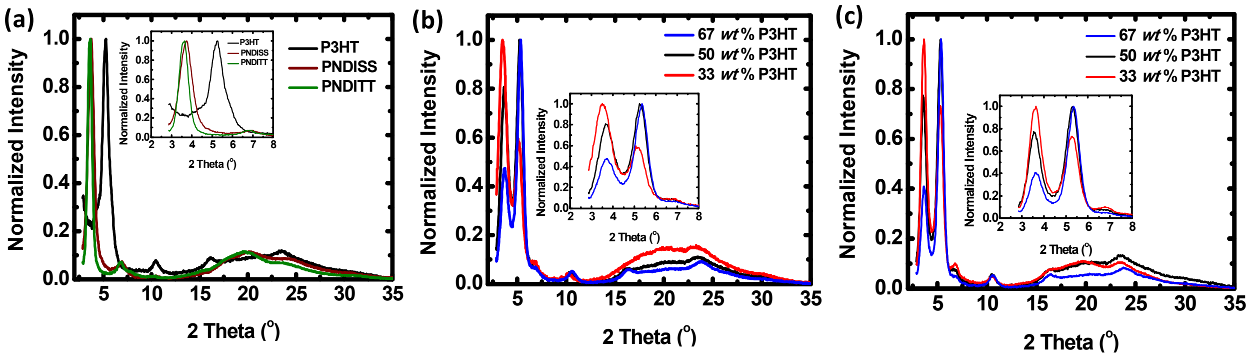

Figure 25. XRD patterns of drop-casted thin films of PNDIs and P3HT (a), P3HT:PNDISS blends (b), and P3HT:PNDITT blends (c).

X-ray Diffraction Analysis of PNDIs and P3HT/PNDI blends. The solid state molecular packing structure of polymers was investigated using X-ray diffraction (XRD). PNDISS and PNDITT showed lamellar crystalline structures as other reported NDI based copolymers with intense lamellar (100) peak at 3.74 ° and 3.64 °, and corresponding *d*-spacing (d_{100}) of 23.60 Å and 24.24 Å, respectively. π- π stacking (010) peaks were also found at 20.35 ° and 19.56 ° with corresponding d_{010} of 4.36 Å and 4.43 Å for PNDISS and PNDITT, respectively. Similarity in the molecular structure of PNDISS and PNDITT resulted in similar solid state packing structures. To investigate the crystallinity of polymers, the mean size of the crystalline domains (L) for PNDISS and PNDITT were calculated from FWHM of the lamellar peaks using Scherrer equation, $L = \frac{K\lambda}{\beta\cos\theta}$ where K is shape factor (0.9), λ is X-ray wavelength (1.54 Å), and β is FWHM in radian. [12] Interestingly, significantly different L were observed, and calculated L for PNDISS and PNDITT were 12.03 nm and 16.88 nm, respectively, which indicates much higher crystallinity of PNIDTT compared to PNDISS. The solid state packing structure of P3HT was also investigated and d_{100} of 16.78 Å, d_{200} of 8.48 Å, d_{300} of 5.44 Å, and d_{010} of 3.78 Å, were observed which is well matching with previous reports (**Figure 25**(**a**)).[13]

In addition to the pure polymers, XRD was performed for P3HT/PNDISS and P3HT/PNDITT blends in different compositions (67, 50, and 33 *wt* % P3HT) (**Figure 25 (b, c)**). Two distinct peaks for both lamellar (100) and π-π stacking (010) were observed which are originated from PNDIs and P3HT. 2θ of the lamellar peaks were in the range of 3-4 ˚ for PNDIs and 5-6 ˚ for P3HT, and 2θ of π-π stacking (010) peaks were in the range of 19-20 ˚ for PNDIs and 23-24 ˚ for P3HT. However, the peak positions and corresponding *d*-spacing of polymer blends were shifted compared to those of the pure polymers as shown in **Figure 25(b, c)**.

More notable shift was observed from the lamellar peaks than the π- π stacking peaks due to the flexibility of alkyl chains between polymer main chains on the lamellar packing direction. The difference of d_{010} (Δd_{010}) between polymer blends and pure polymers were in the range of 0.01-0.08 Å, while large difference up to 1.61 Å were observed in Δd_{100}. PNDISS/P3HT blends found to have more change in solid state morphology compared to the PNDITT/P3HT blends. Less crystalline PNDISS possibly have more chance to mixing with P3HT and affect each other's morphology. The dependence of Δd_{100} on blend composition was also observed and 33 *wt* % of P3HT showed the larger Δd_{100} than other compositions in both P3HT/PNDISS and P3HT/PNDITT blends.

Table 13. The Mean Crystalline Domain Size of P3HT, PNDIs, and P3HT/PNDIs Blends.

blend	P3HT	PNDISS	PNDITT	P3HT/ PNDISS (2:1)	P3HT/ PNDISS (1:1)	P3HT/ PNDISS (1:2)	P3HT/ PNDITT (2:1)	P3HT/ PNDITT (1:1)	P3HT/ PNDITT (1:2)
P3HT (nm)	15.31			12.32	11.07	9.51	15.24	14.99	14.09
PNDIs (nm)		12.03	16.88	8.35	8.72	8.93	16.00	15.47	15.24

The mean size of the crystalline domains (L) of PNDIs and P3HT in blends was also calculated, and the results are summarized in **Table 13**. Compared to L of pure polymers, which was 12.03 nm for PNDISS and 16.88 nm for PNDITT, both polymers showed smaller crystalline domain sizes indicating decreased crystallinity in blends. The L of PNDISS and PNDITT in blends was varied in the range of 8.35-8.93 nm and 15.26-16.00 nm, respectively. The L of P3HT was also decreased in the blends, and L in the range of 9.51-12.32 nm in PNDISS/P3HT blends and L in the range of 14.09-15.24 nm PNDITT/P3HT blends. Moreover, larger decrease of crystalline domain sizes were investigated in the P3HT/PNDISS blends compared to the P3HT/PNDITT blends. This result supports the idea that PNDISS and P3HT has more influence on crystalline structures of each other compared to PNDITT and P3HT has, and possibly indicates better miscibility of P3HT with PNDISS than PNDITT which can be beneficial for solar cells applications.

Photoluminescence (PL) Quenching of P3HT/PNDI Blends. Photoluminescence (PL) of polymer blends was measured and compared with the PL of pure P3HT. Photoluminescence (PL) occurs when the excitons that generated from polymers are emissively recombined before the charge separation.[14] Thus, PL quenching indicates photoinduced charge transfer to donor and acceptor polymers after the charge separation of excitons that diffused to the interface of donor and acceptor. Moreover, miscibility as well as phase separation behavior of donor and acceptor

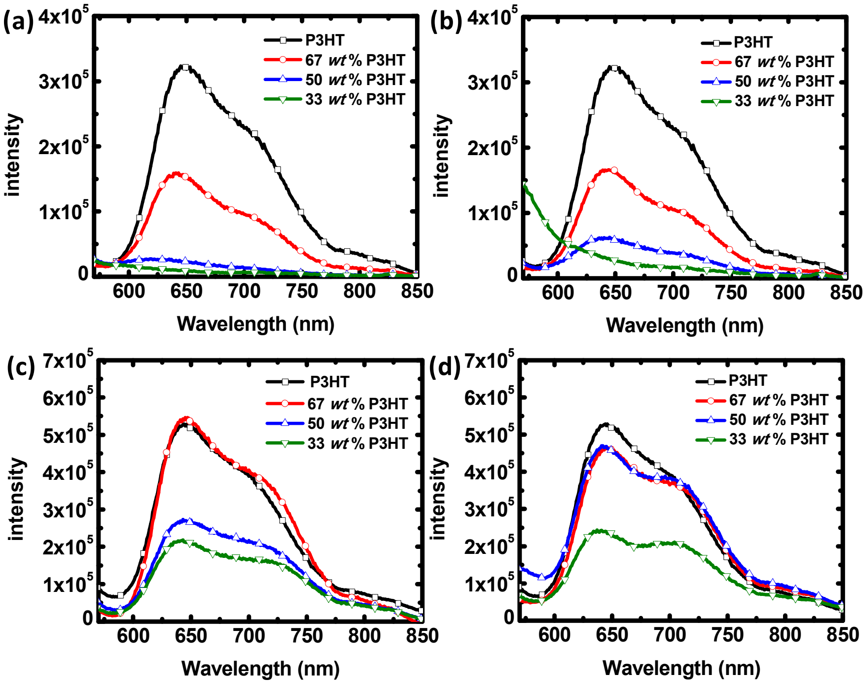

Figure 26. Photoluminescence (PL) spectra of P3HT and P3HT:PNDIs blends in as-casted films (a, b) and annealed films at 175 ˚C for 10 minutes (c, d).

can be estimated by PL quenching due to crystalline domain size and interfacial area of donor and acceptor play important role in charge separation of excitons which has limited diffusion length and life time. PL spectra of P3HT/PNDIs blends, when excited with Xe flash lamp at a wavelength of 550 nm, are shown in **Figure 26**.

In the PL spectra of as-casted blend films (**Figure 26 (a)**), gradual increase of PL quenching was observed with increasing composition of PNDIs. In P3HT/PNDITT blends, the PL quenching rate calculated by area is increased from 50.4 % in 67 *wt* % P3HT blend to 89.4 % in 33 *wt* % P3HT blend. In P3HT/PNDISS blends, more significant PL quenching rate was observed which was quenched from 53.5 % in 67 *wt* % P3HT film to 95.5 % in 33 *wt* % P3HT film. Near 90 % of PL quenching in both blends at the composition of 33 *wt* % P3HT informs that P3HT and PNDIs is mixed intimately in angstrom level with large interface area.

PL Spectra of the films after annealing at 175 ˚C for 10 minutes, which is same condition with solar cell device fabrication, was also measured. Remarkably decreased PL quenching was observed after annealing the films, and this is a strong evidence of phase separation during the annealing process. In P3HT/PNDITT blends, noticeable PL quenching of 48 % was observed only at the composition of 33 *wt* % P3HT while no PL quenching is occurred at the composition of 50 and 67 *wt* % P3HT. This means there is large phase separation with small donor/acceptor interfacial area in P3HT/PNDITT blends, and thus most of excitons that generated in polymers are recombined before they arrive to the interface of P3HT and PNDITT for charge separation. In contrast, P3HT/PNDISS blends started to show 45 % of PL quenching at the composition of 50 *wt* % P3HT, and 58 % of PL quenching at the composition of 33 *wt* % P3HT was observed. These indicate P3HT/PNDISS blend will be more favorable for solar cell applications with their higher charge separation rate due to the larger interface area and smaller phase separated domain sizes compared to P3HT/PNDITT blend. These results are consistent with XRD analysis which showed smaller crystalline domain sizes in P3HT/PNDISS blends for both P3HT and PNDISS.

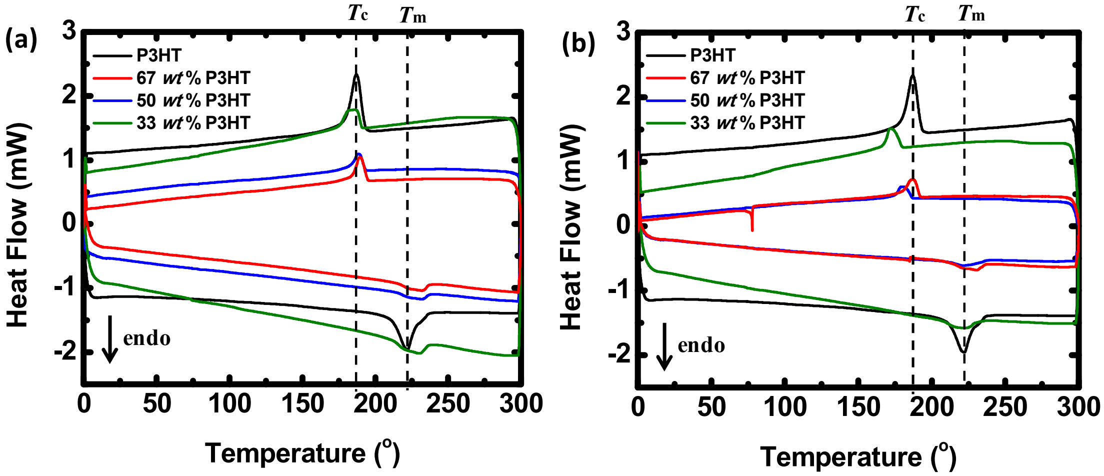

Figure 27. Differential scanning calorimetry (DSC) thermograms of P3HT:PNDISS blends (a) and P3HT:PNDITT blends (b).

Differential Scanning Calorimeter (DSC) Analysis of P3HT/PNDI Blends. Thermal transition of polymer blends was investigated using Differential scanning calorimeter (DSC), and compared with the thermal transition of the pure P3HT. DSC is one of the convenient and useful techniques to study and understand the miscibility and phase separation behavior of polymer/polymer blend systems, since measuring the heat of mixing plays important role in predicting miscibility of two materials.[15] Therefore, we can observe the change in melting temperature (T_m) of polymer blends compared to the T_m of pure polymers (T_m^0) when polymers have miscibility to each other.[1] Moreover, when crystallization temperature (T_c) shows dependence on the composition of polymer blends, this indicates phase separation behavior of polymers.[1] For P3HT, its thermal transitions are well known and it shows clear thermal transition peaks including T_m and crystallization temperature (T_c). In contrast, PNDIs did not show any distinct transition up to 300 ˚C. Thus, in our blend systems of P3HT/PNDIs, thermal transition change was analyzed using T_m and T_c of P3HT (**Figure 27**).

For both P3HT/PNDITT and P3HT/PNDISS blends, the change of T_m in the blends compared to T_m^0 of P3HT (222.11˚C) were observed, and the difference were in the range of 0.20-8.45 ˚C for P3HT/PNDITT blends and 8.46-9.89 ˚C for P3HT/PNDISS blends. This result indicates the presence of miscibility between P3HT and PNDIs. Interestingly, the shift of T_m in P3HT/PNDISS blends was more noticeable compared to P3HT/PNDITT blends, which informs that PNDISS has better miscibility with P3HT than PNDITT. Composition dependence of T_m shift was also observed, and the composition of 33 *wt* % P3HT showed the largest difference for both P3HT/PNDITT and P3HT/PNDISS blends. These results are consistent with the results from the XRD and PL quenching analysis.

The dependence of T_c on the composition of polymer blends was investigated in both P3HT/PNDITT and P3HT/PNDISS blends. With decreasing composition of P3HT, T_c of P3HT was tending to be increased. The change of T_c, however, was more obvious in P3HT/PNDITT blends than in P3HT/PNDISS blends which was opposite trend of the transition in melting temperature. When the composition of P3HT was decreased from 67 *wt* % to 33 *wt* %, the T_c was shifted 3.46 ˚C in P3HT/PNDISS blend and 15.27 ˚C in P3HT/PNDITT blend. More significant T_c dependence on the composition in P3HT/PNDITT blend indicates that P3HT and PNDITT have higher tendency to phase separate compared to P3HT/PNDISS blend. Therefore, from the DSC analysis, we could confirm that PNDISS has better miscibility and lower phase separation tendency in the blend with P3HT than PNDITT.

4.1.4 *Conclusions*

In conclusion, we synthesized two solution processable n-type copolymer semiconductors, PNDISS and PNDITT, based on strong electron withdrawing naphthalene diimide (NDI), as new acceptors in all-polymer solar cells. Photovoltaic properties of polymer blends in different compositions (67, 50, and 33 *wt %)* were investigated and property-performance relationship was studied. P3HT/PNDISS blends showed better performances in all compositions than P3HT/PNDITT blends, and the best performance (PCE = 3.19 %, J_{sc} = 7.46 mA/cm^2, V_{oc} = 0.68 V, and *FF* = 0.63) was achieved in P3HT/PNDISS device with optimum composition of 33 *wt* % P3HT. Based on highly affected crystallinity as well as solid state packing structure of blends with smaller mean crystalline domain size in XRD analysis, higher PL quenching rate, and clear shift of melting temperature in DSC thermal transition analysis better miscibility and lower tendency of phase separation with smaller domain sizes in P3HT/PNDISS blends were expected. Composition dependence of these blend properties were also observed, and the composition of 33 *wt* % P3HT was found to have the highest miscibility with favorable morphology for solar cells. These results show close relationships between blend properties and the performance in all-polymer solar cells, and they can provide new insight of choosing well matching donor/acceptor polymers for good performance in all-polymer solar cells by measuring the miscibility and phase separation behavior of polymer blends using XRD, PL quenching, and DSC analysis.

4.1.5 *References*

[1] a) J. J. M. Halls, C. A. Walsh, N. C. Greenham, E. A. Marseglia, R. H. Friend, S. C. Moratti, A. B. Holmes, *Nature* **1995**, *376*, 498. b) S. A. Jenekhe, S. J. Yi, *J. Appl. Phys. Lett.* **2000**, *77*, 2635. c) M. M. Alam, S. A. Jenekhe, *Chem. Mater.* **2004**, *16*, 4647. d) . W. Holcombe, C. H. Woo, D. F. J. Kavulak, B. C. Thompson, J. M. J. Fréchet, *J. Am. Chem. Soc.* **2009**, *131*, 14160. e) Y. J. Hwang, G. Q. Ren, N. M. Murari, S. A. Jenekhe, *Macromolecules* **2012**, *45*, 9056. f) C. R. McNeill, *Energy Environ. Sci.* **2012**, *5*, 5653. g) M. Schubert, et al. Adv. Energy Mater. **2012**, 2, 369. h) Z. He, C. Zhong, S. Su, M. Xu, H. Wu, Y. Cao, *Nat. Photon.* **2012**, *6*, 591. i) S. Fabiano, S. Himmelberger, M. Drees, Z. Chen, R. M. Altamimi, A. Salleo, M. A. Loi, A. Facchetti, *Adv. Energy Mater.* **2013**, DOI:10.1002/aenm.201301409. j) X. Zhan, Z. Tan, B, Domercq, Z. An, X. Zhang, S. Barlow, Y. Li, D. Zhu, B. Kippelen, S. R. Marder, *J. Am. Chem. Soc.* **2007**, *129*, 7746. k) C. R. McNeil, N. C. Greenham, *Adv. Mater.* **2009**, *21*, 3840. l) T. Earmme, Y. J. Hwang, N. M. Murari, S. Subramaniyan, S. A. Jenekhe, *J. Am. Chem. Soc.* **2013**, *135*, 14960. m) E. Zhou, J. Cong, K. Hashimoto, K. Tajima, *Adv. Mater.* **2013**, *25*, 6991.

[2] a) D. Mori, H. Benten, I. Okada, H. Ohkita, S. Ito, *Adv. Energy Mater.* **2014**, *4*, 1301006. b) P. Cheng, Y. Long, X. Zhao, J. Hou, Y. Li, X, Zhan, *Energy Environ. Sci.* **2014**, *7*, 1351. c) Y. Zhou, et at. *Adv. Mater.* **2014,** DOI:10.1002/adma.201306242.

[3] a) N. Zhou, et al. *Adv. Energy Mater.*, **2014**, *4*, 1300785. b) C. E. Small, S. Chen, J. Subbiah, C. M. Amb, S. -W. Tsang, T. -H. Lai, J. R. Reynolds, F. So, *Nat. Photon*. **2012**, *6*, 115. c) J. You, et al. *Nat. Commun*. **2013**, *4*, 1446.

[4] a) F. Liu, Y. Gu, J. W. Jung, W. H. Jo, T. P. Russell, *J. Polym. Sci. Part B Polym. Phys.* **2012**, *50*, 1018. b) R. Otero, J. M. Gallego, A. L. V. de Parga, N. Martin, R. Miranda, *Adv. Mater.* **2011**, *23*, 5148. c) M. T. Dang, L. Hirsch, G. Wantz, J. D. Wuest, *Chem. Rev*. **2013**, *113*, 3734. d) H. Hoppe, N. S. Sariciftci, *J. Mater. Chem*. **2006**, *16*, 45. e) X. Yang, J. Loos, *Macromolecules* **2007**, *40*, 1353.

[5] a) H. Yan, Z. Chen, Y. Zheng, C. Newman, J. R. Quinn, F. Dotz, M. Kastler, A. Facchetti, *Nature* **2009,** *457*, 679. b) H. Meng, Z. Bao, A. J. Lovinger, B. C. Wang, A. M. Mujsce, *J. Am. Chem. Soc.* **2001,** *123*, 9214. c) J. R. Moore, S. Albert-Seifried, A. Rao, S. Massip, B. Watts, D. J. Morgan, R. H. Friend, C. R. McNeill, H. Sirringhaus, *Adv. Energy Mater.* **2011,** *1*, 230. d) Y. -J. Hwang, G. Ren, N. M. Murari, S. A. Jenekhe, *Macromolecules* **2012,** *45*, 9056.

[6] a) M. Schubert, D. Dolfen, J. Frisch, S. Roland, R. Steyrleuthner, B. Stiller, Z. Chen, U. Scherf, N. Koch, A. Facchetti, D. Neher, *Adv. Energy Mater.* **2012,** *2*, 369. b) E. Zhou, J. Cong, M. Zhao, L. Zhang, K.Hashimoto, K. Tajima, *Chem. Comm.* **2012,** *48*, 5283. e) D. Mori, H. Benten, H. Ohkita, S. Ito, K. Miyake, *ACS Appl. Mater. Interfaces* **2012,** *4*, 3325.

[7] a) F. C. Jamieson, E. B. Domingo, T. McCarthy-Ward, M. Heeney, N. Stingelin, J. R. Durrant, *Chem. Sci*. **2012**, *3*, 485. b) B. Watts, W. J. Belcher, L. Thomsen, H. Ade, P. C. Dastoor, *Macromolecules* **2009**, *42*, 8392. c) D. Chen, A. Nakahara, D. Wei, D. Nordlund, T. P. Russell, *Nano Lett*. **2011**, *11*, 561. d) J. W. Kiel, A. P. R. Eberle, M. E. Mackay, *Phys. Rev. Lett*. **2010**, *105*, 168701. e) N. D. Treat, M. A. Brady, G. Smith, M. F. Toney, E. J. Kramer, C. J. Hawker, M. L. Chabinyc, *Adv. Energy, Mater*. **2011**, *1*, 82. f) B. A. Collins, E. Gann, L. Guignard, X. He, C.

G. McNeill, H. Ade, *J. Phy. Chem. Lett.* **2010**, *1*, 3160. g) W. -R. Wu, U. -S. Jeng, C. -J. Su, K. -H. Wei, M. -S. Su, M. -Y. Chiu, C. -Y. Chen, W. -B. Su, C. -H. Su, A.- C. Su, *ACS Nano* **2011**, *5*, 6233. h) T. Agostinelli, et al, *Adv. Funct. Mater*. **2011**, *21*, 1701.

[8] Y. -J. Hwang, N. M. Murari, S. A. Jenekhe, *Polym. Chem*. **2013**, *4*, 3087.

[9] S. Trasatti, *Pure Appl. Chem.* **1986,** *58*, 955.

[10] S. A. Jenekhe, L. Lu, M. M. Alam, *Macromolecules* **2001,** *34*, 7315.

[11] B. R. Lee, et al. Adv. Mater., 2014, 26, 494.

[12] A. L. Patterson, *Phys. Rev.* **1939,** *56*, 972.

[13] a) P.-T. Wu, G. Ren, S. A. Jenekhe, *Macromolecules* **2010,** *43*, 3306. b) G. Li, Y. Yao, H. Yang, V. Shrotriya, G. Yang, Y. Yang, *Adv. Funct. Mater.* **2007,** *17*, 1636. c) P.-T. Wu, G. Ren, C. Li, R. Mezzenga, S. A. Jenekhe, *Macromolecules* **2009,** *42* (7), 2317.

[14] a) G. Yu, A. J. Heeger, *J. Appl. Phys.* **1995,** *78*, 4510. b) H. Hoppe, M. Niggemann, C. Winder, J. Kraut, R. Hiesgen, A. Hinsch, D. Meissner, N. S. Sariciftci, *Adv. Funct. Mater.* **2004,** *14*, 1005. c) N. C. Cates, R. Gysel, Z. Beiley, C. E. Miller, M. F. Toney, M. Heeney, I. McCulloch, M. D. McGehee, *Nano Lett.* **2009,** *9*, 4153. d) C. R. McNeill, S. Westenhoff, C. Groves, R. H. Friend, N. C. Greenham, *J.Phys.Chem. C* **2007,** *111*, 19153.

[15] a) S. Zheng, J. Huang, Y. Li, Q. Guo, *J. Polym. Sci. Part B Polym. Phys.* **1997,** *35*, 1383. b) N. Stingelin, *Polym. Int.* **2012,** *61*, 866. c) F. C. Jamieson, E. B. Domingo, T. McCarthy-Ward, M. Heeney, N. Stingelin, J. R. Durrant, *Chem. Sci.* **2012,** *3*, 485. d) P. Wolfer, P. E. Schwenn, A. K. Pandey, Y. Fang, N. Stingelin, P. L. Burn, P. Meredith, *J. Mater. Chem. A* **2013,** *1*, 5989.

4.2 SIDE CHAIN ENGINEERING OF N-TYPE CONJUGATED COPOLYMER ENHANCES PHOTOCURRENT AND EFFICIENCY OF ALL-POLYMER SOLAR CELLS.

4.2.1 *Introduction*

The use of electron-conducting (*n*-type) polymer semiconductors as the electron acceptor in polymer solar cells[1,2] offers many potential advantages over fullerene acceptors.[3] The facile tunability of various intrinsic properties of such *n*-type conjugated polymers, including optical absorption, electronic structure, crystallinity, solubility, and charge transport, exemplifies their attractive features. The greater thermal stability and mechanical strength of *n*-type conjugated polymers can ensure more morphologically and environmentally rugged all-polymer solar cells. Compared to the negligible visible and near infrared light harvesting by fullerene acceptors, *n*-type conjugated polymers can contribute to light absorption in the solar cell as much as the donor polymer; an important fundamental consequence of this is that *photoinduced hole transfer* becomes an important pathway for charge photogeneration as is *photoinduced electron transfer*.[4] Unfortunately, the performance of all-polymer solar cells reported to date, is still far behind that of polymer/fullerene systems, with very few papers reporting a power conversion efficiency (PCE) over 3 %.[2] A major limitation of the performance of reported all-polymer solar cells is the low photocurrent of the devices, and thus developing new *n*-type or *p*-type polymers that can enhance the photocurrent while maintaining the other photovoltaic properties is highly desirable.

Many reports have showed that alkyl, alkoxy, or other side chains on *p*-type conjugated polymers can have a large impact on the carrier mobility in thin film transistors[5] and on the performance of polymer/fullerene solar cells.[6] These effects of side chains can be due to size, density, topology (linear vs branched), and in the case of multiple different side chains composition, and distribution (e.g. uniform, random, etc). Although the mechanisms of how the side chains influence charge transport and photovoltaic properties of polymer/fullerene blend systems vary, they all relate to the polymer/fullerene blend film morphology:[6,7] molecular packing of the polymer backbone which can be a “face-on” or “edge-on” orientation relative to the plane of the substrate; crystallinity of both polymer and fullerene; improved compatibility with the fullerene component and overall nanoscale morphology; and enabling or preventing intercalation of fullerene molecules into the polymer side chains. These ideas of side chain engineering of *p*-type conjugated polymers are yet to be similarly explored in *n*-type polymer semiconductors towards improving the performance of all-polymer solar cells.

In this section, I discuss all-polymer bulk heterojunction (BHJ) solar cells with record 4.4 % PCE and 10.4 mAcm^{-2} short circuit current density achieved by means of side chain engineering of the *n*-type polymer semiconductor component. The series of new *n*-type conjugated polymers, PNDIS-*x*BO (*x*=10, 30, 50), are all composed of identical naphthalene diimide (NDI)-selenophene alternating copolymer backbone but have different composition and distribution of the alkyl side chains 2-decyltetradecyl (DT) and 2-butyloctyl (BO) as shown in **Figure 28a**. X-ray diffraction analysis of PNDIS-*x*BO films shows that the crystallinity is increased and π-π stacking distance is decreased with increasing amount *x* of the shorter BO side chains. The photovoltaic and charge transport properties of blends composed of PNDIS-*x*BO as acceptor and a thiazolothiazole-dithienosilole copolymer (PSEHTT)[6d, 8] as donor were investigated by inverted BHJ solar cells and by space charge limited current (SCLC) measurements, respectively. We found that the photocurrent, PCE, and carrier mobilities of the all-polymer solar cells progressively increased with the side chain composition variable *x* up to the 30 mol % BO optimum.

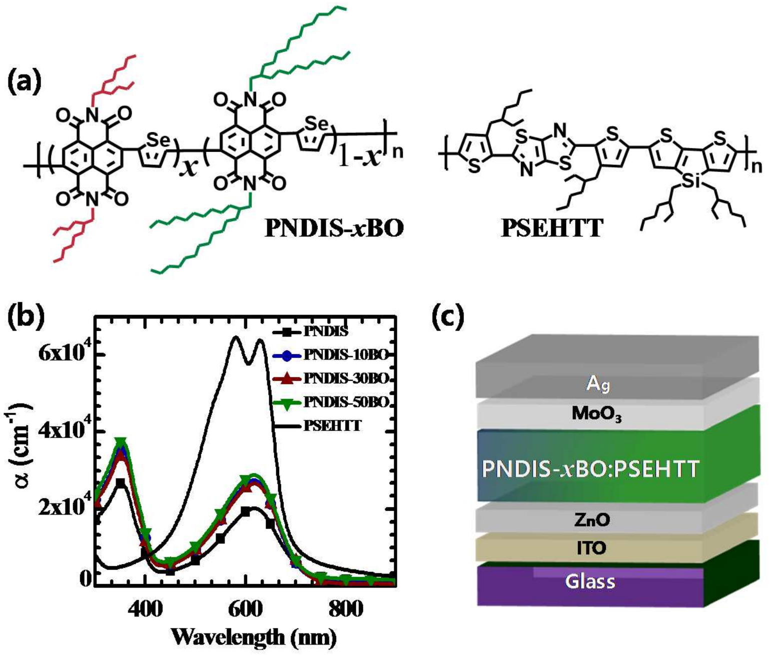

Figure 28. (a) Molecular structures of the n-type polymers, PNDIS-xBO (x=0, 10, 30, 50), and the donor polymer PSEHTT. (b) Absorption spectra of the n-type polymers. (c) The inverted device structure, ITO/ZnO/polymer blend/MoO_3/Ag, used to measure photovoltaic properties.

4.2.2 *Experimental Section*

Materials. 4,9-Dibromo-2,7-bis(2-decyltetradecyl)benzo[lmn][3,8]phenanthroline-1,3,6,8-tetraone was purchased from Suna Tech and all other chemicals were purchased from Sigma-Aldrich and TCI America. 4,9-Dibromo-2,7-bis(2-butyloctyl)benzo[lmn][3,8]phenanthroline-1,3,6,8-tetraone and 2,5-bis(trimethylstannyl)selenophene were synthesized according to the known literature procedures.

2,5-Dibromoselenophene. Selenophene (5 g, 0.038 mol) was added into a 250 mL round-bottom flask and purged with argon before adding 100 mL of chloroform. Afterward, NBS (13.575 g, 0.076 mol) was added portionwise. After stirring the mixture overnight at room temperature in the dark, the reaction was quenched by adding water. The crude product was extracted with chloroform, and purified by column chromatography with 100 % hexane. Slightly yellow oil was obtained and used in next step without further purification. *2,5-Dibromoselenophene* (7.5 g, 68.3 %), ^{1}H NMR (300 MHz, $CDCl_3$): δ (ppm) 7.02 (2H).

2,5-Bis(trimethylstannyl)selenophene. 2,5-Dibromoselenophene (2 g, 6.92 mmol) was added into a 250 mL round-bottom flask. Under argon atmosphere, 50 mL THF was then added. The mixture was cooled to -78 °C in a dry ice bath and 2.5 M butyllithium solution in hexane (6.1 mL, 15.23 mmol) was added dropwise. After stirring the mixture for an hour at -78 °C, 1 M trimethyltinchloride solution in THF (15.9 mL, 15.9 mmol) was added in one portion at -78 °C. Dry ice bath was removed after 5 min and the mixture was warmed up to room temperature. After stirring overnight at room temperature, the reaction mixture was poured into water and extracted with diethyl ether 2 times. The organic phase was dried with anhydrous sodium sulfate and the solvent was evaporated by vacuum rotary evaporator. After recrystallization in MeOH, yellow crystals were obtained and subsequently used in polymerization. *2,5-Bis(trimethylstannyl)selenophene* (500 mg, 15.8 %), ^{1}H NMR (300 MHz, $CDCl_3$): δ (ppm) 7.72 (2H), 0.3 - 0.48 (18H); m.p. 118 °C.

Poly{[N,N'-bis(2-decyltetradecyl)-naphthalene-1,4,5,8-bis(dicarboximide)-2,6-diyl]-alt-5,5'-selenophene)} (PNDIS). 4,9-Dibromo-2,7-bis(2-decyltetradecyl)benzo[lmn][3,8]phenanthroline-1,3,6,8-tetraone (500 mg, 0.456 mmol), 2,5-bis(trimethylstannyl)selenophene (208.1 mg, 0.456 mmol), $Pd_2(dba)_3$ (8.34 mg, 0.0091 mmol) and $P(o\text{-tolyl})_3$ (11.1 mg, 0.0365 mmol) were added into a 100 mL three-neck round-bottom flask. The flask equipped with a condenser was then degassed and filled with argon three times. Afterwards, 21 mL of chlorobenzene was added and degassed and filled with argon three times. The reaction mixture was refluxed for 72 h under argon. After cooling down to room temperature, the polymerization mixture was poured and stirred into 200 mL methanol and 5 mL hydrochloric acid solution for 3 h. The polymer precipitated out as a dark reddish purple solid and was filtered using a filter paper. The polymer was purified by Soxhlet extraction with methanol, hexane, and acetone. GPC: M_w = 44.4 kDa, M_n = 36.8 kDa, PDI = 1.2; TGA: T_d = 414 °C.

Poly{([N,N'-bis(2-decyltetradecyl)-naphthalene-1,4,5,8-bis(dicarboximide)-2,6-diyl]-alt-5,5'-selenophene)-ran-([N,N'-bis(2-butyloctyl)-naphthalene-1,4,5,8-bis(dicarboximide)-2,6-diyl]-alt-5,5'-selenophene))} (PNDIS-10BO, PNDIS-30BO, and PNDIS-50BO). Three monomers, 4,9-dibromo-2,7-bis(2-decyltetradecyl)benzo[lmn][3,8]phenanthroline-1,3,6,8-tetraone, 4,9-dibromo-2,7-bis(2-butyloctyl)benzo[lmn][3,8]phenanthroline-1,3,6,8-tetraone, and 2,5-bis(trimethylstannyl)selenophene, with $Pd_2(dba)_3$ (2 mol%) and $P(o\text{-tolyl})_3$ (8 mol%) were added into a 100 mL three-neck round-bottom flask. The flask equipped with a condenser was then degassed and filled with argon three times. Afterwards, chlorobenzene was added and degassed one time. The reaction mixture was refluxed for 72 h under argon, and cooled down to room temperature. The polymerization mixture was poured into 200 mL methanol and 5 mL hydrochloric acid solution and stirred for 3 h. The polymer precipitated out as a solid and was filtered using a filter paper. The polymer was purified by Soxhlet extraction with methanol, hexane, and acetone sequentially. *PNDIS-10BO,* GPC: M_w = 50.5 kDa, M_n = 44.8 kDa, PDI = 1.1; TGA: T_d = 384 °C; PNDIS-*30BO,* GPC: M_w = 61.8 kDa, M_n = 48.9 kDa, PDI = 1.3; TGA: T_d = 394 °C; *PNDIS-50BO,* GPC: M_w = 72.2 kDa, M_n = 41.7 kDa, PDI = 1.7; TGA: T_d = 403 °C.

Device fabrication and characterization. The solar cells were fabricated with the inverted device structure of ITO/ZnO/active layer/MoO_3/Ag. ITO substrates were sequentially cleaned with acetone and isopropylalchol in ultrasonic bath, and then dried in a vacuum oven overnight. ITO substrates were treated with oxygen plasma before spin coating the solution of zinc acetate (1 g) in 2-methoxyethanol (10 mL) with ethanolamine (0.28 g) at 5000 rpm for 40 sec. After annealed the film for gelation at 250 °C for an hour in air, the active layer was then spin-coated from the polymer mixture solution (15 mg/mL) to make a thin film of 60 - 80 nm thickness and thermally annealed at 175 °C for 10 min in a glovebox. The substrates were then loaded in a thermal evaporator (BOC Edwards, 306) to deposit thin layer of 7.5 nm MoO_3 and 100 nm Ag under high vacuum (2×10^{-6} Torr). The current density–voltage ($J - V$) curves of solar cells were measured using a HP4155A semiconductor parameter analyzer in air. An AM1.5 illumination at 100 $mWcm^{-2}$ was provided by a filtered Xe lamp and calibrated by using an NREL-calibrated Si diode. The external quantum efficiency (EQE) was measured using a QEX10 solar cell quantum efficiency measurement system (PV Measurements, Inc.). For polar solvent treatment of ZnO layer, 1 vol % of ethanolamine in 2-methoxyethanol solution was coated (5000 rpm for 40 seconds) on ZnO film and dried at 110 °C for 10 minutes in air.

4.2.3 *Results and Discussion*

The *n*-type conjugated random copolymers, poly{([N,N'-bis(2-decyltetradecyl)-naphthalene-1,4,5,8-bis(dicarboximide)-2,6-diyl]-alt-5,5'-selenophene)-ran-([N,N'-bis(2-butyloctyl)-naphthalene-1,4,5,8-bis(dicarboximide)-2,6-diyl]-alt-5,5'-selenophene))} which are denoted as PNIDS-*x*BO, were synthesized by Stille coupling polymerization of three monomers: 2,5-bis(trimethylstannyl)selenophene, 9-dibromo-2,7-bis(2-decyltetradecyl)benzo[lmn][3,8] phenanthroline-1,3,6,8-tetraone (NDI-DT), and 4,9-dibromo-2,7-bis(2-butyloctyl)benzo[lmn][3,8]phenanthroline-1,3,6,8-tetraone (NDI-BO). PNDIS-*x*BO, where *x* is the molar percentage of NDI-BO monomer, of 3 different compositions (10, 30, and 50 mol %) were synthesized to control the alkyl side chain composition: PNDIS-10BO; PNDIS-30BO; and PNDIS-50BO. Since the yield of the polymerizations is over 95 %, we expect that the actual alkyl side chain composition of polymers is close to the feed composition. The reference

Table 14. Molecular Weight of *n*-Type Polymers and Donor Polymer Investigated.

Polymer	M_n [kDa]	M_w [kDa]	PDI
PSEHTT	34.3	128.1	3.7
PNDIS	36.8	44.4	1.2
PNDIS-10BO	44.8	50.5	1.1
PNDIS-30BO	48.8	61.8	1.3
PNDIS-50BO	41.7	72.2	1.7

naphthalene diimide (NDI)-selenophene alternating copolymer, which has a uniform 2-decyltetradecyl (DT) side chain composition, PNDIS, was also synthesized for the purpose of comparison. The other reference NDI-selenophene alternating copolymer with uniform BO side chain composition, PNDIS-BO, was also synthesized; However, this polymer was largely insoluble and thus not further studied. The molecular structures of the monomers and copolymers were confirmed by ^{1}H NMR.[2a] PNDIS, PNDIS-10BO, PNDIS-30BO showed excellent solubility (> 40 mg/mL) in common organic solvents (chloroform, chlorobenzene) at room temperature whereas PNDIS-50BO (~10 mg/mL) showed very limited solubility. The molecular weight and polydispersity index (PDI) of the polymers were measured by gel permeation chromatography (GPC) against polystyrene standards in chlorobenzene at 60 °C. The M_n of PNDIS-*x*BOs slightly varied in the range of 41.7 – 48.8 kDa with a PDI of 1.1 – 1.7 (**Table 14**). The reference PNDIS sample had a M_n of 36.8 kDa with a PDI of 1.2. All the polymers showed good thermal stability with an onset decomposition temperature (T_d) of 384 – 403 °C under nitrogen flow.

The solid state morphology of PNDIS-*x*BO and PNDIS was analyzed by using X-ray diffraction (XRD) of their drop-casted films. An intense lamellar crystalline (100) peak (2θ at 3.67 – 3.99 ˚) and a π-π stacking peak (2θ at 21.52 – 22.64 ˚) were observed in all the polymer films. The lamellar *d*-spacing for PNDIS, PNDIS-10BO, PNDIS-30BO, and PNDIS-50BO was

22.14, 23.46, 23.79, and 24.03 Å, respectively, and the π-π stacking distance was 4.12, 4.05, 3.99, 3.92 Å, respectively. This means that the lamellar *d*-spacing increased while the π-π stacking distance decreased as the fraction of BO side chains in the random copolymer increased. We understand this trend as a consequence of reduced steric hindrance between DT alkyl side chains, and thus increased planarity of the polymer backbone. The mean size of the crystalline domains (L) of the polymers was calculated from the lamellar peaks using the Scherrer equation,[7c, 9] $L=K\lambda/\beta\cos\theta$, where K is shape factor (0.9), λ is x-ray wavelength (1.54 Å), and β is the full width at half maximum (FWHM) in radian. The mean crystalline domain size L was found to be 8.4, 8.5, 8.8, and 13.3 nm for PNDIS, PNDIS-10BO, PNDIS-30BO, and PNDIS-50BO, respectively. This result shows that crystallinity is progressively increased by lowering the density of the longer DT side chains while increasing the amount of the shorter BO side chains in the random copolymers.

The electronic structures (LUMO/HOMO levels) and optical absorption of PNDIS-*x*BO and PNDIS were estimated from cyclic voltammetry (CV) and UV-visible spectra of thin films. The LUMO energy level of all the polymers was calculated from the onset reduction potential in their CVs and found to be – 3.9 eV, as expected from their common conjugated backbone. The optical absorption spectra of PNDIS-*x*BO and PNDIS thin films (**Figure 28b**) and in dilute chloroform solutions have the same peak positions with two distinctive absorption bands at 300 – 400 nm and 500 – 750 nm which are due to π-π* transition and intramolecular charge transfer,[10] respectively. Interestingly, PNDIS-*x*BO films have a higher absorption coefficient (α) of (2.7 – 2.9) × 10^4 cm^{-1} at their ICT band absorption maxima in the visible compared to PNDIS which has an α value of 2 × 10^4 cm^{-1}. The observed higher absorption coefficient of the random copolymers PNDIS-*x*BO can be understood from their increased crystallinity.

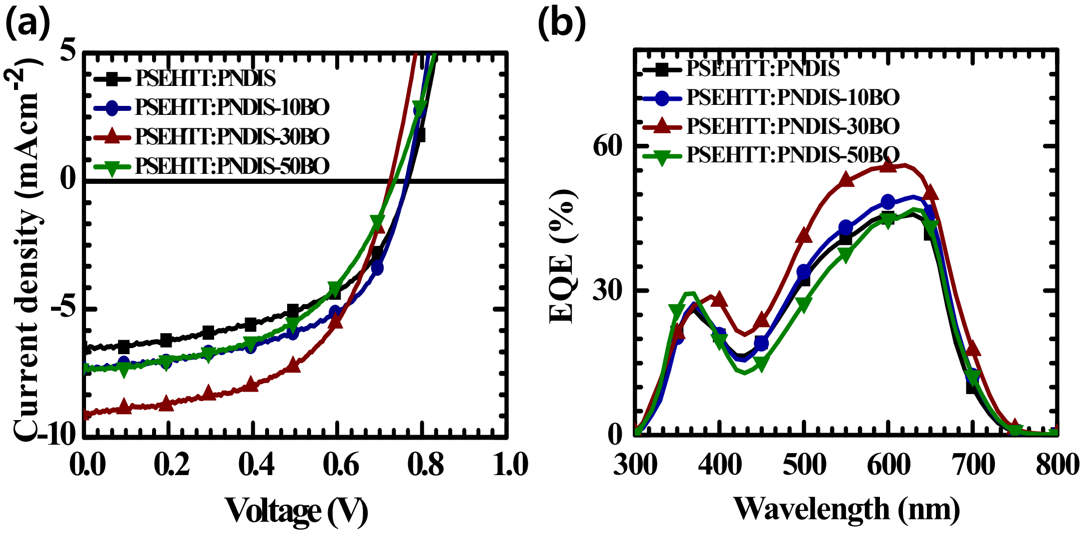

Figure 29. *J* – *V* curves (a) and EQE spectra (b) of all-polymer solar cells.

We investigated the photovoltaic properties of all-polymer BHJ solar cells made from PSEHTT:PNDIS-*x*BO and PSEHTT:PNDIS blends by using the inverted device structure: ITO/ZnO/active layer/MoO_3/Ag (**Figure 28c**), where the active layer is a PSEHTT:PNDIS-*x*BO or PSEHTT:PNDIS blend film with an optimum composition of 1:1.5 *wt/wt* spin coated from a chlorobenzene solution. The solar cells were fabricated in a glovebox and tested under AM 1.5 solar illumination at 100 mWcm^{-2} in ambient air. The current density – voltage (J – V) curves of the BHJ solar cells composed of the side chain engineered *n*-type polymers (PNDIS-*x*BO) compared to the reference PNDIS are shown in **Figure 29a** and the photovoltaic parameters are summarized in **Table 15**.

Table 15. Photovoltaic Properties of PNDIS-*x*BO Blends with PSEHTT.

active layer	J_{sc}b) [mAcm^{-2}]	V_{oc} b) [V]	FF	PCE b) [%]	EQE$_{max}$ [%]
PSEHTT:PNDIS	6.55 (6.39 ± 0.14)	0.76 (0.76 ± 0.00)	0.52	2.62 (2.57± 0.08)	45.8
PSEHTT:PNDIS-10BO	7.38 (7.26 ± 0.10)	0.76 (0.76 ± 0.00)	0.55	3.10 (2.97 ± 0.12)	49.5
PSEHTT:PNDIS-30BO	9.13 (9.10 ± 0.03)	0.74 (0.74 ± 0.00)	0.55	3.61 (3.55 ± 0.06)	56.0
PSEHTT:PNDIS-50BO	7.21 (7.11 ± 0.11)	0.74 (0.74 ± 0.00)	0.51	2.75 (2.66± 0.08)	46.9
PSEHTT:PNDIS-30BO$^{a)}$	10.37 (10.30 ± 0.06)	0.77 (0.77 ± 0.00)	0.56	4.44 (4.35± 0.09)	57.3

a) ZnO surface modified by spin coating of 1 vol % ethanolamine in 2-methoxyethanol. b) The photovoltaic properties were averaged over 10 devices.

The reference PNDIS solar cells had a performance (J_{sc} = 6.55 mAcm^{-2}, V_{oc} = 0.76 V, FF = 0.52, and maximum PCE of 2.62 %) that is comparable to our previous report.[2a] Compared to PNDIS devices, PNDIS-10BO solar cells have enhanced performance with slightly increased photocurrent (7.38 mAcm^{-2}) and fill factor (0.55) while the V_{oc} was unchanged. A significantly enhanced photocurrent of 9.13 mAcm^{-2} was observed in PNDIS-30BO devices, leading to a maximum PCE of 3.61 %. However, the performance of PNDIS-50BO devices (J_{sc} = 7.21 mAcm^{-2}, V_{oc} = 0.74 V, FF = 0.51, PCE = 2.75 %) did not show enhancement relative to PNDIS solar cells. The observed enhancement in photocurrent and overall performance of PNDIS-10BO and PNDIS-30BO devices compared to PNDIS cells is consistent with the reduced π-stacking distance in the acceptor polymers (PNDIS-*x*BO); we show later that reduction in π-stacking distance translates to increased electron mobility.[11] The absence of enhanced performance of PNDIS-50BO devices compared to either PNDIS or PNDIS-*x*BO (*x* = 10, 30) devices is likely a result of the poorer quality of its films, which originates from its poor solubility.

The external quantum efficiency (EQE) spectra shown in **Figure 29b** correspond to the all-polymer BHJ solar cells whose *J* – *V* curves are in **Figure 29a**. The EQE spectra of these devices show that the photoresponse begins at ~750 nm and covers the entire visible region, which demonstrates that the *n*-type polymers contribute to the light harvesting since the donor polymer PSEHTT does not absorb past 700 nm.[6d, 8] For all the devices, a maximum EQE of over 45 % was observed and in the case of PNDIS-30BO cells the EQE peaked at 56 %. The photocurrent values calculated from the EQE spectra were found to be consistent with the J_{sc} values from $J - V$ curves for all the devices, showing a mismatch between the two values of within 13 %.

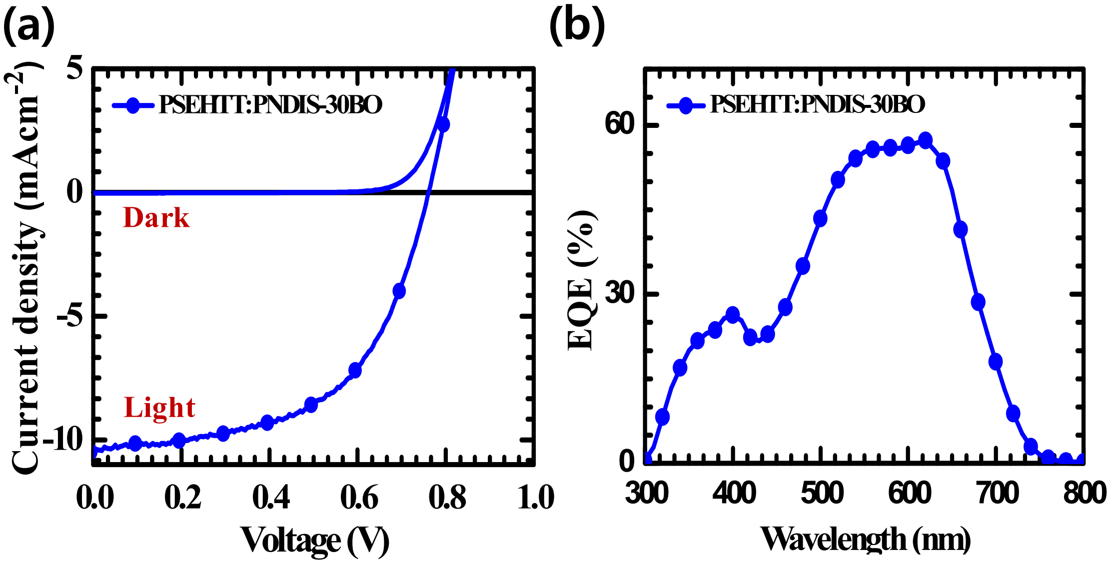

Figure 30. $J - V$ curve (a) and EQE spectrum (b) of PSEHTT:PNDIS-30BO solar cell with surface-treated ZnO layer.

PNDIS-30BO devices were further optimized by surface modification of the electron-collecting ZnO electrode. It was recently reported that treatment of ZnO surface with 1 vol % ethanolamine in methoxyethanol reduced the work function of ZnO from 4.4 to 3.9 eV, resulting in improved performance of polymer/fullerene solar cells.[12] The $J - V$ curves and EQE spectrum of PSEHTT:PNDIS-30BO solar cells with similarly modified ZnO electrodes are shown in **Figure 30** and also summarized in **Table 15**. The performance of these all-polymer solar cells is significantly improved with a PCE of 4.44%, photocurrent of 10.37 mAcm^{-2}, and V_{oc} of 0.77 V. We note that the observed PCE and short-circuit current density for these PSEHTT:PNDIS-30BO devices are the highest reported to date for all-polymer solar cells.

Table 16. Charge Transport Properties of PNDIS-*x*BO Blends with PSEHTT.

active layer	μ_e **[cm^{2}V^{-1}s^{-1}]**	μ_h **[cm^2/Vs]**
PSEHTT:PNDIS	2.6×10^{-5}	9.6×10^{-5}
PSEHTT:PNDIS-10BO	5×10^{-5}	1.1×10^{-4}
PSEHTT:PNDIS-30BO	6.5×10^{-5}	2.1×10^{-4}
PSEHTT:PNDIS-50BO	2.5×10^{-5}	5.7×10^{-5}

The bulk charge transport properties of the all-polymer solar cells were investigated by space-charge-limited current (SCLC) measurements to explore the relationship of bulk transport to the photovoltaic properties. Electron mobility was measured in an ITO/ZnO/active layer/LiF/Al device structure whereas hole mobility was measured in an ITO/PEDOT:PSS/active layer/Au device structure. SCLC fittings to the current-voltage characteristics of the electron-only devices and hole-only devices produced carrier mobilities which are summarized in **Table 16**. Compared to the reference PSEHTT:PNDIS blend system, bulk electron and hole mobilities increased by factors of 2.2 – 2.5 to 6.5×10^{-5} and 2.1×10^{-4} cm^{2}V^{-1}s^{-1}, respectively, in the PSEHTT:PNDIS-30BO blend system. The SCLC carrier mobilities in the PNDIS-50BO blends were comparable or less than observed in the PNDIS devices. These bulk charge transport properties of the active layer blends are consistent with the observed photovoltaic properties of the all-polymer solar cells as well as with the decreased π-stacking distance and increased crystallinity with increasing amount of BO side chains discussed earlier.

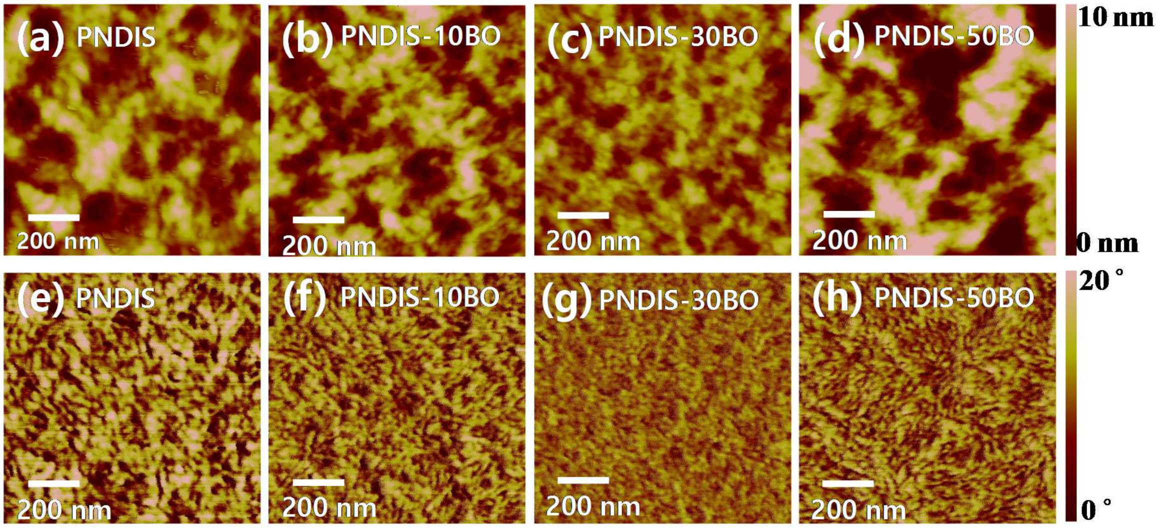

Figure 31. AFM height and corresponding phase images (1 μm×1 μm) of the surfaces of BHJ solar cells: (a, e) PSEHTT:PNDIS; (b, f) PSEHTT:PNDIS-10BO; (c, g) PSEHTT:PNDIS-30BO; and (d, h) PSEHTT:PNDIS-50BO.

AFM imaging of the actual BHJ devices provided information on the surface morphology of the active layer blend in the all-polymer solar cells. AFM height and phase images with a scan area of 1 μm × 1μm are shown in **Figure 31**. PNDIS and PNDIS-10BO blend films showed identical surface morphology with similar domain sizes and roughness (2 nm). However, PNDIS-30BO blend film surface showed significantly reduced domain sizes, better interconnectivity, and small roughness of 1.2 nm, which can all be beneficial for efficient charge photogeneration and transport in solar cells due to limited exciton diffusion length.[1f] This favorable morphology of PNDIS-30BO blend film can partly account for the observed optimum photovoltaic performance of the devices. The highest roughness of 3.4 nm with higher domain size compared to PNDIS-30BO is observed in PNDIS-50BO blend films and this morphology could partly explain the poor performance of PNDIS-50BO blend solar cells.

4.2.4 *Conclusions*

In summary, I have demonstrated a side chain engineering strategy for the facile tuning of the composition and distribution of alkyl side chains on n-type conjugated polymers as a means of improving the photocurrent and performance of all-polymer solar cells. BHJ all-polymer solar cells with record 4.4 % PCE and 10.4 $mAcm^{-2}$ photocurrent were achieved by using a resulting new acceptor polymer, PNDIS-30BO, composed of NDI-selenophene backbone and optimum 2-butyloctyl/2-decyltetradecyl composition. Observed large enhancement in photocurrent and efficiency of PNDIS-30BO solar cells compared to the reference PNDIS devices was explained by the decrease π-stacking distance, increased crystallinity and bulk electron mobility of PNDIS-30BO in conjunction with the optimum polymer/polymer blend morphology.

4.2.5 *References*

[1] a) J. J. M. Halls, C. A. Walsh, N. C. Greenham, E. A. Marseglia, R. H. Friend, S. C. Moratti, A. B. Holmes, *Nature* **1995**, *376*, 498. b) S. A. Jenekhe, S. J. Yi, *J. Appl. Phys. Lett*. **2000**, *77*, 2635. c) M. M. Alam, S. A. Jenekhe, *Chem. Mater*. **2004**, *16*, 4647. d) T. W. Holcombe, C. H. Woo, D. F. J. Kavulak, B. C. Thompson, J. M. J. Fréchet, *J. Am. Chem. Soc*. **2009**, *131*, 14160. e) Y. J. Hwang, G. Q. Ren, N. M. Murari, S. A. Jenekhe, *Macromolecules* **2012**, *45*, 9056. f) C. R. McNeill, *Energy Environ. Sci*. **2012**, *5*, 5653. g) M. Schubert, et al. Adv. Energy Mater. **2012**, 2, 369. h) Z. He, C. Zhong, S. Su, M. Xu, H. Wu, Y. Cao, *Nat. Photon*. **2012**, *6*, 591. i) S. Fabiano, S. Himmelberger, M. Drees, Z. Chen, R. M. Altamimi, A. Salleo, M. A. Loi, A. Facchetti, *Adv. Energy Mater*. **2013**, DOI:10.1002/aenm.201301409. j) X. Zhan, Z. Tan, B, Domercq, Z. An, X. Zhang, S. Barlow, Y. Li, D. Zhu, B. Kippelen, S. R. Marder, *J. Am. Chem. Soc*. **2007**, *129*, 7746. k) C. R. McNeil, N. C. Greenham, *Adv. Mater.* **2009**, *21*, 3840.

[2] a) T. Earmme, Y. J. Hwang, N. M. Murari, S. Subramaniyan, S. A. Jenekhe, *J. Am. Chem. Soc.* **2013**, *135*, 14960. b) E. Zhou, J. Cong, K. Hashimoto, K. Tajima, *Adv. Mater*. **2013**, *25*, 6991. c) D. Mori, H. Benten, I. Okada, H. Ohkita, S. Ito, *Adv. Energy Mater*. **2014**, *4*, 1301006. d) P. Cheng, Y. Long, X. Zhao, J. Hou, Y. Li, X, Zhan, *Energy Environ. Sci.* **2014**, *7*, 1351. e) Y. Zhou, et at. *Adv. Mater*. **2014,** DOI:10.1002/adma.201306242.

[3] a) N. Zhou, et al. *Adv. Energy Mater*., **2014**, *4*, 1300785. b) C. E. Small, S. Chen, J. Subbiah, C. M. Amb, S. -W. Tsang, T. -H. Lai, J. R. Reynolds, F. So, *Nat. Photon*. **2012**, *6*, 115. c) J. You, et al. *Nat. Commun*. **2013**, *4*, 1446.

[4] G. Ren, C. W. Schlenker, E. Ahmed, S. Subramaniyan, S. Olthof, A. Kahn, D. S. Ginger, S. A. Jenekhe, *Adv. Funct. Mater*. **2013**, *10*, 1238.

[5] a) J. Mei, Z. Bao, *Chem. Mater*. **2013**, *26*, 604. b) T. Lei, J. -Y. Wang, J. Pei, *Chem. Mater.* **2013**, *26*, 594. c) S. A. Jenekhe, *Nature Mater*. **2008**, *7*, 354. d) A. Babel, S. A. Jenekhe, *Synth. Met*. **2005**, *148*, 169. d) I. Kang, H. -J. Yun, D. S. Chung, S. -K. Kwon, Y. -H. Kim, *J. Am. Chem. Soc*. **2013**, *135*, 14896.

[6] a) J. M. Szarko, et al. *Adv. Mater*. **2010**, *22*, 5468. b) C. Piliego, T. W. Holcombe, J. D. Douglas, C. H. Woo, P. M. Beaujuge, J. M. J. Fréchet, *J. Am. Chem. Soc*. **2010**, *132*, 7595. c) X. G. Guo, H. Xin, F. S. Kim, F. S. A. D. T. Liyanage, S. A. Jenekhe, M. D. Watson, *Macromolecules* **2011**, *44*, 269. d) S. Subramaniyan, H. Xin, F. S. Kim, S. Shoaee, J. R. Durrant, S. A. Jenekhe, *Adv. Energy Mater*. **2011**, *1*, 854. e) W. -H. Chang, J. Gao, L. Dou, C. -C. Chen, Y. Liu, Y. Yang, *Adv. Energy Mater*. **2013**, DOI:10.1002/aenm/201300864. f) L. Fang, Y. Zhou, Y. -X. Yao, Y. Ding, W. -Y. Lee, A. L. Appleton, R. Allen, J. Reinspach, S. C. B. Mannsfeld, Z. Bao, *Chem. Mater*. **2013**, *25*, 4874. g) J. Lee, M. Kim, B. Kang, S. B. Jo, H. G. Kim, J. Shin, K. Cho, *Adv. Energy Mater*. **2014**, 1400087.

[7] a) I. Meager, et al. *J. Am. Chem. Soc*. **2013**, *135*, 11537. b) E. Wang, M. Wang, L. Wang, C. Duan, J. Zhang, W. Cai, C. He, H. Wu, Y. Cao, *Macromolecules* **2009**, *42*, 4410. c) P. -T. Wu, G. Ren, S. A. Jenekhe, *Macromolecules* **2010**, *43*, 3306.

[8] H. Xin, S. Subramaniyan, T. -W. Kwon, S. Shoaee, J. R. Durrant, S. A. Jenekhe, *Chem. Mater.* **2012**, *24*, 1995.

[9] A. L. Patterson, *Phys. Rev*. **1939**, *56*, 972.

[10] S. A. Jenekhe, L. Lu, M. M. Alam, *Macromolecules* **2001**, *34*, 7315.

[11] a) Y. -J. Hwang, N. M. Murari, S. A. Jenekhe, *Polym. Chem*. **2013**, *4*, 3187. b) R. Steyrleuthner, R. D. Pietro, B. A. Collins, F. Polzer, S. Himmelberger, M. Schubert, Z. Chem, S. Zhang, A. Salleo, H. Ade, A. Facchetti, D. Neher, *J. Am. Chem. Soc*. **2014**, *136*, 4245.

[12] B. R. Lee, et al. *Adv. Mater*., **2014**, *26*, 494.

4.3 N-TYPE SEMICONDUCTING NAPHTHALENE DIIMIDE-PERYLENE DIIMIDE COPOLYMERS: CONTROLLING CRYSTALLINITY, BLEND MORPHOLOGY, AND COMPATABILITY TOWARD HIGH PERFORMANCE ALL-POLYMER SOLAR CELLS.

4.3.1 *Introduction*

All-polymer solar cells,[1] composed of an electron-donating polymer and an electron-accepting polymer components, are of growing interest because of their potential advantages over the more widely studied donor polymer/fullerene acceptor systems.[1, 2] Although significant progress has been made in investigating and developing all-polymer solar cells, their performance in terms of the power conversion efficiency (PCE) of single-junction devices remains limited to about 5 %[3-6] while that of polymer/fullerene systems is over 9 %.[7] One of the major challenges to further progress in developing highly efficient all-polymer solar cells is that besides having a suitable offset in the frontier molecular orbital (HOMO/LUMO) energy levels of the polymer/polymer donor/acceptor pair, the other key factors that govern *compatibility* and blend morphology of the blend pair towards achieving efficient bulk heterojunction (BHJ) solar cells are not known or clear.[3-6, 8] The longstanding useage of the term *compatibility* of a blend or *compatible blend* adapted here does not imply a specific scale of miscibility or microstructure in the blend but rather denotes a blend with enhanced or useful new properties compared to the components.[9] Furthermore, unlike universally applicable fullerene derivatives such as phenyl-C_{71}-butyric acid methyl ester ($PC_{71}BM$) and phenyl-C_{61}-butyric acid methyl ester ($PC_{61}BM$), current electron acceptor polymers are rarely compatible with multiple donor polymers in BHJ solar cells.[3-6] An important exemption to the universal compatibility of fullerene acceptors with multiple donor polymers (i.e. gives rise to high photovoltaic efficiency) is the indene-C_{60}-

bisadduct, 1′,1″,4′,4″-tetrahydro-di[1,4]methanonaphthaleno[1,2:2′,3′,56,60:2″,3″][5,6]fullerene-C_{60} (ICBA). ICBA is an amorphous material which is found to be only compatible with a very few semicrystalline polymers, notably poly(3-hexylthiophene) (P3HT)[10] and poly[(4,4′-bis(2-ethylhexyl)dithieno[3,2-b:2′,3′-d]silole)-2,6-diyl-alt-(2,5-bis(3-(2-ethylhexyl)thiophen-2-yl)thiazolo[5,4-d]thiazole)] (PSEHTT).[11] Studies of amorphous ICBA and crystalline fullerene acceptors ($PC_{61}BM$ and $PC_{71}BM$) with various donor polymers have led to the hypothesis that material crystallinity control polymer/fullerene compatibility and blend microstructure and thus charge photogeneration efficiency and transport in such BHJ devices.[12] There are as yet no analogous or other studies of the role of crystallinity of the acceptor (or donor) polymer component on the compatibility, blend morphology, and performance of polymer/polymer BHJ solar cells.

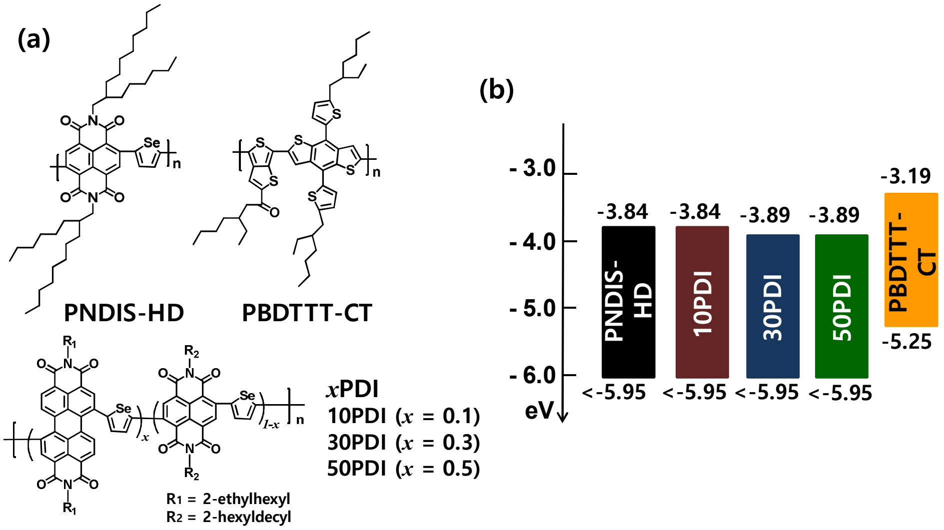

Chart 4. Molecular structure (a) and electronic structure (b) of PNDIS-HD, *x*PDI and PDBTTT-CT.

In this section, I show that an incompatible polymer/polymer blend system with poor photovoltaic efficiency can be rendered compatible with over four-fold enhancement in power conversion efficiency by controlling the bulk crystallinity of the acceptor polymer while holding the donor polymer constant. Our initial studies of the reference all-polymer blend system, composed of a known crystalline electron-accepting NDI-selenophene copolymer PNDIS-HD[6] and a known crystalline benzodithiophene-thieno[3,4-b]thiophene copolymer (PBDTTT-CT)[13] donor (**Chart 4**) showed that the extensively optimized PNDIS-HD:PBDTTT-CT blend solar cells had PCEs of only 1.2 – 1.4 % and thus it constitutes an incompatible blend despite the very favorable HOMO/LUMO energy offset of the pair (**Chart 4**). To test the hypothesis that polymer crystallinity is a critical factor that controls the compatibility, blend morphology, and performance of polymer/polymer blend solar cells, we designed a series of new *n*-type semiconducting NDI-selenophene/PDI-selenophene random copolymers (**Chart 4**), *x*PDI (10PDI, 30PDI, 50PDI), in which the bulk crystallinity (e.g. mean crystalline domain size L_c determined by X-ray diffraction analysis) decreased with increasing amount of PDI moiety substituted for NDI moiety in the reference PNDIS-HD. Pairing of the new 30PDI copolymer with substantially decreased and optimal crystallinity as acceptor with PBDTTT-CT donor is found to give compatible blends and all-polymer solar cells with enhanced performance (PCE = 6.3 %, J_{sc} = 18.6 mA/cm^2, external quantum efficiency = 91 %). Charge transport in neat films of the reference PNDIS-HD and the new NDI/PDI copolymers (10PDI, 30PDI, 50PDI) was investigated by using organic field-effect transistors (OFETs) and bulk charge transport in the polymer/polymer BHJ active layers was studied by the space-charge-limited current method. The surface and bulk morphologies of the PNDIS-HD/PBDTTT-CT and *x*PDI/PBDTTT-CT blend systems were investigated by atomic force microscopy (AFM) and transmission electron microscopy imaging, respectively.

4.3.2 *Experimental Section*

Materials: 4,9-Dibromo-2,7-bis(2-hexyldecyl)benzo[lmn][3,8]-phenanthroline-1,3,6,8-tetraone (NDI) and 2,5-bis(trimethylstannyl)-selenophene were synthesized according to the known literature procedures.[6] N,N'-bis(2-ethylhexyl)-1,7-dibromo-3,4,9,10-perylene diimide (PDI) was purchased from Sunatech Inc. and the donor polymer PBDTTT-CT (M_n > 20 kDa, $M_w/M_n \sim 3$) was purchased from Solarmer Energy, Inc. and both were used as received. The ZnO precursor solution was prepared by dissolving 1 g of zinc acetate dihydrate (99.999% trace metals basis, Aldrich) in 10 mL of 2-methoxyethanol (99.8%, anhydrous, Aldrich) with 0.28 g of ethanolamine ($\geq$ 99.5%, Aldrich) as a surfactant and stirring overnight under ambient conditions.

Poly{([N,N'-bis(2-hexyldecyl)-naphthalene-1,4,5,8-bis(dicarboximide)-2,6-diyl]-*alt*-5,5'-selenophene)-*ran*-([N,N'-bis(2-ethylhexyl)-1,7-dibromo-3,4,9,10-perylene diimide]-*alt*-5,5'-selenophene))} (10PDI, 30PDI, and 50PDI). In the case of 10PDI, 4,9-dibromo-2,7-bis(2-hexyldecyl)benzo[lmn][3,8]-phenanthroline-1,3,6,8-tetraone (NDI) (250 mg, 0.286 mmol), N,N'-bis(2-ethylhexyl)-1,7-dibromo-3,4,9,10-perylene diimide (PDI) (22.42 mg, 0.0318 mmol) and 2,5-bis(trimethylstannyl)selenophene (145.12 mg, 0.318 mmol), with $Pd_2(dba)_3$ (5.82 mg, 2 mol%) and $P(o\text{-tolyl})_3$ (7.74 mg, 8 mol%) were added into a 100 mL three-neck round-bottom flask. The flask equipped with a condenser was then degassed and filled with argon three times. Afterwards, 12.6 mL of chlorobenzene was added and degassed one time. The highly concentrated reaction mixture (34 mg/mL) was refluxed under magnetic bar stirring for 72 h under argon, and cooled down to room temperature. The polymerization mixture was poured into 200 mL methanol and 5 mL hydrochloric acid solution and stirred overnight. The polymer precipitated out as a solid and was filtered using a filter paper. The polymer was purified by

Soxhlet extraction with methanol, acetone, and hexane, sequentially. **10PDI** (260 mg; yield = 98 %), GPC: M_w = 320.4 kDa, M_n = 90.3 kDa, M_w/M_n = 3.5; TGA: T_d = 400 °C.

30PDI. 4,9-Dibromo-2,7-bis(2-hexyldecyl)benzo[lmn][3,8]-phenanthroline-1,3,6,8-tetraone (NDI) (250 mg, 0.286 mmol), N,N'-bis(2-ethylhexyl)-1,7-dibromo-3,4,9,10-perylene diimide (PDI) (94.83 mg, 0.123 mmol) and 2,5-bis(trimethylstannyl)selenophene (186.8 mg, 0.409 mmol), with $Pd_2(dba)_3$ (7.5 mg, 2 mol%) and $P(o\text{-tolyl})_3$ (9.96 mg, 8 mol%) in 16 mL of chlorobenzene. 30PDI (329 mg; yield = 97.6 %), GPC: M_w = 428.7 kDa, M_n = 126.7 kDa, M_w/M_n = 3.4; TGA: T_d = 420 °C.

50PDI. 4,9-Dibromo-2,7-bis(2-hexyldecyl)benzo[lmn][3,8]-phenanthroline-1,3,6,8-tetraone (NDI) (169.5 mg, 0.194 mmol), N,N'-bis(2-ethylhexyl)-1,7-dibromo-3,4,9,10-perylene diimide (PDI) (150 mg, 0.194 mmol) and 2,5-bis(trimethylstannyl)selenophene (177.2 mg, 0.388 mmol), with $Pd_2(dba)_3$ (7.1 mg, 2 mol%) and $P(o\text{-tolyl})_3$ (9.45 mg, 8 mol%) in 15 mL of chlorobenzene. 50PDI (305 mg; yield = 98.4 %), GPC: M_w = 264.6 kDa, M_n = 103.5 kDa, M_w/M_n = 2.6; TGA: T_d = 415 °C.

Characterization: The structure and physical properties of the new polymers were investigated by ^1H NMR, gel permeation chromatography (GPC) analysis and thermogravimetric analysis (TGA). ^1H NMR spectra at 300 MHz were recorded on a Bruker-AF300 spectrometer to verify the molecular structure, and the molecular weight was measured using a Waters 1515 GPC with a refractive index detector against polystyrene standards in *o*-dichlorobenzene at 130 ˚C. TGA thermograms of the polymers were acquired on a TA Instruments Q50 TGA at a heating rate of 20 ˚C per minute under nitrogen gas flow.

Electrochemical properties of the polymers were investigated by cyclic voltammetry (CV). CV experiments were done on an EG&G Princeton Applied Research potentiostat/galvanostat (model 273A) in an electrolyte solution of 0.1 M tetrabutylammonium hexafluorophosphate (Bu_4NPF_6) in acetonitrile at a scan rate of 40 m/Vs. Platinum wires were used as counter and working electrodes, and Ag/Ag$^+$ (Ag in 0.1 M $AgNO_3$ solution, Bioanalytical System, Inc.) was used as a reference electrode. Ferrocene/ferrocenium was used as an internal standard, and the reference potential was converted to the saturated calomel electrode (SCE) scale. Each sample for CV was prepared by dip-coating the copolymer solutions in chloroform onto Pt wires.

Optical absorption spectra of the polymers were measured on a Perkin-Elmer model Lambda 900 UV/vis/near-IR spectrophotometer. Solution and solid state absorption spectra were obtained from dilute (10^{-6} M) polymer solutions in chloroform and as thin films on glass substrates, respectively. Thin films (95 – 110 nm) were spin coated from 20 mg/mL solutions in chlorobenzene.

X-ray diffraction patterns were obtained from Bruker F8 power XRD with a Cu Kα radiation as the X-ray source, and the solid samples were prepared by drop-casting of highly concentrated polymer solutions (30 mg/mL) in chloroform onto glass substrates and followed by annealing in a hot plate at 175 ˚C for 10 minutes or film-aging in a argon filled glovebox at room temperature for 96 hours. The mean size of the crystalline domains (L_c) of the polymers was calculated from the lamellar peaks using the Scherrer equation, $L_c = K\lambda/\beta\cos\theta$, where K is shape factor (0.9), λ is X-ray wavelength (1.54 Å), and β is the full width at half maximum (FWHM) in radian. The peak center and the FWHM were obtained by fitting the lamellar peak using Gaussian function in Origin software.

***AFM and TEM imaging*:** AFM characterization of surface morphology was done on the active layers of the actual BHJ solar cells by using a Veeco Dimension 3100 Scanning Probe Microscope (SPM) system. Bright field transmission electron microscopy (BF-TEM) images were measured on an FEI Tecnai G2 F20 TEM at 200 kV accelerating voltage and acquired with a CCD camera and recorded with Gatan Digital Micrograph software with proper exposure time (0.1 sec). The TEM images were slightly defocused to enhance the phase contrast. The sample films were spin-casted on top of ITO/PEDOT:PSS substrates and peeled off by putting the samples in water. A peeled-off film was deposited on a TEM grid (Electron Microscopy Sciences, Inc.) and dried overnight in a vacuum oven.

Fabrication and Characterization of Field-Effect Transistors: A heavily *n*-doped silicon substrate with a 200nm thermally grown silicon oxide layer acted as a gate electrode and insulating layer, respectively (C_i = 17 nF/cm^2). The substrate was cleaned by ultrasonication in acetone and isopropyl alcohol for 30 min each and dried under a flow of nitrogen gas. The substrate was further cleaned using ozone-plasma for 5 min. A dilute chloroform solution (0.1 M) of octyltrichlorosilane (OTS8) was spin-coated onto the silicon dioxide layer at 3000 rpm in air for 10 sec. The substrates were then annealed for 10 min at 100 °C, washed with toluene, then annealed for 10 min at 150°C. The polymer semiconductors were spin coated onto the OTS8 treated substrate from a solution in chloroform (8 mg/mL) at 2000 rpm for 60 sec in an argon filled glove box. The films were annealed at 175 °C for 10 min and then source/drain electrodes were deposited via thermal evaporation of silver (100 nm) that defined a channel width (W) of 1000 μm and length (L) of 100 μm. Current-voltage characteristics of the completed transistors were measured under nitrogen atmosphere using a Signatone probe station and a semiconductor parameter analyzer. The saturation region field-effect mobility (μ) and threshold voltage (V_{th}) were calculated from plots of $I_{ds}^{1/2}$ *vs* V_{gs} in a forward scan with V_{ds} at 80 V by using the saturation-region transistor equation: $I_{ds}=(\mu W C_i)(V_{gs}-V_{th})^2/(2L)$.

***Fabrication and Characterization of All-Polymer Solar Cells*:** ITO glass substrates were cleaned sequentially in ultrasonic baths with acetone and isopropyl alcohol for 20 minutes, dried using nitrogen gas, and stored in a vacuum oven. The ITO glass substrate was O_2 plasma treated for 90 seconds right before coating the ZnO layer. The ZnO precursor solution was spin-coated onto the ITO glass at 5000 rpm for 40 sec, annealed at 250 ˚C on a hot plate in air for 1 hr to make 20 – 30 nm thick ZnO layer and the glass/ITO/ZnO substrate was transferred into an Argon-filled glove box. A 1.0 vol % ethanolamine or 0.05 wt % polyethylenimine in 2-methoxyethanol solution was spin-coated onto the ZnO layer and dried at 110 °C on a hot plate for 10 minutes right before use. Each active layer (PNDIS-HD:PBDTTT-CT or *x*PDI:PBDTTT-CT blend (1:1 *wt/wt*) solution (25 mg/mL) in chlorobenzene with 3 *vol* % DIO solvent additive was spin-coated at 1000 rpm for 20 seconds. After spin-coating, the wet film was film-aged inside the glove box at room temperature for 96 hours (4 days) followed by thermal vacuum deposition of MoO_3 (7.5 nm) and Ag anode (100 nm). All the active layers have thicknesses of 90 ± 10 nm. Five pixels, each with an active area of 4 mm^2, were fabricated per ITO substrate. The photovoltaic cells were tested under AM 1.5 solar illumination at 100 mW/cm^2 in ambient condition using a Solar Simulator (model 16S, Solar Light Co., Philadelphia, PA) with a 200W Xenon Lamp Power Supply (Model XPS 200, Solar Light Co., Philadelphia, PA) calibrated by NREL certified Si photodiode (Model 1787–04, Hamamatsu Photonics K.K., Japan) and a HP4155A semiconductor parameter analyzer (Yokogawa Hewlett-Packard, Japan). After the *J-V* measurement, the external quantum efficiency (EQE) was measured by using a solar cell quantum efficiency measurement system (Model QEX10, PV Measurements, Inc., Boulder, CO) with a 2 mm^2 (2 mm×1mm) size masked incident light source and TF Mini Super measurement apparatus for multiple devices in a single substrate. The EQE system was calibrated with a Si photodiode before each measurement.

Space-Charge-Limited Current (SCLC) Measurement: Current-voltage (*J-V*) characteristics of the SCLC devices were measured by using a HP4155A semiconductor parameter analyzer (Yokogawa Hewlett-Packard, Tokyo). The carrier mobility was extracted by fitting the *J-V* curves in the near quadratic region according to the modified Mott-Gurney equation,[25] The SCLC device structures for electron-only and hole-only measurements were ITO/ZnO/active-layer/LiF/Al and ITO/PEDOT:PSS/active-layer/Au, respectively. Each active layer (PNDIS-HD:PBDTTT-CT or *x*PDI:PBDTTT-CT blend (1:1 *wt/wt*)) solution (25 mg/mL) in chlorobenzene with 3 *vol*% DIO solvent additive was spin-coated at 1000 rpm for 20 seconds. After spin-coating, the wet film was film-aged inside the glove box at room temperature for 96 hours (4 days) followed by thermal vacuum deposition of LiF (1 nm)/Al (100 nm) or Au (40 nm).

4.3.3 *Results and Discussions*

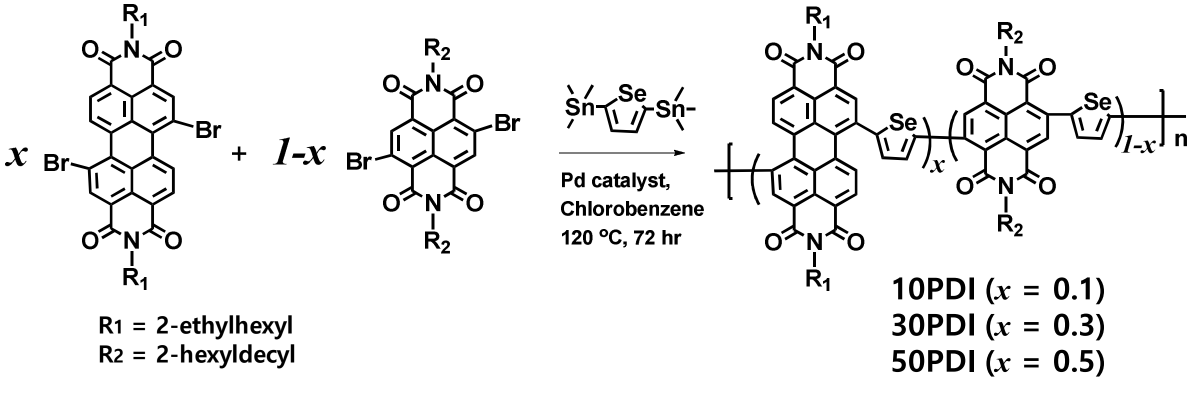

Scheme 7. Synthesis of *n*-type semiconducting NDI/PDI random copolymers, *x*PDI.

Synthesis, Absorption Spectra, and Electronic Structure. The new *n*-type semiconducting, random, NDI-selenophene/PDI-selenophene, copolymers denoted as *x*PDI where *x* is the molar percentage of PDI-selenophene segments, were synthesized by Stille coupling copolymerization of three monomers, 4,9-dibromo-2,7-bis(2-hexyldecyl)benzo[lmn][3,8]-phenanthroline-1,3,6,8-tetraone (4,9-dibromo-NDI), N,N'-bis(2-ethylhexyl)-1,7-dibromo-3,4,9,10-perylene diimide (1,7-dibromo-PDI), and 2,5-bis(trimethylstannyl)-selenophene (**Scheme 7**). The 4,9-dibromo-NDI and selenophene monomers were synthesized and purified by following our previous reports[6] whereas the 1,7-dibromo-PDI monomer was obtained commercially (SunaTech Inc.) and was used without further purification. Three different compositions of *x*PDI, i.e. 10PDI, 30PDI, and 50PDI were synthesized and investigated. In addition, the benchmark NDI-selenophene copolymer, PNDIS-HD,[6] as well as PDI-selenophene copolymer was also synthesized for the purpose of comparison. PNDIS-HD, 10PDI, 30PDI, and 50PDI showed good solubility (>30 mg/mL) in common organic solvents, including chloroform, chlorobenzene, and dichlorobenzene, at room temperature. However, PPDIS precipitated out during the polymerization and showed very limited solubility due to the short alkyl side chains, 2-ethylhexyl, and thus PPDIS was not further studied. The molecular structures of the monomers and copolymers were confirmed by ^{1}H NMR spectra. The molecular weight and polydispersity index (M_w/M_n) of the polymers were measured by gel permeation chromatography (GPC) against polystyrene standards in *o*-dichlorobenzene at 130 ˚C. The reference polymer, PNDIS-HD, had a weight average molecular weight (M_w) of 42.6 kDa with M_w/M_n of 1.5. The M_w of *x*PDI was comparable with PNDIS-HD

Table 17. Molecular Weight, Thin Film Optical Absorption, Electronic Structure and Field-Effect Electron Mobility of PNDIS-HD and *x*PDIs.

Polymer	M_w (kDa)	M_w/ M_n	λ_{max} (nm)	E_g^{opt} (eV)	LUMO (eV)	μ_e (cm2/Vs)	V_{th} (V)	I_{on}/I_{off}
PNDIS-HD	42.6	1.5	348, 622	1.65	3.84	9.2×10^{-2}	10	10^3
10PDI	57.2	1.3	352, 615	1.70	3.84	5.5×10^{-2}	10	10^3
30PDI	52.5	1.4	349, 578	1.77	3.89	7.1×10^{-3}	5	10^3
50PDI	32.1	1.4	347, 544	1.77	3.89	4.0×10^{-3}	5	10^3

sample and was in the range of 32.1 – 57.2 kDa with a M_w/M_n of 1.3 – 1.4 (**Table 17**). Initially, GPC was performed in chlorobenzene at a lower temperature (60˚C), and *x*PDI showed significantly higher M_w in the range of 269.1 – 430.8 kDa with high M_w/M_n in the range of 2.6 – 3.5, indicating aggregation of the samples. The *p*- type polymer PBDTTT-CT had M_n > 20 kDa with M_w/M_n ~ 3. Thermogravimetric analysis (TGA) of all the *n*-type polymers showed good thermal stability with onset decomposition temperature (T_d) of over 400 ˚C under nitrogen flow.

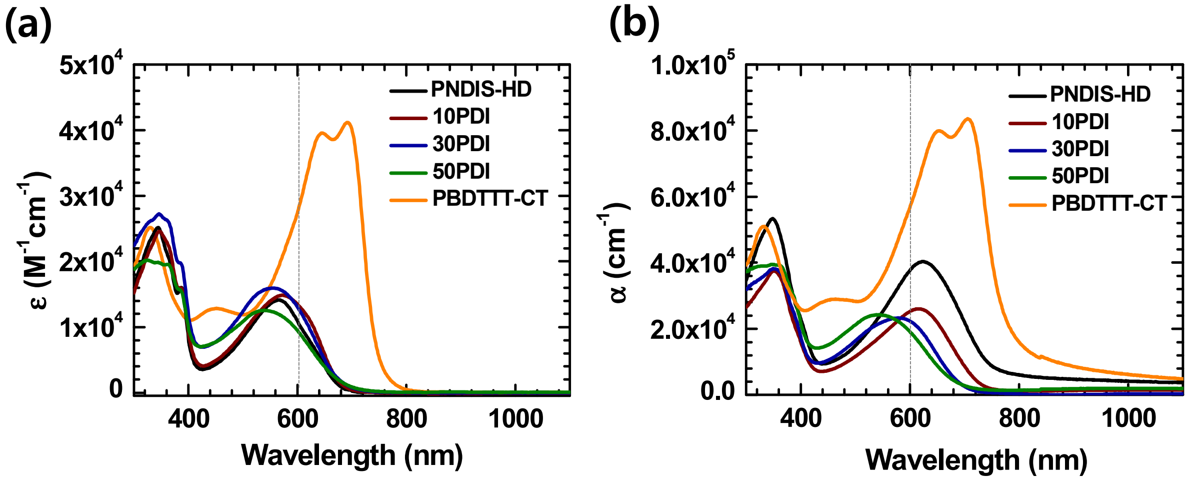

Figure 32. UV-Vis absorption spectra of *x*PDI, PNDIS-HD, and PBDTTT-CT in dilute chloroform solution (a) and as thin films on glass substrates (b).

The optical absorption of the new NDI/PDI copolymers, *x*PDI, was characterized by UV-visible absorption spectroscopy of dilute (10^{-6} M) chloroform solutions (**Figure 32a**) and of thin films (95 – 110 nm) on glass substrates (**Figure 32b**). The optical absorption spectra of the reference PNDIS-HD acceptor and donor polymer, PBDTTT-CT, were also obtained for the purpose of comparison. In solution, *x*PDI materials showed two distinct absorption bands at 300 – 400 nm and 500 – 700 nm which can be assigned to π-π* or n-π* transition of the NDI and PDI chromophores and an intramolecular charge transfer (ICT) band, respectively. These absorption features are typically observed in NDI-based conjugated copolymers.[6, 14] 10PDI has absorption maxima (λ_{max}) at 570 nm (maximum molar extinction coefficient, $\varepsilon_{max} = 1.48 \times 10^4$ $M^{-1}cm^{-1}$) and at 346 nm ($\varepsilon_{max} = 2.46 \times 10^4$ $M^{-1}cm^{-1}$) which are very similar to those of PNDIS-HD ($\lambda_{max} = 568$ nm and 344 nm). By increasing the amount of PDI moiety in the polymer backbone, however, the λ_{max} of the ICT band is blue shifted to 555 nm ($\varepsilon_{max} = 1.59 \times 10^4$ $M^{-1}cm^{-1}$) in 30PDI and to 539 nm ($\varepsilon_{max} = 1.25 \times 10^4$ $M^{-1}cm^{-1}$) in 50PDI. The enhanced absorption near 500 nm in 30PDI and 50PDI originates from the PDI-selenophene moiety, and can be explained by the fact that PDI copolymers typically have absorption maximum in the 500 – 560 nm range.[4] Our measured solution absorption spectrum of PBDTTT-CT has two peaks at 645 nm and 693 nm ($\varepsilon_{max} = 4.1 \times 10^4$ $M^{-1}cm^{-1}$) with much higher molar extinction coefficient compared to the acceptor polymers. However, we note that the molar extinction coefficient of the new acceptor polymers, *x*PDI, is more than an order of magnitude higher than fullerene acceptors in the visible region.[15]

The thin film absorption spectra are very similar to the solution spectra but the longer wavelength (ICT) bands are red-shifted due to the increased conjugation and intermolecular interactions in the solid state. The reference PNDIS-HD has a visible region λ_{max} at 622 nm ($\alpha_{max} = 4.0 \times 10^4$ cm^{-1}) which is 54 nm red-shifted compared to that in solution. An important consequence of the incorporation of PDI moieties into the *n*-type semiconducting copolymers, *x*PDI, is that the absorption coefficient is slightly lowered while the visible region absorption maximum λ_{max} progressively decreases from 615 nm ($\alpha_{max} = 2.6 \times 10^4$ cm^{-1}) in 10PDI to 578 nm ($\alpha_{max} = 2.3 \times 10^4$ cm^{-1}) in 30PDI and finally to 544 nm ($\alpha_{max} = 2.4 \times 10^4$ cm^{-1}) in 50PDI. This trend is largely explained by the progressive decrease in planarity of the polymer backbone due to the increasing steric hindrance from the large PDI moiety. We note that the absorption maximum of 50PDI is already comparable to those of known PDI-containing alternating conjugated copolymers.[4] The measured α values for PNDIS-HD and *x*PDI are comparable with other reported NDI and PDI-based acceptor polymers.[3, 4] The optical band gap (E_g^{opt}), determined from the onset absorption band edge of the acceptor polymers, increased from 1.65 eV in the reference PNDIS-HD to 1.70 eV in 10PDI and to 1.77 eV in 30PDI and 50PDI. Our measured thin film absorption spectrum of PBDTTT-CT has an absorption maximum at 706 nm and E_g^{opt} of 1.55 eV, which are in good agreement with previous report of λ_{max} of 692 nm and E_g^{opt} of 1.58 eV.[13] Although the absorption coefficient of PBDTTT-CT is not previously reported, our measured α_{max} of 8.3×10^4 cm^{-1} in PBDTTT-CT is in good agreement with α_{max} values ($7 \times 10^4 - 9 \times 10^4$ cm^{-1}) of other benzodithiophene-thieno[3,4-b]thiophene copolymers (PTB7 and PTB7-Th).[3b, 3f]

The electronic structures of the acceptor (*x*PDI, PNDIS-HD) and donor (PBDTTT-CT) polymers were investigated by using cyclic voltammetry (CV) of thin films. The ferrocene/ferrocenium (Fc/Fc$^+$) reference was used as an internal standard, which was assigned an absolute energy of – 4.8 eV vs vacuum level.[16] Based on the onset reduction potentials of the polymers obtained from the cyclic voltammograms, the lowest unoccupied molecular orbital (LUMO) energy levels were determined (LUMO = – (eE$_{red}^{onset}$ (V vs Fc/Fc$^+$) + 4.8 eV)). In this way, we obtained LUMO energy levels of – 3.84 eV for PNDIS-HD and 10PDI and – 3.89 eV for 30PDI and 50PDI (**Chart 4**). The very similar LUMO energy levels of these polymers is to be expected from the similar electron-accepting strengths of the NDI and PDI moieties. Oxidation wave was not observed up to 2 V (vs SCE) in CV experiments on the acceptor polymers. Therefore, the highest occupied molecular orbital (HOMO) energy levels were estimated in two ways: (i) by subtracting the E_g^{opt} from the above CV-determined LUMO energy levels and (ii) considering that the HOMO energy level of –5.95 eV was experimentally observed for NDI-biselenophene copolymer,[14a] the real HOMO energy levels of each acceptor polymer (PNDIS-HD, 10PDI, 30PDI, 50PDI) should thus be lower-lying than – 5.95 eV, since selenophene is a weaker electron-donating moiety than biselenophene. We consider the HOMO energy levels (-5.95 eV) from the later estimate to be more reliable than those from using E_g^{opt}. The HOMO/LUMO energy levels of PBDTTT-CT were also measured by using the onset oxidation/reduction potentials of CV scans, giving−5.25 eV/−3.19 eV. These HOMO/LUMO energy levels of PBDTTT-CT provide sufficient energy offsets (> 0.3 eV) with each of the acceptor polymers (PNDIS-HD, 10PDI, 30PDI, 50PDI) for efficient electron transfer[17] and hole transfer[18] essential for photovoltaic devices.

Table 18. XRD Data and the Mean Crystalline Domain Size (L_c) of Thermally Annealed Neat Polymers.

Sample	**(100) (°)**	d_{100} **(Å)**	**(010) (°)**	d_{010} **(Å)**	L_c **(nm)**
PBDTTT-CT	4.50	19.61	22.42	3.96	9.15
PNDIS-HD	4.10	21.53	22.54	3.94	10.22
10PDI	4.26	20.72	21.88	4.06	9.47
30PDI	4.76	18.54	21.24	4.18	5.11
50PDI	5.08	17.37	20.38	4.35	3.62

Crystallinity of Neat Polymer Films. We used wide angle X-ray diffraction (XRD) analysis of thermally annealed (175 ˚C, 10 min) drop casted films on glass substrates to characterize the molecular packing structure and bulk crystallinity of the new *n*-type copolymers (10PDI, 30PDI, and 50PDI), the reference acceptor polymer (PNDIS-HD), and the donor polymer (PBDTTT-CT) as neat films and the data are summarized in **Table 18**. Such solution cast films have randomly oriented crystallites which facilitate analysis and interpretation of the XRD patterns shown in **Figure 33a**. XRD patterns of the reference PNDIS-HD showed an intense lamellar (100) peak at $2\theta = 4.1$ ˚ and a π-π stacking (010) peak at $2\theta = 22.54$ ˚, giving a lamellar packing distance of 21.53 Å and a π-π stacking distance of 3.94 Å. The mean size of crystalline domains (L_c) was also calculated from the Scherrer equation[19] by using the full-width-at-half-maximum (FWHM) value of the lamellar (100) peak. The PNDIS-HD film has a large L_c of 10.22 nm, implying a highly crystalline film.

A similar X-ray diffraction analysis of the *x*PDI copolymers shows that the molecular packing and crystallinity of drop cast neat films of 10PDI, 30PDI, and 50PDI are significantly different from those of the reference PNDIS-HD. The lamellar (100) peaks of *x*PDIs are found with 2θ of 4.26 °, 4.76 °, and 5.08 ° and *d*-spacings of 20.72 Å, 18.54 Å, and 17.37 Å in 10PDI, 30PDI, and 50PDI films, respectively (**Figure 33a**). This represents a large progressive decrease of the lamellar *d*-spacing with increasing amount of the PDI moiety in the chain. In contrast, the π-π stacking distance is increased linearly from 3.94 Å in PNDIS-HD to 4.06 Å, 4.18 Å, and 4.35 Å in 10PDI, 30PDI, and 50PDI films, respectively (**Figure 33b**). The observed progressive decrease of lamellar packing distance with increasing amount of PDI moiety results from the shorter ethylhexyl side chains on the PDI moieties in good agreement with similar observations when side chains of different sizes are randomly mixed in other conjugated polymer backbones.[3d, 20] The progressive increase of the π-π stacking distance with increasing amount of PDI moiety incorporated into the copolymer chain can be understood as a consequence of lattice

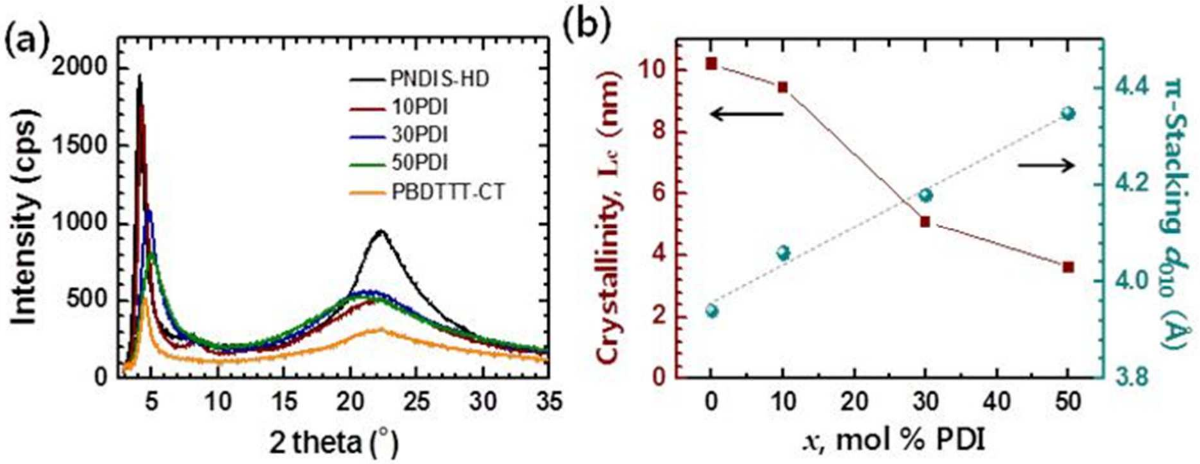

Figure 33. (a) X-ray diffraction patterns of solution casted neat films of PNDIS-HD, *x*PDIs, and PBDTTT-CT on glass substrates annealed at 175 °C for 10 min. (b) Dependence of the mean crystalline domain size (L_c) and π-stacking distance on random copolymer composition.

distortion and decrease in polymer backbone planarity as PDI replaces some NDI units.[3d] The average crystalline domain size L_c decreased slightly from 10.22 nm in the reference PNDIS-HD to 9.47 nm in 10PDI and much more dramatically to 5.11 nm and 3.62 nm in 30PDI and 50PDI, respectively (**Figure 33b**). We conclude that random copolymerization has enabled the tuning of the bulk crystallinity of NDI/PDI-based *n*-type semiconducting polymers.

X-ray diffraction patterns of the donor polymer PBDTTT-CT film showed a lamellar (100) peak at $2\theta = 4.50$ ° and a π-π stacking (010) peak at $2\theta = 22.42$ ° with corresponding *d*-spacings of 19.61 Å and 3.96 Å, respectively (**Figure 33a**). These results are in good agreement with the previously reported XRD patterns for this polymer.[13, 21] The average crystalline domain size L_c of PBDTTT-CT was found to be 9.15 nm, which is comparable with those of PNDIS-HD and 10PDI but is much larger compared to the new random copolymers 30PDI and 50PDI.

We also performed XRD analysis of the film-aged ((25 °C, 96 hrs) electron-accepting polymer (PNDIS-HD, *x*PDIs) films to understand how film-forming conditions affect the bulk crystallinity and molecular packing. The lamellar (100) peaks of PNDIS-HD and *x*PDIs were found with 2θ of 4.48 °, 4.88 °, 5.89 °, and 6.02 ° and *d*-spacing of 19.70 Å, 18.09 Å, 14.99 Å, and 14.66 Å in PNDIS-HD, 10PDI, 30PDI, and 50PDI films, respectively. The π-π stacking distance in these room temperature-aged neat films, d_{010}, was 3.82 Å, 3.84 Å, 3.93 Å, and 4.00 Å in PNDIS-HD, 10PDI, 30PDI, and 50PDI films, respectively. The trend of progressive decrease of the lamellar packing distance d_{100} with increasing amount of PDI moiety is observed similar to what was seen in the thermally annealed films. Also, similar to the observed trend in the thermally annealed films, the π-stacking distance d_{010} increased with increasing amount of the PDI moiety in the copolymer. However, the d_{100} and d_{010} spacings in the room temperature-aged films are decreased by 9 – 19 % and 3 – 8 %, respectively, compared to the corresponding thermally annealed films. The averaged crystalline domain size L_c of these room temperature-aged films decreased from 5.22 nm in PNDIS-HD and 3.42 nm in 30PDI to 1.60 nm in 50PDI (Table S2). Thus, the observed variation of bulk crystallinity with copolymer composition is maintained under the different film-forming conditions.

Field-Effect Electron Mobility. The intrinsic electron mobility of the *n*-type semiconducting polymers was investigated by fabricating and testing field-effect transistors with bottom-gate and top-contact geometry.[14] The electrical parameters are summarized in **Table 17**. All the new polymers (10PDI, 30PDI, and 50PDI) along with the reference PNDIS-HD showed *unipolar n*-channel characteristics and no *p*-channel charge transport as expected from their low-lying LUMO and HOMO energy levels (Chart 1). PNDIS-HD neat films showed the highest saturation region field-effect electron mobility of 0.092 cm^2/Vs with a threshold voltage (V_{th}) of 10 V and on/off ratio of 10^3; this electron mobility is comparable with the previously reported values for PNDIS-HD[6] and other NDI copolymers.[14, 22] The electron mobility slightly decreased to 0.055 cm^2/Vs in 10PDI films whereas it decreased substantially to 7.1×10^{-3} cm^2/Vs and 4.0×10^{-3} cm^2/Vs for 30PDI and 50PDI films, respectively. The observed trend of decreasing electron mobility from the highest value in PNDIS-HD to the lowest value in 50PDI is in excellent agreement with the XRD data which showed a progressive lowering of the crystallinity and increasing of the π-π stacking distance as NDI moieties are progressively substituted with PDI moieties in the reference PNDIS-HD (Figure 2b). We also note that the observed electron mobility of 4.0×10^{-3} – 0.055 cm^2/Vs in neat films of the NDI/PDI random copolymers is comparable to those of other acceptor polymers used in all-polymer solar cells.[3-5]

All-Polymer BHJ Solar Cells. The photovoltaic properties of all-polymer solar cells based on *x*PDI:PBDTTT-CT (1:1 *wt/wt*) and PNDIS-HD:PBDTTT-CT (1:1 *wt/wt*) blend active layers were investigated by fabricating and evaluating diodes with the inverted structure (ITO/ZnO/polymer blend /MoO_3/Ag) and they were tested under 100 mW/cm^2 AM 1.5 solar illumination in ambient air. The polymer/polymer blend active layer was prepared under optimized conditions of spin coating from a chlorobenzene solution containing 3 *vol* % 1,8-diiodooctane (DIO), and aging of the blend film at room-tempaerature for 96 hours to facilitate slow solvent evaporation and self-organization in an argon-filled glove box. The current density – voltage (*J-V*) curves and the external quantum efficiency (EQE) spectra of the devices are given in **Figure 34a** and **Figure 34b**, respectively. The photovoltaic parameters, including the short-circuit current density (J_{sc}), the open-circuit voltage (V_{oc}), fill factor (*FF*), and power conversion efficiency (PCE), are summarized in **Table 19**.

Table 19. Photovoltaic Properties of PNDIS-HD:PBDTTT-CT and *x*PDI:PBDTTT-CT Blend Solar Cells.

Blend^a	J_{sc} **(mA/cm2)**	V_{oc} **(V)**	***FF***	**PCE$_{max}$ (%)**	**R$_S$ (Ω cm2)**	**R$_{SH}$ (Ω cm2)**
PNDIS-HD: PBDTTT-CT	5.39 (5.19 ± 0.20)	0.69 (0.66 ± 0.02)	0.35 (0.35 ± 0.002)	1.23 (1.19 ± 0.05)	85.0	290.7
10PDI: PBDTTT-CT	6.94 (6.55 ± 0.33)	0.78 (0.77 ± 0.01)	0.51 (0.51 ± 0.005)	2.80 (2.56 ± 0.16)	19.7	616.1
30PDI: PBDTTT-CT	15.55 (15.26 ± 0.38)	0.77 (0.76 ± 0.005)	0.43 (0.42 ±0.01)	5.10 (4.90 ± 0.17)	14.0	219.2
50PDI: PBDTTT-CT	9.68 (9.44 ± 0.25)	0.73 (0.73 ± 0.003)	0.38 (0.38 ± 0.003)	2.66 (2.58 ± 0.09)	21.9	199.2
PNDIS-HD: PBDTTT-CT^b	4.16 (4.13 ± 0.03)	0.81 (0.80 ± 0.01)	0.40 (0.39 ± 0.01)	1.36 (1.31 ± 0.05)	18.2	211.5
30PDI: PBDTTT-CT^b	18.55 (18.22 ± 0.28)	0.79 (0.78 ± 0.002)	0.45 (0.43 ±0.01)	6.29 (6.17 ± 0.10)	11.3	160.6

^{a} The photovoltaic properties were averaged over 10 devices. ^{b} ZnO layer modified by a spin-coated polyethylenimine (PEI) interfacial layer.

The reference PNDIS-HD:PBDTTT-CT solar cells gave a maximum PCE of 1.23 % with J_{sc} of 5.39 mA/cm^2, V_{oc} of 0.69, and *FF* of 0.35. This poor photovoltaic performance of the PNDIS-HD/PBDTTT-CT blend system means that it is incompatible. The incompatibility of this reference polymer/polymer BHJ active layer is not obvious in light of the following facts. The

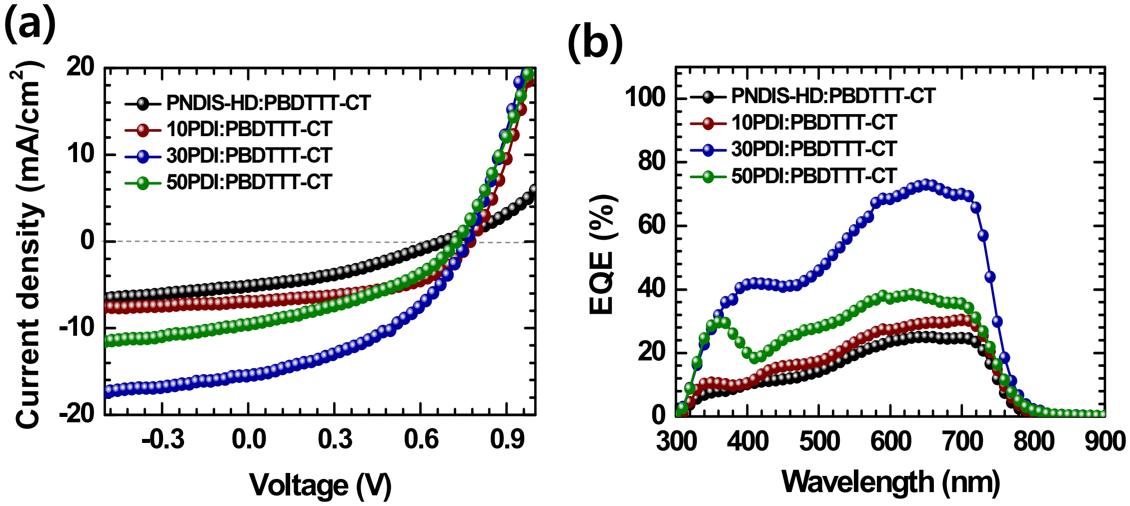

Figure 34. Current density-voltage (*J* - *V*) curves (a) and external quantum efficiency (EQE) spectra (b) of PNDIS-HD:PBDTTT-CT (1:1 *wt/wt*) and *x*PDI:PBDTTT-CT (1:1*wt/wt*) blend solar cells with film-aged (25 ˚C, 96 hr) active layer.

HOMO/LUMO energy level offsets between PNDIS-HD acceptor and PBDTTT-CT donor (**Chart 4**) are excellent for enabling efficient electron/hole transfer processes and charge separation.[17,18] PNDIS-HD is known to have a relatively high electron mobility (**Table 17**) and prior reports have showed that its blends with other donor polymers (e.g. PSEHTT) can create high efficiency all-polymer photovoltaic devices (PCE = 3 – 5 %).[6] By virtue of its broad optical absorption in the 500 – 800 nm region and small optical bandgap (E_g^{opt} = 1.55 eV), the PBDTTT-CT donor has previously been used to produce high performance (PCE > 7%) polymer/[70]PCBM devices.[13] We conclude that incompatibility of PNDIS-HD/PBDTTT-CT blend system implies that these factors are not sufficient to *a priori* predict compatibility of a polymer/polymer blend pair for BHJ solar cells.

Compared to the reference PNDIS-HD:PBDTTT-CT blend system, all the new *x*PDI acceptors (10PDI, 30PDI, 50PDI) respectively paired with the same PBDTTT-CT donor gave rise to enhanced photovoltaic performance of the BHJ devices. In the case of 10PDI:PBDTTT-CT

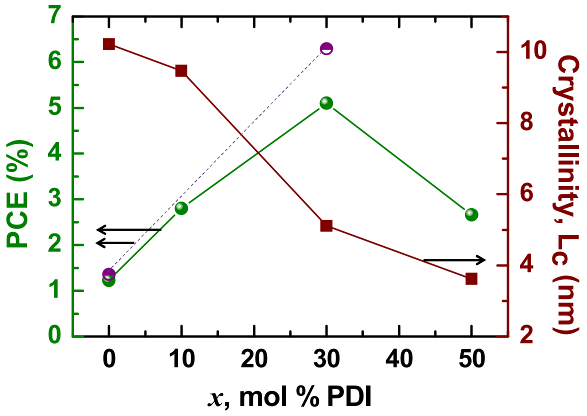

Figure 35. Dependence of power conversion efficiency (PCE) and the mean crystalline domain size (L_c) on random copolymer composition. Half-filled purple circles are the PCE of the devices with polyethylenimine interfacial layer modified ZnO layer.

blends, the performance of the BHJ solar cells (PCE = 2.8 %, J_{sc} = 6.94 mA/cm^2, V_{oc} = 0.78 V, and FF = 0.51) is significantly improved even though the change from PNDIS-HD to 10PDI is relatively minor. A dramatic enhancement in photovoltaic performance is observed in 30PDI:PBDTTT-CT blend solar cells with V_{oc} of 0.77 V, fill factor of 0.43, J_{sc} of 15.55 mA/cm^2, and thus a high PCE of 5.10 %. This observed efficiency in 30PDI blends represents a 4.15-fold enhancement of PCE compared to the reference PNDIS-HD blend devices. It is also to be noted that the observed photocurrent in 30PDI:PBDTTT-CT devices is comparable to those seen in the best fullerene-based PC$_{71}$BM:PBDTTT-CT solar cells[13] (15.5 – 17.5 mA/cm^2). Although the performance of 50PDI:PBDTTT-CT BHJ solar cells (PCE = 2.66 %, J_{sc} = 9.68 mA/cm^2, V_{oc} = 0.73 V, and FF = 0.38) is still significantly higher compared to the reference PNDIS-HD devices, however, it is clear that further increase in the amount of PDI moieties in the NDI/PDI copolymers results in decrease in performance relative to the 30PDI acceptor. The dependence of the PCE on the NDI/PDI copolymer composition is shown in **Figure 35**, revealing that the 30 mol% PDI is the optimum.

The external quantum efficiency (EQE) spectra of the best xPDI:PBDTTT-CT and PNDIS-HD:PBDTTT-CT blend devices are shown in **Figure 34b**. The photoresponse of each of the blend photodiodes starts at 800 nm, which corresponds to the onset absorption of the donor polymer, and covers the entire visible down to the UV at ~ 300 nm. The EQE spectra peak at about 600 – 700 nm, where both the *p*-type and *n*-type polymers strongly absorb. The observed EQE spectra indicate that the *n*-type polymer in each blend contributes to light harvesting and photocurrent generation. In the case of the 30PDI:PBDTTT-CT blend devices, the EQE peaks at 73 %. We note that the photocurrent density calculated from the EQE spectra (**Figure 34b**) are in good agreement with the J_{sc} values measured directly from the $J-V$ curves in **Figure 34a**.

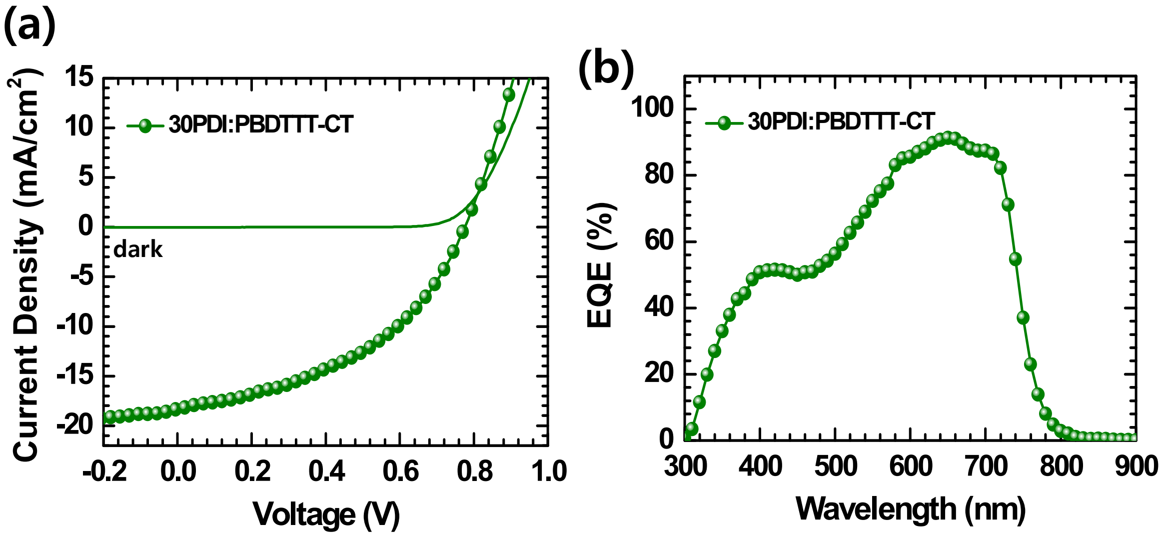

Figure 36. Current density-voltage (J - V) curve (a) and EQE spectrum (b) of 30PDI:PBDTTT-CT (1:1*wt/wt*) blend solar cells with film-aged (25 ˚C, 96 hr) active layer and a polyethylenimine interfacial layer modified ZnO layer.

The 30PDI:PBDTTT-CT blend and the reference PNDIS-HD:PBDTTT-CT blend devices were further optimized by using a polyethylenimine (PEI) surface modifier on the top of the zinc oxide (ZnO) layer which is known to lower the cathode work-function and thus can provide better electron injection and collection.[23] The $J-V$ curve and EQE spectrum of the

30PDI:PBDTTT-CT blend devices are shown in **Figure 36** and a summary of the photovoltaic parameters is given in **Table 19**. A large increase in short-circuit current density (18.55 mA/cm^2) is observed with V_{oc} of 0.79 V and FF of 0.45, leading to a PCE of 6.29 %. The EQE spectrum of the 30PDI:PBDTTT-CT photodiode (**Figure 36b**) has a maximum of 91 % at 650 nm. The calculated J_{sc} from the EQE spectrum is 17.47 mA/cm^2, which is in good agreement (5.8 % mismatch) with that from the *J-V* measurement (18.55 mA/cm^2). The best performance of the reference PNDIS-HD:PBDTTT-CT blend devices with PEI-modified ZnO layer (PCE = 1.36 %, J_{sc} = 4.16 mA/cm^2, V_{oc} = 0.82 V, and FF = 0.40) is only slightly improved relative to devices without the PEI interlayer. Thus the photovoltaic efficiency of the 30PDI blend devices is 4.6-fold enhanced compared to the reference PNDIS-HD blend cells. We note that the photocurrent (18.55 mA/cm^2), PCE (6.29 %), and EQE (91 %) seen in the present 30PDI:PBDTTT-CT BHJ solar cells are the best observed to date in all-polymer solar cells.[3-6] Furthermore, the short-circuit current density (J_{sc} = 18.55 mA/cm^2) and EQE (91 %) are also the highest measured for the donor polymer PBDTTT-CT, including PC$_{71}$BM:PBDTTT-CT devices.[13]

The observed high power conversion efficiency (6.29 %) of the 30PDI:PBDTTT-CT BHJ solar cells implies that this polymer/polymer blend system is definitely compatible whereas the reference PNDIS-HD:PBDTTT-CT blend is not. Given the far inferior photovoltaic properties of the 10PDI:PBDTTT-CT and 50PDI:PBDTTT-CT blends, compared to the 30PDI blends, we conclude that they are also incompatible like the reference PNDIS-HD blends. The dependence of the crystallinity (i.e. average crystalline domain size L_c) on copolymer composition shown in **Figure 35** suggests that there is an *optimum bulk crystallinity* of the acceptor polymer (L_c = 5.11 nm for 30PDI) that facilitates its compatibility in blends with a given donor polymer (PBDTTT-CT). The fact that the crystallinity in 50PDI (L_c = 3.62 nm), which pairs with PBDTTT-CT to produce incompatible blends, is much smaller than in 30PDI that partners with the same donor polymer to produce compatible blends, highlights our use of random copolymerization as a facile means to discover the optimum bulk crystallinity of the acceptor polymer essential to compatibility. Although these results demonstrate that bulk crystallinity of the acceptor polymer paired with a given donor polymer (PBDTTT-CT) is a critical factor that dictates compatibility and photovoltaic efficiency, the detailed mechanism of how an optimal crystallinity endows blend compatibility and enhances performance of photovoltaic devices is not yet clear and its elucidation would require much future studies on various blend pairs. Nevertheless, we believe that the optimal crystallinity exerts its influence through the bulk morphology and bulk charge transport of the polymer/polymer blend systems as will be further discussed in subsequent sections.

Finally, we compare the observed best photovoltaic properties of 30PDI:PBDTTT-CT blends (PCE = 6.29 %, J_{sc} = 18.55 mA/cm^2, V_{oc} = 0.79 V, and FF = 0.45) with those reported for the best PC$_{71}$BM:PBDTTT-CT blends.[13] As already pointed out above, the measured short-circuit current density in the present all-polymer photodiodes is significantly higher than the maximum J_{sc} (15.5 – 17.7 mA/cm^2) observed in PC$_{71}$BM:PBDTTT-CT[13] while the V_{oc} is also slightly higher. However, much higher power conversion efficiencies (6.91 – 7.59 %) and fill factors (58.7 – 59.5 %) have been reported for the PC$_{71}$BM devices.[13] The low fill factor (45 %) is the main limitation of the efficiency of 30PDI:PBDTTT-CT BHJ solar cells. Indeed, if fill factors comparable to the PC$_{71}$BM device values (e.g. 59.5 %) could be obtained in the 30PDI:PBDTTT-CT blend devices, PCEs exceeding 8 % and thus comparable to the corresponding fullerene-based solar cells would be achieved. The observed much higher maximum EQE (91 %) for 30PDI:PBDTTT-CT blend devices compared to 66 % for

$PC_{71}BM$:PBDTTT-CT[13] suggests feasibility of such high PCEs if the low fill factor due to recombination losses could be addressed by further device optimization, including exploration of methods of facilitating vertical phase segregation.[24]

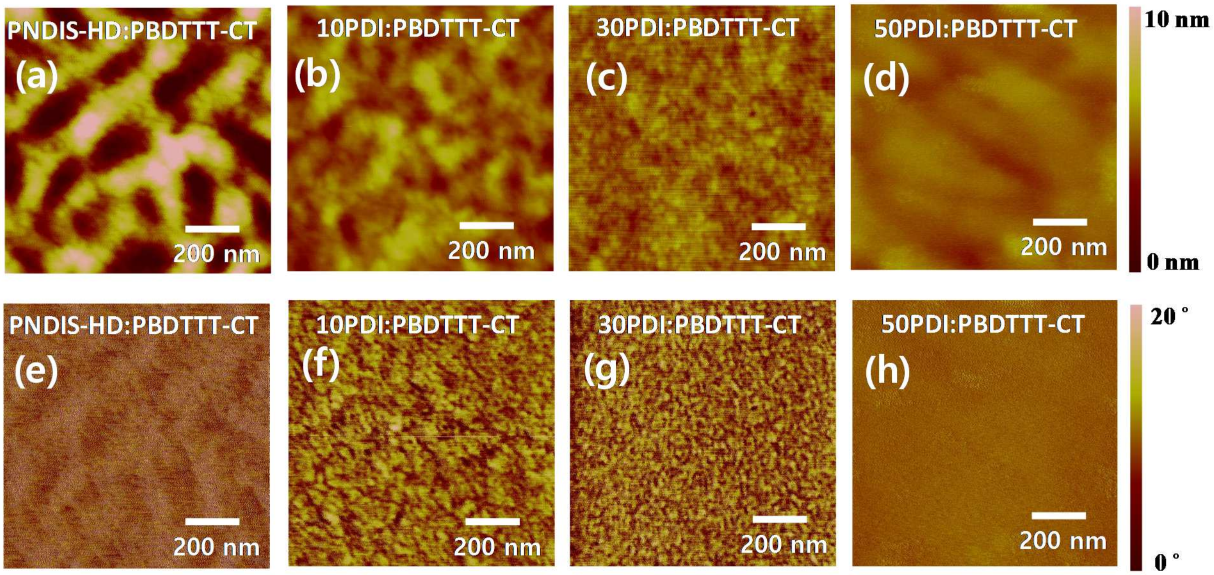

Figure 37. AFM height (a-d) and phase (e-h) images (1 μm × 1μm) of PNDIS-HD:PBDTTT-CT (1:1 *wt/wt*) and *x*PDI:PBDTTT-CT (1:1*wt/wt*) blend solar cells.

Morphology of BHJ Solar Cells. The surface and bulk morphologies of the *x*PDI:PBDTTT-CT (1:1 *wt/wt*) blend films as well as the reference PNDIS-HD:PBDTTT-CT (1:1 *wt/wt*) blend films prepared in identical ways as for the solar cells (film aged at room temperature for 96 hours in an argon-filled glovebox) were investigated by atomic force microscopy (AFM) and bright-field transmission electron microscopy (BF-TEM) imaging, respectively. AFM height and phase images (1 μm × 1 μm) are shown in **Figure 37.** The reference PNDIS-HD:PBDTTT-CT blend films showed the largest phase-separated domains (~200 nm) with a roughness of 2.25 nm, indicating a strong tendency of the two components to phase separate into large domains. A dramatic change in the blend surface morphology is observed by increasing the amorphous PDI-selenophene component and thus decreasing the crystallinity of the acceptor polymer paired with

PBDTTT-CT. First, the surface roughness decreased from 2.25 nm in PNDIS-HD blends to 1.61 nm and 0.62 nm in 10PDI and 30PDI blends, respectively. Second, the phase-separated domain sizes observed in *x*PDI:PBDTTT-CT blends decreased significanlty compared to the PNDIS-HD:PBDTTT-CT blends. Although crystallinity (L_c = 9.47 nm) of 10PDI is only slightly lower than that of PNDIS-HD (L_c = 10.22 nm), the observed phase-separated domain sizes (~100 nm) in the 10PDI:PBDTTT-CT blend morphology is decreased by half, indicating that small differences in the crystallinity of the component polymers can have a large impact on the surface morphology of the blends. In the case of 30PDI:PBDTTT-CT blends, a uniform phase-separated morphology with domains of about 20 nm in size was observed and domain size was estimated from 200 × 200 nm^2 phase images. However, a clear phase-separated microstructure with distinct domains was not observed in the 50PDI:PBDTTT-CT blends; a surface roughness of 0.33 nm was determined from the AFM phase image of this blend. The phase-separated microstructure with ~ 20 nm distinct domain sizes observed in the surface morphology of 30PDI:PBDTTT-CT blends is consistent with the observed high performance photovoltaic devices and our above earlier conclusion that this blend system is compatible. We note that based on the previously discussed photovoltaic properties, we concluded that the 50PDI:PBDTTT-CT blend system is incompatible; the AFM images of the surface morphology of this blend do not reveal a phase-separated microstructure with distinct domains, implying that its incompatibility may originate elsewhere. Overall, these results of AFM imaging demonstrate that the surface morphology of polymer/polymer blend solar cells is controlled by the crystallinity of the components, which in turn is controlled by the NDI/PDI random copolymer composition.

The bright field TEM images of the bulk morphologies of similarly prepared polymer/polymer blends are shown in **Figure 38**. The overall trend of phase-separated domains in

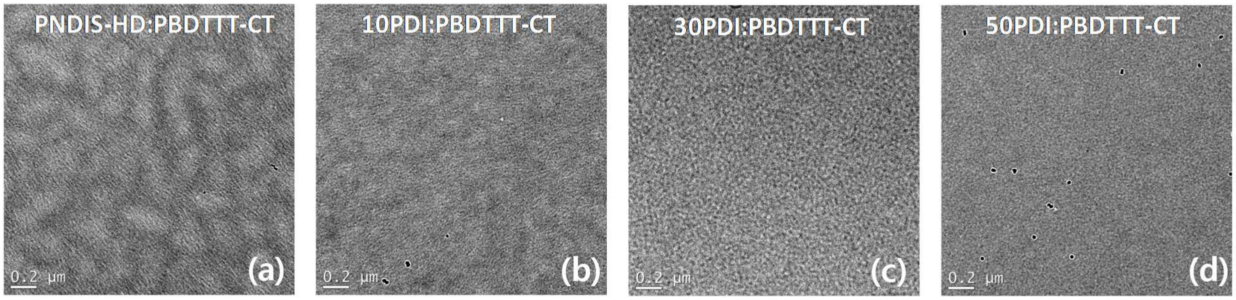

Figure 38. Bright-field transmission electron microscopy (BF-TEM) images of PNDIS-HD:PBDTTT-CT (1:1 *wt/wt*) and *x*PDI:PBDTTT-CT (1:1*wt/wt*) blend films.

the blends decreasing in size progressively from PNDIS-HD to 50PDI blends is seen in the BF-TEM results similar to the trend seen in the AFM images. In the PNDIS-HD:PBDTTT-CT blend film, isolated domains with sizes of about 200 nm are observed (**Figure 38a**). Such isolated domains could act as a charge traps, impede charge transport, and act as recombination centers and thus may explain the incompatibility and the poor photovoltaic properties of PNDIS-HD:PBDTTT-CT blends. In general, the *x*PDI:PBDTTT-CT blends showed much smaller and better interconnected phases compared to the PNDIS-HD blends. The 10PDI blend has significantly decreased phase-separated domain sizes (~100 nm) while the 30PDI blends has phases separated on the scale of 20 nm. In the 50PDI:PBDTTT-CT blends, however, a clear contrast between two phases is not observed (**Figure 38d**). The observed well interconnect nanoscale domains in the bulk morphology of 30PDI:PBDTTT-CT blend as seen in the BF-TEM image (Figure 7c) is consistent with compatibility of this blend system and its excellent photovoltaic properties. From these results, we conclude that the bulk morphology of polymer/polymer blend solar cells can be controlled by tuning the crystallinity of one of the polymer components.

Bulk Charge Transport in BHJ Blend Films. We investigated the bulk charge carrier mobilities in the polymer/polymer blend films, which were prepared similarly to the photovoltaic devices, by using space-charge-limited-current (SCLC) measurement. The electron mobility was measured in an ITO/ZnO/active layer/LiF/Al device structure and the hole mobility was measured in an ITO/PEDOT:PSS/active layer/Au device structure. The current-voltage curves and SCLC fittings of the data are shown in **Figure 39.**

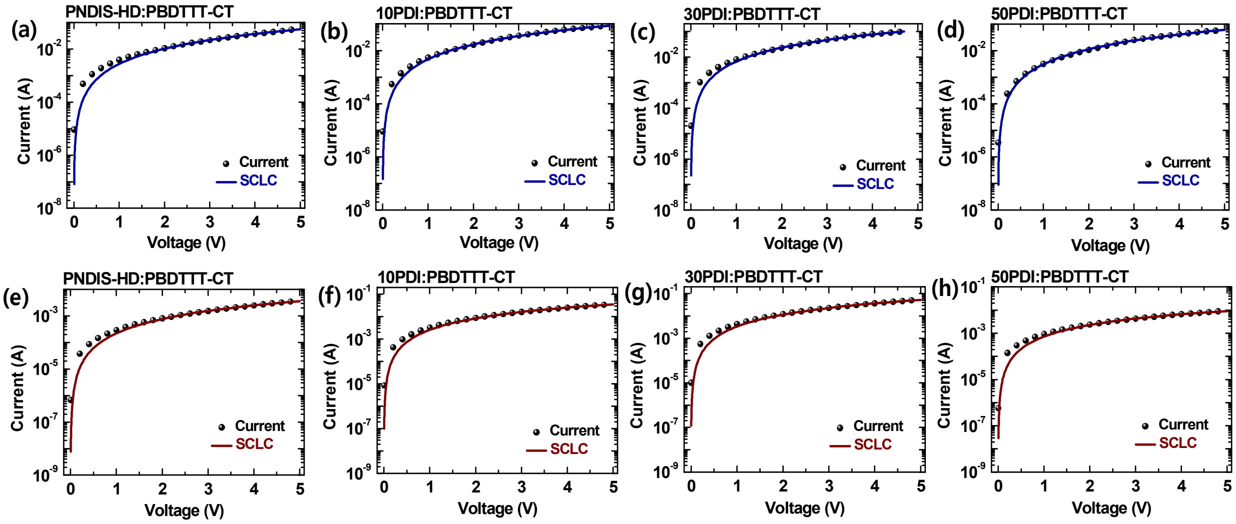

Figure 39. Current-voltage curves and space-charge-limited current (SCLC) fittings of PNDIS-HD:PBDTTT-CT and *x*PDI:PBDTTT-CT blend films. Hole-only SCLC devices (a-d): ITO/PEDOT:PSS/blend/Au and electron-only SCLC devices (e-h): ITO/ZnO/blend/LiF/Al.

The observed bulk hole and electron mobilities in the polymer/polymer blends were found to vary substantially with crystallinity of the acceptor polymer component and thus with the copolymer composition. The reference PNDIS-HD:PBDTTT-CT blend system have low bulk hole and electron mobilities of 7.5×10^{-4} cm^2/Vs and 7.2×10^{-5} cm^2/Vs, respectively, and this result can be understood from the observed blend morphology in which large phase-separated isolated domains are not interconnected. This low and unbalanced bulk charge carrier mobilities ($\mu_h/\mu_e = 2.6$) of PNDIS-HD:PBDTTT-CT blends can explain the poor performance of the solar cells. Compared to the reference PNDIS-HD blends, the *x*PDI:PBDTTT-CT blends showed significantly enhanced bulk charge carrier mobilities. The hole mobility of *x*PDI/PBDTTT-CT blends varied from 6.0×10^{-4} cm^2/Vs in 50PDI to 1.7×10^{-3} cm^2/Vs in 10PDI and to 2.6×10^{-3} cm^2/Vs in 30PDI. The hole mobility in 30PDI blends is enhanced by a factor of 3.3 compared to the hole mobility in the reference PNDIS-HD blends. Clearly, the bulk morphology in 30PDI:PBDTTT-CT is more favorable to hole transport in this blend than in either PNDIS-HD or 10PDI or 50PDI blends even though the donor polymer is identical in all the blends. The bulk electron mobility varied from 1.8×10^{-4} cm^2/Vs in 50PDI blends to 8.5×10^{-4} cm^2/Vs in 10PDI blends and to 1.0×10^{-3} cm^2/Vs in 30PDI blends. It is to be noted that electron mobility in 30PDI blends has increased by a factor of 13.8 compared to the electron mobility in the reference PNDIS-HD blends. We point out that both electron and hole mobilities are highest and the carrier asymmetry ($\mu_h/\mu_e = 2.6$) lowest in the 30PDI:PBDTTT-CT blends, which are highly benefitial to high photocurrent and conversion efficiency in the BHJ solar cells. These results can be understood in terms of the previously discussed bulk morphology as imaged by BF-TEM (**Figure 38**), which revealed a phase-separated, interconnected microstructure with small (~ 20 nm) domains in 30PDI:PBDTTT-CT blends.

It is very instructive that the trends observed in the field-effect electron mobility of neat films (**Table 17**) of the acceptor polymers (PNDIS-HD, 10PDI, 30PDI, and 50PDI) in which μ_e decreased monotonically from PNDIS-HD to 50PDI is not observed in the bulk electron transport in the blends. This means that the electron mobility of neat films *per se* could not be a useful guide in selecting components that would form compatible blends in all-polymer solar cells. However, the present results demonstrate that the bulk crystallinity, quantified here in terms of L_c, could be used as an important criterion in selecting compatible donor/acceptor pairs in polymer/polymer blend solar cells.

4.3.4 *Conclusions*

Our study has investigated the problem of how to control the crystallinity of the acceptor polymer component of polymer/polymer blend solar cells and its impact on blend compatibility, blend morphology, and performance of all-polymer solar cells. We have found that the crystallinity (e.g. L_c) of new n-type semiconducting NDI/PDI-selenophene random copolymers *x*PDI (x = 10, 50, 50 mol% PDI), synthesized by Stille copolymerization, varies with the copolymer composition, which thus provides a synthetic means of controlling the crystallinity of a polymer component of BHJ solar cells. Blends of the reference crystalline (L_c = 10.22 nm) acceptor polymer PNDIS-HD with crystalline (L_c = 9.47 nm) donor polymer PBDTTT-CT were found to be incompatible with poor photovoltaic properties (PCE = 1.4 %). However, similar blends of the new NDI/PDI copolymer (30PDI) acceptor with optimal crystallinity (L_c = 5.11 nm) and the same PBDTTT-CT were found to be compatible with substantially enhanced photovoltaic properties (PCE = 6.3 %, J_{sc} = 18.6 mA/cm^2, and EQE = 91 %), which are the highest to date for all-polymer solar cells. Indeed, the observed J_{sc} and EQE in 30PDI:PBDTTT-CT blend solar cells are higher than reported values for PC$_{71}$BM:PBDTTT-CT devices.

AFM and bright-field TEM imaging of the surface and bulk morphologies of the various polymer/polymer blends found that the blend microstructure varied substantially with the crystallinity of the acceptor polymer component. Both surface and bulk morphologies of the reference PNDIS-HD:PBDTTT-CT blends revealed a phase-separated microstructure with large (~ 200 nm) isolated domains whereas the 30PDI:PBDTTT-CT blends had a phase-separated microstructure with small (~ 20 nm) interconnected domains. The bulk hole (μ_h) and electron (μ_e) mobilities and carrier asymmetry ($\mu_{h/}\mu_e$) in the polymer/polymer blends varied dramatically with crystallinity of the acceptor polymer component, reaching their optimal values at the optimum crystallinity found in 30PDI. The results of this study demonstrate that the bulk crystallinity of a polymer component in polymer/polymer blend solar cells is a critical factor that determines blend compatibility, blend morphology, and photovoltaic properties; furthermore, this crystallinity can be controlled by molecular design. The bulk crystallinity quantified here in terms of the average crystalline domain size L_c is a material property that can be used as an important criterion for selecting donor/acceptor pairs in polymer/polymer blend solar cells.

4.3.5 *References*

(1) (a) Halls, J. J. M.; Walsh, C. A.; Greenham, N. C.; Marseglia, E. A.; Friend, R. H.; Moratti, S. C.; Holmes, A. B. *Nature* **1995**, *376*, 498. (b) Jenekhe, S. A.; Yi, S. J. *Appl. Phys. Lett*. **2000**, *77*, 2635. (c) Alam, M. M.; Jenekhe, S. A. *Chem. Mater*. **2004**, *16*, 4647. (d) C. R. McNeill, *Energy Environ. Sci*. **2012**, *5*, 5653.

(2) (a) Ahmed, E.; Ren, G.; Kim, F. S.; Hollenbeck, E. C.; Jenekhe, S. A. *Chem. Mater*. **2011**, *23*, 4563. (b) Li, H.; Earmme, T.; Ren, G.; Saeki, A.; Yoshikawa, S.; Murari, N. M.; Subramaniyan, S.; Crane, M. J.; Seki, S.; Jenekhe, S. A. *J. Am. Chem. Soc*. **2014**, *136*, 14589. (c) Guo, X.; Facchetti, A.; Marks, T. J. *Chem. Rev.* **2014**, *114*, 8943.

(3) (a) Schubert, M.; Dolfen, D.; Frisch, J.; Roland, S.; Steyrleuthner, R.; Stiller, B.; Chen, Z.; Scherf, U.; Koch, N.; Facchetti, A.; Neher, D. *Adv. Energy Mater.* **2012,** *2*, 369. (b) Zhou, E.; Cong, J.; Hashimoto, K.; Tajima, K. *Adv. Mater.* **2013,** *25*, 6991. (c) Mori, D.; Benten, H.; Okada, I.; Ohkita, H.; Ito, S. *Energy Environ. Sci*. **2014**, *7*, 2939. (d) Hwang, Y. J.; Earmme, T.; Subramaniyan, S.; Jenekhe, S. A. *Chem. Commun*. **2014**, *50*, 10801. (e) Mori, D.; Benten, H.; Okada, I.; Ohkita, H.; Ito, S. *Adv. Energy Mater*. **2014**, *4*, 1301006. (f) Kang, H.; Kim, K. H.; Choi, J.; Lee, C.; Kim, B. J. *ACS Macro Lett*. **2014**, *3*, 1009. (g) Zhou, N.; Lin, H.; Lou, S. J.; Yu, X.; Guo, P.; Manley, E. F.; Loser, S.; Hartnett, P.; Huang, H.; Wasielewski, M. R.; Chen, L. X.;

Chang, R. P. H.; Facchetti, A.; Marks, T. J. *Adv. Energy Mater.* **2014**, *4*, 1300785. (h) Mu, C.; Liu, P.; Ma, W.; Jiang, K.; Zhao, J.; Zhang, K.; Chen, Z.; Wei, Z.; Yi, Y.; Wang, J.; Yang, S.; Huang, F.; Facchetti, A.; Ade, H.; Yan, H. *Adv. Mater*. **2014**, *26*, 7224.

(4) (a) Zhan, X.; Tan, Z.; Domercq, B.; An, Z.; Zhang, X.; Barlow, S.; Li, Y.; Zhu, D.; Kippelen, B.; Marder, S. R. *J. Am. Chem. Soc*. **2007**, *129*, 7246. (b) Zhou, E.; Cong, J.; Wei, Q.; Tajima, K.; Yang C.; Hashimoto, K. *Angew. Chem. Int. Ed.* **2011**, *50*, 2799. (c) Zhou, Y.; Yan, Q.; Zheng, Y. Q.; Wang, J. Y.; Zhao, D.; Pei, J. *J. Mater. Chem. A* **2013**, *1*, 6609. (d) Zhan, Y.; Kurosawa, T.; Ma, W.; Guo, Y.; Fang, L.; Vandewal, K.; Diao, Y.; Wang, C.; Yan, Q.; Reinspach, J.; Mei, J.; Appleton, A. L.; Koleilat, G. I.; Gao, Y.; Mannsfeld, S. C. B.; Salleo, A.; Ade, H.; Zhao, D.; Bao, Z. *Adv. Mater*. **2014**, *26*, 3767. (e) Kozycz, L. M.; Gao, D.; Tilley, A. J.; Seforos, D. S. *J. Polym. Sci. A Polym. Chem*. **2014**, *52*, 3337.

(5) (a) Kietzke, T.; Horhold, H. H.; Neher, D. *Chem. Mater*, **2005**, *17*, 6532. (b) Holcombe, T. M.; Woo, C. H.; Kavulak, D. F. F.; Thompson, B. C.; Frechet, J. M. J. *J. Am. Chem. Soc*. **2009**, *131*, 14160. (c) Mori, D.; Benten, H.; Ohkita, H.; Ito, S.; Miyake, K. *ACS Appl. Mater. Interfaces* **2012**, *4*, 3325. (d) Guo, C.; Lin, Y. H.; Witman, M. D.; Smith, K. A.; Wang, C.; Hexemer, A.; Stzalka, J.; Gomez, E. D.; Verduzco, R. *Nano Lett*. **2013**, *13*, 2957. (e) Li, W.; Roelofs, W. S. C.; Turbiez, M.; Wienk, M. M.; Janssen, R. A. J. *Adv. Mater*. **2014**, *26*, 3304. (f) Jung, I. H.; Lo, W. Y.; Jang, J.; Chen, W.; Zhao, W.; Landry, E. S.; Lu, L.; Talapin, D. V.; Yu, L. *Chem. Mater*. **2014**, *26*, 3450.

(6) (a) Earmme, T.; Hwang, Y. J.; Murari, N. M.; Subramaniyan, S.; Jenekhe, S. A. *J. Am. Chem. Soc.* **2013**, *135*, 14960. (b) Earmme, T.; Hwang, Y. J.; Subramaniyan, S.; Jenekhe, S. A. *Adv. Mater*. **2014**, *26*, 6080.

(7) (a) Small, C. E.; Chen, S.; Subbiah, J.; Amb, C. M.; Tsang, S. W.; Lai, T. H.; Reynolds, J. R.; So, F. *Nat. Photon*. **2012**, *6*, 115. (b) He, Z.; Zhong, C.; Su, S.; Wu, H.; Cao, Y. *Nat. Photon*. **2012**, *6*, 591. (c) Liao, S. H.; Jhuo, H. J.; Cheng, Y. S.; Chen, S. A. *Adv. Mater*. **2013**, *25*, 4766. (d) Cabanetos, C.; Labban, A. E.; Bartelt, J. A.; Douglas, J. D.; Mateker, W. R.; Frechet, J. M. J.; McGehee, M. D.; Beaujuge, P. M. *J. Am. Chem. Soc.* **2013**, *135*, 4656. (e) Chen, J. D.; Cui, C.; Li, Y. Q.; Zhou, L.; Ou, Q. D.; Li, C.; Li, Y.; Tang, J. X. *Adv. Mater.* **2015**, *27*, 1035. (f) Xu, T.; Yu, L. *Mater. Today* **2014**, *17*, 11.

(8) (a) Anthony, J. E.; Facchetti, A.; Heeney, M.; Marder, S. R.; Zhan, X. *Adv. Mater*. **2010**, *22*, 3876. (b) Facchetti, A. *Mater. Today* **2013**, *16*, 123.

(9) (a) Utracki, L. A. Polymer Alloys and Blends, Hanser Publishers, New York, **1990**. (b) Alam, M. M.; Tonzola, C. J.; Jenekhe, S. A. *Macromolecules*, **2003**, *36*, 6577.

(10) Zhao, G.; He, Y.; Li, Y. *Adv. Mater*. **2010**, *22*, 4355.

(11) (a) Subramaniyan, S.; Xin, H.; Kim, F. S.; Shoaee, S.; Durrant, J. R.; Jenekhe, S. A. *Adv. Energy Mater*. **2011**, *1*, 854. (b) Xin, H.; Subramaniyan, S.; Kwon, T.-W.; Shoaee, S.; Durrant, J. R.; Jenekhe, S. A. *Chem. Mater*. **2012**, *24*, 1995.

(12) (a) Shoaee, S.; Subramaniyan, S.; Xin, H.; Keiderling, C.; Tuladhar, P. S.; Jamieson, F.; Jenekhe, S. A.; Durrant, J. R. *Adv. Funct. Mater*. **2013**, *23*, 3286. (b) Jamieson, F. C.; Domingo, E. B.; McCarthy-Ward, T.; Heeney, M.; Stingelin, N.; Durrant, J. R. *Chem. Sci*. **2012**, *3*, 485.

(13) (a) Huo, L.; Zhang, S.; Guo, X.; Xu, F.; Li, Y.; Hou, J. *Angew. Chem. Int. Ed.* **2011,** *50*, 9697. (b) Fan, X.; Fang, G.; Cheng, F.; Qin, P.; Huang, H.; Li, Y. *J. Phys. D: Appl. Phys*. **2013**, *46*, 305106.

(14) (a) Hwang, Y. J.; Ren, G. Q.; Murari, N. M.; Jenekhe, S. A. *Macromolecules* **2012**, *45*, 9056. (b) Hwang, Y. J.; Murari, N. M.; Jenekhe, S. A. *Polym. Chem.* **2013,** *4*, 3187.

(15) Kronholm, D.; Hummelen, J. C. *Material Matters* **2007**, *2*, 16.

(16) Pavlishchuk, V. V.; Addison, A. W. *Inorg. Chim. Acta* **2000**, *298*, 97.

(17) Heeger, A. J. *Adv. Mater.* **2014,** *26*, 10.

(18) Ren, G.; Schlenker, C. W.; Ahmed, E.; Subramaniyan, S.; Olthof, S.; Kahn, A.; Ginger, D. S.; Jenekhe, S. A. *Adv. Funct. Mater*. **2013**, *23*, 1238.

(19) Patterson, A. L. *Phys. Rev*. **1939**, *56*, 972.

(20) (a) Wu, P. T.; Ren, G.; Jenekhe, S. A. *Macromolecules* **2010**, *43*, 3306. (b) Burkhart, B.; Khlyabich, P. P.; Thompson, B. C. *ACS Macro Lett*. **2012**, *1*, 660.

(21) Yan, H.; Zhu, L.; Li, D.; Zhang, Y.; Yi. Y.; Yang, Y.; Wei, Z.; Bredas, J. L. *J. Phys. Chem. C* **2014**, *118*, 29473.

(22) Guo, X.; Kim, F. S.; Seger, M. J.; Jenekhe S. A.; Watson, M. D. *Chem. Mater*. **2012**, *24*, 1434.

(23) Zhou, Y.; Fuentes-Hernandez, C.; Shim, J.; Meyer, J.; Giordano, A. J.; Li, H.; Winget, P.; Papadopoulos, T.; Cheun, H.; Kim, J.; Fenoll, M.; Dindar, A.; Haske, W.; Najafabadi, E.; Khan, T. M.; Sojoudi, H.; Barlow, S.; Graham, S.; Bredas, J. L.; Marder, S. R.; Kahn, A.; Kippelen, B. *Science* **2012**, *336*, 327.

(24) (a) Kim, Y.; Cook, S.; Tuladhar, S. M.; Choulis, S. A.; Nelson, J.; Durrant, J. R.; Bradley, D. D. C.; Giles, M.; McCulloch, I.; Ha, C. S.; Ree, M. *Nature Mater*. **2006**, *5*, 197. (b) Murari, N. M.; Crane, M. J.; Earmme, T.; Hwang, Y. J.; Jenekhe, S. A. *Appl. Phys. Lett*. **2014**, *104*, 223906.

(25) Mott, N. F.; Gurney, R. W. *Electronic Processes in Ionic Crystals*; Oxford University Press; London; **1940.**

Chapter 5. DEVICE ENGINEERING OF HIGH PERFORMANCE ALL-POLYMER SOLAR CELLS

5.1 7.7 % Efficient All-Polymer Solar Cells

5.1.1 *Introduction*

All-polymer solar cells, in which both the donor and acceptor materials that absorb light and transport charges are semiconducting polymers, have a great potential to replace fullerene/polymer devices.[1] Although considerable progress has been made in advancing the performance of polymer solar cells by using fullerene-based electron acceptors, with single-junction power conversion efficiencies (PCEs) of over 9 %,[2] the use of *n*-type semiconducting polymers as acceptors has potential to overcome the high cost, poor thermal/photochemical stability, limited light absorption in the visible-near infrared region, and other limitations of fullerene derivatives.[3] Among the various *n*-type semiconducting polymers investigated as electron acceptors in all-polymer bulk heterojucntion (BHJ) solar cells to date,[4-6] perylene diimide (PDI)-arylene[5] and nanphthalene diimide (NDI)-arylene[6] copolymers have emerged as the most promising. However, the performance of all-polymer solar cells composed of low band gap donor conjugated polymers and NDI- or PDI-based *n*-type semiconducting polymers has so far remained significantly lower than the corresponding fullerene/polymer devices. The main limitations of the PCE of all-polymer solar cells reported to date (~ 5 – 6 %) are the generally low short-circuit current ($\leq$ 14 mA cm^{-2}) and low fill factor ($\leq$ 50 – 60 %) compared to fullerene/polymer devices.[5, 6] Overcoming the limitations of current all-polymer BHJ devices requires exploration of new donor/acceptor polymer/polymer blend systems and blend processing strategies towards more optimal light harvesting, blend morphology, charge photogeneration, and bulk electron and hole mobilities.

Diverse methods have been successfully used for controlling the morphology of fullerene/polymer BHJ devices, including thermal annealing,[7] solvent vapor annealing,[8] self-assembly of polymer nanowires,[9] and use of processing additives.[10] These approaches have also been explored to varying degrees in polymer/polymer blend systems.[4-6] However, the self-organization behavior of polymer/polymer blends can be expected to be very different from that of the corresponding fullerene/polymer blends owing to the difference in molecular geometry of fullerene acceptors (spherical nanoparticles) and *n*-type semiconducting polymer acceptors (linear semi-flexible/semi-rigid chains). The self-organization kinetics and morphology of polymer/polymer blend films processed from solution could be influenced by factors such as the solvent, solubilities of both polymers, crystalline or amorphous nature of each polymer, molecular weight, glass and/or melt transitions of both polymers, flexibility/rigidity of the chains, miscibility of the polymers, and chain entanglements.[11] Most of these factors are largely fixed for a given polymer/polymer blend solution being processed into thin films and thus the blend self-organization rate and subsequent blend morphology will be dominated by the post-deposition annealing temperature and solvent evaporation rate from a spin coated wet film.

In this section, I show high performance all-polymer solar cells with record 7.7 % power conversion efficiency, record short-circuit current density (18.8 mA cm^{-2}) and 85 % peak external quantum efficiency. We show that solvent evaporation rate and self-organization of the polymer/polymer blend films, composed of a high-mobility crystalline naphthalene diimide (NDI)-selenophene copolymer acceptor (PNDIS-HD) and small band gap benzodithiophene (BDT)-thieno[3,4-b]thiophene (TT) copolymer donor (PBDTT-FTTE), can be controlled by film aging at room temperature and leads to a two-fold enhancement in efficiency compared to the thermally (175 ˚C) annealed devices. The slower self-organization of polymer/polymer blends facilitated by room temperature film aging, results in enhanced electron mobility as well as a more favorable bulk morphology as observed by photoluminescence (PL) quenching analysis and grazing incidence wide-angle X-ray scattering (GIWAXS) studies. We note that the performance of these all-polymer (PNDIS-HD:PBDTT-FTTE) blend solar cells is currently limited by the fill factor (~ 50%), which is largely caused by a significant imbalance in charge carrier mobilities and high bimolecular recombination. Indeed, the observed short-circuit current density (18.8 mA cm^{-2}) and EQE (96 %) are superior to values reported for the corresponding $PC_{71}BM$/PBDTT-FTTE solar cells.[2c, 12] Power conversion efficiencies exceeding 10 % can thus be expected in the *n*-type polymer:PBDTT-FTTE (all-polymer) blend solar cells if fill factors exceeding 65 – 70 % could be achieved as observed in the $PC_{71}BM$ devices.[2c, 12]

5.1.2 *Experimental Section*

Materials: PNDIS-HD was synthesized according to the known literature procedures.[6b] PBDTT-FTTE (PTB7-Th, $M_n > 25$ kDa, PDI = 1.8 – 2.2) was purchased from Solarmer Energy, Inc. and used as received. ZnO precursor solution was prepared by dissolving 1 g of zinc acetate dihydrate (99.999% trace metals basis, Aldrich) in 10 mL of 2-methoxyethanol (99.8%, anhydrous, Aldrich) with 0.28 g of ethanolamine (≥ 99.5%, Aldrich) as a sulfactant and stirring overnight under ambient conditions.

Fabrication and Characterization of All-Polymer Solar Cells: ITO glass substrate was cleaned sequentially in ultrasonic baths with acetone and isopropyl alcohol for 30 minutes, dried using air duster, and stored in vacuum oven. The ITO glass substrate was O_2 plasma treated for 90 seconds right before coating the ZnO layer. The ZnO precursor solution was spin-coated onto the

ITO glass at 5000 rpm for 40 sec, annealed at 250 °C on a hot plate in air for 1 hr to make 20 – 30 nm thick ZnO layer and the glass/ITO/ZnO substrate was transferred into an Argon-filled glove box. A 0.05 *wt*% polyethylenimine (PEI, M_w ~ 25000, Aldrich 408727) in 2-methoxyethanol solution was spin-coated onto the ZnO layer and dried at 110 °C on a hot plate in air for 10 minutes and the glass/ITO/ZnO/PEI substrate was transferred into an argon-filled glove box. Active layer (e.g. PNDIS-HD:PBDTT-FTTE blend (1:1 *wt/wt*)) solution in chlorobenzene was spin-coated at 1000 rpm for 20 seconds. After spin-coating, the wet film was either thermally annealed at 175 °C for 10 min or film-aged inside the glove box for 72 hours (3 days) followed by thermal vacuum deposition of MoO_3 (7.5 nm) and Ag anode (100 nm). All the active layers have thicknesses of 115 ± 7 nm. Five pixels, each with an active area of 4 mm^2, were fabricated per ITO substrate. The photovoltaic cells were tested under AM 1.5 G solar illumination at 100 mW cm^{-2} in ambient condition using a Solar Simulator (model 16S, Solar Light Co., Philadelphia, PA) with a 200W Xenon Lamp Power Supply (Model XPS 200, Solar Light Co., Philadelphia, PA) calibrated by NREL certified Si photodiode (Model 1787–04, Hamamatsu Photonics K.K., Japan) and a HP4155A semiconductor parameter analyzer (Yokogawa Hewlett-Packard, Japan). After the *J-V* measurement, the external quantum efficiency (EQE) was measured by using a solar cell quantum efficiency measurement system (Model QEX10, PV Measurements, Inc., Boulder, CO) with a 2 mm^2 (2 mm×1mm) size masked incident light source and TF Mini Super measurement apparatus for multiple devices in a single substrate. The EQE system was calibrated with a Si photodiode before measurement. Current-voltage (*J*−*V*) characteristics of the space-charge-limited current (SCLC) devices were measured by using a HP4155A semiconductor parameter analyzer (Yokogawa Hewlett-Packard, Tokyo) in dark ambient conditions. Grazing incidence wide angle X-ray scattering (GIWAXS) was performed at the Stanford Synchrotron Radiation Lightsource (SSRL) on beamline 11-3 using a wavelength of 0.942 Å and sample to detector distance of 400 mm. Samples were prepared using all of the same processing methods described above with the difference being that the active layer was spun onto silicon, rather than ITO substrates.

5.1.3 *Results and Discussions*

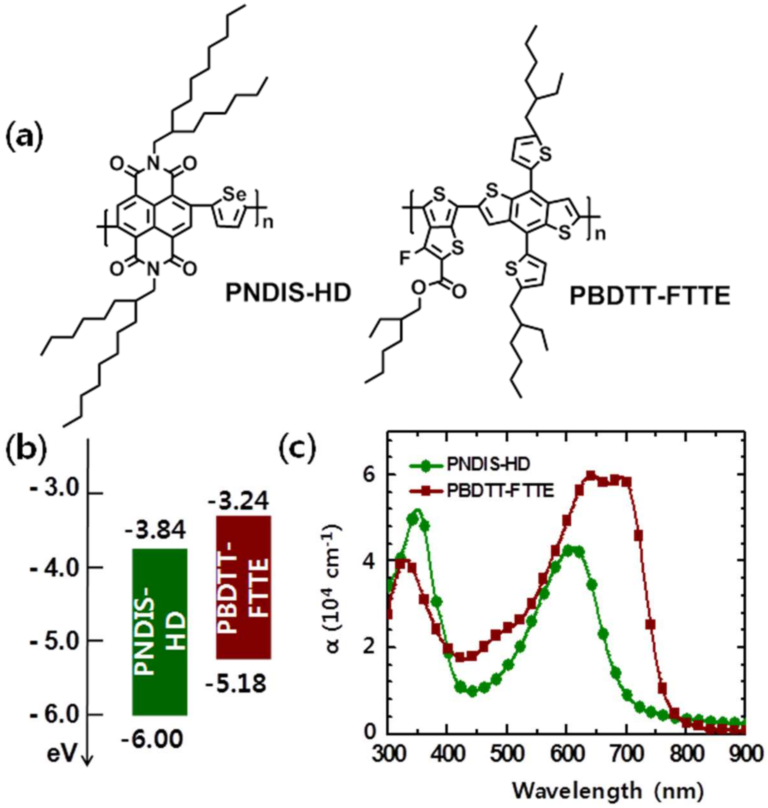

Figure 40. (a) Molecular structures of acceptor polymer (PNDIS-HD) and donor polymer (PBDTT-FTTE). (b) HOMO/LUMO energy levels of the acceptor and donor polymers. (c) Optical absorption spectra (α) of the acceptor and donor polymers.

The naphthalene diimide (NDI)-selenophene copolymer acceptor, PNDIS-HD, was synthesized and purified following our previous report;[6b] the PNDIS-HD sample has a weight average molecular weight (M_w) of 42.6 kDa with a polydispersity index (PDI) of 1.5. The donor polymer, PBDTT-FTTE (M_n > 25 kDa, PDI = 1.8 – 2.2), was purchased from Solarmer Energy, Inc. and was used as received. The molecular and electronic structures of PNDIS-HD and PBDTT-FTTE polymers are shown in **Figure 40a** and **b**, respectively. PNDIS-HD has a low lying lowest unoccupied molecular orbital (LUMO) energy level, with an energy of – 3.84 eV relative to vacuum, as determined from the onset reduction potential (– 0.8 eV vs SCE) in cyclic voltammetry (CV). CV scans up to 2 V (vs SCE) did not show an oxidation wave due to its weak electron donating nature. We thus expect the HOMO energy level of PNDIS-HD to be either at or lower lying than – 6.0 eV. This is reasonable, considering that a HOMO energy level of –5.95 eV was observed for NDI-biselenophene copolymer.[6a, 13] We measured the HOMO/LUMO energy levels of PBDTT-FTTE to be – 5.18 eV/– 3.24 eV. The energy level offsets versus PNDIS-HD is thus ideal for efficient photoinduced electron and hole transfer. The thin film optical absorption spectra of both PNDIS-HD and PBDTT-FTTE (**Figure 40c**) reveal optical band gap (E_g^{opt}) of 1.76 eV and 1.59 eV, respectively. The two distinct absorption bands centered at 350 nm with a maximum absorption coefficient (α_{max}) of 5.09×10^4 cm^{-1} and centered at 609 nm with a α_{max} of 4.32×10^4 cm^{-1} in PNDIS-HD correspond to the π-π* or n-π* transition band and an intramolecular charge transfer (ICT) band,[14] respectively, were observed. The absorption bands of PBDTT-FTTE are mostly overlapped with those of PNDIS-HD, except in the near IR region where PBDTT-FTTE extends light harvesting up to 800 nm with higher α_{max} of 5.98×10^4 cm^{-1} at 645 nm compared to those of PNDIS-HD.

Polymer/polymer BHJ solar cells based on PNDIS-HD:PBDTT-FTTE (1:1 *wt/wt*) active layer were fabricated with the inverted device structure of ITO/ZnO/PEI/active layer/MoO_3/Ag and tested under 100 mW cm^{-2} air mass 1.5 global (AM 1.5 G) solar illumination in ambient air, using poly(ethylenimine) (PEI) is as a cathode interlayer. The active layer spin coated from chlorobenzene (CB) solution was either (i) thermally annealed at 175 ˚C for 10 min (fast solvent evaporation), which is the most common annealing process in OPVs, or (ii) placed in an argon-filled glove box to dry at room temperature (25 – 28 ˚C) for 72 hours (3 days) to facilitate slow solvent evaporation and slow blend film self-organization. The current density – voltage (*J-V*) curves and the external quantum efficiency (EQE) spectra are shown in **Figure 41a** and **Figure 41b**, respectively, and the photovoltaic properties are summarized in **Table 20**.

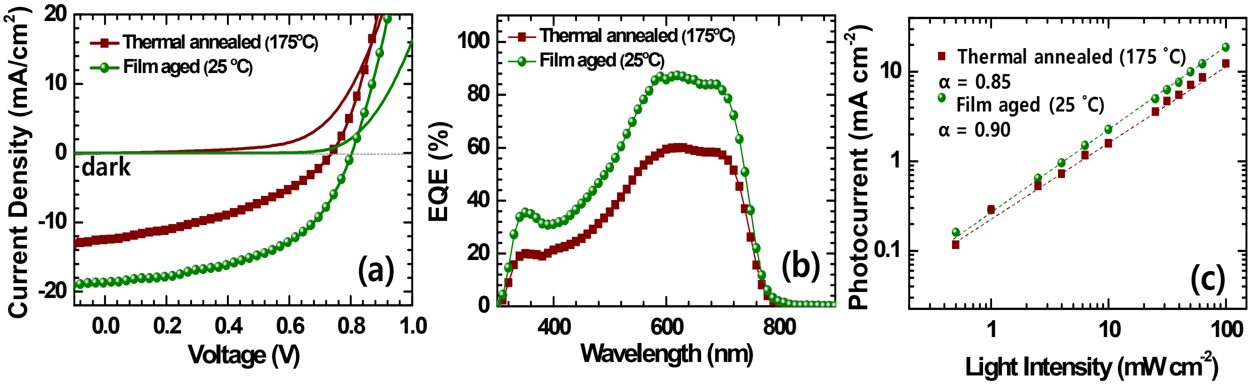

Figure 41. Current density-voltage ($J-V$) curves (a) and external quantum efficiency (EQE) spectra (b) of PNDIS-HD:PBDTT-FTTE (1:1 *wt/wt*) blend solar cells with thermally annealed (175 ˚C, 10 min) or film-aged (25 ˚C, 72 hr) active layer. (c) Short-circuit current density (J_{sc}) versus light intensity (P_{light}) data and power-law ($J_{sc} \propto P_{light}^{\alpha}$) fit for PNDIS-HD:PBTT-FTTE solar cells.

The thermally annealed devices have an average power conversion efficiency of 3.53 % while the maximum PCE is 3.66 % with a short-circuit current density (J_{sc}) of 12.64 mA cm^{-2}, open circuit voltage (V_{oc}) of 0.74 V, and a fill factor (*FF*) of 0.39. However, the photovoltaic properties of PNDIS-HD:PBDTT-FTTE solar cells where the active layers were dried at room temperature for 72 hours (3 days) have dramatically enhanced photovoltaic properties. These slowly dried devices have an average PCE of 7.21 % with a maximum PCE of 7.73 %, J_{sc} of 18.80 mA cm^{-2}, V_{oc} of 0.81 V, and *FF* of 0.51 (**Table 20**). Clearly, by slowing the solvent evaporation rate and thereby facilitating the gradual self-organization or phase separation of the PNDIS-HD:PBDTT-FTTE blend system, performance of the photovoltaic devices is substantially improved. First, we note that both of the observed short-circuit current and PCE of these film-aged PNDIS-HD:PBDTT-FTTE blends are the highest values reported to date for all-polymer solar cells. Second, it is also noteworthy that the observed short-circuit current density of 18.80 mA cm^{-2} (average J_{sc} = 18.61 ± 0.21 mA cm^{-2}) is even higher compared to the high performance PC$_{71}$BM:PBDTT-FTTE devices (J_{sc} = 15.0 – 17.9 mA cm^{-2}) with power conversion efficiencies of up to 10.3 %.[2c, 12] Third, it is clear that the observed *FF* value of 51 % for the present PNDIS-HD:PBDTT-FTTE blend solar cells is substantially lower than the reported 69 – 74 % for the corresponding PC$_{71}$BM:PBDTT-FTTE devices,[11] which suggests that the fill factor is the primary factor limiting the photovoltaic efficiency of the present all-polymer solar cells.

Table 20. Photovoltaic Properties of PNDIS-HD:PBDTT-FTTE Blend Solar Cells.[a)]

Processing Condition[b)]	J_{sc} (mA cm^{-2})	V_{oc} (V)	*FF*	PCE (%)	R_S (Ω cm^2)	R_{SH} [c)] (Ω cm^2)
175 ˚C, 10 min	*12.64* (12.16 ± 0.41)	*0.74* (0.73 ± 0.01)	*0.39* (0.39 ± 0.01)	*3.66* (3.53 ± 0.12)	15.25	167.95
25 ˚C, 72 hr	*18.80* (18.61 ± 0.21)	*0.81* (0.80 ± 0.00)	*0.51* (0.48 ± 0.01)	*7.73* (7.21 ± 0.24)	8.12	239.38

a)The photovoltaic properties were averaged over 20 devices. The values in italic are the photovoltaic parameters of solar cells with the highest PCEs. b) Spin coated active layer drying condition. c) The shunt resistances were extracted from the slop at 0V of *J-V* curves in the range of -0.1 – 0.1 V.

The external quantum efficiency (EQE) spectra of the best PNDIS-HD:PBDTT-FTTE blend devices are shown in **Figure 41b**. For both thermally (175 ˚C) annealed and room temperature film-aged devices, the photoresponse starts at 800 nm due to the smaller optical band gap of the donor polymer. The EQE of the thermally annealed device peaks at 60 % in the 580 – 700 nm region. In contrast, the EQE of the room temperature film-aged device rises to a maximum of 85 % in the 580 – 700 nm range and remains over 50% in the 500 – 750 nm range, where the optical absorption bands of the donor and acceptor polymers are overlapped. This indicates that both photoinduced electron and hole transfer are efficiently contributing to charge photogeneration.[15] The short-circuit current density (J_{sc}) values calculated from the EQE spectra (11.18 mA cm^{-2} for thermally annealed devices and 16.81 mA cm^{-2} for film-aged devices) were lower than the J_{sc} values directly measured from the J-V curves (**Figure 41a**), and the mismatch between the two values were within 10 %. This mismatch could be due to the initial degradation of the performance under ambient condition as well as the spectral mismatch between the simulated light source and the AM1.5 G solar spectrum. The much lower EQE in the 300 – 500 nm is also a major factor in the loss in efficiency of the present all-polymer solar cells compared to the corresponding $PC_{71}BM$:PBDTT-FTTE devices.

Short-circuit current as a function of illumination intensity (P_{light}) in thermally annealed and film-aged PNDIS-HD:PBDTT-FTTE blend photodiodes was measured to understand charge recombination kinetics in the devices (**Figure 41c**). The J_{sc} was measured and averaged for three devices at each of 12 different light intensities, which were varied from 100 mW cm^{-2} to 0.5 mW cm^{-2} by using neutral density filters. In general, J_{sc} has a power-law dependence on P_{Light} ($J_{sc} \propto P_{\mathrm{Light}}^{\alpha}$), and linearity ($\alpha \approx 1$) indicates weak charge carrier losses due to bimolecular recombination.[16] The observed power-law exponent (α) was 0.85 for the thermally annealed devices and 0.90 for the film-aged devices. Although $\alpha < 1$ in both thermally annealed and film-aged PNDIS-HD:PBDTT-FTTE blend devices mean that there is a significant amount of bimolecular recombination, the results indicate less recombination in the aged-film devices. This result can partially explain the lower fill factor (39 %) in the thermally annealed solar cells with high series resistance (R_S) of 15.25 Ω cm^2 and low shunt resistance (R_{SH}) of 167.95 Ω cm^2

compared to those seen in the film-aged solar cells (*FF* = 51 %, R_S = 8.13 Ω cm^2, R_{SH} = 239.38 Ω cm^2) (**Table 20**).

The bulk charge transport properties of the active layer can provide insight into the photovoltaic properties of the polymer/polymer blend solar cells, including the fill factor which depends on the carrier sweep-out rate relative to bimolecular charge recombination rate.[7] The bulk electron and hole mobilities of the PNDIS-HD:PBDTT-FTTE blend system were measured by using the space charge limited current (SCLC) method. The SCLC device structures for electron-only and hole-only measurements were ITO/ZnO/PEI/active layer/LiF/Al and

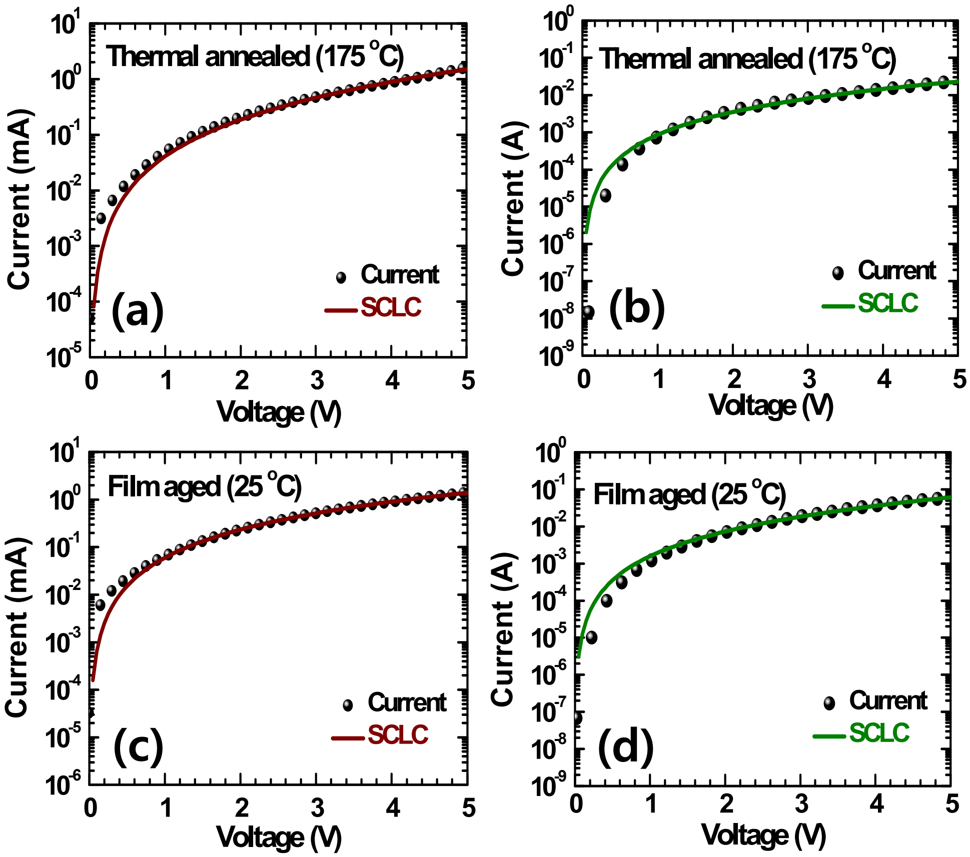

Figure 42. Space-charge-limited current (SCLC) fittings of thermally annealed devices (a, b) and film-aged devices (c, d) measured in ambient conditions. Electron-only SCLC devices (a, c): ITO/ZnO/PEI/blend/LiF/Al and hole-only SCLC devices (b, d): ITO/PEDOT:PSS/blend/Au.

ITO/PEDOT:PSS/active layer/Au, respectively. The measured *J-V* curves and Mott-Gurney equation fitting of the data are shown in **Figure 42** for the two processing conditions: thermally (175 ˚C) annealed and room-temperature (25 ˚C) film-aged. The hole mobility (μ_h) of the donor polymer (PBDTT-FTTE) in the thermally annealed blends is 2.74×10^{-4} cm^2 V^{-1} s^{-1}, which is essentially the same as in the room-temperature film-aged blends (3.11×10^{-4} cm^2 V^{-1} s^{-1}). This hole mobility value is also very comparable to μ_h values reported for other polymer:PBDTT-FTTE[6e] and PC$_{71}$BM:PBDTT-FTTE[2c, 12] blends. In contrast, the bulk electron mobility in the PNDIS-HD:PBDTT-FTTE blends is found to increase three-fold from 2.37×10^{-3} cm^2 V^{-1} s^{-1} in the thermally annealed blend films to 7.25×10^{-3} cm^2 V^{-1} s^{-1} in the room-temperature film-aged blends. It is important to note that the observed hole mobilities in both cases are about one order of magnitude lower than the electron mobilities, and there is thus significant imbalanced bulk charge transport in both thermally annealed ($\mu_h/\mu_e = 0.115$) and film-aged blend devices ($\mu_h/\mu_e = 0.043$). Although the higher in electron mobility in the film-aged blend solar cells leads to the enhanced fill factor (FF = 0.48) of these devices relative to those annealed at 175 ˚C (FF = 0.39) [17], the fill factor of these devices is still much lower than the corresponding fullerene/polymer photodiodes (FF > 0.6) [2c, 12]. This result suggests that the bulk hole transport properties of PNDIS-HD:PBDTT-FTTE blend system remains to be fully optimized for balanced bulk charge transport and advances in this area could substantially improve the FF and thus efficiency of these all-polymer BHJ solar cells.

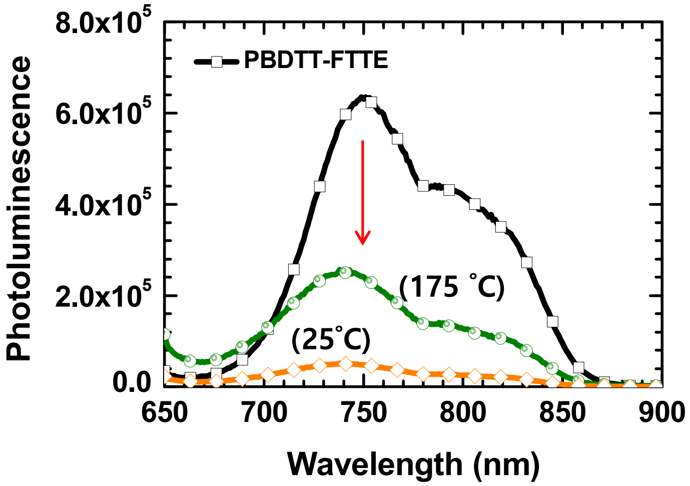

Figure 43. Photoluminescence (PL) spectra of PBDTT-FTTE film (open square) and the PBDTT-FTTE:PNDIS-HD blend films after thermal annealing at 175 ˚C (open circle) and after film aging at room temperature (open diamond). The excitation wavelength was 645 nm.

We performed photoluminescence (PL) quenching experiments to gain insight into the nanoscale morphology and molecular miscibility of the polymer/polymer blends. The PL spectra of PBDTT-FTTE film and PNDIS-HD:PBDTT-FTTE (1:1 *wt/wt*) blend films under the two different film-forming conditions (thermally annealed and room-temperature film-aged) were measured and the PL quenching rate was calculated by integrating the PL spectra. The PL spectra when excited with Xe flash lamp at a wavelength of 645 nm are shown in **Figure 43**. PL emission band of PBDTT-FTTE was found in the range of 670 – 860 nm with a peak at 750 nm. The PL spectrum of the blend films was quenched 92 % in the film-aged blend films compared to 78 % in the thermally-annealed blend films. This indicates that more efficient charge transfer occurs in the film-aged blend films due to the existence of smaller phase-separated domain sizes and/or greater molecular miscibility in the film-aged blend films than in the thermally-annealed blend films. This result is also consitent with the X-ray diffraction analysis that showed smaller mean crystalline domain sizes in the film-aged blend films (6.38 nm) compared to the themally annealed blend films (7.69 nm) calculated using Scherrer's equation.[18] However, no significant difference was observed by bright field transmission electron microscopy (TEM) imaging of the thermally annealed and film-aged blend films. We also note that there is a possibility of vertical phase separation in the blend films due to surface energy difference in PBDTT-FTTE and PNDIS-HD as found from the difference in water contact angle (θ = 104.8 ° in PBDTT-FTTE and θ = 110.6 ° in PNDIS-HD).[19]

Grazing incidence wide angle X-ray scattering (GIWAXS) analysis gives further insight into the morphology of the pure polymer films and the BHJ blend films (**Figure 44**). By looking at both the in-plane and out-of-plane directions of the 2D diffractograms, as shown in **Figure 44c** and **Figure 44d**, the molecular orientations of the polymers in the films were determined. In the

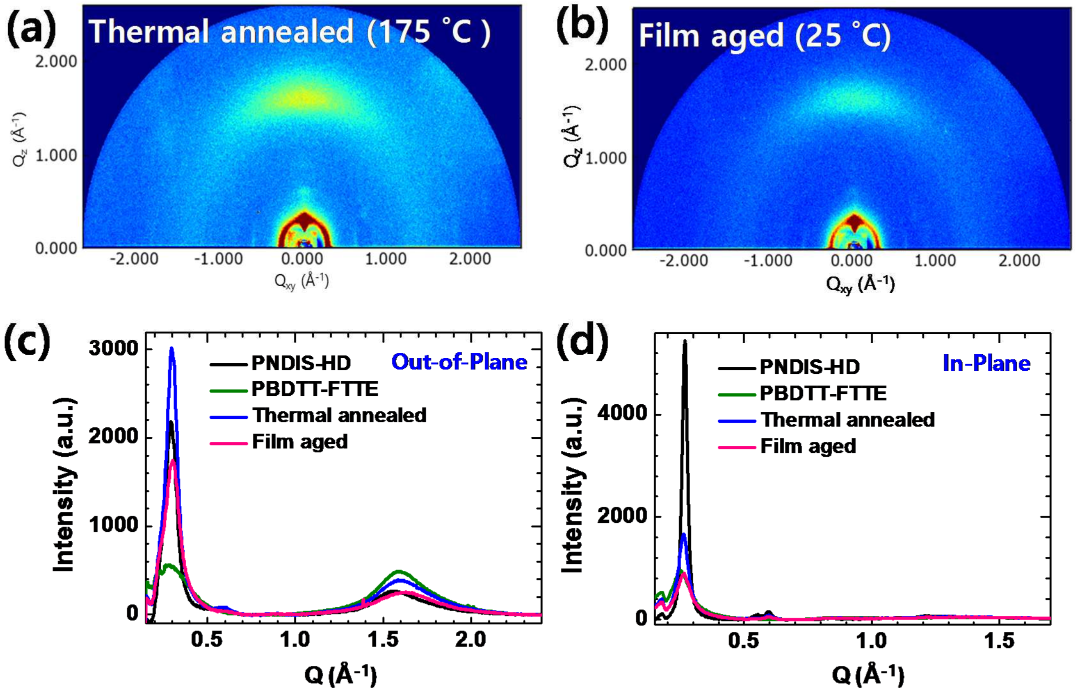

Figure 44. Grazing incidence wide-angle X-ray scattering (GIWAXS) patterns of thermally annealed (175 ˚C, 10 min) (a) or film-aged (25 ˚C, 72 hr) (b) PNDIS-HD:PBDTT-FTTE (1:1 *wt/wt*) blend films. Line cut of GIWAXS images in the out-of-plane (c) and in-plane (d) of neat polymer films of PNDIS-HD and PBDTT-FTTE, and their 1:1 *wt/wt* blend films.

neat PBDTT-FTTE films, the polymer adopts a face-on orientation with a strong π-π interaction, as seen from the large out-of-plane (010) peak centered at about 1.5 Å^{-1}. Neat films of PNDIS-HD also showed a face-on orientation, with very strong lamellar packing peaks observed in the in-plane direction. These films exhibit a shift in the *d*-spacing, and a peak broadening of the lamellar (100) peak in the out-of-plane direction, however, indicating some edge-on polymer chains with less ordered lamellar stacking. When we turn to blended PNDIS-HD:PBDTT-FTTE films, a shift of the lamellar peak to larger *d*-spacing was oberved in both the thermal annealed and the aged blend films, indicating that some mixing of the two polymers disorders the face-on stacking in the blend films. In the aged, blend film, a much lower peak intensity with a larger peak shift (0.7 – 0.9 Å) was observed compared to the thermally annealed films (0.4 – 0.5 Å). This indicates the existance of more amorphous mixed regions in the aged films, compared with thermally annealed samples. Moreover, a strong lamellar peak in the out-of-plane direction of thermally annealed blend films indicates more edge-on oriented regions compared to the film-aged blend film. From this result, we conclude that slow self-organization or crystallization process by room temperature film aging produces a more favorable bulk morphology with more mixed regions to facilitate charge spearation and less edge-on oriented polymer chains to facilitate carrier mobility through the film. Both are favorable for photovoltaic applications.

5.1.4 *Conclusions*

In conclusion, I have demonstrated that high performance all-polymer solar cells can be achieved by employing suitable donor and acceptor polymers and by controlling the polymer/polymer blend film self-organization rate through a simple film aging process at room temperature. The resulting all-polymer (PNDIS-HD:PBDTT-FTTE) blend solar cells combined a record 7.7 % PCE and 18.8 mA cm^{-2} short-circuit current density with an EQE of 85 %. The observed photovoltaic performance of the film-aged polymer/polymer blend solar cells is about two-fold enhanced compared with the related thermally (175 ˚C) annealed devices, which could be explained by the slower solvent evaporation rate enabled improvement in electron mobility and the favorable bulk morphology. The observed very high bulk electron mobility in these all-polymer blend devices suggests that even higher photocurrents are possible depending on a matching high-mobility donor polymer component. Our finding that the photocurrent of PNDIS-HD:PBDTT-FTTE BHJ devices is superior whereas their fill factors are much lower compared to those of $PC_{71}BM$:PBDTT-FTTE solar cells suggests that further optimization of materials and device engineering to achieve higher fill factors will enable the efficiency of all-polymer solar cells to exceed 10%.

5.1.5 *References*

[1] a) J. J. M. Halls, C. A. Walsh, N. C. Greenham, E. A. Marseglia, R. H. Friend, S. C. Moratti, A. B. Holmes, *Nature* **1995**, *376*, 498. b) S. A. Jenekhe, S. J. Yi, *Appl. Phys. Lett.* **2000**, *77*, 2635. c) J. E. Anthony, A. Facchetti, M. Heeney, S. R. Marder, X. Zhan, *Adv. Mater.* **2010**, *22*, 3876. d) M. M. Alam, S. A. Jenekhe, *Chem. Mater.* **2004**, *16*, 4647. d) A. Facchetti, *Mater. Today* **2013**, *16*, 123.

[2] a) C. E. Small, S. Chen, J. Subbiah, C. M. Amb, S. W. Tsang, T. H. Lai, J. R. Reynolds, F. So, *Nat. Photon*. **2012**, *6*, 115. b) Z. He, C. Zhong, S. Su, H. Wu, Y. Cao, *Nat. Photon*. **2012**, *6*, 591. c) S. H. Liao, H. J. Jhuo, Y. S. Cheng, S. A. Chen, *Adv. Mater*. **2013**, *25*, 4766.

[3] a) E. Ahmed, G. Ren, F. S. Kim, E. C. Hollenbeck, S. A. Jenekhe, *Chem. Mater*. **2011**, *23*, 4563. b) H. Li, T. Earmme, G. Ren, A. Saeki, S. Yoshikawa, N. M. Murari, S. Subramaniyan, M. J. Crane, S. Seki, S. A. Jenekhe, *J. Am. Chem. Soc*. **2014**, *136*, 14589.

[4] a) D. Mori, H. Benten, H. Ohkita, S. Ito, K Miyake, *ACS Appl. Mater. Interfaces* **2012**, *4*, 3325. b) W. Yu, D. Yang, X. Zhu, X. Wang, G. Tu, D Fan, J. Zhang, C. Li, *ACS Appl. Mater. Interfaces* **2014**, *6*, 2350. c) W. Li, W. S. C. Roelofs, M. Turbiez, M. M. Wienk, R. A. J. Janssen, *Adv. Mater*. **2014**, *26*, 3304. d) I. H. Jung, W. Y. Lo, J. Jang, W. Chen, D. Zhao, E. S. Landry, L. Lu, D. V. Talapin, L. Yu, *Chem. Mater*. **2014**, *26*, 3450. e) P. P. Khlyabich, A. E. Rudenko, B. Burkhart, B. C. Thompson, *ACS Appl. Mater. Interfaces* **2015**, *7*, 2322.

[5] a) X.W. Zhan, Z. A. Tan, B. Domercq, Z. S. An, X. Zhang, S. Barlow, Y. F. Li, D. B. Zhu, B. Kippelen, S. R. Marder, *J. Am. Chem. Soc*. **2007**, *129*, 7246. b) E. Zhou, K. Tajima, C. Yang, K Hashimoto, *J. Mater. Chem*. **2010**, *20*, 2362. c) E. Zhou, J. Cong, Q. Wei, K. Tajima, C. Yang and K. Hashimoto, *Angew. Chem. Int. Ed.* **2011**, *50*, 2799. d) Y. Zhan, T. Kurosawa, W. Ma, Y.guo, L. Fang, K. Vandewal, Y. Diao, C. Wang, Q. Yan, J. Reinspach, J. Mei, A. L. Appleton, G. I. Koleilat, Y. Gao, S. C. B. Mannsfeld, A. Salleo, H. Ade, D. Zhao, Z. Bao, *Adv. Mater*. **2014**, *26*, 3767. e) W. Liu, R. Tkachov, H. Komber, V. Senkovskyy, M. Schubert, Z. Wei, A. Facchetti, D. Neher, A. Kiriy, *Polym. Chem*. **2014**, *5*, 3404. f) Y. J. Hwang, T. Earmme, B. A. E. Courtright, F. N. Eberle, S. A. Jenekhe, *J. Am. Chem. Soc*. **2015**, *137*, 4424.

[6] a) Y. J. Hwang, G. Q. Ren, N. M. Murari, S. A. Jenekhe, *Macromolecules* **2012**, *45*, 9056. b) T. Earmme, Y. J. Hwang, N. M. Murari, S. Subramaniyan, S. A. Jenekhe, *J. Am. Chem. Soc.* **2013**, *135*, 14960. c) E. Zhou, J. Cong, K. Hashimoto, K. Tajima, *Adv. Mater.* **2013**, *25*, 6991. d) N. Zhou, H. Lin, S. J. Lou, X. Yu, P. Guo, E. F. Manley, S. Loser, P. Hartnett, H. Huang, M. R. Wasielewski, L. X. Chen, R. P. H. Chang, A. Facchetti, T. J. Marks, *Adv. Energy Mater.* **2014**, *4*, 1300785. e) D. Mori, H. Benten, I. Okada, H. Ohkita, S. Ito, *Energy Environ. Sci*. **2014**, *7*, 2939. f) Y. J. Hwang, T. Earmme, S. Subramaniyan, S. A. Jenekhe, *Chem. Cummun*. **2014**, *50*, 10801. g) T. Earmme, Y. J. Hwang, S. Subramaniyan, S. A. Jenekhe, *Adv. Mater*. **2014**, *26*, 6080. h) D.

Mori, H. Benten, I. Okada, H. Ohkita, S. Ito, *Adv. Energy Mater*. **2014**, *4*, 1301006. i) H. Kang, K. H. Kim, J. Choi, C. Lee, B. J. Kim, *ACS Macro Lett*. **2014**, *3*, 1009. j) C. Lee, H. Kang, W. Lee, T. Kim, K. H. Kim, H. Y. Woo, C. Wang, B. J. Kim, *Adv. Mater*. **2015**, DOI: 10.1002/adma.201405226.

[7] W. Ma, C. Yang, X. Gong, K, Lee, A. J. Heeger, *Adv. Funct. Mater*. **2005**, *15*, 1617.

[8] B. A. Gregg, *J. Phys. Chem*. **1996**, *100*, 852.

[9] H. Xin, F. S. Kim, S. A. Jenekhe, *J. Am. Chem. Soc*. **2008**, *130*, 5424.

[10] a) J. Peet, J. Y. Kim, N. E. Coates, W. L. Ma, D. Moses, A. J. Heeger, G. C. Bazan, *Nature Mater*. **2007**, *6*, 497. b) H. Xin, X. Guo, G. Ren, M. D. Watson, S. A. Jenekhe, *Adv. Energy Mater*. **2012**, *2*, 575.

[11] a) J. M. Frost, F. Cheynis, S. M. Tuladhar, J. Nelson, *Nano Lett*. **2006**, *6*, 1674. b) C. R. McNeill, N. C. Greenham, *Adv. Mater*. **2009**, *21*, 3840. c) C. R. McNeill, *Energy Environ. Sci*. **2012**, *5*, 5653. d) M. M. Alam, C. J. Tonzola, S. A. Jenekhe, *Macromolecules*, **2003**, *36*, 6577. e) L. A. Utracki, Polymer Alloys and Blends, Hanser Publishers, New York, **1990**.

[12] a) C. Cui, W. Y. Wong, Y. Li, *Energy Environ. Sci*. **2014**, *7*, 2276. b) S. H. Liao, H. J. Jhuo, P. N. Yeh, Y. S. Cheng, Y. L. Li, Y. H. Lee, S. Sharma, S. A. Chen, *Sci. Rep*. **2014**, *4*, 6813.

[13] B. C. Thompson, P. P. Khlyabich, B. Burkhart, A. E. Aviles, A. Rudenko, G. V. Shultz, C. F. Ng, L. B. Mangubat, *Green*, **2011**, *1*, 29.

[14] S. A. Jenekhe, L. Lu, M. M. Alam, *Macromolecules* **2001**, *34*, 7315.

[15] G. Ren, C. W. Schlenker, E. Ahmed, S. Subramaniyan, S. Olthof, A. Kahn, D. S. Ginger, S. A. Jenekhe, *Adv. Funct. Mater*. **2013**, *10*, 1238.

[16] P. Schilinsky, C. Waldauf, C. J. Brabec, *Appl. Phys. Lett.* **2002**, *81*, 3885.

[17] L. M. Andersson, C. Muller, B. H. Badada, F. Zhang, U. Wurfel, O. Inganas, *J. Appl. Phys.* **2011**, *110*, 024509.

[18] A. L. Patterson, *Phys. Rev*. **1939**, *56*, 978.

[19] N. M. Murari, M. J. Crane, T. Earmme, Y. J. Hwang, S. A. Jenekhe, *Appl. Phys. Lett*. **2014**, *104*, 223906.

Chapter 6. EFFICIENT POLYMER PHOTOVOLTAICS BASED ON NONFULLERENE SMALL MOLECULE ACCEPTORS

6.1 NONFULLERENE POLYMER SOLAR CELLS WITH 8 % EFFICIENCY ENABLED BY A HIGHLY TWISTED ELECTRON ACCEPTOR

6.1.1 *Introduction*

Advances in the design and synthesis of nonfullerene acceptors in the last few years have enabled a tremendous progress in developing more efficient nonfullerene organic photovoltaics (OPVs) and showed a great potential to replace the problematic fullerene acceptors[1-15]. The drawbacks of fullerene-based OPVs, including the small open-circuit voltage (V_{oc}), poor light harvesting, high cost, and poor photochemical stability[1-15], can be addressed by using suitable nonfullerene acceptors with their readily tunable molecular structure. However, the power conversion efficiency (PCE) of nonfullerene polymer solar cells (4 – 6 %)[1-15] is remained inferior to the fullerene-based devices (8 – 10 %)[16-21]. The major limitations on the efficiency of current nonfullerene OPV devices include the generally much lower short-circuit current density J_{sc} and fill factor (FF) values[1-15] compared to their $PC_{71}BM$ counterparts[16-21]. These limitations are ultimately rooted in the compatibility and morphology of the acceptor molecule/donor polymer blend and the three-dimensional (3D) structure of the acceptor. The spherical 3D structure of fullerene acceptors appears to facilitate their universal compatibility with numerous donor polymers[9, 15 22], resulting in interconnected 10 – 30 nm phase-separated domains with high mobility, isotropic, electron transport[23]. Known nonfullerene acceptors are rarely compatible (PCE > 3.0 %) with more than one donor polymer in OPV devices[24].

In our previous studies, we reported the synthesis of dimeric nonfullerene acceptors, DBFI-Ar, which two large, planar, monomeric, tetraazabenzodifluoranthene diimide (BFI) building blocks connected by various linker units, including thiophene (T), selenophene (S), 3,4-dimethylthiophene (DMT) to 3,4-dimethylthienothiophene (MTT) (**Scheme 8**)[9, 15]. DBFI-Ar showed dramatically different 3D molecular structures depending on the linker, and the resulted bulk heterojunction (BHJ) blends with the donor, thiazolothiazole-dithienosilole copolymer (PSEHTT)[25] gave a large disparity in PCE (2.6 – 6.4 %)[9, 15]. The results established the critical role of the linker connecting the dimer as well as the substituent groups on the aromatic linkers, and a large dependence of the twisted angle (θ) between large BFIs and the photovoltaic performances were found; the best PCE was achieved in DBFI-DMT which has the largest twisted angle of 62 °.[15] It was suggested that further increase in θ could lead to a large increase in photovoltaic efficiency by virtue of decreased anisotropy and enhanced charge photogeneration and isotropic electron transport[9].

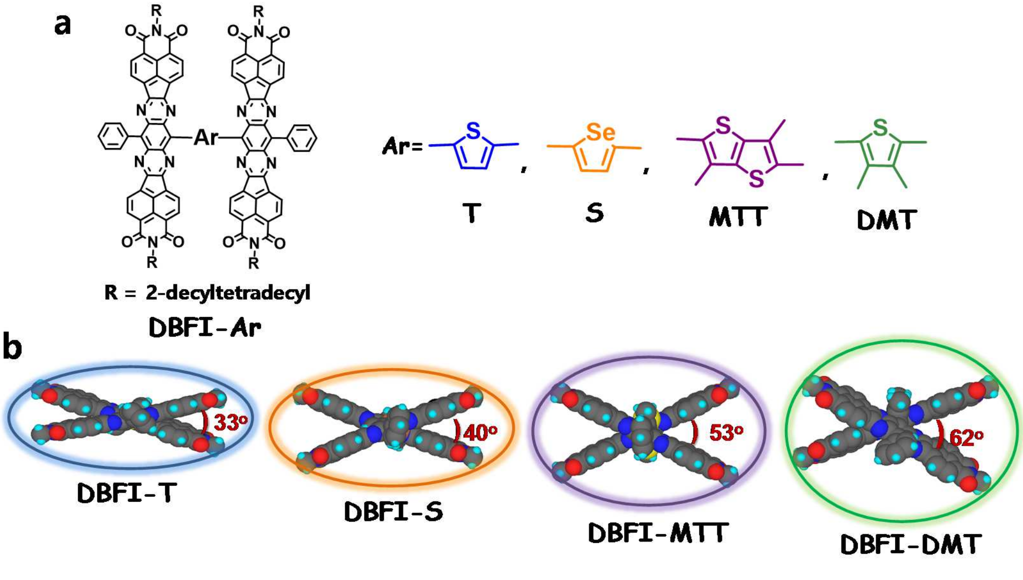

Scheme 8. Molecular structures (a) and optimized 3D geometry side view of DBFI-Ar (b) by DFT calculations at the B3LYP/(6-31G(d)) level.

I herein test the hypothesis that significant increase in the twisting angle θ between the planar building blocks of DBFI-type dimer acceptors could enhance the efficiency of bulk heterojunction (BHJ) solar cells incorporating such a highly twisted electron acceptor. The θ is further increased up to 76 ° by using 3,4-ethylenedioxythiophene (EDOT) as a linker, which has a much bulkier substituent group compared to methyl groups on DMT or MTT. We demonstrate a major milestone (PCE ≥ 8 %) in the performance of nonfullerene polymer solar cells by using this new electron acceptor, DBFI-EDOT, with a rationally designed nonplanar 3D structure. Compared to $PC_{71}BM$, DBFI-EDOT has enhanced absorption that spans 300 – 730 nm, a smaller electron affinity (3.65 eV), and enhanced bulk electron mobility. We show, for the first time, that nonfullerene OPV devices can combine high V_{oc} with high J_{sc} and FF values, resulting in PCEs that are far superior to the corresponding $PC_{71}BM$ devices. We also show, for the first time, that a nonfullerene acceptor can be used to develop highly efficient (> 6.5 % PCE) organic solar cells based on two different donor polymers.

6.1.2 *Experimental Section*

Materials: PSEHTT (M_n = 33.9 kDa, PDI = 3.9) was synthesized according to the known procedure[25]. PBDTT-FTTE (M_n > 25 kDa, PDI = 1.8 – 2.2) and $PC_{71}BM$ were purchased from Solarmer Energy, Inc. and American Dye Source, Inc. (Quebec, Canada), respectively, and were used as received without further purification.

Synthesis of 2,5-bis(8-(17-phenyl)-7,9,16,18-tetraazabenzodifluoranthene-3,4,12,13-tetracarboxylic acid diimide)-3,4-ethylenedioxythiophene (DBFI-EDOT): Under argon, Ph-BFI-Br (200 mg, 0.14 mmol), 2,5-bis(trimethylstannyl)-3,4-ethylenedioxythiophene (32.8 mg, 0.07 mmol), $Pd_2(dba)_3$ (9 mg) and $P(o\text{-}Tol)_3$ (12 mg) were transferred into a Schlenk tube and dissolved in 14 mL of degassed toluene. The mixture was heated to reflux and kept stirring for

72 hours. After removing all the volatile materials, the solid residue was purified by chromatography with chloroform and a few drops of methanol as the eluent. The product was isolated as a green solid. Yield: 101 mg, 52.1%. 1H NMR (CDCl3, 0 ˚C, 500 MHz): □ = 9.25 (br, 4H), 8.75 (s, 4H), 8.65 (s, 4H), 8.53 (s, 4H), 7.97 (br, 4H), 7.80 (m, 6H), 4.14 (d, 8H), 2.77 (br, 10H), 2.39 (br, 4H), 1.20 (s, 4H), 1.4-1.1 (m, 150H), 0.83 (m, 24H). Elemental analysis calcd for C182H226N12O8S: C 78.80%, H 8.21%, N 6.06%; found C 79.26%, H 8.00%, N 5.99%. HRMS (m/z): [M]+ calcd. for C182H226N12O10S, 2772.73; found, 2773.39.

Characterization: ^{1}H NMR spectra at 300 MHz was recorded on a Bruker-AF300 spectrometer to verify the molecular structure. TGA thermogram was acquired on a TA Instruments Q50 TGA at a heating rate of 20 ˚C per minute under argon gas flow.

HOMO/LUMO energy levels were estimated by cyclic voltammetry (CV). CV experiments were done on an EG&G Princeton Applied Research potentiostat/galvanostat (model 273A) in an electrolyte solution of 0.1 M tetrabutylammonium hexafluorophosphate (Bu_4NPF_6) in acetonitrile at a scan rate of 40 m/Vs. Platinum (Pt) wires were used as counter and working electrodes, and Ag/Ag+ (Ag in 0.1 M AgNO3 solution, Bioanalytical System, Inc.) was used as a reference electrode. Ferrocene/ferrocenium (Fc/Fc+) was used as an internal standard, and the reference potential was converted to the saturated calomel electrode (SCE) scale. Each sample for CV was prepared by dip-coating the solution in chloroform onto Pt wires.

Optical absorption spectra were measured on a Perkin-Elmer model Lambda 900 UV/vis/near-IR spectrophotometer. Solution and solid-state absorption spectra were obtained from dilute (10-6 M) solutions in chloroform and as thin films on glass substrates, respectively.

X-ray diffraction (XRD) patterns were obtained from a Bruker F8 power XRD with a Cu Kα radiation as the X-ray source, and the film samples were prepared by drop-casting of highly concentrated polymer solutions (30 mg/mL) in chlorobenzene onto glass substrates and followed by annealing on a hot plate at 175 ˚C for 10 minutes. The mean size of the crystalline domains (L_c) of the polymers was calculated from the lamellar peaks using the Scherrer equation[36], $Lc = K\lambda/\beta \cos \theta$, where K is shape factor (0.9), λ is X-ray wavelength (1.54 Å), and β is the fwhm in radian. The peak center and the fwhm were obtained by fitting the lamellar peak using Gaussian function in Origin software.

Bright field transmission electron microscopy (BF-TEM) images were acquired on an FEI Tecnai G2 F20 TEM at 200 kV accelerating voltage and acquired with a CCD camera and recorded with Gatan Digital Micrograph software with proper exposure time (0.1 sec). The TEM images were slightly defocused to enhance the phase contrast. The sample films were spin-casted on top of ITO/PEDOT:PSS substrates and peeled off by putting the samples in water. A peeled-off film was deposited on a TEM grid (Electron Microscopy Sciences, Inc.) and dried overnight in a vacuum oven.

Nonfullerene OPV Device Fabrication: ITO glass substrates were cleaned sequentially in ultrasonic baths with acetone and isopropyl alcohol for 20 minutes, dried using nitrogen gas, and stored in a glove box. Each ITO glass substrate was UV-ozone treated for 5 minutes right before coating the ZnO layer. The ZnO precursor solution (5 g of zinc acetate, 0.14 g of ethanolamine and 5 mL of 2-methoxyethanol) was spin-coated onto the ITO glass at 5000 rpm for 40 sec, annealed at 250 ˚C on a hot plate in air for 1 hr to make ~ 20 nm thick ZnO layer. A 0.05 wt % polyethylenimine (PEI, M_w ~ 25000, Aldrich 408727) in 2-methoxyethanol solution was spin-coated onto the ZnO layer and dried at 110 °C on a hot plate in air for 10 minutes and the glass/ITO/ZnO/PEI substrate was transferred into an argon-filled glove box. Each active layer was spin-coated from the acceptor:polymer blend solution in chlorobenzene solvent. The solution for the active layer, DBFI-EDOT:PSEHTT blend (2:1 wt/wt), was prepared from the DBFI-EDOT (20 mg/mL) and PSEHTT (10 mg/mL) solutions in chlorobenzene, mixed and stirred overnight at room temperature in the glove box. The solution for the active layer, DBFI-T:PBDTT-FTTE blend (2.5:1 wt/wt), was prepared from the DBFI-EDOT (20 mg/mL) and PBDTT-FTTE (20 mg/mL) solutions in chlorobenzene, mixed and stirred overnight at room temperature in the glove box. Each active layer was spin-coated at 1000 rpm for 30 seconds. After spin-coating, the blend film was thermally annealed at 175 ˚C on a hot plate in the glove box for 10 minutes. MoO_3 (7.5 nm) and Ag anode (100 nm) were thermally deposited onto the active layer. Five pixels, each with an active area of 4 mm^2, were fabricated per ITO substrate.

OPV Device Characterization: The photovoltaic cells were tested under AM 1.5 G solar illumination at 100 mW/cm^2 in ambient air using a Solar Simulator (model 16S, Solar Light Co., Philadelphia, PA) with a 200W Xenon Lamp Power Supply (Model XPS 200, Solar Light Co., Philadelphia, PA) calibrated by NREL certified Si photodiode (Model 1787–04, Hamamatsu Photonics K.K., Japan) and a HP4155A semiconductor parameter analyzer (Yokogawa Hewlett-Packard, Japan). After the *J-V* measurement, the external quantum efficiency (EQE) was measured by using a solar cell quantum efficiency measurement system (Model QEX10, PV Measurements, Inc., Boulder, CO) with a 2 mm^2 (2 mm×1mm) size masked incident light source and TF Mini Super measurement apparatus for multiple devices in a single substrate. The EQE system was calibrated with a Si photodiode before each measurement.

Space-Charge-Limited Current (SCLC) Measurement: Current-voltage (*J-V*) characteristics of the SCLC devices were measured by using a HP4155A semiconductor parameter analyzer (Yokogawa Hewlett-Packard, Tokyo). The carrier mobility was extracted by fitting the *J-V* curves in the near quadratic region according to the modified Mott-Gurney equation.[25]

The SCLC device structures for electron-only and hole-only measurements were ITO/ZnO/active-layer/LiF/Al and ITO/PEDOT:PSS/active-layer/Au, respectively. Each active layer (PNDIS-HD:PBDTTT-CT or *x*PDI:PBDTTT-CT blend (1:1 *wt/wt*)) solution (25 mg/mL) in chlorobenzene with 3 *vol*% DIO solvent additive was spin-coated at 1000 rpm for 20 seconds. After spin-coating, the wet film was film-aged inside the glove box at room temperature for 96 hours (4 days) followed by thermal vacuum deposition of LiF (1 nm)/Al (100 nm) or Au (40 nm).

6.1.3 *Results and Discussions*

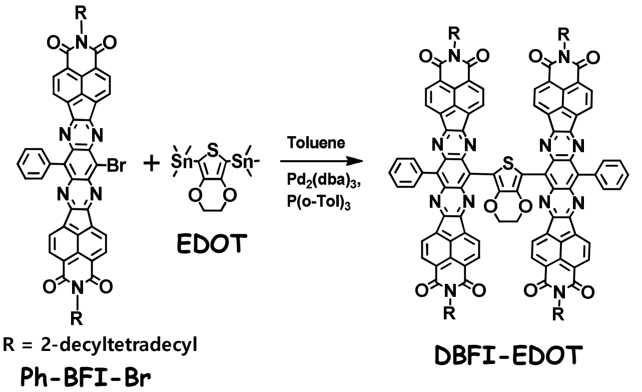

Scheme 9. Synthesis of DBFI-EDOT.

Synthesis, 3D Geometry, Absorption Spectra, and Electronic Structure. The new electron acceptor, 2,5-bis(8-(17-phenyl)-7,9,16,18-tetraazabenzodifluoranthene-3,4,12,13-tetracarboxylic acid diimide)-3,4-ethylenedioxythiophene (DBFI-EDOT) was synthesized by the Stille cross-coupling reaction of the previously reported 8-bromo-17-phenyl-7,9,16,18-tetraazabenzodifluoranthene -3,4,12,13-tetracarboxylic acid diimide (Ph-BFI-Br)[9] with 2,5-bis(trimethylstannyl)-3,4-ethylenedioxythiophene (**Scheme 9**). The molecular structure of DBFI-EDOT was confirmed by ^{1}H NMR spectroscopy at 0 ˚C, elemental analysis and high resolution mass spectroscopy. DBFI-EDOT has good solubility (>30 mg/mL) in common organic solvents, e.g. chloroform, chlorobenzene, toluene, etc. at room temperature, which is suitable for solution-based device fabrication techniques i.e. spin-coating, inkjet or roll-to-roll printing, etc. DBFI-EDOT is thermally stable over 420 ˚C (5% weight loss) according to thermogravimetric analysis (TGA); differential scanning calorimetry (DSC) scans did not show any thermal transitions in the 20 – 300 ˚C range.

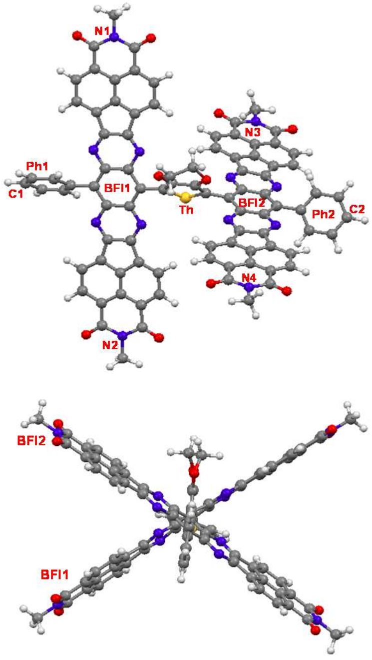

Figure 45. Front and side views of the optimized geometry of DBFI-EDOT. The DFT calculations were performed at the B3LYP/6-31G(d) level by replacing the 2-decyltetradecyl groups with methyl groups.

The optimized 3D molecular geometry of DBFI-EDOT is shown in **Figure 45.** Replacing the decyltetradecyl (R) groups in DBFI-EDOT with methyl groups simplified the DFT calculations at the B3LYP/(6-31G(d) level, giving the geometry optimized structure. Representative geometry parameters show that DBFI-EDOT has a highly twisted 3D structure with 76 ˚ twisting angle θ between the BFI units. Moreover, both BFI units rotated a larger angle (52^{o}□55^{o}) with respect to the central thiophene plane in DBFI-EDOT than in DBFI-T to avoid large steric hindrance induced by the ethylenedioxy group. Thus, incorporating a 3,4-ethylenedioxy-2,5-

thienylene linker between the BFI units in the DBFI dimer framework has dramatically twisted the molecular structure into a nearly perpendicular and more isotropic arrangement.

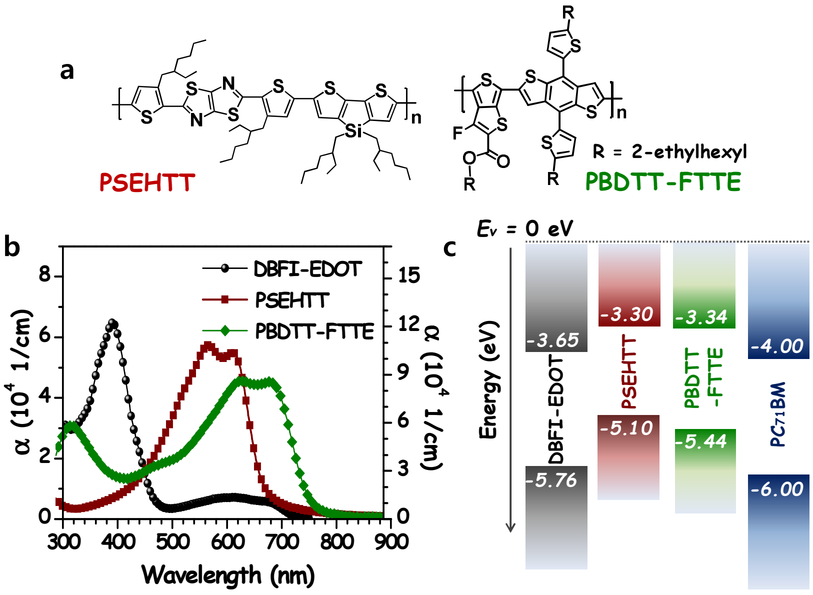

Figure 46. (a) Thin film optical absorption spectra of DBFI-EDOT, PSEHTT and PBDTT-FTTE. (b) Energy level diagram based on cyclic voltammetry-derived HOMO/LUMO energy levels of DBFI-EDOT, PSEHTT, PBDTT-FTTE, and $PC_{71}BM$.

We used two donor polymers, PSEHTT[25] and poly(4,8-bis(5-(2-ethylhexyl)thiophen-2-yl)benzo[1,2-b;4,5-b']dithiophene-2,6-diyl-alt-(4-(2-ethylhexyl)-3-fluorothieno[3,4-b]thiophene-)-2-carboxylate-2-6-diyl)) (PBDTT-FTTE)[19, 21], shown in **Figure 46a**, to evaluate the photovoltaic properties of the new acceptor. Both polymers have previously been used to produce high performance BHJ solar cells when paired with $PC_{71}BM$[19, 21, 25] or with some nonfullerene acceptors[9, 14]. The thin film absorption spectrum of DBFI-EDOT overlaid with that of the donor polymers, PSEHTT and PBDTTT-FTTE, is shown in **Figure 46b**. DBFI-EDOT has an intense high-energy absorption band centered at 391 nm with a maximum absorption coefficient (α_{max}) of 6.5×10^4 cm^{-1}, which compensates the poor absorption of the donor polymers PSEHTT and PBDTT-FTTE in this region. An additional broad low-energy absorption band was observed in the 500-730 nm region ($\alpha_{max} = 7.10\times10^3$ cm^{-1} at 615 nm), giving rise to an optical band gap (E_g) of 1.70 eV. The smaller absorption coefficient of DBFI-EDOT compared to PSEHTT ($E_g = 1.77$ eV, $\alpha_{max} = 1.08\times10^5$ cm^{-1} at 580 nm) and PBDTT-FTTE ($E_g = 1.57$ eV, $\alpha_{max} = 8.61\times10^4$ cm^{-1} at 645 nm) suggests that acceptor/donor blend ratio of greater than 1 would be needed to maximize light harvesting in BHJ devices.

The electronic structures of DBFI-EDOT and donor polymers (PSEHTT and PBDTT-FTTE) were investigated by using cyclic voltammetry (CV) of thin films. The ferrocene/ferrocenium (Fc/Fc^+) reference was used as an internal standard, which was assigned an absolute energy of −4.8 eV vs vacuum level.[26] The highest occupied molecular orbital (HOMO)/the lowest unoccupied molecular orbital (LUMO) energy levels of DBFI-EDOT calculated from the onset oxidation/reduction potentials of cyclic voltammograms are -5.72 eV/-3.65 eV, respectively. The HOMO/LUMO energy levels of PSEHTT and PBDTT-FTTE were -5.10 eV/-3.30 eV and -5.44 eV/-3.34 eV, respectively. The frontier molecular orbital energy of DBFI-EDOT forms good energetic offsets (~0.3 eV) with the donor polymers (**Figure 46c**), providing sufficient driving energy for photoinduced charge transfer in BHJ cells[27, 28]. Note the higher lying LUMO level of DBFI-EDOT compared to $PC_{71}BM$ (-4.0 eV)[16, 29], which could facilitate achievement of higher V_{oc} in photovoltaic device applications.

Photovoltaic Properties. We fabricated photodiodes with an inverted structure (ITO/ZnO/DBFI-EDOT:polymer/MoO_3/Ag) (**Figure 47a**) and tested them under 100 mW/cm^2 air mass 1.5 global (AM 1.5 G) solar illumination in ambient air. The DBFI-EDOT:polymer blend active layer was prepared under optimized conditions of spin coating from a chlorobenzene solution and thermally annealed at 175 ˚C for 10 minutes in an argon-filled glovebox. The active layer composition was optimized by evaluating DBFI-EDOT:polymer blend ratios from 1.5:1 to 3:1 (*wt:wt*) and found the optimized composition to be 2:1 and 2.5:1 for DBFI-EDOT:PSEHTT and DBFI-EDOT:PBDTT-FTTE blends, respectively. Current density versus voltage (*J*-*V*) curves and external quantum efficiency (EQE) spectra of the best DBFI-EDOT:polymer photodiodes are shown in **Figure 47b** and **Figure 47c**, respectively. The photovoltaic parameters, including J_{sc}, V_{oc}, *FF*, and PCE, extracted from the *J*-*V* curves for the DBFI-EDOT:polymer devices, are summarized in **Table 21** along with those of the reference $PC_{71}BM$:polymer photodiodes.

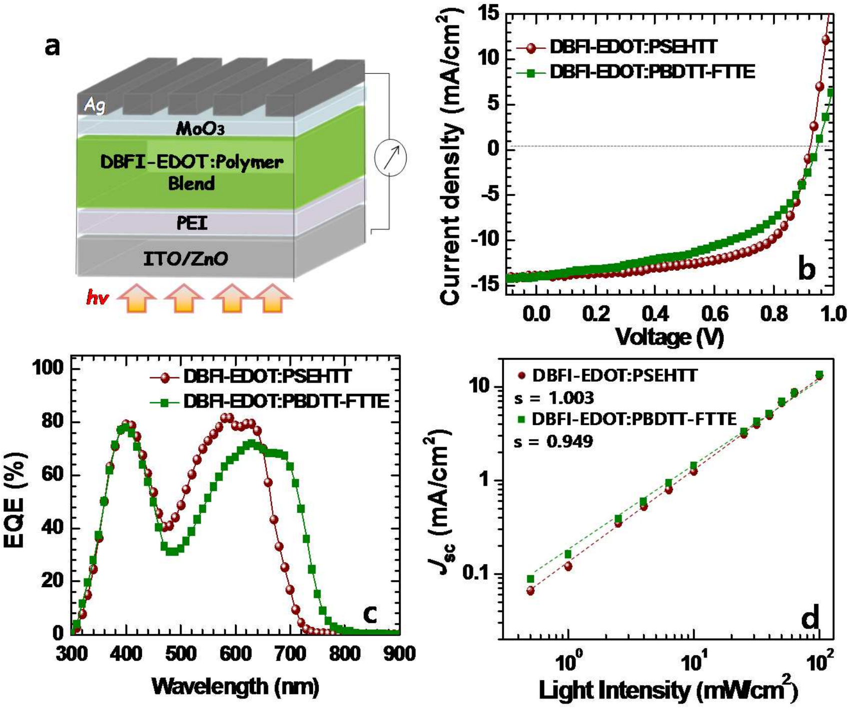

Figure 47. (a) Schematic of the inverted photovoltaic cell. Current density-voltage characteristics (b), external quantum efficiency (EQE) curves (c), and short-circuit current density (Jsc) versus light intensity (Plight) data and power-law (Jsc ∝Plights) fit (d) of DBFI-EDOT:PSEHTT (2:1, wt/wt) and DBFI-EDOT:PBDTT-FTTE (2.5:1, wt/wt) devices.

A maximum PCE of 8.10 % and an average PCE of 7.85±0.18 % were achieved in the optimized DBFI-EDOT:PSEHTT devices (**Table 21**). Both of these values are by far the best performance seen in nonfullerene polymer solar cells to date. For comparison the reference optimized $PC_{71}BM$:PSEHTT photodiodes, gave the best PCE of 5.62 % with an average PCE of 5.52±0.09 %. Thus, for the same donor polymer PSEHTT, the conversion efficiency of the nonfullerene acceptor, DBFI-EDOT, exceeds that of $PC_{71}BM$ by 44 %. The enhanced performance of DBFI-EDOT devices is largely a result of the enhanced Voc (0.93 V) compared to the $PC_{71}BM$ cells (0.67 V).

Table 21. Photovoltaic properties of DBFI-EDOT:polymer and $PC_{71}BM$:polymer blends under optimized conditions.

Blend	J_{sc} **(mA/cm^2)**	V_{oc} **(V)**	**FF**	**PCE (%)**	R_{SH} **(Ωcm2)**	R_S **(Ωcm2)**
DBFI-EDOT: PSEHTT	13.82 (13.51±0.34)	0.93 (0.921±0.005)	0.63 (0.631±0.004)	8.10 (7.85±0.18)	497.13	5.74
$PC_{71}BM$: PSEHTT	13.18 (12.78±0.26)	0.67 (0.667±0.003)	0.64 (0.648±0.007)	5.62 (5.52±0.09)	696.19	5.40
DBFI-EDOT: PBDTT-FTTE	13.99 (13.50±0.34)	0.95 (0.947±0.003)	0.51 (0.50±0.01)	6.70 (6.42±0.19)	286.13	10.01
$PC_{71}BM$: PBDTT-FTTE	16.59 (16.22±0.61)	0.79 (0.784±0.006)	0.63 (0.606±0.019)	8.12 (7.67±0.25)	391.01	6.51

The photovoltaic properties were averaged over 20 devices.

Optimized DBFI-EDOT:PBDTT-FTTE devices had a maximum PCE of 6.70 % and an average of 6.42±0.19 %. This performance is also among the best for nonfullerene polymer solar cells[1-15]. However, the reference optimized $PC_{71}BM$:PBDTT-FTTE devices had a maximum PCE of 8.12 % and an average of 7.67±0.25 %, which are in agreement with previously reported values for this BHJ system[19, 21]. Although the V_{oc} of DBFI-EDOT devices with PBDTT-FTTE is larger (0.95 V) compared to that of $PC_{71}BM$ devices (0.79 V), the J_{sc} and FF values of the fullerene devices are much higher. Such differences in J_{sc} and FF values are likely due mainly to a non-optimal morphology[30] in DBFI-EDOT:PBDTT-FTTE blends.

The EQE spectra of the best DBFI-EDOT:polymer devices are given in **Figure 47**c, with photoresponses spanning 300 – 730 nm for PSEHTT and 300 – 800 nm for PBDTT-FTTE. Note the valleys in the 440 – 540 nm range of the EQE spectra of both BHJ devices. Observed peak EQE values of 79.1 % at 400 nm and 81.6 % at 580 – 650 nm in DBFI-EDOT:PSEHTT devices are the highest observed so far in nonfullerene polymer solar cells and are comparable to the best $PC_{71}BM$:polymer devices[16-21]. Also note that observed photocurrent generation above 700 nm in DBFI-EDOT:PSEHTT comes from excitons in DBFI-EDOT since PSEHTT does not absorb above 700 nm. As with PSEHTT devices, the peak EQE values (78 % at 400 nm and 72 % at 600 – 700 nm) in PBDTT-FTTE devices are due to contributions from photoinduced hole and electron transfer processes, respectively. Given the observed high EQE values, optical band gap losses ($E_{\mathrm{loss}} = E_g - eV_{\mathrm{oc}}$) in the DBFI-EDOT devices, 0.77 eV for PSEHTT and 0.62 eV for PBDTT-FTTE, are remarkably low among high efficiency polymer solar cells[28]. Theoretical J_{sc} values calculated from the EQE spectra and the AM 1.5 G solar spectrum are 13.07 mA cm^{-2} for PSEHTT device and 13.25 mA cm^{-2} for PBDTT-FTTE device, which are in good agreement with the values obtained from the *J–V* curves.

The effect of processing additive, 1,8-diiodooctane (DIO)[32. 33], on photovoltaic performance in the best DBFI-EDOT:PSEHTT (1:1 *wt/wt*) devices was also investigated by varying the composition of DIO from 0 vol % to 5 vol % with the primary solvent chlorobenzene. Unlike the well-known positive effect of DIO in fullerene-based polymer solar cells[32, 33], a dramatically decreased photocurrent and fill factor are observed using DIO in our nonfullerene system. Even with very small amount of DIO (1 vol %), the PCE decreased to 4.89 % with significantly lower J_{sc} and *FF* of 9.66 mA/cm^2 and 0.55, respectively, while the V_{oc} (0.93 V) was consistent. By increasing the composition of DIO, further decreased performance was observed. PCE of 2.92 %

(J_{sc} = 5.91 mA/cm^2, V_{oc} = 0.92 V, and FF = 0.54) in 3 vol % DIO device and PCE of 2.44 % (J_{sc} = 5.31 mA/cm^2, V_{oc} = 0.91 V, and FF = 0.51) in 5 vol % DIO device were observed. These results show that our current device fabrication condition without processing additive is optimal.

Charge Recombination Kinetics and Charge Transport Properties. To gain insight into the charge recombination kinetics in DBFI-EDOT:polymer solar cells, we measured J_{sc} as a function of illumination intensity P_{light} as presented in **Figure 47d**. Linearity (s = 1) in the power-law dependence ($J_{sc} \propto P_{light}^s$) generally indicates weak charge carrier losses due to bimolecular recombination, whereas sublinearity (s < 1) implies significant bimolecular recombination[34]. The observed power-law exponent in DBFI-EDOT:PSEHTT devices (s = 1.003) and DBFI-EDOT:PBDTT-FTTE devices (s = 0.949) means that there is much less bimolecular recombination in the PSEHTT devices than in the PBDTT-FTTE devices. The increased bimolecular recombination in PBDTT-FTTE devices can partly explain their lower fill factor and J_{sc}, smaller shunt resistance R_{SH}, and larger series resistance R_S compared to the PSEHTT devices (**Table 21**).

To further understand the observed trends in J_{sc} and FF values, we measured the bulk charge transport in the DBFI-EDOT:polymer and PC$_{71}$BM:polymer blend active layers, which were prepared similarly to the photovoltaic devices, by using the space charge limited current (SCLC) method. The electron mobility was measured in an ITO/ZnO/PEI/active layer/LiF/Al device structure, and the hole mobility was measured in an ITO/PEDOT:PSS/active layer/Au device structure. The current–voltage curves and SCLC fittings of the data are shown in **Figure 48** and the hole and electron mobilities (μ_h, μ_e) are summarized in **Table 22**. The results show that the hole transport ($\mu_h \sim (0.7 - 1.0) \times 10^{-2}$ cm^2 V^{-1}s^{-1}) is comparable in all the blend active layers. Electron mobility is much higher in all the blends due largely to the presence of the PEI interlayer[35], varying from 8.60×10^{-3} cm^2 V^{-1}s^{-1} in DBFI-EDOT:PBDTT-FTTE to 6.80×10^{-2} cm^2 V^{-1}s^{-1} in DBFI-EDOT:PSEHTT. The resulting carrier asymmetry ($\mu_h/\mu_e = 0.11$) in the DBFI-EDOT:PSEHTT devices suggests that their further improvement is possible either through a different polymer or by means of a suitable anode interlayer.

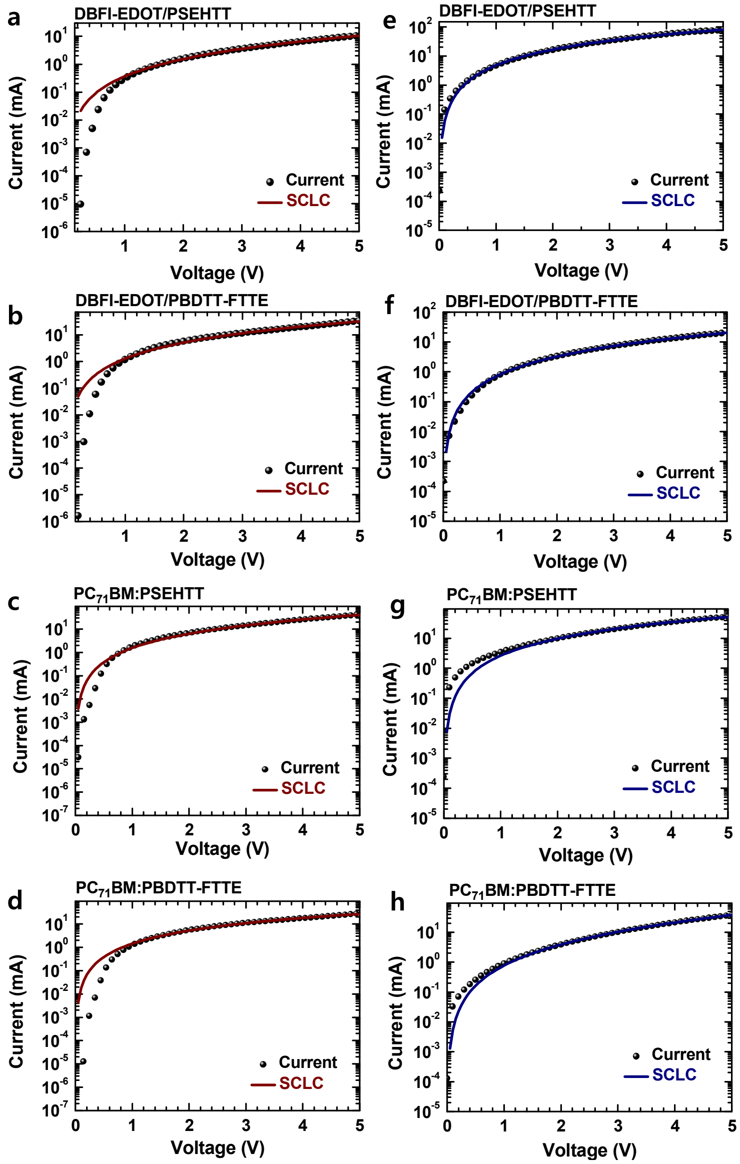

Figure 48. Current−voltage curves and SCLC fittings of DBFI-EDOT:PSEHTT, DBFI-EDOT:PBDTT-FTTE blend films and corresponding PC$_{71}$BM blends. Hole-only SCLC devices (a−d): ITO/PEDOT:PSS/blend/Au and electron-only SCLC devices (e−h): ITO/ZnO/PEI/blend/LiF/Al.

Table 22. bulk charge carrier mobilities of DBFI-EDOT:polymer and $PC_{71}BM$:polymer blends under optimized conditions.

Blend	**μ_h (cm²/Vs)**	**μ_e (cm²/Vs)**
DBFI-EDOT:PSEHTT	7.53×10^{-3}	6.80×10^{-2}
$PC_{71}BM$:PSEHTT	7.90×10^{-3}	1.28×10^{-2}
DBFI-EDOT:PBDTT-FTTE	6.95×10^{-3}	8.60×10^{-3}
$PC_{71}BM$:PBDTT-FTTE	9.75×10^{-3}	1.02×10^{-2}

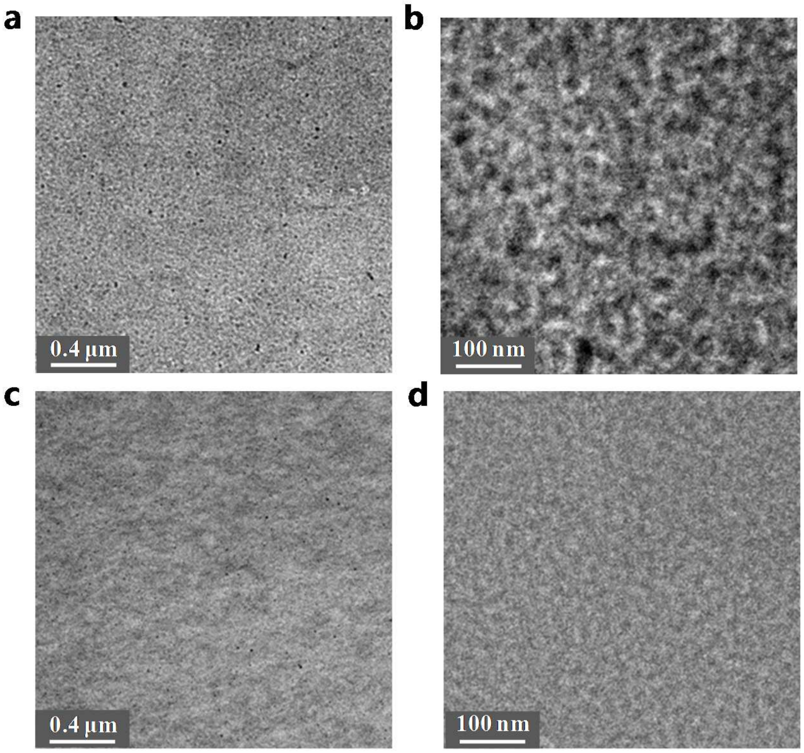

Figure 49. Bright-field (BF)-TEM images of DBFI-EDOT:PSEHTT (2:1 wt/wt) blend film (a, b) and DBFI-EDOT:PBDTT-FTTE (2.5:1 wt/wt) blend film (c, d).

Morphology of BHJ Solar Cells. We used bright-field transmission electron microscopy (BF-TEM) to observe the bulk morphology of DBFI-EDOT:polymer blend films (**Figure 49**). Interconnected phase-separated domains of about 20 nm size are observed in the DBFI-EDOT:PSEHTT blend. In contrast, a less defined phase separation was observed in DBFI-

EDOT:PBDTT-FTTE blend film, which is possibly due to the poorer crystallinity of PBDTT-FTTE compared to PSEHTT. X-ray diffraction (XRD) characterization of both the pure polymer films and the DBFI-EDOT:polymer blend films confirmed the difference in crystallinity. Mean crystalline domain size (L_c)[36] of 8.02 nm and 7.62 nm was observed in pure PSEHTT film and its blend film, respectively, compared with 4.01 nm and 4.55 nm in pure PBDTT-FTTE and its blend, respectively. These observations are in agreement with the previously discussed lower bulk charge carrier mobilities, higher rate of bimolecular recombination, and lower exciton dissociation probability in the DBFI-EDOT:PBDTT-FTTE devices compared to DBFI-EDOT:PSEHTT photodiodes.

6.1.4 *Conclusions*

In conclusion, I have successfully demonstrated fullerene-free polymer solar cells with efficiency comparable to some of the best $PC_{71}BM$/polymer devices by using DBFI-EDOT electron acceptor. Success of DBFI-EDOT demonstrates that the twisting angle between building block elements in a molecule is a promising rational design strategy towards more efficient OPV electron acceptors. Observed high V_{oc} (0.93 – 0.95 V), high quantum efficiency (~ 80 %) and rather low optical band gap energy loss (0.62 – 0.77 eV) in DBFI-EDOT devices offer opportunity for deepening understanding of OPV device physics beyond fullerene limits[31]. The finding that efficiency (8.1 %) of DBFI-EDOT:PSEHTT devices exceeds that of $PC_{71}BM$:PSEHTT photodiodes by 44 %, suggests that further advances in materials and device engineering will enable nonfullerene OPVs to surpass current fullerene-based solar cells.

6.1.5 *References*

(1) Sonar, P.; Lin, J. P. F.; Chan, K. L *Energy Environ. Sci.* **2011**, *4*, 1558.

(2) Woo, C. H.; Holcombe, T. W.; Unruh, D. A.; Sellinger, A.; Frechet, J. M. J. *Chem. Mater.* **2010**, *22*, 1673.

(3) Ahmed, E.; Ren, G.; Kim, F. S.; Hollenbeck, E. C.; Jenekhe, S. A. *Chem. Mater*. **2011**, *23*, 4563.

(4) Anthony, J. E. *Chem. Mater*. **2011**, *23*, 583.

(5) Zhou, Y.; Ding, L.; Shi, K.; Dai, Y. Z.; Ai, N.; Wang, J.; Pei, J. *Adv. Mater*. **2012**, *24*, 957.

(6) Hartnett, P. E.; Timalsina, A.; Ramakrishna Matte, H. S. S.; Zhou, N.; Guo, X.; Zhao, W.; Facchetti, A.; Chang, R. P. H.; Hersam, M. C.; Wasielewski, M. R.; Marks, T. J. *J. Am. Chem. Soc*. **2014**, *136*, 16345.

(7) Bloking, J. T.; Giovenzana, T.; Higgs, A. T.; Ponec, A. J.; Hoke, E. T.; Vandewal, K.; Ko, S.; Bao, Z.; Sellinger, A.; McGehee, M. D. *Adv. Energy Mater*. **2014**, *4*, 1301426.

(8) Pho, T. V.; Toma, F. M.; Tremolet de Villers, B. J.; Wang, S.; Treat, N. D.; Eisenmenger, N. D.; Su, G. M.; Coffin, R. C.; Douglas, J. D.; Fréchet, J. M. J.; Bazan, G. C.; Wudl, F.; Chabinyc, M. L. *Adv. Energy Mater*. **2014**, *4*, 1301007.

(9) Li, H.; Earmme, T.; Ren, G.; Saeki, A.; Yoshikawa, S.; Murari, N. M.; Subramaniyan, S.; Crane, M. J.; Seki, S.; Jenekhe, S. A. *J. Am. Chem. Soc*. **2014**, *136*, 14589.

(10) Zhong, Y.; Trinh, M. T.; Chen, R.; Wang, W.; Khlyabich, P. P.; Kumar, B.; Xu, Q.; Nam, C. Y.; Sfeir, M. Y.; Black, C.; Steigerwald, M. L.; Loo, Y. L.; Xiao, S.; Ng, F.; Zhu, X. Y.; Nuckolls, C. *J. Am. Chem. Soc*. **2014**, *136*, 15215.

(11) Zhang, X.; Zhan, C.; Yao, J. *Chem. Mater*. **2015**, *27*, 166.

(12) Holliday, S.; Ashraf, R. S.; Nielsen, C. B.; Kirkus, M.; Röhr, J. A.; Tan, C. H.; Collado-Fregoso, E.; Knall, A. -C.; Durrant, J. R.; Nelson, J.; McCulloch. I. *J. Am. Chem. Soc*. **2015**, *137*, 898.

(13) Zhao, J.; Li, Y.; Lin, H.; Liu, Y.; Jiang, K.; Mu, C.; Ma, T.; Lai, J. Y. L.; Hu, H.; Yu, D.; Yan, H. *Energy Environ. Sci*. **2015**, *8*, 520.

(14) Lin, Y.; Zhang, Z. G.; Bai, H.; Wang, J.; Yao, Y.; Li, Y.; Zhu, D.; Zhan, X. *Energy Environ. Sci*. **2015**, *8*, 610.

(15) Li, H.; Hwang, Y. J.; Courtright, B. A. E.; Eberle, F. N.; Subramaniyan, S.; Jenekhe, S. A. *Adv. Mater.* **2015**, DOI:10.1002/adma.201500577.

(16) He, Z.; Zhong, C.; Su, S.; Wu, H.; Cao, Y. *Nature Photon.* **2012***, 6*, 591.

(17) Li, G.; Zhu, R.; Yang, Y. *Nature Photon.* **2012***,* 6, 153.

(18) Guo, X.; Zhou, N.; Lou, S. J.; Smith, J.; Tice, D. B.; Hennek,J.W.; Ortiz, R. P.; López Navarrete, J. T.; Li, S.; Strzalka, J.; Chen, L. X.; Chang, R. P. H.; Facchetti, A.; Marks, T. J. *Nature Photon*. **2013**, *7*, 825.

(19) Liao, S. H.; Jhuo, H. J.; Cheng, Y. S.; Chen, S. A. *Adv. Mater*. **2013**, *25*, 4766.

(20) Brabec, C. J.; Gowrisanker, S.; Halls, J. J. M.; Laird, D.; Jia, S.; Williams, S. P. *Adv. Mater*. **2010**, *22*, 3839.

(21) Cui, C.; Wong, W. Y.; Li, Y. *Energy Environ. Sci*. **2014**, *7*, 2276.

(22) Savoie, B. M.; Rao, A.; Bakulin, A. A.; Gelinas, S.; Movaghar, B.; Friend, R. H.; Marks, T. J.; Ratner, M. A. *J. Am. Chem. Soc*. **2014**, *136*, 2876.

(23) Roncali, J.; Leriche, P.; Cravino, A. *Adv. Mater*. **2007**, *19*, 2045.

(24) Li, H.; Earmme, T.; Subramaniyan, S.; Jenekhe, S. A. *Adv. Energy Mater*. **2015**, *5*, 1402041.

(25) Subramaniyan, S.; Xin, H.; Kim, F. S.; Shoaee, S.; Durrant, J. R.; Jenekhe, S. A. *Adv. Energy Mater*. **2011**, *1*, 854.

(26) Pavlishchuk, V. V.; Addison, A. W. *Inorg. Chim. Acta* 2000, 298, 97.

(27) Heeger, A. J. *Adv. Mater*. **2014**, *26*, 10.

(28) Ren, G.; Schlenker, C. W.; Ahmed, E.; Subramaniyan, S.; Olthof, S.; Kahn, A.; Ginder, D. S.; Jenekhe, S. A. *Adv. Funct. Mater*. **2013**, *23*, 1238.

(29) Wienk, M. M.; Kroon, J. M.; Verhees, W. J. H.; Knol, J.; Hummelen, J. C.; van Hal, P. A.; Janssen, R. A. J. *Angew. Chem. Int. Ed*. **2003**, *42*, 3371.

(30) Jackson, N. E.; Savoie, B. M.; Marks, T. J.; Chen, L. X.; Ratner, M. A. *J. Phys. Chem. Lett*. **2015**, *6*, 77.

(31) Li, W.; Hendriks, K. H.; Furlan, A.; Wienk, M. M.; Janssen, R. A. J. *J. Am. Chem. Soc*. **2015**, *137*, 2231.

(32) Peet, J.; Kim, J. Y.; Coates, N. E.; Ma, W. L.; Moses, D.; Heeger, A. J.; Bazan, G. C. *Nature Mater*. **2007**, *6*, 497.

(33) Xin, H.; Guo, X.; Ren, G.; Watson, M. D.; Jenekhe, S. A. *Adv. Energy Mater*. **2012**, *2*, 575.

(34) Zhou, Y.; Fuentes-Hernandez, C.; Shim, J.; Meyer, J.; Giordano, A. J.; Li, H.; Winget, P.; Papadopoulos, T.; Cheun, H.; Kim, J.; Fenoll, M.; Dindar, A.; Haske, W.; Najafabadi, E.; Khan, T. M.; Sojoudi, H.; Barlow, S.; Graham, S.; Brédas, J. -L.; Marder, S. R.; Kahn, A.; Kippelen, B. *Science* **2012**, *336*, 327.

(35) Schilinsky, P.; Waldauf, C.; Brabec, C. J. *Appl. Phys. Lett*. **2002**, *81*, 3885.

(36) Patterson, A. L. *Phys. Rev*. **1939**, *56*, 978.

Chapter 7. CONCLUSIONS AND OUTLOOK

7.1 CONCLUSIONS

The results of this thesis research have addressed several major challenges in the field of organic electronics and photonics, including the scarcity of *n*-type semiconducting polymers, the low electron mobilities in *n*-channel OFETs, and the low photocurrent and efficiency of all-polymer solar cells. Throughout this work, I have studied factors that govern the performance of *n*-channel OFETs and all-polymer solar cells, and this can provide guidelines to develop better *n*-type polymer semiconductors and future low cost organic electronics and solar energy technologies.

I have developed new polymer semiconductors using the donor (D)-acceptor (A) design strategy to explore new building blocks and facile tuning of the material properties, including electronic structures, optical properties, solid state packing structure, and solubility. In the study of thieno[3,4-c][1,2,5]thiadiazole (TTD)-based copolymers, various comonomer moieties, including phenylene, benzodithiophene, vinylene, and dithienopyrrole, were utilized, and the HOMO/LUMO energy levels were varied in the range of 4.9 – 5.1 eV/3.4 – 3.6 eV below vacuum depending on the donor moiety. Moderate *p*-channel field effect mobilities in the range of $\sim 10^{-3}$ – $\sim 10^{-4}$ cm^2/Vs were achieved, and small optical band gaps (~ 1 eV) with broad light absorption, which extended up to 1400 nm, were observed. These results suggest that the TTD moiety is a strong electron-accepting building block for the development of D-A copolymers and the resulting polymers have potential applications in electronic and optoelectronic devices.

I also explored a series of poly(naphthalene diimides) (PNDIs) based on the well-known strong electron-withdrawing naphthalene diimide (NDI) building block combined with various selenophene derivatives as comonomer in a D-A conjugated polymer structure. The combination of low lying LUMO enegy levels (-3.8 – -4.0 eV) and highly ordered lamellar crystalline structures in the PNDIs gave rise to high performance *n*-channel OFETs with field-effect electron mobilities of up to 0.24 cm^2/Vs. The photovoltaic properties of the PNDIs in bulk heterojunction (BHJ) all-polymer solar cells, with various electron-donating (*p*-type) polymers, including poly(3-hexylthiophene) (P3HT) and thiazolothiazole-dithienylsilole copolymer (PSEHTT), were investigated. A record performance (PCE = 3.3 %, J_{sc} = 7.78 mA/cm^2, and EQE = 47 %) was achieved in all-polymer solar cells incorporating NDI-selenophene copolymer with relatively short 2-hexyldecyl (HD) alkyl side chain (PNDIS-HD) as an acceptor and PSEHTT as a donor. The superior photovoltaic properties of PNDIS-HD compared to other PNDIs suggest that the choice of comonomer, unipolar electron transport with high bulk mobility and size of alkyl side chains are important factors in the design of suitable acceptor polymers for BHJ solar cells.

To further explore the effects of side chains, a series of new *n*-type conjugated copolymers, PNDIS-*x*BO (*x*=10, 30, 50), which have different composition and distribution of the alkyl side chains (2-decyltetradecyl (DT) and 2-butyloctyl (BO)) was synthesized, and their photovoltaic properties were investigated. In this study, I found that the enhanced backbone planarity of PNDIS-*x*BO with higher composition, *x*, of the short side chain (BO) up to 30 % leads to higher bulk charge carrier mobility, and thus enhanced photocurrent (10.4 mA/cm^2) and efficiency (PCE = 4.4 %) of all-polymer solar cells. Therefore, this study suggests that side chain engineering is an effective strategy to overcome inferior photocurrent in all-polymer solar cells.

A hypothesis that material crystallinity controls polymer/polymer compatibility and blend morphology and thus photovoltaic properties was tested by designing a series of new semiconducting naphthalene diimide (NDI)-selenophene/perylene diimide (PDI)-selenophene random copolymers, *x*PDI (10PDI, 30PDI, 50PDI), whose crystallinity varies with composition, and investigated them as electron acceptors in BHJ solar cells. In this study, I observed that an incompatible polymer/polymer blend system composed of the crystalline (L_c = 10.22 nm) acceptor polymer PNDIS-HD with crystalline (L_c = 9.47 nm) donor polymer PBDTTT-CT had a low PCE of 1.4 %, however, the blend system becoms compatible with a high PCE of 6.3 % when the crystallinity (L_c = 5.11 nm) of the acceptor polymer was optimized. The highly enhanced photovoltaic performance originates from the dramatically changed surface and bulk morphologies of the polymer/polymer blends, depending on the bulk crystallinity of the acceptor polymer. This study suggests that the bulk crystallinity quantified in terms of the average crystalline domain size L_c is a material property that can be used as an important criterion for selecting donor/acceptor pairs in polymer/polymer blend solar cells.

In addition, I demonstrated that high performance all-polymer solar cells can be achieved by controlling the film forming conditions. Two different film forming conditions, including thermal (175 ˚C) annealing and room temperature film aging, were applied to all-polymer (PNDIS-HD:PBDTT-FTTE) blend system. Slow self-organization of the polymers facilitated by film-aging process enabled improvement in electron mobility and the favorable bulk morphology, and the resulting all-polymer solar cells showed about two-fold enhanced power conversion efficiency of 7.7 % compared to the thermally annealed devices.

Finally, the effects of the 3D molecular structure on the photovoltaic properties was studied using a highly twisted tetraazabenzodifluoranthene diimide (BFI) based dimeric small molecule acceptor (DBFI-EDOT) as a model compound. In this study, a strong correlation between twisted angle in the acceptor and photovoltaic performance was revealed, and for the first time, a superior photovoltaic performance (PCE = 8.1 %) was observed in nonfullerene OPVs compared with the corresponding $PC_{71}BM$ based devices. This result suggests that optimizing 3D conformation of acceptor is a promising rational design strategy towards more efficient small molecule and polymer acceptors in non-fullerene OPVs.

Overall, the results of this research have helped to advance some areas of the field of organic electronic and photonics. In particular, the results of this work provide guidelines to develop better *n*-type polymer semiconductors for future low cost organic electronics and solar energy technologies.

7.2 OUTLOOK

My finding throughout this work that the photocurrent and open-circuit voltage of all-polymer solar cells can be superior compared to those of fullerene/polymer OPVs showed a bright future of all-polymer solar cells as a next generation of OPVs whereas observed low fill factors in the system suggests that the future studies have to focus on improving fill factors to achieve all-polymer solar cells that outperform the fullerene based OPVs. Fill factor is a morphology dominated property and is tightly related to the charge recombination process, including both geminate and bimolecular recombination. Mixed phases that can provide large interfacial area between donor and acceptor polymers are important to reduce the geminate recombination in the system due to the limited diffusion length of excitons, and well interconnected phase separated domains are also important for efficient charge transport and preventing bimolecular charge recombination. Therefore, further optimization of materials and device engineering to understand miscibility and phase separation kinetics in polymer/polymer blends and achieve this ideal polymer/polymer blend morphology are necessary to prevent charge recombinations and improve fill factor in the near future.

In addition, there are many remaining challenges to be addressed for commercialization of polymer electronic and photonics in the future. Most of the conjugated polymers have been synthesized using Suzuki or Stille coupling copolymerization, which involves tedious preparation of unstable and toxic organometallic reagents, and this is not suitable for large quantity manufacturing process. Moreover, batch to batch variation of such polymerizations with large polydispersity index causes more problems. Thus, development of green chemistry providing ways to avoid toxic reagents, simplify the synthetic route, and improve consistency in molecular weights of conjugated polymers will be an important future study topic. Furthermore, studies on large area devices fabricated utilizing low cost solution processing techniques (blade coating or roll-to-roll coating) are also desired for commercialization. A typical OPV devices fabricated in the lab, however, are in millimeter scale using spin coating technique, and device performance tends to be decreased dramatically by increasing the device area due to the increasing probability of defects and inconsistent film morphology.

VITA

Ye-Jin Hwang was born in Daejon, South Korea, on May 19, 1985. She earned a Bachelor of Science in Chemical Engineering, *summa cum laude*, in 2008 from Inha University, South Korea and a Master of Science in Chemical Engineering from the University of Washington, Seattle, in 2012. She pursued her Ph.D. degree in Chemical Engineering at University of Washington, and performed her research on polymer semiconductors for organic electronics and photonics under the guidance of Professor Samson A. Jenekhe. During her graduate studies, she was recognized by the American Chemical Society Polymer Division for Excellence in Graduate Polymer Research in 2014, and was a 2014 Graduate Student Award Finalist, Area 8E (Electronics and Photonics), American Institute of Chemical Engineers. She received the 2014 High Impact Publication Award from the Department of Chemical Engineering and three travel grants from The Graduate School Fund for Excellence and Innovation and The Clean Energy Institute, University of Washington. She is a member of the Materials Research Society, the American Chemical Society, the American Institute of Chemical Engineers, and the Korean-American Scientists and Engineers Association.

The following is the list of the author's publications:

1. **Hwang, Y. –J.***; Li, H.*; Courtright, B. A. E.; Subramaniyan, S.; Jenekhe, S. A. "Nonfullerene polymer solar cells with 8 % efficiency enabled by a highly twisted electron acceptor," *J. Am. Chem. Soc.* **2015**, *to be submitted*. (* Denotes equal contribution).

2. **Hwang, Y. –J.**; Earmme, T.; Murari, N. M.; Jenekhe, S. A. "Miscibility, Phase Separation, and Photovoltaic Properties of Naphthalene Diimide Copolymer/Poly(3-hexylthiophene) Blends," *in preparation.*

3. Li, H.*; **Hwang, Y. –J.***; Earmme, T.; Courtright, B. A. E.; Eberle, F. N.; Subramaniyan, S.; Jenekhe, S. A. "Fine Tuning the 3D Structure of Nonfullerene Electron Acceptors Towards High

Performance Organic Solar Cells," *Adv. Mater*. **2015**, *27*, 3266-3272. (*Denotes equal contribution).

4. **Hwang, Y. –J.**; Earmme, T.; Courtright, B.; Eberle, F. N.; Jenekhe, S. A. "n-Type Semiconducting Naphthalene Diimide-Perylene Diimide Copolymers: Controlling Crystallinity, Blend Morphology, and Compatability Toward High Performance All-Polymer Solar Cells," *J. Am. Chem. Soc.* **2015**, *137*, 4424-4434.

5. **Hwang, Y. –J.**; Courtright, B. A. E.; Ferreira, A.; Tolbert, S. H.; Jenekhe, S. A. "7.7 % Efficient All-Polymer Solar Cells," *Adv. Mater*. **2015**, *accepted.*

6. Li, H.; **Hwang, Y. –J.**; Earmme, T.; Kim, F. S.; Ren, G.; Subramaniyan, S.; O'Brien, C.; Jenekhe, S. A. "Polymer/Polymer Blend Solar Cells Using Tetraazabenzodifluoranthene Diimide Conjugated Polymers as Electron Acceptors," *Macromolecules* **2015**, *48,* 1759-1766.

7. **Hwang, Y. –J.***; Courtright, B. A. E.*; Jenekhe, S. A. "Ternary blend all-polymer solar cells: enhanced performance and evidence of parallel-like bulk heterojunction mechanism," *MRS Communications* **2015**, *accepted*. (* Denotes equal contribution).

8. **Hwang, Y. –J.***; Earmme, T.*; Subramaniyan, S.; Jenekhe, S. A. "Side Chain Engineering of *n*-Type Conjugated Polymer Enhances Photocurrent and Efficiency of All-Polymer Solar Cells," *Chem. Commun.* **2014***, 50,* 10801-10804. (* Denotes equal contribution).

9. Earmme, T.*; **Hwang, Y. –J.***; Subramaniyan, S.; Jenekhe, S. A. "All-Polymer Bulk Heterojuction Solar Cells with 4.8 % Efficiency Achieved by Control of Blend Morphology," *Adv. Mater.* **2014**, *26*, 6080-6085. (* Denotes equal contribution).

10. Murari, N. M.; Crane, M. J.; Earmme, T.; **Hwang, Y. –J.**; Jenekhe, S. A. "Annealing Temperature Dependence of The Efficiency and Vertical Phase Segregation of Polymer/Polymer Bulk Heterojunction Photovoltaic Cells," *Appl. Phys. Lett.* **2014**, *104*, 223906.

11. Earmme, T.; **Hwang, Y. -J.**; Murari, N. M.; Subramaniyan, S.; Jenekhe, S. A. "All-Polymer Solar Cells with 3.3% Efficiency Based on Naphthalene Diimide-Selenophene Copolymer Acceptor," *J. Am. Chem. Soc.* **2013,*135*, 14960-14963.**

12. **Hwang, Y. –J.**; Murari, N. M.; Jenekhe, S. A. "New n-type polymer semiconductors based on naphthalene diimide and selenophene derivatives for organic field-effect transistors," *Polym. Chem*. **2013**, *4*, 3187-3195.

13. **Hwang, Y. –J.**; Ren, G.; Murari, N. M.; Jenekhe, S. A. "n-Type naphthalene diimide-biselenophene copolymer for all-polymer bulk heterojunction solar cells," *Macromolecules* **2012**, *45*, 9056-9062.

14. **Hwang, Y. –J.**; Kim, F. S.; Xin, H.; Jenekhe, S. A. "New thienothiadiazole-based conjugated copolymers for electronics and optoelectronics," *Macromolecules* **2012**, *45*, 3732-3739.